Numerical Modelling of Proton Exchange Membrane Water Electrolysis

by

Michael Moore

A thesis submitted in partial fulfillment of the requirements for the degree of

Doctor of Philosophy

Department of Mechanical Engineering
University of Alberta

Abstract

Proton exchange membrane water electrolysis (PEMWE) is a promising technology in the drive to reach net zero for its ability to generate hydrogen from renewable energy, thereby allowing for large scale renewable energy storage. However, a number of issues prevent widespread deployment, such as the cost of the iridium based anode catalyst layer (ACL). An improved understanding of the processes occurring in the ACL will be needed to design and optimise the layer, and allow for lower loadings to be used. Recent studies have identified charge transport in the ACL as a limiting factor, particularly electron transport. In addition, the importance of two-phase flow in the anode is an open question, with mass transport effects being difficult to isolate and investigate. In this work numerical modelling is used to provide insights that can guide future research efforts, with a focus on the ACL.

As part of understanding charge transport in the ACL, the protonic conductivity of the layers needed to be measured. While the hydrogen pump technique has been successfully applied to catalyst-free carbon/ionomer layers, there is the possibility of protonic phase being bypassed by a reactive pathway in the unsupported catalyst layers used in PEMWE. Numerical modelling and experimental studies are used to prove the existence of the bypass in platinum/carbon based layers, and to assess its impact in iridium (Ir) and iridium oxide (IrOx) based layers. The high frequency resistance (HFR) is used to isolate the contact resistance between the catalyst layer and the membranes, and parametric studies show the importance of the electronic conductivity, in addition to the activity, of the catalyst layer. Unsupported layers comprised of IrOx were found to be unaffected by the bypass, while Ir black layers

were strongly affected.

Next, two-phase flow in the ACL of a PEMWE cell was investigated. The microstructure of the porous media was captured using a pore size distribution (PSD) model that allowed for the impact of parameters such as pore size and contact angle to be analysed. The model predicts that an Ir based ACL will produce bubbles close to the membrane that can induce very high gas pressures, however very little impact on performance is predicted. Significant displacement of water did not occur due to the pores in the ACL being very small and hydrophilic. Any mass transport losses that are induced in PEMWE cells are therefore likely caused by blanking of large sections of the ACL by bubbles in the PTL, as such it is recommended that experimental studies focus on characterising such events. Finally, the saturation in the PTL was found to be weakly coupled to that of the ACL, due to their very different intrusion curves.

Finally, the impact of the low ACL electronic conductivity was studied. First, the extremely low conductivity reported in the literature was validated using a novel ex-situ experiment that also revealed the dependence of the electronic conductivity on compression. Next, the model was used to breakdown the losses that are induced by the low ACL conductivity, which shows how it adds a significant resistance not captured by the HFR, and potentially adds significant error when estimating Tafel parameters. The model predicts that the catalyst loading of poorly conducting ACLs could be significantly reduced, explaining experimental trends that been reported in the literature. Finally, strategies to mitigate the poor ACL conductivity were explored experimentally, namely increasing cell compression and using electronically conducting polymers. Both improved performance significantly by increasing the active area and reducing the HFR, underscoring just how impactful the poor ACL electronic conductivity is on performance.

In summary, this work sought to understand the impact of charge and mass transport in the ACL of PEMWE cells. This was achieved by first developing a numerical

model to validate techniques used to measure the protonic conductivity of ACLs. An electrolyser model was developed that allowed for the parametrisation of the ACL microstructure and therefore understand its impact on two-phase flow. Finally, the model was used to assess the extent to which the ACL electronic conductivity affects cell performance, and discussed methods to mitigate this limitation and improve cell performance.

Keywords: numerical modelling, water electrolysis, hydrogen pump, anode catalyst layer, conductivity, two-phase flow

Preface

Parts of Chapter 2 of this thesis have been published as the following research article: M. Moore, M. Mandal, A. Kosakian, and M. Secanell, *Good practices and limitations of the hydrogen pump technique for catalyst layer protonic conductivity estimation*, ACS Applied Materials & Interfaces, vol. 15, no. 31, 2023. In addition, parts of this chapter were published in: M. Mandal, M. Moore, and M. Secanell, *Measurement of the protonic and electronic conductivities of PEM water electrolyzer electrodes*, ACS Applied Materials & Interfaces, vol. 12, no. 44, 2020. For the first work, I performed the literature review, designed the numerical and experimental study, performed the numerical simulations, performed data analysis and wrote the manuscript. M. Mandal contributed to the design of the study, performed the experiments, contributed to the data analysis and editing of the manuscript. A. Kosakian contributed to the development of the numerical model, data analysis and the editing of the manuscript. M. Secanell was the supervisory author and was responsible for the original concept, design of the study, and the writing and editing of the manuscript. For the second paper, M. Mandal was responsible for the literature review, design of the study, performed the experiments, data analysis and manuscript writing. I developed the numerical model and performed the simulations, analysed the data and contributed to writing and editing the manuscript. M. Secanell was the supervisory author, developed the original concept, contributed to the design of the study, and to the writing and editing of the manuscript.

Parts of Chapter 3 have been published as the following research article: M. Moore, M. Mandal, A. Kosakian, and M. Secanell, *Numerical study of the impact*

of two-phase flow in the anode catalyst layer on the performance of proton exchange membrane water electrolysers, Journal of The Electrochemical Society, vol. 170, no. 4, 2023. I performed the literature review, designed the numerical study, performed the numerical simulations, performed data analysis and wrote the manuscript. M. Mandal provided the experimental data, contributed to the data analysis and editing of the manuscript. A. Kosakian contributed to the development of the two-phase model, data analysis and the editing of the manuscript. M. Secanell was the supervisory author and was responsible for the original concept, design of the study, and the writing and editing of the manuscript.

Parts of Chapter 4 are being prepared for an upcoming publication: M. Moore, E. Beaulieu, M. Mandal, M. Secanell *A Numerical Study on the Impact of Anode Catalyst Layer Electronic Conductivity on Performance in Proton Exchange Membrane Water Electrolysis* (in preparation). I performed the literature review, designed the numerical and experimental studies, performed the numerical simulations, contributed to the experimental studies, performed data analysis and wrote the manuscript. E. Beaulieu, M. Mandal both contributed to the design of the experimental study, provided experimental data, contributed to the data analysis and editing of the manuscript. Marc Secanell was the supervisory author and was responsible for the original concept, design of the study, and the writing and editing of the manuscript.

To my parents

Acknowledgements

I would like to first acknowledge my supervisor, Marc Secanell. He first convinced me to come to Canada to study fuel cells for my Masters, and when I decided to do a PhD, I didn't have anyone else in mind. We had a lot of very interesting discussions on research and other topics, and just a few arguments that were even more interesting! I was very grateful for the support and guidance, and looking forward to working together in future.

I'm also very grateful for all my colleagues at the Energy Systems Design Lab. Special mention to Manas and Eric who put up with my demands and got me the experimental data I needed and provided a lot of discussion and insights. I also have to mention Aslan who helped tremendously in the model development and put up with having me as a roommate, especially during the lockdown! Everyone at the ESDL was a pleasure to work with, and I'll always remember the beers after work, trips to restaurants from different countries and especially the lab trips to the Rockies.

I acknowledge the financial support from Future Energy Systems (FES). As a part of the University of Alberta Future Energy Systems research initiative, this research was made possible; thanks to funding from the Canada First Research Excellence Fund (https://futureenergysystems.ca; Grant No. T06-P04).

Finally, I'd like to thank my family who have given me constant support during my travels. In particular, I like to thank my parents for helping me get to this point, with all the help and advice that I could ever need.

Table of Contents

List of Tables

List of Figures

List of Symbols

Latin

A	electrode area
A_v	volumetric active area
a_w	water activity
$c_{H_2}^{ref}$	reference hydrogen concentration
C_{dl}	double layer capacitance
c_{H_2}	hydrogen concentration
c_{tot}	total concentration
D_{λ}^{eff}	sorbed water diffusion coefficient
$D_{H_2}^{eff}$	effective hydrogen diffusion coefficient
D_{wv}^{eff}	effective water vapour diffusion coefficient
e^-	electron
F	fraction of hydrophobic or hydrophilic pore space
f	fraction of pore space assigned to a particular mode
H^+	proton
H_2	hydrogen
H_2O	water
i	geometric current density
j	volumetric current density
j_0	exchange current density
k_{λ}	rate of adsorption/desorption of water into the ionomer
k_g	gas permeability
k_l	liquid permeability

L_{CL} catalyst layer thickness

n_d electro-osmotic drag coefficient

O_2 oxygen

p_c capillary pressure

p_g gas pressure

p_l liquid pressure

r_c critical radius

R_{ct} charge transfer resistance

R_e electronic resistance

R_{mem} membrane resistance

R_p protonic resistance

S Source term

s standard deviation of particular mode

s_L liquid saturation

T temperature

$X(r)$ normalised volume of liquid invaded pore space

x_{H_2} hydrogen mole fraction

x_{wv} water vapour mole fraction

Greek

α_1 transfer coefficient of reaction one

α_2 transfer coefficient of reaction two

α_a anodic transfer coefficient

α_c cathodic transfer coefficient

ΔG^0 free energy of activation

ΔG^0_{ad} free energy of adsorption

η overpotential

λ sorbed water content

λ_{eq} equilibrium water content

λ_{PSD} pore interconnectivity

μ	porosity network constant
μ_g	gas viscosity
μ_l	liquid viscosity
ϕ_m	ionomer potential
ϕ_s	solid potential
ρ_g	gas density
ρ_{ion}	ionomer density
ρ_l	liquid density
σ_m^{eff}	effective protonic conductivity
σ_p	membrane conductivity
σ_s^{eff}	effective solid conductivity
θ	contact angle
θ_H	hydrogen coverage
θ_O	oxide coverage
ε_p	layer porosity
ε_p^{th}	layer porosity threshold

Abbreviations

ACL Anode catalyst layer.

CCL Cathode catalyst layer.

CCM Catalyst coated membrane.

CL Catalyst layer.

CV Cyclic voltammetry.

ECSA Electrochemical active surface area.

EIS Electrochemical impedance spectroscopy.

EW Equivalent weight.

FF Flow field.

GDL Gas diffusion layer.

HER Hydrogen evolution reaction.

HFR High frequency resistance.

HOR Hydrogen oxidation reaction.

ICR Interfacial contact resistance.

IL Intermediate layer.

LFR Low frequency resistance.

LGDL liquid/gas diffusion layers.

MEA Membrane electrode assembly.

MPL Microporous layer.

OER Oxygen evolution reaction.

ORR Oxygen reduction reaction.

PEM Proton exchange membrane.

PEMFC Proton exchange membrane fuel cells.

PEMWE Proton exchange membrane water electrolysis.

PSD Pore size distribution.

PTE Porous transport electrode.

PTL Porous transport layer.

RDE Rotating disk electrode.

RH Relative humidity.

SEM Scanning electron microscopy.

TKK Tanaka Kikinzoku Kogyo.

Chapter 1

Introduction

1.1 Motivation

The latest Intergovernmental Panel on Climate Change (IPCC) Special Report [1] reported that even under the most optimistic mitigation scenarios, it was more likely than not that global temperatures would reach 1.5℃ above pre-industrial levels between 2030 and 2052, leading to an increased frequency of extreme weather events such as floods and droughts. The trend is attributed to anthropogenic emissions, in particular carbon dioxide (CO_2) and methane (CH_4). In order to limit the global temperature change to 1.5℃ by 2100 with limited overshoot, CO_2 emissions would need to decline by 48% by 2030, reaching net zero by 2050. To achieve net zero emissions, the International Energy Agency (IEA) [2] predicts that 66% of primary energy should be provided by renewable energy sources, such as solar, wind, hydro and geothermal, with CO_2 emissions from traditional technologies being offset by carbon capture and storage and carbon dioxide removal.

Development of enabling technologies, such as energy storage, heat pumps and electric vehicles, is required to aid the further integration of solar and wind generation into the energy systems, as their variability complicates widespread deployment. Energy storage is currently primarily in the form of pumped hydro (160 GW of storage in 2018), while battery storage is estimated to comprise of 3 GW [3]. The IEA report cites renewable electrolysis of hydrogen as an important pathway for sector

integration of renewable energies. The global hydrogen economy is estimated to grow from 90 million tonnes today to 530 million tonnes in 2050, with 60% of the hydrogen generated from electrolysis.

Hydrogen storage offers a number of advantages compared to the more commonly used batteries, such as longer storage time scales and flexibility [4]. The latter refers to the fact that produced hydrogen can be used to generate electricity via a fuel cell, to produce synthetic hydrocarbons, and as a feedstock for many industrial processes such as ammonia production. The main electrolysis technologies are differentiated based on the operating temperature and the ion exchanged during operation. The three main technologies are: proton exchange membrane (PEM), alkaline and solid-oxide [5–9]. Solid-oxide electrolysis offers the possibility of high efficiency, as it operates at very high temperatures, and does not use expensive noble metal catalysts. The operating temperature presents a significant challenge to the materials used, resulting in durability issues. Alkaline electrolysis typically operates at low temperatures (below 100℃), and is based on transport of hydroxide ions across a membrane or diaphragm that separates produced hydrogen and oxygen. This form of electrolysis using a diaphragm is the most developed, and numerous commercial products are available [9, 10]. Non-noble metal catalysts and materials are used, contributing to a relatively cheap cost, however the low cell conductivity prevents high current density operation, and the crossover rates of the product gases result in low hydrogen purity, which necessitates low pressure operation and prevents partial load operation. Partial load operation is desirable as fluctuating energy demand and weather conditions will result in renewable energy systems producing electricity over a wide power range. The development of anion exchange membranes (AEM) over the past decade is fueling a renaissance in alkaline technology as these can provide high conductivity and gas purity [11]. However, AEMs still lack durability and are currently in the initial R&D stage.

While it has not been in development for as long as alkaline electrolysis, interest in

proton exchange membrane water electrolysis (PEMWE) is growing in recent years as demonstrated by Carmo et al. [7], and a number of commercial products are available [9, 12]. This form of electrolysis operates at low temperature, and transport protons through a perfluorosulphonated ionomer membrane, such as Nafion, which offers a number of advantages. The low crossover of hydrogen to the oxygen electrode allows the electrolysis to operate at low partial loads (when there is less diluting oxygen being produced), and at higher hydrogen pressures, which lowers the requirement on the hydrogen compressor. The membrane can be thinner, which, along with the higher mobility of the proton compared to the hydroxide ion, results in lower ohmic losses and improved performance at higher current densities. The latter allows for a more compact design and lower capital costs. Therefore, PEMWEs will be the focus of study in this work.

PEMWEs suffer from a number of limitations which prevent further commercialisation. The anode of the electrolyser is highly acidic, wet, hot and operates at a high potential. As such, the materials must exhibit high resistance to corrosion, particularly given the desire for long term operation. Structural components in the anode are machined from titanium, while the catalyst used is typically iridium oxide in the anode, and platinum in the cathode. These components, along with membrane, are estimated to make up 40% of the cost of the electrolyser stack [13], with the rest being the balance of stack and assembly. The design and optimisation of the individual cells will be crucial to maximising electrolyser efficiency and minimising the costs. Doing this experimentally is expensive and time consuming, so the overall goal of this work is to use numerical modelling to first understand the underlying phenomena occurring within the cell, such as transport of water and charged species, to then allow for the optimisation of the components and operating conditions of the cell.

1.2 Background

PEM electrolysers are devices that consume electricity in order to produce hydrogen and oxygen from the electrochemical splitting of water [10, 14, 15]. The overall reaction and two half-cell reactions are:

$$\text{Overall: } 2H_2O \rightleftarrows 2H_2 + O_2 \tag{1.1}$$

$$\text{Anode: } 2H_2O \rightleftarrows O_2 + 4H^+ + 4e^- \tag{1.2}$$

$$\text{Cathode: } 4H^+ + 4e^- \rightleftarrows 2H_2 \tag{1.3}$$

The reaction in the anode is the oxygen evolution reaction (OER), while the hydrogen evolution reaction (HER) occurs in the cathode. The half cell reactions show the requirements on the electrolyser cell. The anode must be supplied with water (typically in liquid form) and the produced oxygen must be removed. Pathways are provided for electron transport, which is applied through an external power supply, and for proton transport, which is through a conducting membrane that separates the anode from the cathode. Similarly, pathways are required for the charged species in the cathode, which must also remove the produced hydrogen.

Figure 1.1 shows the layout of a PEM electrolyser, its components and the primary transport processes. At the centre of the cell is the membrane, typically Nafion. The membrane needs to be thick enough to ensure there is not a significant crossover of gases, however a thicker membrane will increase the overall ohmic resistance of the cell. This resistance comes from the transport of ions from the anode to the cathode and is one of the largest sources of resistance in the cell. The Nafion membrane is comprised of a Teflon backbone that includes sulphonic acid sidechains. The hydration of the membrane allows for the formation of hydronium ions which provide good ionic conductivity.

Deposited on either side of the membrane are the catalyst layers (CL), in which the reactions occur. Typically, platinum is used as the catalyst in the cathode for

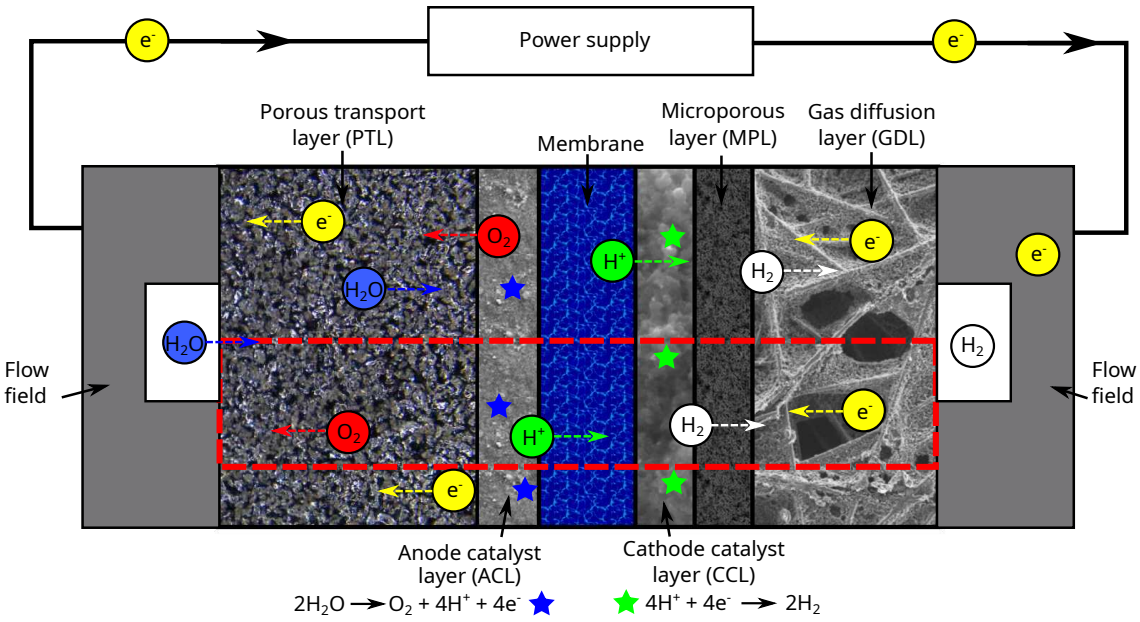

Figure 1.1: Schematic of the PEMWE cell, showing the main transport processes and the computational domain (red box).

the hydrogen reaction. Due to the facile nature of the reaction, low loadings of less than 0.1 mg/cm$^2_{geo}$ can be used [16]. The low loading is achieved by depositing the platinum on carbon particles that provide structural support and pathways for electron transport. An ionomer such as Nafion is used to provide an ionic pathway, and the layers are designed to have a porosity that allows the produced hydrogen to escape. A carbon fibre based layer called a gas diffusion layer (GDL) provides further structural support to the catalyst layer and ensures an even distribution of gases and current within the electrode. The flow field (FF) is made of ribs and channels that provide pathways for the current and the hydrogen respectively. The cathode electrode does not make a significant contribution to performance losses in an electrolyser.

The anode electrode catalyses the oxygen evolution reaction, a much more sluggish reaction compared to the HER. Iridium oxide is typically used as the catalyst as it

exhibits good activity, along with good durability at the high potentials and acidity seen in the anode. Due to the higher kinetic losses, higher loadings are commonly used compared to the cathode, 1 mg/cm$^2_{geo}$ and higher [16]. There is a lack of suitable supporting materials that can be used to increase surface area [17], as carbon does in the cathode. As a consequence of the lack of support in most cases, the catalyst is also providing the structural support and electronic transport, which is partly the reason for the higher loadings used. An ionomer is used for proton transport and the layer porosity provides pathways for the water to access the catalyst surface and for oxygen to leave. As carbon based GDLs cannot be used on the anode, a porous transport layer (PTL) is used instead, which is commonly made from sintered titanium powders or titanium meshes and felts. The FF is also made from titanium, and allows for the transport of water into the cell and oxygen out. The anode catalyst layer (ACL) is a significant source of losses: the kinetic losses are much larger than the cathode, the iridium oxide layer and titanium PTL incur significant ohmic losses, and the two phase water/oxygen mixture is thought to incur mass transport losses.

An example breakdown of the cost of the components was recently provided by the International Renewable Energy Agency (IRENA) [13] and is shown in Figure 1.2. Note that the breakdown considered the entire system, with the balance of plant accounting for 55% of the total cost. The balance of plant is not included in Figure 1.2, so the figure only shows the remaining 45% from the stack. This thesis will focus on the single cells that the stack is comprised of, as a detailed analysis of the power conversion and control systems that make up the balance of plant are beyond the scope of this work. The cost of the stack is primarily due to the flow fields. In a stack, these layers are termed bipolar plates as they separate the anode and cathode. Complex fluid dynamics are occurring within the channels of the bipolar plates, the modelling of which is beyond the scope of this work.

The porous layers and the catalyst coated membrane (CCM) contribute approximately 18.6% of the total system cost due to the use of materials such as iridium

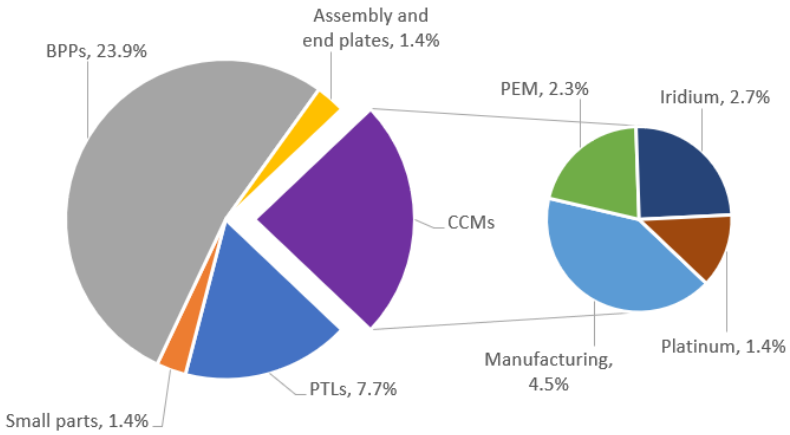

Figure 1.2: Breakdown of the stack costs, with the indicated percentages based on full system costs. The stack costs are 45% of the total cost, with the remainder attributed to the balance of plant that is not shown. Reproduced from IRENA with permission [13].

and titanium. The use of an iridium catalyst is particularly problematic despite only contributing 2.7% to the total cost, due the scarcity of the supply. Iridium is primarily obtained as a by-product of platinum mining, with only 7-8 tons produced per year [18]. As such, minimising the usage of iridium is of paramount importance to reaching net zero emissions by 2050, as 3.6 TW of electrolyser capacity is estimated to be required. Clapp et al. [18] estimated that the iridium loading would need to fall by more than an order of magnitude to 0.1 mg/cm^2 to achieve such installed capacities, coupled with other factors such as improved catalyst activity, catalyst recycling and membrane thinning. As such, the focus will be on understanding the phenomena occurring within the ACL and its interaction with the PTL so that these layers can be optimised and their cost minimised.

1.2.1 Experimental characterisation

There are a number of key indicators that are used to characterise electrolyser performance, such as efficiency at a given power, capital expenditure, and degradation rates [9]. The United States Department of Energy developed the Energy Earthshots,

a series of initiatives designed to accelerate the energy transition, which includes the Hydrogen Shot. This initiative set a target of producing clean hydrogen at a price of $1 per kilogram by the end of the decade, a reduction of 80% compared to the cost in 2021 [19, 20]. The kilograms of hydrogen produced is determined by the current at which the electrolyser operates, while the power is determined by the product of the applied voltage and current. Therefore, the relationship between the applied current and the resulting voltage is the main performance indicator for electrolysers, which is displayed on a polarisation curve.

Polarisation curve

A polarisation curve is obtained by measuring the potential at a particular current at steady state, an example of which is shown in Figure 1.3. The reversible potential is given by the Nernst equation and corresponds to the potential developed across the cell when zero current is drawn for the particular redox reaction occurring in the cell [21]. This potential depends on the operating conditions of the cell. The polarisation curve then shows three distinct regions: kinetic, ohmic and mass transport, where particular losses dominate. The kinetic region is at low overpotentials, is exponential in nature and corresponds to the losses incurred from the two electrochemical reactions in the cell: the HER in the cathode and the OER in the anode. At higher current densities, the losses from charge transport in the cell start to dominate over the kinetic losses, and the polarisation curve becomes linear. These ohmic losses are determined by the conductivity of the materials making up the layers. Mass transport includes the treatment of two phenomena: the advective transport of bulk gas and liquid phases and a mixture of the two, and the transport of individual species via diffusion. Many works in the literature examine the impact of channel design and water flow rates in the channel; research of this nature is beyond the scope of this work. Of interest is the transport in the porous media and capturing the impact of the gas phase in addition to the water. In particular, presence of gas bubbles in the

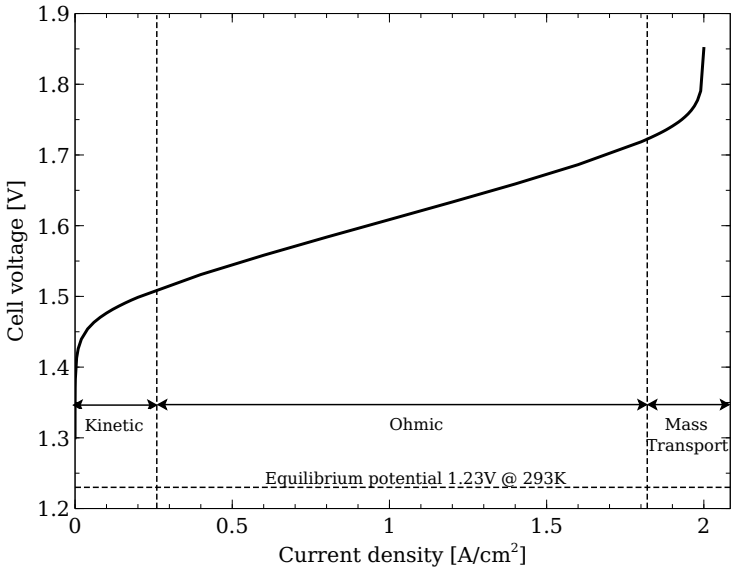

Figure 1.3: Representative polarisation curve for an PEM electrolyser.

anode can block water from reaching the active sites and reduce the utilisation of the catalyst, thereby reducing the cell performance. There is some uncertainty as to how impactful mass transport losses are, as will be discussed later.

Significant reduction of each of these losses is required in order for PEMWE to become a cost-effective option for hydrogen production. The performance is often broken down into these individual components when characterising a cell [22–25]. This breakdown requires fitting of a simple 0-D model to experimental data, that results in the aggregation of losses. For example, the ohmic losses of the numerous individual layers cannot be deconvoluted, limiting the insight that can be gained. A multi-dimensional model can be used to further breakdown the losses into contributions from the individual layers and processes, which helps guide further research.

Electrochemical impedance spectroscopy

It is difficult to deconvolute the individual processes occurring within the cell using a polarisation curve, as the performance obtained is the summation of a number of losses. Electrochemical impedance spectroscopy (EIS) can be used to provide further

insight [26–30], by superimposing sinusoidal voltage or current signals at varying frequencies and measuring the sinusoidal response. Different processes will proceed at different time scales, for example the movement of charged particles is significantly faster than the movement of gaseous species. Therefore mass transport losses can be isolated by studying the cell response to AC signals at low frequencies, while charge transport losses dominate at high frequencies. The signal is applied over a wide spectrum of frequencies, typically from 100 kHz to 1 mHz. The resulting impedance at each frequency, which will have a real and imaginary component, can be obtained from the ratio of the voltage signal to the current signal. Equivalent circuits using electrical circuit elements are typically applied to interpret the impedance, e.g. resistors represent ohmic losses in the layers and charge transfer resistances, and capacitors represent the double layer between the proton and electron conducting phases. Of particular interest is the high-frequency resistance (HFR) which is the resistance obtained at high frequency (above 1 kHz) for which the imaginary impedance is zero. The HFR is typically considered to represent the total resistance of the cell.

Cyclic voltammetry

In order to determine the electrochemical active surface area (ECSA) of the catalyst, cyclic voltammetry (CV) is commonly used [27, 28]. During a CV, the potential of the working electrode is scanned at a fixed rate (typically 10-40 mV/s) and the resulting current is measured. This is generally done with hydrogen in the reference electrode and nitrogen in the working electrode. The current will include the charging of the double layer in the working electrode but more importantly, the charge associated with species adsorbing onto the surface of the catalyst to form a monolayer. At potentials close to the standard hydrogen electrode (SHE), a hydrogen monolayer adsorbs onto platinum and other platinum group metals. At more positive potentials various oxides can form, which can also be used to estimate the ECSA and to study the oxidation state of the catalyst.

1.3 Literature review

There are a number of key processes occurring in the cell of a PEMWE electrolyser that contribute to the losses revealed in the polarisation curve and EIS spectra. In particular, the following phenomena are of interest: a) the reaction kinetics in each electrode, b) the transport of electrons and protons in the solid and ionomer phase respectively; and, c) the transport of reactants (water) and products (hydrogen and oxygen). These phenomena have been studied in detail experimentally, as will be described in the sections that follow. A number of issues will be identified that are thought to limit PEMWE performance that will be the focus of this work, as numerical modelling can be used to provide deeper insights into the mechanisms behind the losses.

Numerical modelling is a powerful tool in electrochemical research that is beginning to gain popularity in the electrolyser literature [7, 31, 32]. Models are differentiated by their dimensionality and by the treatment of the physical processes. This field is relatively new, however many of the processes described here are similar to those seen in PEM fuel cells. The majority of the PEMWE models seen in the literature are 0-D models [33–56]. They provide limited insight into the phenomena occurring within the cell, as distributions of the potentials, reactants and products are not available. Instead they are typically used for parameter estimation or as part of a larger system model [46–50], to investigate bubble dynamics [51–53] or for crossover modelling [54–56]. Multi-dimensional modelling is required in order to investigate a number of issues highlighted in this work, such as determining the reaction distribution within the anode catalyst layer and capturing two-phase flow in the anode. There are a few multi-dimensional models in the literature [57–72], which will be used as a basis for the numerical model in this work.

1.3.1 Activation losses

Experimental studies

The activation losses are incurred by the HER on the cathode side and the OER on the anode. In the cathode, the platinum/carbon based electrodes that have been studied extensively in PEM fuel cells are typically used. The overpotentials incurred from the HER are significantly smaller than other losses, due to the fast kinetics of the HER on platinum catalysts [73, 74]. The use of platinum group metals in the cathode is a considerable expense, leading to the investigation of alternative catalysts such as transition metal compounds [75, 76]. These catalysts are not yet widely used, with a particular need to demonstrate stability limiting their application [77]. The evolution and oxidation of hydrogen on platinum catalysts has been studied experimentally [78–80] and theoretically [81–86]. The reaction mechanism is known to follow the Tafel-Heyrovsky-Volmer pathway [86]. For hydrogen evolution, the Volmer reaction involves the absorption of a proton onto the catalyst surface, while the Tafel and Heyrovsky reactions involve the chemical and electrochemical desorption of the hydrogen molecule from the surface, respectively.

In contrast to the HER, the OER induces significant overpotentials and is a major source of performance loss. The highly corrosive nature of the anode where the OER occurs also causes significant catalyst and supporting material degradation, making the investigation of the OER a highly active area of research in PEM electrolysis [8, 77, 87–91]. There are few materials that can catalyse the OER without degrading rapidly, the most commonly used OER catalyst is iridium and its oxides [92–96]. The high cost and rarity of iridium has seen numerous attempts to improve its activity and stability, including changing its structure [97, 98], using a support such as titanium [99] and ATO [100], changing how the catalyst is produced [101] and how the catalyst layers are fabricated [102]. The mechanism for the OER is not well understood, with a number of mechanisms proposed though none are considered to be experimentally validated [88,

90, 91]. The mechanism is complicated by the degradation of the IrO_x catalyst which is changing oxidation state continuously under the working potential of the electrode, some of which lead to dissolution [103, 104]. In addition, the reaction mechanism may lead to a change in the Tafel slope, which has been observed experimentally [105, 106], and should be considered in any modelling works.

Numerical studies

Almost all the models in the literature used either the Butler-Volmer or Tafel equation to describe the reaction kinetics in both electrodes [57–69, 71, 72]. The focus in these works with regard to the kinetics is primarily on the OER, as the HER does not cause significant potential losses. There are a number of models in the literature that describe the hydrogen reaction [84–86] beyond the standard Butler-Volmer model, however the theoretical model from the group of Wang et al. [81–83] captures the two pathways in the Tafel-Heyrovsky-Volmer mechanism. The model is applicable to both the HOR (hydrogen oxidation reaction) and HER, and can reproduce experimentally obtained polarisation curves, while being relatively simple to implement. Hence it will be used to model the HER in this work.

When using the Butler-Volmer model for the OER, the exchange current density is typically used as a fitting parameter [57–63, 65, 66, 69], as part of a parameter study [64, 67] or taken as a constant from another source [68, 71, 72], with Aubras et al. [57] noting a range of exchange current densities in the literature that span several orders of magnitude. The transfer coefficient is given less attention, with some authors fitting it [60, 66, 68], or assuming a value, which may be taken from the literature [57, 59, 67, 71, 72], with values varying between one-half to two. There is little consensus as to the correct treatment of the OER kinetics; necessitating the use of a model that has been shown to reproduce kinetic data for the OER obtained from ex-situ experimentation.

Tracking the oxidation states and their interactions with the reactants and products

is complex and there are not many multi-step reaction mechanism models, such as that proposed by Wang et al. [83] for the HER, that have been proposed for the OER. Oliveira et al. [107] developed a model that considered O_{ads}, OH_{ads}, OOH_{ads}, and H_2O_{ads} intermediates; however, the model requires an additional nano-scale model that accounts for anion adsorption. Garcia-Osorio et al. [108] considered the same intermediates plus $O_{2,ads}$ for their model, developed to study the OER on 'inactive' catalysts used in wastewater treatments. The model is generic enough that it could be fit to IrO_x data, however, the authors noted the difficulty experienced in fitting the model. It also does not account for catalyst degradation. Ma et al. [106] used a simplified model that considered only O_{ads} using the same methodology used by Wang et al. [109]. The model has only two intermediate reactions that were stated to include the formation of other species, which were the same as those considered by Oliveira et al. [107]. The model was fit to kinetic data for an IrO_2 catalyst immersed in a sulphuric acid solution. The model is simple, so it does not account for the dissolution of the catalyst, however it does capture the change in Tafel slope that is seen experimentally. This model was implemented by Wrubel et al. into their 2D model [110], however the impact of the change in Tafel slope was not a focus of the work. An aim of this thesis is to integrate this multi-step model into a multi-dimensional PEMWE model as it is hypothesised to be needed to accurately track changes in Tafel slope that would otherwise be misdiagnosed as mass transport losses.

1.3.2 Ohmic losses

Experimental studies

On the cathode side, the porous layer and CL are the same as those used in proton exchange membrane fuel cells (PEMFC) and their conductivities have been studied in detail. These components have high conductivity and will not have a major impact on the cell performance. The membrane and PTL are considered the main source of ohmic resistance in the cell, with less attention paid to the ACL [6, 7, 17, 31]. Ohmic

losses in the ACL will be incurred from both the protonic and electronic phases, with the former being studied extensively in the PEMFC literature as it is a major source of performance [111]. However, in recent years there has been an increasing focus on the electronic conductivity of the catalyst as a possible limiting factor in ACL design, with Bernt et al. [112] noting that the catalyst conductivity is often not taken into account in catalyst studies. It is possible, therefore, that both phases will impact PEMWE performance and need to be studied.

The recent interest in the ACL electronic conductivity as a limiting factor in PEMWE performance tends to focus on the interaction between the ACL and the PTL, which was precipitated by the works from the group of Zhang et al. [113–118]. These works used a transparent cell and tunable liquid/gas diffusion layers (LGDL) that allowed for the ACL to be visualised during operation. It was observed that bubble formation from the OER only occurred at the interface between the LGDL and the ACL, which can be explained by the low in-plane electronic conductivity of the ACL preventing electrons from reaching parts of the ACL far from the LGDL. When a platinum black catalyst was used, bubble formation was observed within the LGDL pore, as the platinum has a higher conductivity, allowing for a greater utilisation of the catalyst. Bernt et al. [112] used thermal annealing to vary the conductivity of a novel amorphous hydrous iridium oxide to obtain a more crystalline form of the iridium oxide. While a higher conductivity catalyst was obtained, the activity was reduced as compared to the amorphous hydrous catalyst, which was also observed by Karimi et al. [119]. For Bernt et al. [112] the focus was on the interaction between the ACL and the PTL, with the authors noting extremely poor performance for the novel catalyst with a sintered titanium PTL, but a performance superior to a commercial CCM when the PTL has a Pt coating. After thermal annealing, the novel catalyst had a comparable performance to the commercial CCM when combined with an unplatinised standard PTL, which was attributed to the improved electronic conductivity, while also having a significantly lower Ir loading. Kroschel et al. [120]

used a modified rotating disk electrode (RDE) that included a PTL as part of the electrode and had similar conclusions. The choice of PTL was found to impact cyclic voltammetry scans and Tafel plots. These experiments typically only draw current densities of the order of milliamps, indicating that the electronic conductivity is extremely low. Alia et al. [121] studied the electrochemical surface area (ECSA) of a number of common catalysts using an RDE and noted that the ECSA was lower at higher loadings, speculating that it was due to electronic isolation of the layer. Ma et al. [122] investigated Ir layers of varying thicknesses and noted a reduced performance at very low and high loadings, the former of which was attributed to poor catalyst connectivity, and the latter to increased ohmic resistances in the CL as the layer is thicker. Rozain et al. [123] and Babic et al. [124] also performed a loading study and came to the same conclusions, with proton transport assumed to be the primary cause of the increased ohmic resistance. Rozain et al. [123] also noted that the volumetric charge measured on IrO_2 CLs plateaued with increasing loading, which may be indicative of a poor electronic conductivity preventing thicker layers from being fully utilised, though the authors attributed it to the reduced access of protons to active sites for thicker layers.

Mandal et al. [125, 126] measured the electronic through-plane conductivity of an ACL comprised of Ir and IrOx catalysts, and showed that the IrOx electronic conductivity was two to three orders of magnitude lower than the protonic, while the electronic was ten times higher for the Ir. Such a low electronic conductivity for the IrOx CLs explains the very low utilisation of the ACL observed by Mo et al. [113] and the origin of the interfacial contact resistance with the PTL. The difference between the Ir and IrOx CLs is also expected based on the thermal annealing studies performed by Karimi et al. [119] and Bernt et al. [112]. Schuler et al. [127] showed a significantly higher conductivity for the TiO supported IrOx (the catalyst used by Mandal et al. was unsupported), however a four point probe method was used, therefore only the in-plane conductivity was measured. The difference is conductivity

was approximately five orders of magnitude, which can be attributed to a difference in the catalyst, ionomer loading and the direction of the measurement. A three order of magnitude difference in the electronic conductivity was also observed between the in- and through-plane directions by Ahadi et al. [128] for carbon based catalyst layers used in PEM fuel cells, so the low conductivity of the IrOx in the through-plane is not unreasonable. That the IrOx electronic conductivity was so low is not normally seen in PEMWE or PEMFC electrodes, making it is difficult to explain why the IrOx based ACL exhibited reasonable performance. Numerical modelling will be used to determine the voltage losses in the cell to understand how much performance is lost through the electronic phase.

The electronic conductivity has also been estimated by measuring the powder conductivity of the catalyst. The powder conductivity is typically measured by compressing the catalyst in a small pellet and measuring its resistance [119]. At a certain compression, the resistance is independent of the compression, which is used to calculate the bulk conductivity of the sample [129]. The powder conductivity can range significantly, from 10^{-6} to 10^{-1} S/cm depending on the morphology and the oxidation state [130], therefore the difference in conductivity measured by Mandal et al. may be reasonable. In addition, the compression used can be very high, potentially higher than that experienced in a PEMWE cell. Bernt et al. [112] used a compression of 1 GPa to obtain the conductivity of one catalyst, while Bohm et al [130] and Hao et al. [131] used 15 and 30 MPa respectively. That such a high pressure was used may indicate that the catalyst conductivity varied significantly with compression. If the catalyst powder varies with compression, the ACL effective conductivity will likely show a higher variance, as the addition of the ionomer will further reduce catalyst connectivity. A compression dependent conductivity in the ACL will have implications on the performance of cells under different compressions, and on the interface between the PTL and ACL, as the ACL in contact with the PTL will have a higher conductivity than the ACL that is not in contact.

The protonic conductivity of the ACL has also seen limited research. Ionomer loading studies have been performed, with the primary purpose of finding a loading that achieves the optimum performance [24, 132]. These works estimated the protonic resistance of the ACL using a basic numerical model, however did not directly measure the protonic conductivity. Babic et al. [133] measured the ACL resistance using EIS, however it was found to depend on the morphology of the PTL used, possibly due to variations in the water content of the ionomer phase when using each PTL. Mandal et al. [125, 126] measured the protonic conductivity of an ACL directly using the hydrogen pump method proposed by Iden et al. [134, 135], and found that the protonic conductivity was of a similar order of magnitude to the Pt/C layers used in PEMFC. In addition, the relationship between the ionomer loading and conductivity varied significantly depending on whether an iridium black or iridium oxide was used, which maybe an artifact of the measurement technique. This observation will be discussed further in a later section.

An interesting consequence of the large difference in electronic and protonic conductivity for the IrOx catalyst measured by Mandal et al., is that most of the current density in the ACL will likely be produced very close to the PTL interface. The impact of this reaction distribution has been discussed in the literature [60, 124, 128, 136–138], and it may have a significant impact on how much of the catalyst layer is utilised. The idea of poor catalyst utilisation caused by the poor electronic conductivity of the catalyst has gained interest in recent years [113, 120, 128, 139–141], however it is often in the context of the in-plane conductivity and a poor contact between the PTL and the ACL [113, 120, 139], the impact in the through-plane direction is only discussed qualitatively [140, 141]. Ahadi et al. [128] provided an order of magnitude analysis of the impact of a poorly distributed reaction in a PEM fuel cell. They noted the need for a more quantitative approach that would require numerical modelling to capture the various ohmic and kinetic losses, and thereby quantify the impact of the reaction distribution. This work hypothesises that for an ACL with a very poor

electronic conductivity a reduction in catalyst loading (e.g. from 1 to 0.25 mg/cm^2) would have a minimal impact on the kinetic region of a polarisation curve, as the reaction is not occurring in much of the layer. The performance of the thinner layer can also be improved in the ohmic region as charge transport through the ACL is reduced. A number of authors have performed ACL catalyst loading studies, in which one or both of these trends are observed. Jang et al. [142] performed a loading study with an Alfa Aesar Premion catalyst and their results clearly demonstrate both trends discussed. Loadings of 0.5, 1 and 1.5 mg/cm^2 have very similar performance in the kinetic region, while in the ohmic region loadings of 0.25 and 0.5 mg/cm^2 significantly outperform loadings of 1 and 1.5 mg/cm^2, with the higher loadings exhibiting a higher slope. The electronic conductivity of this catalyst has not been measured to the author's knowledge, however Cruz Ortiz et al. [143] showed that the electronic conductivity of this catalyst does limit performance. Some studies found that the performance in the kinetic region changed with loading, while the ohmic region did not show the predicted trend. Fujita et al. [144] tested an IrOx catalyst at 0.1 and 2 A/cm^2 for different loadings and found the performance at each current to be independent of the loading once the loading was higher than 0.3 mg/cm^2. Rozain et al. [123] had similar results: at 0.12 A/cm^2 the performance is independent of loading above 1 mg/cm^2, whereas at 1 A/cm^2 independence is achieved above 0.5 mg/cm^2. Taie et al. [102] investigated ultra-low loaded ACLs made with an IrOx catalyst and show that loadings of 0.17 and 0.039 mg/cm^2 have near identical performance in the kinetic region, while the ohmic resistance increased with increasing loading. The opposite trends have also been observed, where there is an expected change in performance in the kinetic region, but the performance gets worse in the ohmic region. Bernt et al. [145] performed a loading study with a 75 wt% IrO_2 catalyst supported on TiO_2, which Schuler et al. [127] showed to have a relatively high conductivity, and showed a minor change in the kinetic region that was expected from a simple Tafel analysis, while the performance worsens at high current densities. Similarly, Bühler et al. [146]

studied IrO_2 ACLs applied to the PTL (porous transport electrode or PTE) rather than the membrane and showed a higher slope in the ohmic region for a loading of 1.9 mg/cm^2 as compared to 1.4 mg/cm^2, with the difference in the kinetic region explained by the Tafel analysis. Based on the studies presented, it is not clear how the performance varies with catalyst loading, and more research is needed in this area. Studying the reaction distribution, particularly in the through plane direction, and its impact on catalyst loading is not easy to do experimentally. Numerical modelling can be particularly helpful in this regard, hence studying the impact of the reaction distribution will be a focus of this work.

It is further hypothesised in this work that the impact of the low ACL conductivity can be mitigated by compressing the cell, due to the aforementioned discussion on the compressions used during powder conductivity measurements. A number of works have demonstrated that higher cell compression can improve performance, though none expressly linked the improvement to increased ACL conductivity. Al Shakhshir et al. [147] found that increasing the compression improved the performance for all current densities, with improvements seen in the HFR and charge transfer resistance obtained from EIS. Borgardt et al [148] showed that the optimum compression was 2.5 MPa when using a standard Ti sinter, with performance reduction at higher compression attributed to reduced proton conductivity in the membrane as it is compressed. Frensch et al. [149] used an IrO_2 ACL with an additional iridium black interlayer between the ACL and PTL to improve the contact resistance and showed a monotonic improvement in performance with increasing pressure from 0.77 - 3.45 MPa. Martin et al. [150] used different pinches on the cathode GDL and showed improved performance and HFR with increasing compression. Stähler [151] showed similar results, though the performance increase was more pronounced at lower compression. An alternative method to improve ACL electronic conductivity is to use electronically conducting polymers, such as the PEDOT-PSS used by Cruz-Ortiz et al. [143]. The authors achieved a significantly higher performance (120 mV at 3 A/cm^2) compared

to the same ACL without the PEDOT. A reduction in the HFR is observed, up to a certain PEDOT content, which was attributed to a lower contact resistance, however it may also be indicative of a broadening of the reaction distribution, allowing for a shorter path for proton transport. The improvement in the performance is despite an apparent reduction in the cell performance at low current densities. The addition of the PEDOT:PSS may be impacting the kinetic performance, e.g. reducing the ECSA, making the improved performance more impressive. The impact of the compression on ACL conductivity and on in-situ cell performance will be studied in this work, along with the use of electronically conductive polymers to improve the ACL electronic conductivity.

Numerical studies

Ohm's law is used in all the models in the literature to describe charge transport, however, it's typically not applied to all the components in the cell. As the membrane is considered the largest source of ohmic resistance in the cell, it is considered by all authors. The majority use a temperature and water content based conductivity model [57–59, 61, 62, 65, 67–70, 72], while others assume a constant conductivity [60, 63, 64, 71]. Of those that use a water content based model, only two have a water content that is not constant [57, 59], with both considering electro-osmostic drag and diffusion of water. The impact of the water content is not considered by either author in the catalyst layers however. Other components, such as the PTL, CL and contact resistance, are often not considered [57, 60, 67, 70–72] or are lumped into a single resistance [59, 63–66]. Some authors considered the PTL only [58, 68, 69]. Only one group considered the contact resistance separately from other resistances [61, 62], though little detail was given regarding its effects. As discussed above, only one paper discusses the conductivities of the CL pathways [60], but uses a simple model that only considers CL and membrane resistance. They used an ACL electronic conductivity of approximately 2000 S/cm so their results would likely not be applicable to the low

electronic conductivity catalysts that have been studied in recent years. The authors do show that some reduction in the catalyst loading is possible given the reaction distribution, which would likely be exacerbated by more extreme ACL conductivities. There is a clear lack of modelling work examining charge transport limitations in the ACL, therefore this will be an objective of this thesis. Voltage breakdowns can be used to help understand where performance is lost in the ACL and can be computed using numerical modelling. Losses from the ohmic resistance can be calculated using the ohmic heating method [152], while losses from the electochemical reactions can be found using the irreversible heat loss [153].

1.3.3 Hydrogen pump

As discussed previously, the hydrogen pump method is an experimental, ex-situ technique used to obtain the protonic conductivity of catalyst layers. Iden et al. [134, 135] applied the technique to carbon based catalyst layers used in PEM fuel cells, though the layers were unplatinised. The protonic conductivity was measured for CLs of varying carbon supports and relative humidities. Sabarirajan et al. [154] measured the conductivity of premade carbon CLs that did not contain platinum, allowing for the stacking of the layers and accounting for the contact resistances in the MEA. They computed the tortuosity of the ionomer phase in the layers and how it was impacted by the RH and ionomer content. Mandal et al. [125] used the technique to obtain the conductivity of PEM water electrolyser ACLs, which were composed of unsupported iridium oxide (IrO_x) and found that protonic conductivity of these layers was comparable to carbon based layers, however the electronic conductivity was considerably lower. Qi et al. [155] used hydrogen/nitrogen EIS to obtain the effective protonic conductivity and compared to the conductivities obtained by Sabarirajan et al. using the hydrogen pump technique. The conductivity measured using EIS was significantly higher, particularly at low RH. The difference was attributed to dead ended ionomer pathways within the CL which would not be used in the hydrogen

pump, but would be used in the EIS measurement. The authors noted that it is not easy to determine which method should be applied, as the EIS technique will likely overestimate the conductivity, while the hydrogen pump will underestimate it. Therefore, both methods would ideally be considered.

The hydrogen pump method is based on creating a membrane electrode assembly (MEA) that is composed of two membranes with an intermediate layer (IL) placed between them. The resistance of the cell was obtained using the hydrogen pump technique, where the facile nature of the hydrogen reactions in the anode and cathode minimises the kinetic losses. The resistance of another MEA without the IL was obtained and subtracted from the resistance of the cell with the IL, giving the resistance of the IL. To date, the carbon based catalyst layers that have been tested using the hydrogen pump method have not included the platinum catalyst that is near universally applied in PEM fuel cells. The layers are only comprised of carbon and ionomer, hence are termed pseudo-catalyst layers (PCL). If platinum is included in the PCL, the facile nature of the hydrogen reaction on platinum may cause the protons that reach the PCL from the anode to evolve hydrogen, with a corresponding oxidation reaction at the cathode side of the PCL providing the electrons for the evolution [125, 154]. The protons resulting from the oxidation continue to the cathode. This 'reactive' pathway, illustrated in Figure 1.4, sees the charge being transferred via the reaction through to the electronic phase, rather than travelling exclusively through the protonic phase as desired (termed here as the ionic pathway), thereby providing an inaccurate measurement of the protonic conductivity of the IL. While this issue can be bypassed to an extent for PEM fuel cell electrodes by excluding the platinum, this is not the case for the unsupported ACLs used in PEM water electrolysers. Mandal et al. [125] used numerical modelling to show the electronic conductivity of an IrO_x based ACL was sufficiently low to make the reactive pathway insignificant, however this might not be the case for other catalyst layers. The measurement of the protonic conductivity of a catalyst that is active towards the HER, such as iridium

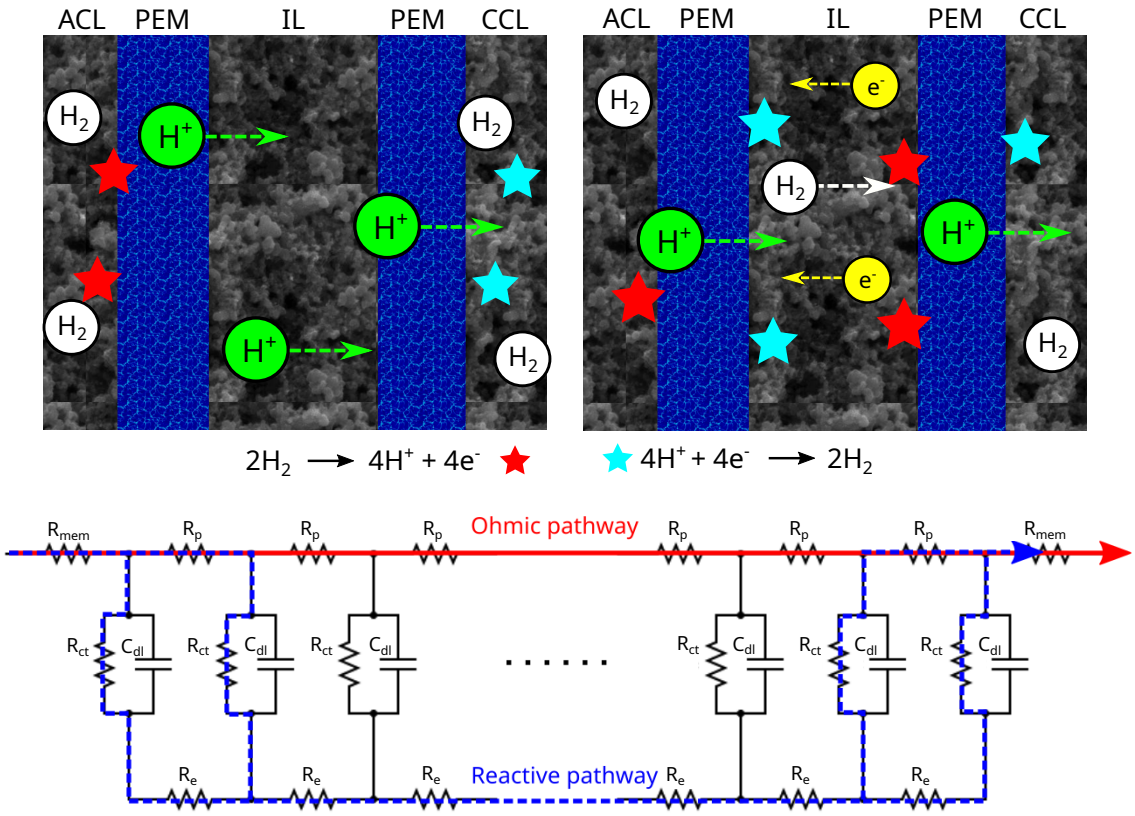

Figure 1.4: Illustration of the ohmic (top left) and reactive (top right) pathways in an active IL. (Bottom) Transmission line model for the IL, incorporating electronic, R_e, protonic, R_p, and kinetic, R_{ct}, resistances as well as the double layer capacitance C_{dl}. R_{mem} is the resistance of each membrane on either side of the IL.

black ACLs, displayed very different trends to that seen for the IrOx, in particular the conductivity did not drop sharply at low ionomer loadings which the IrOx ACL did, which may be evidence of the reactive pathway [126]. To date no research has been done to understand the reactive pathway, how significant its impact is on the predicted resistance of the IL nor on how to discern whether a potentially active IL is inducing the reactive pathway during hydrogen pump experiments.

Iden et al. [134] proposed an alternative to the DC method described above based on EIS. The so-called AC method involves using EIS to obtain the HFR of the cell, which is subtracted from the cell resistance obtained with direct current. The method

assumes that at high frequency the double layer capacitance shorts the kinetic resistance of reactions, again bypassing the protonic resistance of the PCL. If the electronic resistance of the PCL is negligible, the HFR of the cell should only include the resistances from the remaining layers of the cell. If the HFR is subtracted from the cell resistance (obtained using direct current), what remains is thought to consist of the protonic resistance of the PCL, as well as the kinetic resistances of the hydrogen reaction in anode and cathode which are also assumed to be negligible. A slight modification to this method was used by Sabarirajan et al. [154] who subtracted the HFR from the low frequency resistance (LFR) of the cell obtained from EIS; this method is in theory equivalent to the method from Iden et al. [134] as the LFR should be the same as the slope of the polarisation curve at the operating current density [26], which is equal to the cell resistance. The accuracy of the AC method depends on the assumptions that the hydrogen reaction kinetics in the anode and cathode are negligible, as is the transport through the electronic phase in each of the CLs at high frequency. The validity of these assumptions has not been assessed to date.

Numerical studies

There has been very little in terms of numerical modelling of hydrogen pumps for this particular application. Kulikovsky [156] used analytical modelling to study the impedance of the IL under alternating current. Analyical formulae were formulated that describe characteristic points on the EIS spectra, allowing for properties such as the double layer capacitance and protonic conductivity to be calculated by fitting measured spectra. The model assumed that the IL was inactive so it was not used to study the impact of the reactive pathway on performance. Sabarirajan et al. [154] noted the need for numerical modelling of hydrogen pumps to understand how the IL activity impacts the measurement of the IL protonic conductivity. Therefore an objective of this work will be to develop a hydrogen pump model that can be used to investigate the impact of the reactive pathway and assess the applicability of the

method.

1.3.4 Mass transport

Experimental studies

Mass transport losses have received increased focus in recent years [157, 158], with DeAngelis et al. [159] noting that "The influence of this intricate two-phase flow on PEMWE cell performance has been controversially debated for the last decade and, to date, the underlying governing processes remain non-conclusive". Part of the reason for this lack of certainty is the lack of unequivocal evidence for the mass transport losses in PEMWE. In proton exchange membrane fuel cells (PEMFC), mass transport losses are readily apparent from the limiting current that is observed at high current densities, the magnitude of which is determined by the ability of the cell to transport oxygen to the reaction site [28]. This limiting current can be reliably studied, and therefore the factors that influence the transport of oxygen to reaction sites examined, by methods such as varying the cathode pressure and oxygen content [160]. In PEMWE such a distinct indicator of mass transport limitations is rarely seen. For example, Rozain et al. [161] presented polarisation data up to 5 A/cm^2 and saw no mass transport limitations, the reason for which they attributed to choosing a PTL of correct porosity. Lettermeier et al. [162] tested membrane electrode assemblies (MEAs) from a number of suppliers up to 4 A/cm^2 without any mass transport limitations. A more extreme example comes from Lewinski et al. [163], who used 3M's nanostructured thin film (NSTF) support to make an iridium based ACL which operated at over 15 A/cm^2 without reaching a limiting current.

A number of works have identified mass transport limitations however, by separating the losses through the use of a 0-D model [22, 23, 66, 164–167]. The Tafel slope and the HFR are used to characterise the kinetic and ohmic losses respectively, and any deviation between experimentally obtained polarisation curves and the curve obtained using the model is attributed to mass transport losses. Suermann et al. [22]

used this method to show that mass transport limitations can be substantial over a wide current density and operating pressure range. The authors [165] also investigated the impact of PTL pore size and noted that higher transport resistances were observed for higher pore sizes which was contrary to what was expected. Kim et al. [166] studied the impact of bilayer titanium meshes and noted the importance of the interfacial contact between the PTL and ACL and the uniformity of the compression of the PTL on the ACL. Zhao et al. [167] increased the hydrophilicity of a titanium PTL and noted a substantial increase in the performance, due to a reduced gas saturation in the PTL. More extreme examples that clearly showed mass transport limitations include using fully humidified gases to provide water to the anode, rather than liquid water [168], and using cathode water feed instead of anode water feed [169]. These methods are unlikely to be representative of a large PEMWE system however.

The use of a 0-D model to estimate mass transport losses from a polarisation curve is problematic however, as it assumes that the kinetic losses can be characterised by a simple Tafel model, with a slope determined from an in-situ measurement, and that the HFR represents all ohmic losses. The kinetics of the oxygen evolution reaction (OER) are complex, with a number of mechanisms being proposed [87, 88, 139]. It is possible that the Tafel slope for the OER may change at higher overpotentials [106, 170], as has been recorded for the oxygen reduction reaction (ORR) in platinum-carbon (Pt/C) based catalyst layer in PEMFCs [82, 171, 172]. Measuring the Tafel slope itself is also difficult, as the very low electronic conductivity of the iridium oxide based catalysts that are commonly used may limit the range of current densities for which the ohmic resistance is negligible. For example, Schuler et al. [139] measured the HFR of an MEA at very low current densities with an ACL composed of IrO_2 on TiO_2, and found that the HFR increased with increasing current density after only 10 mA/cm^2, therefore the authors considered less than 10 mA/cm^2 to be the kinetic region. This method for defining the kinetic region does not take in account that

the HFR may not be representative of the total ohmic resistance of the cell, as a catalyst layers contribution to the overall HFR is dominated by the more conductive phase [30, 173]. In contrast to Pt/C based CLs in PEMFCs, both phases in the ACL of a PEMWE can have poor conductivity [125], i.e., charge transport through each phase is non-negligible. As such, it is possible that the upper limit of the kinetic region may be even lower than 10 mA/cm^2. Unfortunately, it is very common to assume the kinetic region extends substantially beyond 10 mA/cm^2 [22, 166, 167], as a linearity in the Tafel plot is still sometimes observed. In terms of the ohmic losses, the use of the HFR to characterise the entire cell resistance may neglect part of the CL resistance, as discussed. In addition, it is not known how well the interfacial resistance between the PTL and ACL is captured by the HFR, and this resistance is gaining increased attention in recent years due to the high electronic resistance of the ACL [113]. This discussion is not intended to invalidate the previously cited works that quantified the mass transport resistance using the 0-D model method described, as it will likely depend on the specific electronic conductivity of the ACL used in each work, which is rarely measured. However, care should be taken when using a simple 0-D model to quantify the mass transport losses, as a number of additional losses are not accounted for. This point was also raised by Etzold et al. [158], who noted that the use of lumped parameters such as the Tafel parameters and the HFR to characterise complex phenomena fail to provide deeper insight into the causes of performance loss.

A number of researchers have attempted visualisation studies to gain insights into the nature of the two phase flow regime, which is crucial for the formulation of a mechanistic model. Neutron imaging [66, 174–176], X-ray tomography [176–178] and direct visualisation [174, 179–183] have been used to investigate the nature of the water and oxygen mixture in a working PEMWE. The focus of these works was to understand the nature of bubble formation, movement through the PTL and into the channel. Dedigama et al. [179] and Li et al. [180] found that at intermediate

current densities there is a transition from bubble to slug flow in the channel. The diameter of the bubbles increases with current density and decreases with increasing temperature and water flow rates. Wang et al. [118, 182, 183] used an etched PTL with straight-through pores to allow for the bubbles emerging from the ACL to be imaged, allowing for comparison with those emerging from an PTL. The authors showed that bubbles emerging directly from the ACL tend to be smaller than those from the PTL, allowing for easier removal from the channel and a reduction in the number of slugs. Seweryn et al. [175], Leonard et al. [178] and Zlobinski et al. [176] noted that despite the hydrophilicity of the titanium PTL, a significant portion of the PTL is filled with oxygen even at low current densities. A gradient in water thickness builds up through the PTL at low current densities that is unaffected by changes in the operating current density, implying that a network of oxygen filled pores is built that transports all of the oxygen out of the ACL. Capillary forces are, therefore, thought to be the dominant transport mechanism. Arbabi et al. [177] used a microfluidic cell to mimic the transport of oxygen out of the anode PTL and had similar conclusions. Based on these visualisation studies, two-phase flow in PEMWE modelling papers are commonly described using capillary pressure models. This work will use a capillary pressure model to capture two-phase effects and attempt to shed some light on the impact of mass transport on PEMWE performance.

Numerical studies

Etzold et al. [158] cited the need for more detailed mechanistic simulations of mass transport in PEMWE. As Lettenmeier et al. [184] noted however, the nature of the two-phase flow in the anode is not well understood, and also called for numerical modelling to elucidate the impact of mass transport limitations when high current density operation is used. A number of numerical models have been developed that have investigated mass transport effects in PEMWE. Bulk transport of either the water or gas is generally solved for in the porous media using Darcy's Law or the

Brinkmann equation [57, 59, 61–64, 68, 71, 72]. Typically, only a single phase is solved for, however some authors do consider two-phase flow. Ojong et al. [68] accounted for the oxygen bubbles by introducing an empirical mass transport term that was based on the oxygen production rate and the water supply rate. Such empirical equations lack design capability and will not be considered here. Of particular interest are higher dimensional models that resolve transport through the individual layers, allowing for better design of the layers. However often the ACL is not resolved, preventing a direct study of the interaction between the two-phase flow and the OER. Han et al. [61, 62] developed a model that considers only the PTL, and solves for the liquid saturation using Darcy's law and the Leverett-J function to describe the relationship between capillary pressure (the pressure difference between two phases in a pore) and saturation. Boundary conditions are not easy to apply for saturation based models: Han et al. used a function based on the current density with a fitting parameter as the boundary condition at the PTL/channel interface. Furthermore, the saturation based models usually result in continuity in the saturation throughout the domain, which is non-physical at the interface between two layers with different intrusion curves. The pressure of each phase will be continuous, which will result in a jump in saturation at these interfaces. Instead of saturation based models, many authors have used a capillary pressure model, where the gas and liquid pressures are obtained using Darcy's law, with the saturation obtained using a variety of methods. Olesen et al. [69] determined the saturation using a model based on the breakthrough pressure of the medium. However, the ACL was not resolved, as the focus of the work was on the channel. The ACL was assumed to be infinitely thin, with the liquid saturation in the PTL, at the ACL interface, assumed to be equal to that of the ACL. Chen et al. [185] used the same Leverett-J function as Han et al. [62]. While the CL appeared to be resolved, no discussion was given regarding the gas saturation in the ACL, as the focus was on land/channel effects and liquid saturation distribution in the PTL.

A number of works do resolve the ACL and describe the two-phase phenomena

within. Garcia-Salaberri [186] used a capillary pressure/saturation correlation model based on the breakthrough pressure of the medium with van Genuchten's equation. He noted the importance of the electronic conductivity to PEMWE performance and found that concentration losses were negligible for the current densities studied. Wu et al. [187] used the Leverett-J function from Han et al. [62] to relate the capillary pressure and liquid saturation. The oxygen content at the PTL/channel interface was obtained by solving a volume-of-fluid model in the channel only, with the resulting saturation being used as a boundary condition for the 3D model that captures the MEA. Wu et al. noted the importance of capturing the oxygen content in the channel, as the local current density and liquid saturation in the ACL were significantly affected. Wang et al. [181] also used the same Leverett-J function and studied along-the-channel effects as well as performing a parametric study on operating conditions and PTL properties. Wrubel et al. [110] used a capillary pressure model, where intrusion curves were used to relate the pressure to the liquid saturation. The authors noted the lack of data for intrusion curves corresponding to PEMWE ACLs in the literature and so used a curve obtained on a platinum/carbon based catalyst layer. The ACL was resolved in their model and they noted the dependence of the local current density on the ACL liquid saturation.

The aforementioned numerical models have studied the impact of two-phase flow on PEMWE performance, however their investigative abilities are somewhat limited by the need to use the Leverett-J function, an intrusion curve from a PEM fuel cell catalyst layer, or the van Genuchten model that was fitted to PEM fuel cell porous media. As such, it was not possible to vary parameters that characterise the microstructure of PEMWE ACLs, such as the characteristic pore radius, the distribution of pore radii in the layer, or the wettability of the ACL, and determine their impact on the cell performance. An alternative is to use a pore size distribution (PSD) model, which has been studied extensively in the PEM fuel cell literature [188–193], and captures such microstructural information. To the knowledge of the

authors, such a model has not been used to study two-phase flow in PEM water electrolysis, therefore it was pursued in this thesis.

1.4 Objectives

Based on the literature review, it is clear that there are a number of gaps in our understanding of PEM electrolysers that should be investigated using numerical modelling. The overall objective of this thesis, therefore, is to develop a multi-dimensional model of a PEM electrolyser that can capture the main phenomena occurring in an actual cell, namely: transport of charged particles and two phase flow, and the kinetics of the primary reactions occurring in the anode and cathode. With this model, a number of specific physical processes will be analysed:

- Protonic conductivity measurement: This objective will focus on the development of a hydrogen pump model that can be used to study the impact of testing ILs that are active to the hydrogen reaction, verifying the accuracy of the method with regard to the Ir black catalyst and assessing the validity of the AC method.

- Two phase flow: This objective will focus on the development of a two phase flow model, based on capillary pressure and a pore size distribution of each layer, so that the impact of the shielding of the electrochemical surface area by oxygen bubbles in the ACL can be studied.

- Anode catalyst layer electronic conductivity: This objective will focus on understanding the impact of low electronic conductivity in the ACL, particularly with regard to the reaction distribution and the catalyst loading. The impact of improving the catalyst conductivity through cell compression and the use of electronically conductive polymers will also be assessed.

1.5 Structure of the thesis

The thesis is organised into five chapters. Chapter 1 describes the motivation for the work, and details how PEM water electrolysers are constructed, how they are operated, and how their performance is assessed. The literature review describes the primary areas of research in this field and highlights shortcomings that this work seeks to address. Chapter 2 focuses on the development of a hydrogen pump model that is used to study the measurement of the proton conductivity of PEMWE ACLs. The model and solution strategy is described, as well as the methods to obtain experimental data for model validation. The model validation is presented, before the model is used to study the impact of the reaction in the intermediate layer, for platinum/carbon and Ir black compositions. The accuracy of the AC method is assessed, and parametric studies are carried out. Chapter 3 describes the development of the PEM electrolyser model that includes a PSD-based two phase model. The model is used to assess the impact of oxygen bubble formation on cell performance for a number of PSDs, with parametric studies carried out on parameters such as the hydrophilicity. Two catalyst are studied so as to understand the role of the reaction distribution on pressure build up in the ACL. The impact of the PTL is investigated and recommendations for experimenters are suggested. Chapter 4 investigates the implications of having an extremely low electronic conductivity. The role of the reaction distribution on catalyst utilisation is studied and compared to experimental data obtained in-house and in the literature. Mitigation strategies for having a low conductivity are assessed, namely the use of higher cell compression and electronically conducting polymers. Finally, Chapter 5 presents a summary of the work and the main conclusions, and discusses possible areas for future research.

Chapter 2

Estimating the protonic conductivity of unsupported CLs using the hydrogen pump method[1]

2.1 Introduction

In this chapter, the hydrogen pump technique used to measure the protonic conductivity of CLs is studied. The possibility of the reactive pathway described in Chapter 1 impacting the measurement of the protonic conductivity is explored, using numerical modelling and experimental testing. This validation is crucial, as the previous works that used this technique only studied unplatinised carbon based ILs to ensure there was no activity to the hydrogen reaction. Removing the catalyst is not possible for the unsupported ACLs used in PEMWE, requiring numerical modelling to assess whether the technique can be accurately applied. The hydrogen pump model is described and is first validated against a hydrogen pump cell without an IL, and then compared to cells with a carbon based IL. The presence of a significant contact resistance is revealed using the model, which can be estimated using the change in HFR between a cell with and without an IL. The measured conductivity of the Ketjen

[1]This chapter has been published: M. Moore, M. Mandal, A. Kosakian, and M. Secanell, *Good practices and limitations of the hydrogen pump technique for catalyst layer protonic conductivity estimation*, ACS Applied Materials & Interfaces, vol. 15, no. 31, 2023,

Parts of this chapter have also been published in: M. Mandal, M. Moore, and M. Secanell, *Measurement of the protonic and electronic conductivities of PEM water electrolyzer electrodes*, ACS Applied Materials & Interfaces, vol. 12, no. 44, 2020.

black based IL is in close agreement with the literature, once the contact resistance is accounted for.

The model is then used to assess the impact of the addition of platinum to the carbon IL. In cases where a catalyst active to the hydrogen reaction is placed in the IL, the IL is predicted to be bypassed almost entirely by the reactive pathway, a result that is confirmed experimentally. The reactive pathway is studied in detail by computing the resistance induced by electron and proton transport, as well as charge transfer, with and without a catalyst active to the hydrogen reaction. Parametric studies are used to reveal the reactivity and conductivity of the IL for which the reactive pathway is significant. The accuracy of the method for measuring the protonic conductivity of unsupported Ir and IrOx is assessed, with the latter deemed to be unaffected by the reactive pathway, while the former is significantly affected. The model is used to provide bounds for the true protonic conductivity of the Ir based IL. The experimental data was obtained in-house by Manas Mandal, with Aslan Kosakian providing modelling support for the EIS studies.

2.2 Numerical model

The numerical model employed in this work is based on the transient, 2-D and across-the-channel fuel cell model by Kosakian et al. [29]. To simulate a hydrogen pump, the oxygen reduction reaction model in the cathode is replaced with the hydrogen evolution reaction model. The new assumptions for this model are:

- the cell is assumed to be isothermal given the small currents and overpotentials during hydrogen pump experiments
- transport of hydrogen and water vapour is assumed to be purely diffusive, with a binary diffusion coefficient based on hydrogen in water vapour. This is a simplification of the infinitely dilute solution typically used with Fick's law, under the assumption that the low current densities used in hydrogen pumps

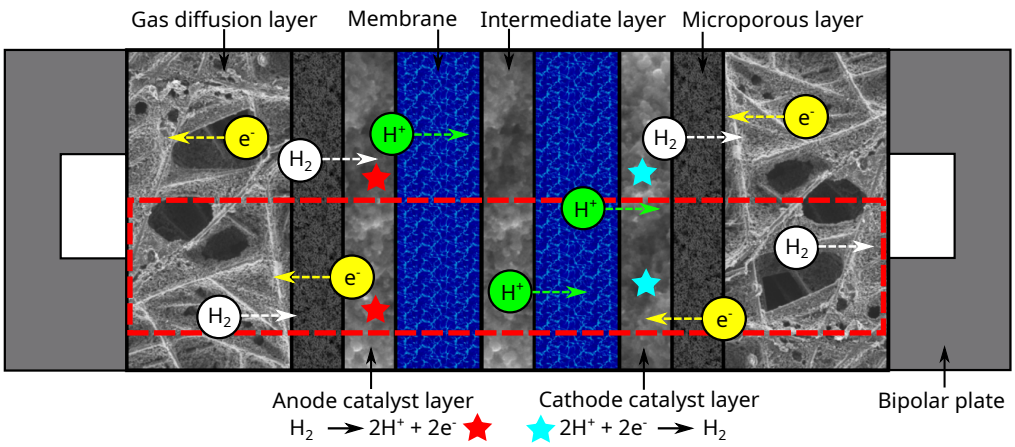

Figure 2.1: Transport processes within the cell, for the case of an inactive IL. The computational domain for all simulations is shown in the red dashed line.

will not significantly alter the concentration of hydrogen throughout the cell.

- as mass transport losses are not likely to be significant, microscale transport effects are not included, i.e. the additional resistance to the transport of hydrogen through ionomer thin films covering the catalyst is neglected.

- the transport of hydrogen through the membranes is also governed by Fick's law using a diffusion coefficient of 2×10^{-7} $cm^2.s^{-1}$ obtained by Moore et al. [194].

The model solves for the potential of the solid phase, ϕ_s, and ionomer phase, ϕ_m, using Ohm's law, the mole fraction of hydrogen, x_{H_2}, and water vapour, x_{wv}, using Fick's law, and absorbed water in the ionomer, λ, using a Springer model [195]. Figure 2.1 shows the domain in which the simulations are performed, which includes two NRE 211 membranes sandwiching the intermediate layer, the anode and cathode catalyst layers, with an SGL 28BC GDL and MPL on both the anode and cathode. The left and right boundary includes half of the channel and half of the land.

2.2.1 Governing equations

The governing equations are:

$$-C_{dl}\frac{\partial(\phi_s-\phi_m)}{\partial t}-\nabla\cdot\left(\sigma_m^{eff}\nabla\phi_m\right) = S_{H^+} \quad (2.1)$$

$$C_{dl}\frac{\partial(\phi_s-\phi_m)}{\partial t}-\nabla\cdot\left(\sigma_s^{eff}\nabla\phi_s\right) = S_{e^-} \quad (2.2)$$

$$\varepsilon_p c_{tot}\frac{\partial x_{wv}}{\partial t}-\nabla\cdot\left(c_{tot}D_{wv}^{eff}\nabla x_{wv}\right) = S_{wv} \quad (2.3)$$

$$\varepsilon_p c_{tot}\frac{\partial x_{H_2}}{\partial t}-\nabla\cdot\left(c_{tot}D_{H_2}^{eff}\nabla x_{H_2}\right) = S_{H_2} \quad (2.4)$$

$$\varepsilon_m\frac{\rho_{ion}}{EW}\frac{\partial\lambda}{\partial t}-\nabla\cdot\left(n_d\frac{\sigma_m^{eff}}{F}\nabla\phi_m+\frac{\rho_{ion}}{EW}D_\lambda^{eff}\nabla\lambda\right) = S_\lambda \quad (2.5)$$

where the source terms for each equation are shown in Table 2.1. The boundary conditions are shown in Figure 2.2 and are the same as those in reference [29], with the exception of zero electronic potential being applied at the cathode, as the cell potential is applied at the anode in this case. The hydrogen and water vapour mole fractions at the anode and cathode is determined by the relative humidity of the input gas.

2.2.2 Charge transport

The electronic conductivity was applied directly for each layer. The GDL had a conductivity of 3.75 and 180 S/cm in the through- and in-plane direction respectively, while the MPL conductivity was 0.95 and 121 S/cm respectively. The protonic

Table 2.1: Source terms for the governing equations.

Source term	Anode	Cathode
S_{H^+}	j_{HOR}	$-j_{HER}$
S_{e^-}	$-j_{HOR}$	j_{HER}
S_{wv}	$-\varepsilon_m k_\lambda\frac{\rho_{ion}}{EW}(\lambda_{eq}-\lambda)$	$-\varepsilon_m k_\lambda\frac{\rho_{ion}}{EW}(\lambda_{eq}-\lambda)$
S_{H_2}	$-j_{HOR}/2F$	$j_{HER}/2F$
S_λ	$\varepsilon_m k_\lambda\frac{\rho_{ion}}{EW}(\lambda_{eq}-\lambda)$	$\varepsilon_m k_\lambda\frac{\rho_{ion}}{EW}(\lambda_{eq}-\lambda)$

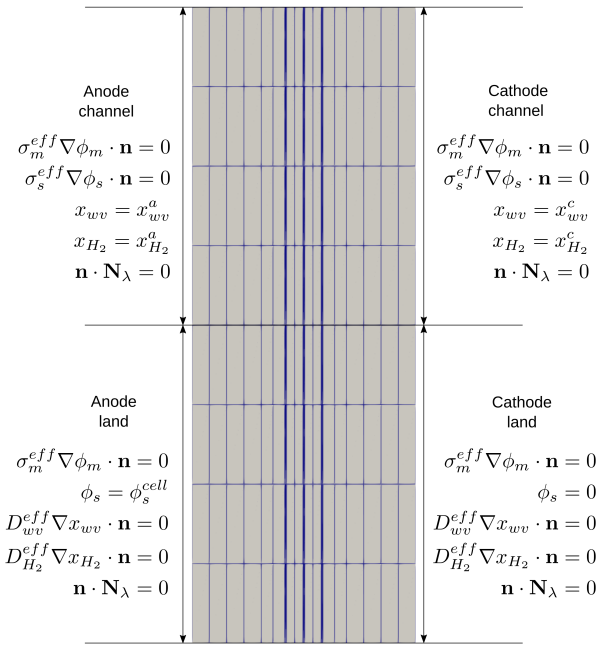

Figure 2.2: Boundary conditions applied for the hydrogen pump simulations, displayed using the coarsest mesh from Figure 2.3.

conductivity in the membrane is computed using:

$$\sigma_m = \left(-1.0125 \times 10^{-4}\lambda^2 + 1.052 \times 10^{-2}\lambda - 2.0634 \times 10^{-2}\right) \exp\left(\frac{1}{303} - \frac{1}{T}\right) \quad (2.6)$$

where the water content, λ, is computed using Equation (2.7) and T is the applied temperature.

CL conductivity

The relative humidity dependent protonic conductivities of the Ketjen-black based Pt/C layers and the Ir black layers were obtained using the methodology described in reference [125], which reported the conductivity of the IrOx layers. A relationship between the relative humidity/water activity, a_w, and the equilibrated ionomer water content, λ_{eq}, was obtained by Kosakian et al. [196] and is given as:

$$\lambda_{eq} = (31.7a_w^3 - 37.46a_w^2 + 18.37a_w)\exp\left(66.28\left(\frac{1}{T_0} - \frac{1}{T}\right)\right) \quad (2.7)$$

where T_0 is the reference temperature of 303 K. It is assumed that this equation, which was fitted to a number of experimentally obtained sorption isotherms for Nafion membranes, holds for both carbon types and for the Ir and IrOx based CLs. This equation is used to convert the relative humidity dependent conductivity to be with respect to the water content. Then third order polynomials are fitted to relate the protonic conductivity to the local ionomer water content. It should be noted that the term 'conductivity' as applied to catalyst layers in this work actually refers to the effective conductivity of these layers. The word 'effective' is omitted throughout for readability. If the conductivity of a constituent phase is referred to, the term 'intrinsic conductivity' will be used instead.

2.2.3 Kinetic model

The Butler-Volmer equation is used to obtain the volumetric current density in each active layer:

$$j = A_v j_0 \left(\frac{c_{H_2}}{c_{H_2}^{ref}} \exp\left(\frac{\alpha_a F \eta}{RT} \right) - \exp\left(-\frac{\alpha_c F \eta}{RT} \right) \right) \tag{2.8}$$

where j_0 is the exchange current density, $\alpha_{a,c}$ is the anodic/cathodic transfer coefficient and A_v is the volumetric active area, i.e. in units of electrochemical surface area per CL volume. This equation was used instead of more advanced multi-step kinetic models, as the kinetic parameters for both the hydrogen oxidation and evolution reactions were available from Durst et al. [80] for platinum and iridium catalysts on a Vulcan type carbon. It was found that the Butler-Volmer equation accurately captured the kinetic behaviour at low overpotentials, which are expected in a hydrogen pump. The IrOx parameters were obtained using a hydrogen pump experiment as described in reference [125].

2.2.4 Species diffusion

The GDL parameters matched those for the compressed case in reference [29]. The effective diffusion coefficients D^{eff} for the transport of hydrogen and water vapour

are computed using percolation theory:

$$D^{eff} = \begin{cases} D\left(\frac{\varepsilon_p - \varepsilon_p^{th}}{1-\varepsilon_p^{th}}\right)^{\mu}, & \varepsilon_p > \varepsilon_p^{th} \\ 0, & \varepsilon_p \leq \varepsilon_p^{th} \end{cases} \tag{2.9}$$

where D is the molecular diffusion coefficient from Chapman-Enskog theory for a hydrogen and water vapour gas mixture [197]. ε_p is the porosity of the layer, ε_p^{th} is the theoretical porosity threshold and μ is the porosity network constant.

2.2.5 Sorbed water content

The model used for sorbed water transport is the same as that used by Kosakian et al. [29]. The electro-osmotic drag coefficient, n_d, for the membrane and CLs is computed using:

$$n_d = \frac{2.5\lambda}{22} \tag{2.10}$$

In the membrane, the water diffusion coefficient, D_λ, is computed using the following:

$$D_\lambda = \begin{cases} 3.2 \cdot 3.10 \times 10^{-3}\lambda(-1.0 + \exp(0.28\lambda))\exp(-2436.0/T), & \lambda \leq 3 \\ 3.2 \cdot 4.17 \times 10^{-4}\lambda(1.0 + 161\exp(-\lambda))\exp(-2436.0/T), & \lambda > 3 \end{cases} \tag{2.11}$$

whereas the equation below is used in the CLs:

$$D_\lambda = 5.44 \times 10^{-5} f_{\mathrm{V}} \frac{\partial \ln a_w}{\partial \ln \lambda_{eq}} \exp\left[\frac{20000}{R}\left(\frac{1}{303} - \frac{1}{T}\right)\right] \tag{2.12}$$

where f_{V} is given by:

$$f_{\mathrm{V}} = \frac{\lambda V_w}{V_e + \lambda V_w}, V_m = \frac{M_{H_2O}}{\rho_l}, V_e = \frac{\mathrm{EW}}{\rho_{m,dry}} \tag{2.13}$$

where M_{H_2O} and ρ_l are the molecular weight and density of water, EW is the equivalent weight of the ionomer and $\rho_{m,dry}$ is the ionomer dry density. The Darken factor is given by:

$$\frac{\partial \ln a_w}{\partial \ln \lambda_{eq}} = \begin{cases} \exp(0.7647\lambda_{eq.corr}^{2.305}), & \lambda_{eq.corr} < 1.209 \\ 3.266 + 2.930\left[\exp(-6.735(\lambda_{eq.corr} - 1.209)\lambda_{eq.corr}^{-0.8994}) - 1\right], & \lambda_{eq.corr} \geq 1.209 \end{cases} \tag{2.14}$$

where $\lambda_{eq.corr}$ is given by:

$$\lambda_{eq.corr} = \lambda_{eq} \exp\left(2509\left(\frac{1}{T} - \frac{1}{303.15}\right)\right) \tag{2.15}$$

The rate of water absorption/desorption by the electrolyte, k_λ, is given by:

$$k_\lambda = \frac{\alpha}{L_{cl}} f_{\mathrm{V}} \exp\left[\frac{20000}{R}\left(\frac{1}{303} - \frac{1}{T}\right)\right] \tag{2.16}$$

where L_{cl} is the CL thickness and α is 4.59×10^{-5} cm/s if $\lambda < \lambda_{eq}$ and 41.31×10^{-5} cm/s if $\lambda \geq \lambda_{eq}$.

2.2.6 Input parameters

The cells were simulated at a cell temperature and pressure of 353 K and 101325 Pa, with hydrogen at an RH of either 50% or 100% fed into both electrodes. Table 2.2 shows structural inputs and parameters for species diffusion. The thickness of the membranes was modified from 25.4 μm to account for swelling with water uptake, using data from Iden et al. [134]. The swelling was 1.5% at 50% RH, and 7.7% at 100%. The thicknesses of the CLs were measured using SEM. The kinetic parameters from Durst et al. [80] were obtained for Pt nanoparticles on a Vulcan type carbon. It is assumed that the kinetics are the same as on the Ketjen-black carbon used in this work in the ACL, CCL and platinised ILs. The data at 353 K was used. The anodic and cathodic Tafel slopes were converted to transfer coefficients for use in Equation (2.8). The active area and double layer capacitance from Kosakian et al. [29] were taken as a starting point since they used a different catalyst (HyPlat K-40, i.e. 40 wt.% Pt on Ketjen carbon). It is not certain whether the catalyst activity or active area, which were obtained on a different carbon to that studied in this work are representative of the CLs tested, hence the active area of the CLs were used as a fitting parameter. The active area needed to be reduced from 212,000 $\mathrm{cm}^2_{cat}/\mathrm{cm}^3_{CL}$ to 110,000 $\mathrm{cm}^2_{cat}/\mathrm{cm}^3_{CL}$, indicating that the TKK catalyst was not as active as the HyPlat. The parameters used are shown in Table 2.3. The electronic conductivity for

the carbon based CLs is that fitted by Secanell [198] to packed Vulcan XC-72 carbon particles, due to a lack of data on the effective electronic conductivity of different carbon based CLs.

Table 2.2: Diffusion coefficient parameters for GDLs, MPLs and CLs. 'X' and 'Y' refer to the through-plane and in-plane directions respectively.

	GDL	MPL	CL
Structural			
Thickness, [μm]	109	37	C: 2.8, Ir: 3.83, IrOx: 4.1
Porosity [%]	81	58	37
Diffusion			
Porosity threshold X [-]	0.12	0.05	0.05
Porosity threshold Y [-]	0.12	0.05	0.05
Porosity network constant X [-]	4.9	1.9	1.9
Porosity network constant Y [-]	2.0	1.9	1.9

2.2.7 Post-processing

The Ohmic heating method [152] was used to obtain the resistance to charge transport of the layer:

$$R_{ohmic,protonic} = \frac{1}{i^2 A} \int (\sigma_m^{eff} \nabla \phi_m \cdot \nabla \phi_m) dV, \tag{2.17}$$

$$R_{ohmic,electronic} = \frac{1}{i^2 A} \int (\sigma_s^{eff} \nabla \phi_s \cdot \nabla \phi_s) dV \tag{2.18}$$

where i is the current density of the cell and A is the geometric area of the cell. It is important to note that the resistance computed from these equations will be related to the intrinsic resistivity of most of the components. This will not be the case, however, for the CLs, as the cell current does not necessarily tranverse the entirety of the layer, depending on how the reaction is distributed. Instead, the method computes the heat dissipated in each phase in the CL and, by normalising to the cell current density, returns the contribution of each phase in the CL to the total cell resistance. In the

Table 2.3: Kinetic and structural parameters for the Ketjen-black ACL, CCL and IL simulated in this work. Also shown are parameters used for the Ir IL with an ionomer loading of 15% wt and the IrOx IL with an ionomer loading of 35% wt.

	Carbon	Ir	IrOx
Anodic trans. coeff. [-]	0.47	0.53	1.15
Cathodic trans. coeff. [-]	0.53	0.48	0.965
Exchange current density [A/cm$^2_{cat}$]	0.24	0.10	2.51x10^{-6}
Active area [cm$^2_{cat}$/cm$^3_{CL}$]	110,000	561,350	1,800,000
Double layer capacitance [F/cm^3]	81.50	183.70	-
Electronic conductivity [S/m]	3.70	0.05	4.5x10^{-5}

ACL and CCL, the same current density is flowing in each phase, however, in the IL the current densities are likely to be different. The dissipated heat is still normalised to the cell current density rather than the individual phase current density, as this still returns the contribution of the IL to the total cell resistance. The summation of resistance from every layer computed using this method matches the total cell resistance, i.e. that found from the slope of the polarisation curve.

The model is used to compute the HFR of the cells simulated in two ways, a) numerical EIS and b) ohmic heating. Numerical EIS, such as that discussed in Section 2.4.1, is used to obtain a Nyquist plot from which the HFR is extracted by finding the high frequency of the spectrum with the real axis. In the ohmic heating method, the ohmic resistances of each layer besides the CL are summed. The contribution from the CL is given as [30, 199]:

$$R_{CL}^{HFR} = \frac{L_{CL}}{\sigma_m^{eff} + \sigma_s^{eff}} \tag{2.19}$$

where L_{CL} is the CL thickness and σ_i^{eff} is the conductivity of the protonic and electronic phase. This method was found to match that from the numerical EIS in the case of the cell with a carbon based IL at 50 and 100%, and was therefore applied at other RH used in this work.

The apparent resistance from the kinetic reaction was computed by considering the kinetic overpotential, [153]:

$$R_{kinetic} = \frac{1}{i^2 A} \int j_{rxn} \eta_{rxn} dV \tag{2.20}$$

where η_{rxn} and j_{rxn} are the local overpotential and volumetric current density for either the HER or OER, depending on the electrode.

In Section 2.4.4, the perceived or apparent protonic conductivity of the IL is computed using the numerical model as part of a parametric study on IL properties. The DC method is applied to the numerical data, i.e. the total cell resistance is obtained from the polarisation curve for a cell that includes the IL, and the resistance of the cell without an IL is subtracted from it to get the resistance of the IL. The apparent conductivity is obtained by dividing the IL thickness by the IL resistance.

The cell current density is computed in the ACL and CCL by integrating the volumetric current:

$$i = \int_{\Omega} j d\Omega \tag{2.21}$$

where the volumetric current density is computed using equation (2.8). If the IL is active, there will be both oxidation and reduction currents present. Individual currents are computed by only summing positive or negative currents, allowing them to be compared to ensure charge conservation.

2.2.8 Implementation and solution strategy

The model described was implemented in OpenFCST, an in-house, open-source software developed to model electrochemical systems [200, 201]. Second order Lagrange finite elements are used, with approximately 5,000 cells, for a total of approximately 70,000 degrees of freedom. A refinement study was carried to ensure this number of cells was mesh independent, as shown in Figure 2.3. A cell with a platinised carbon IL was simulated, using the current density at 0.4 V. In addition, the mesh is adaptively refined, in which 30% of the cells that have the largest error, as estimated

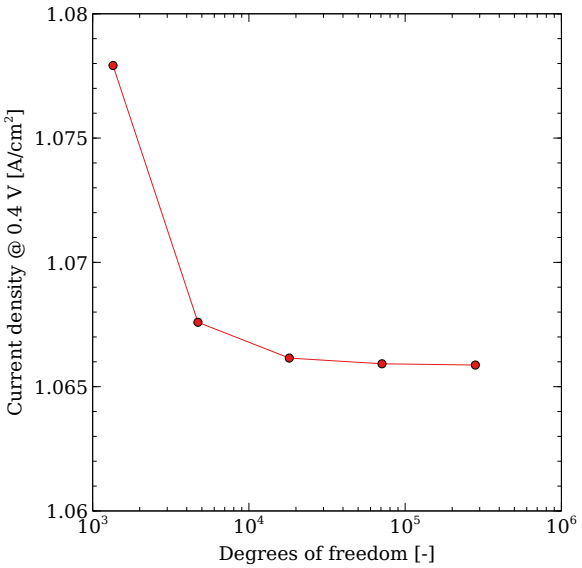

Figure 2.3: Refinement study showing that the predicted current density at 0.4 V is independent of the mesh.

using an estimator from Kelly et al. [202], are divided into four cells. The governing equations are linearised using Newton's method and the resulting linear system is solved using UMFPACK. A tolerance of 10^{-8} was used for the residual of the Newton solver. A steady-state polarisation curve up to a current density of 0.5 A/cm^2 took approximately 6.5 minutes to obtain, using an Intel ® Core™ i7-8700K CPU at 3.7 GHz.

Transient simulations were carried out to obtain EIS spectra using the methodology and parameters in reference [29]. A linear ramp of 0.5 mV in one nanosecond was used instead of 1 mV. In this case, the implicit Euler method was used for time integration using adaptive time stepping via Richardson extrapolation, with an initial step size of 0.1 nanoseconds. A full transient response was obtained in 28 hours on a single core. Current and voltage signals were post-processed as described in reference [29] to obtain the impedance spectrum.

2.3 Experimental

The protonic conductivity of carbon based ILs was obtained with and without platinum, with a summary provided in Table 2.4. In addition, polarisation data from Ir and IrOx ILs published in reference [126] was used. The label given to each cell is referred to throughout the text, including in numerical modelling simulations that aim to replicate the corresponding experiment. The process for the fabrication, assembly and testing of the hydrogen pump cells was the same as in reference [125], and is described here briefly. Catalyst inks for the ACL and CCL, as well as the platinised carbon based ILs, used Ketjen-black 46.7 wt.% Pt/C (TEC10EA50E) from Tanaka Kikinzoku Kogyo (TKK). For the platinum free ILs, a similar Ketjen-black carbon powder (E-type) was used from TKK. The platinum loading was maintained at 0.1 mg/cm^2, with an ionomer loading of 30 wt.%. The platinum free IL had the equivalent carbon and ionomer content, which corresponded to an I/C ratio of 0.9. Repeability of the setup for an inactive IL was demonstrated by Mandal et al. [125]. As platinised ILs have not been studied in the literature to date, two cells were tested to ensure repeatability. The layers were fabricated using a commercial inkjet material printer (Fujifilm Dimatix DMP-2831), and were printed directly onto the NRE211 membranes with an area of 5 cm^2. GDLs from Sigracet (SGL 28BC) were used.

The single serpentine channel cells were operated by flowing 0.5 slpm of hydrogen into both the anode and cathode at relative humidities between 30-100%, at ambient pressure and a cell temperature of 80 ℃. The cell was maintained at a constant RH for at least 30 minutes to allow for the humidification of the cell. Chronopotentiometry was then performed in the current density range of 0-0.6 A/cm^2, with current steps of 0.02 A/cm^2 at lower RH and 0.1 A/cm^2 at higher RH, and a hold of 3 minutes per step. The cell resistance was obtained by taking the slope of the polarisation curves that resulted. The resistance of the cell without an IL was reported in reference [125]. The difference in the resistance of the cell with and without an IL is used to obtain

Table 2.4: Summary of the ILs tested experimentally. The Ir and IrOx cells are from reference [126].

Name	Catalyst	Support	Catalyst loading [mg/cm^2]	Ionomer loading [wt. %]	Cells tested	IL thickness [μm]
C-IL	-	Carbon	-	30	1	2.8
Pt/C-IL	Pt	Carbon	0.1	30	2	2.8
Ir-5-IL	Ir	-	1	5	1	4.5
Ir-10-IL	Ir	-	1	10	1	3.4
Ir-15-IL	Ir	-	1	15	1	3.1
Ir-25-IL	Ir	-	1	25	1	3.8
IrOx-35-IL	IrOx	-	1	35	1	4.1
No-IL	-	-	-	-	3	-

the IL resistance, using the DC method. The conductivity can then be calculated by dividing the catalyst thickness by the IL resistance, assuming that no reaction is present in the IL. EIS was performed between frequencies of 1-100 kHz in order to obtain the HFR, however full spectra were not obtained.

2.4 Results and discussion

2.4.1 Supported ILs

Polarisation data

First, intermediate layers composed of a supported catalyst were tested, in particular the carbon based layers used in PEM fuel cells. Figure 2.4 shows the fit of the numerical model to experimentally obtained polarisation curves at 50% and 100% RH. The data shown is from a cell without an IL (No-IL), and from a cell with an IL that does not contain platinum (C-IL). The base parameters shown in Section 2.2.6 provide close agreement between the model and experimental data for No-IL at both RH, where the active area was used as a fitting parameter. The HFR computed using

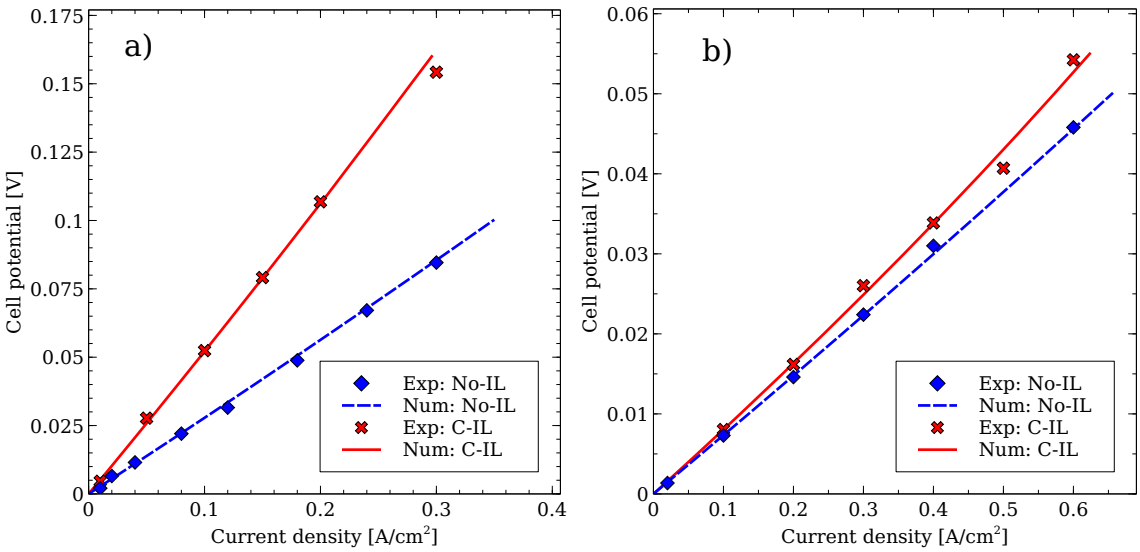

Figure 2.4: Numerically and experimentally obtained polarisation data for the No-IL and C-IL cells. The RH is (a) 50%, and (b) 100%.

numerical EIS had close agreement with the HFR obtained experimentally, at 50% RH the HFR was 210 and 214 mΩ.m^2, while at 100% RH it was 55 and 61 mΩ.m^2, for the numerical and experimental HFR respectively. The polarisation curves for the C-IL case at both RH are also accurately reproduced by the model. However, the experimental polarisation data shown in Figure 2.4 needed to be corrected to obtain this fit, as is discussed in the following section.

ICR correction

Figure 2.5 a) shows the change in HFR with changing RH for the ILs tested experimentally in this work. The HFR of the No-IL case is also shown, and it can be seen that there is a marked increase in HFR when the IL is included compared to when it is not. The increase is similar regardless of the composition of the IL. This increase in HFR was not seen in the numerical model, as is discussed in Section 2.4.1. Sabarirajan et al. [154] reported experimentally obtained HFR values with and without a carbon based IL and showed the HFR did not change with the addition on an

IL[1]. The increase in the HFR observed in this work was attributed to the interfacial contact resistance (ICR) between the IL and the two membranes, which should be removed before computing the conductivity. This ICR correction involves computing the difference in the HFR of the cell with and without an IL at each RH, and subtracting that resistance from the resistance of the cell with an IL, before applying the standard DC method. The AC method from Iden et al. [134] relies on the HFR being independent of the IL, therefore an experimenter should ensure that the ICR is minimised before applying the AC method. Note that while the ILs tested in this work did not contribute to the HFR, other IL compositions may have an electronic conductivity lower than those tested here, which will cause the IL to have a contribution. Equation (2.19) should be used to determine the contribution of the IL to the HFR which should not be part of the ICR correction. The protonic conductivity will be unknown prior to assessing the ICR correction. So if the electronic conductivity is not high enough to ensure that the IL does not contribute to the HFR, there will be uncertainty regarding the contribution of the IL. In this case, the IL should be made thicker to ensure that the IL resistance dominates any interfacial resistance.

Figure 2.5 b) shows the conductivity obtained with and without the correction. The use of the correction gives a closer match to the protonic conductivity reported by Iden at el. [134], giving confidence that the ICR correction is valid. However, the conductivity at 100% RH appears to be overestimated. Figure 2.4 b) shows that there is very little difference between the resistance of the No-IL and C-IL cells at 100% RH, indicating that the sensitivity of the experimental setup is not sufficient to capture the low resistance of the IL at this RH. A thicker IL, such as that used by Iden et al. or by Sabarirajan et al. [154], would help in this regard by inducing a higher IL resistance that is easier to isolate. The cited works did not account for

[1]Note that the cell without an IL from Sabarirajan et al. [154] did show a HFR that jumped at lower RHs, and was therefore higher than the other cells, which was attributed to a poor contact between the membranes. The contact between the gas diffusion electrodes used and the membrane may also have been a factor. Such a jump was not seen in this work for the case of a cell without an IL.

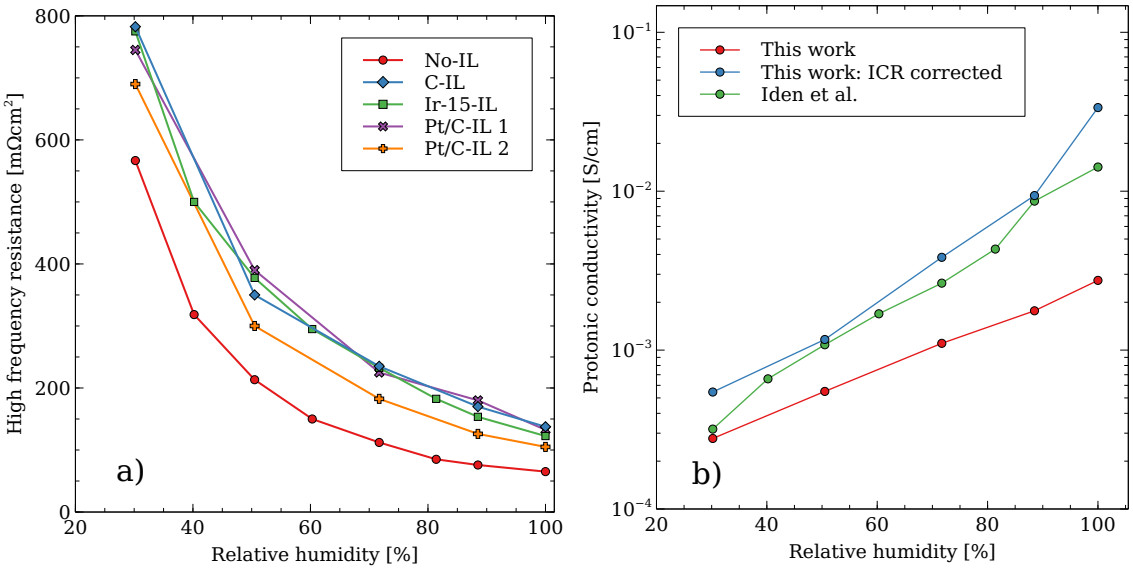

Figure 2.5: (a) Experimentally obtained HFR for each cell tested with changing RH. (b) Protonic conductivity of the unplatinised Ketjen black IL, with and without a correction for the ICR. Also shown is the conductivity reported by Iden et al. [134] for a similar IL.

the ICR correction, however as discussed above, the use of the thicker layer makes the correction less important, as the ICR is likely to be negligible compared to the resistance of the thick ILs.

If after testing an IL there is concern about the ICR, the thickness required to minimise the contribution from the ICR could be estimated. After applying the ICR correction method, the IL protonic conductivity and the difference between the HFR with and without an IL are known. An IL thickness could be computed that would induce an IL resistance that is 10-20 times higher than the ICR, thereby minimising the contribution of the ICR. For example, at 50% RH, the carbon based IL has an ICR of approximately 150 mΩ.cm^2, while the protonic conductivity is approximately 1x10^{-3} S/cm. Therefore, a thickness of 15 μm should be used (using $R_{IL} = L_{IL}/\sigma_p$) to obtain an IL resistance that is ten times higher than the ICR, i.e., 1500 mΩ.cm^2.

Platinised IL

Figure 2.6 shows impact of including the hydrogen reaction in the IL using the numerical model. The slope of the polarisation curve of the platinised IL decreases considerably, becoming very similar to that of the No-IL cell. This result is confirmed by the experimental data, which shows that there is very little additional resistance in the platinised IL (Pt/C-IL) compared to that without an IL. The ICR correction is required here, as the two Pt/C-IL cells showed different polarisation curves despite having the same composition, as is shown in Figure 2.7. As is shown in Figure 2.5 a) however, the HFR of these two cells is also quite different, such that the ICR correction causes both to exhibit the same resistance. That the correction causes both cells to have the same performance gives more confidence to the validity of the method.

Note that there is a small error in the fit between the model and experiment at 50% RH. The IL has the same composition as that used in the ACL and CCL, so the same parameters were used in the model for each layer. It is possible that the microstructure of the IL is not the same as the ACL and CCL, as the membranes provide additional shielding during the hot-pressing process, which may impact the IL activity. However, the hypothesised trend is clearly demonstrated, i.e. that the reaction in the IL reduces the IL resistance, so no attempt was made to tune the IL parameters to match the experiment.

Resistance analysis

The resistance of the ionic and reactive pathways in the IL can be predicted by the model, where the former refers to the resistance induced by the protonic phase only, i.e. equation (2.17), while the latter refers to the sum of the electronic transport and kinetic resistance, i.e. equations (2.18) and (2.20). The resistances are shown in Table 2.5. At 50% RH and a total cell current (which refers to the current passed from anode to cathode) of 200 mA/cm^2, the model predicted a reaction current density of 193 mA/cm^2 in the Pt/C-IL, i.e. 193 mA/cm^2 of current is transferred to the

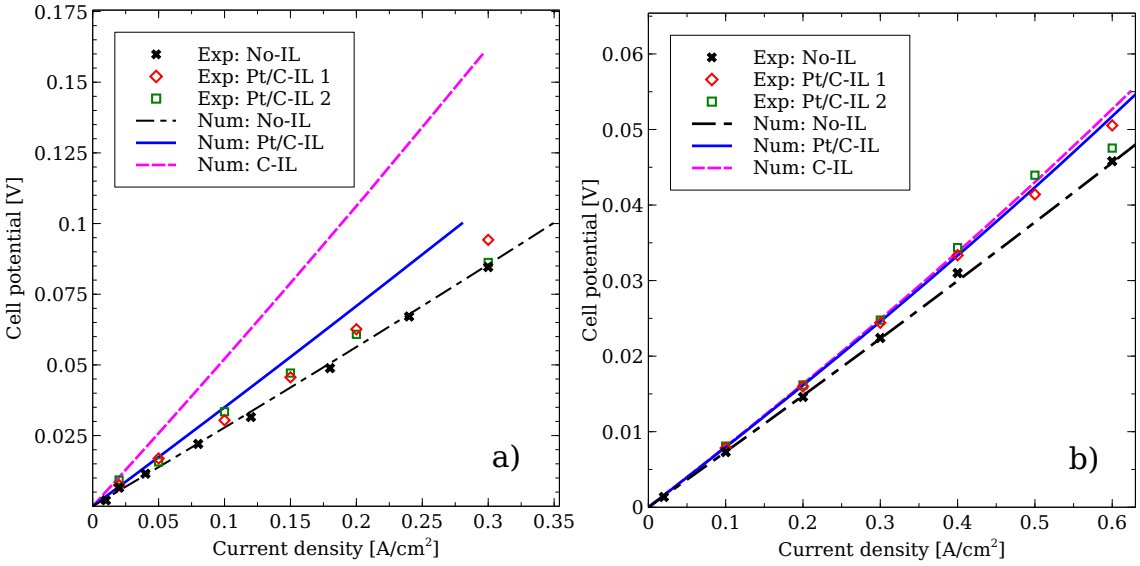

Figure 2.6: Numerically obtained polarisation curves for the No-IL, C-IL and Pt/C-IL cells. Also shown are experimentally obtained polarisation curves from both Pt/C-IL cells. The RH is at (a) 50% and (b) 100%.

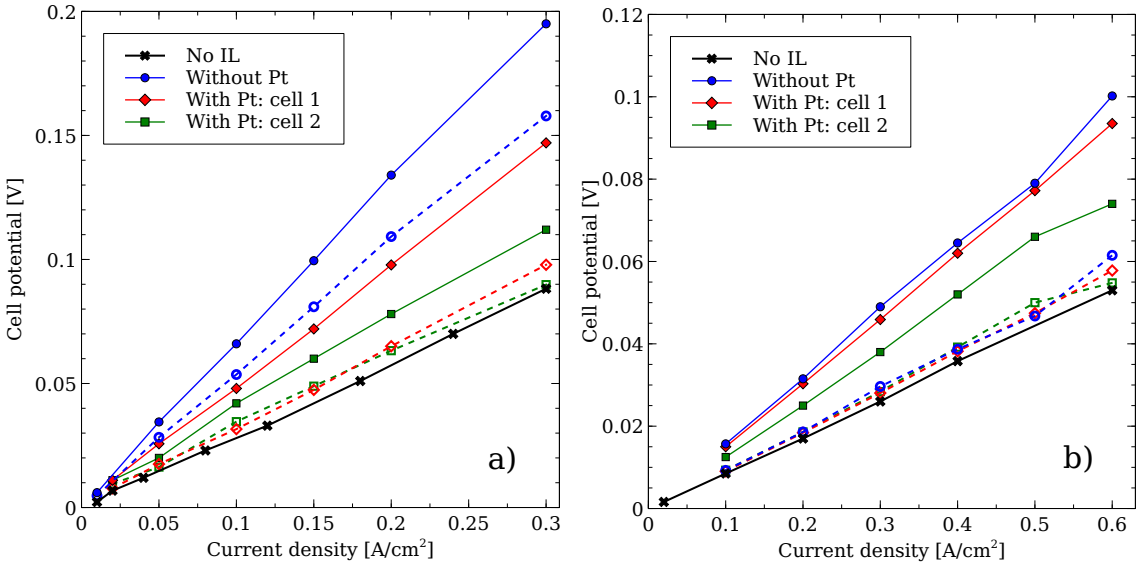

Figure 2.7: Experimentally obtained polarisation curves without an IL, and with a Ketjen black IL. Platinised and unplatinised IL are shown, at 50% RH (left) and 100% RH (right). The dashed lines with open symbols are corrected for the ICR.

Table 2.5: Resistances induced in the carbon based ILs. Note that the protonic resistance in the IL will be the same as that for the ionic pathway.

Humidity	Cell ID	R^{ele}	R^{rxn}	$R^{reactive}$	$R^{protonic}$	R^{total}
50%	Pt/C-IL	0.046	31.7	31.7	32.1	63.9
50%	C-IL	-	-	-	249	249
100%	Pt/C-IL	0.002	1.03	1.03	6.4	7.4
100%	C-IL	-	-	-	8.7	8.7

electronic phase via the hydrogen reaction in the IL. This transfer is demonstrated in Figure 2.8, which shows the predicted electron and proton flux in the IL. The total resistance of the IL (i.e. the summation of the resistance from proton and electron transport along with that from both reactions) in this case is 63.9 $m\Omega.cm^2$, with the reactive pathway accounting for approximately half and the ionic pathway for the other half. The resistance from the electronic phase is negligible, due to the high intrinsic conductivity of the carbon. If there is no reaction in the IL (i.e. C-IL), the model predicts a protonic resistance of 249 $m\Omega.cm^2$, so the addition of the platinum induces a reduction of 185.1 $m\Omega.cm^2$ in the total resistance in the IL. In contrast, at 100% RH, there is a reaction current of only 39 mA/cm^2 in the Pt/C-IL at a total cell current of 200 mA/cm^2. The protonic resistance is 6.4 $m\Omega.cm^2$, with a further resistance of 1.03 $m\Omega.cm^2$ from the reactions. The IL protonic resistance of the C-IL is only slightly higher at 8.7 $m\Omega.cm^2$.

It is interesting to note that at 50% RH the ionic and reactive pathways in the Pt/C-IL have nearly the same resistance. The protonic resistance is therefore not entirely bypassed, as the hydrogen reaction cannot occur at an infinitely thin interface between the membrane and the IL, as shown in Figure 2.8. Reducing the extent to which the protons penetrate the IL will also reduce the total electrochemical surface area available to the reaction, thereby increasing the resistance of the reaction. This tradeoff appears to be balanced at 50% RH, where the reactive and ionic pathways

induce the same resistance.

At 100% RH for the Pt/C-IL, it appears the protonic resistance could be further reduced if more current is passed through the reactive pathway. The reason this does not occur is shown in Figure 2.9, which shows the profiles of the overpotential and the solid and ionomer potentials through the centre of the IL in the through-plane direction. The location of this line is shown in Figure 2.10. At both RH, the electronic potential has risen from zero volts to bisect the profile of the protonic potential. In doing so, the overpotential (which is given by $\eta = \phi_s - \phi_m - E_{th}$) can be positive at one side of the IL and negative at the other side, thereby allowing for the oxidation reaction at one side and the reduction at the other. The electronic potential changes very little across the IL, as the conductivity is high. In order to induce large overpotentials, and therefore the large reaction current densities in the Pt/C-IL, the protonic potential must vary significantly across the layer. At 50% RH, there is a change of 15 mV in the protonic potential across the IL, allowing for the relatively high reaction current density predicted in the IL. The low protonic conductivity of the IL at this RH allows for this gradient in the potential to be generated, even if much of the protonic phase is bypassed by the reactive pathway. At 100% RH, there is very little change in the protonic potential, less than 2 mV. The protonic conductivity is much higher compared to at 50% RH, which causes the limited variation in the protonic potential, therefore limiting the overpotential and the reaction current density that can be achieved. To illustrate this point, note that if the reaction current density was arbitrarily made higher at 100% RH, there would be less proton transport through the ionomer as more current is transferred instead to the electronic phase. This would reduce the gradient of the protonic potential, reducing the overpotential, and therefore reducing the reaction current density that can be achieved. Hence an equilibrium is reached that does not necessarily cause the ionic and reactive pathways to have the same resistance. This analysis shows that the interplay between the reactive and ionic pathway can be complex, making it

necessary to use a computational model to deconvolute the individual resistances in the IL.

Numerical EIS

Figure 2.11 shows a Nyquist plot and a plot of how the real and imaginary impedance changes with frequency, both of which were obtained using the numerical model at 50% RH and a cell current of 40 mA/cm^2. The shape of the simulated spectra agree with those obtained numerically by Kulikovsky [156] using an analytical model, and experimentally by Sabarirajan et al. [154]. The Nyquist plots show that including the IL induces additional resistance that does not contribute to the HFR, as expected. This is also illustrated by the real impedance against the frequency plot; the real impedance for each cell converges to approximately 210 mΩ.cm^2 at high frequencies. The resistance from the IL is part of the capacitive arc, whether there is reaction occurring in the IL or not. There is not a distinct feature in the Nyquist plot that can be attributed to the presence of the reaction, making it difficult to use EIS to ascertain whether the reaction is present, and impossible to deconvolute the resistance from the reaction to that from proton transport. There is a noticeable difference between the spectra with and without the reaction, as the reactive pathway bypasses almost all the resistance in the IL. It could be said that if the EIS spectra of the cell with the IL is similar to that without an IL, then it is very likely that the reaction is present. However that would also be apparent from the polarisation curves. If the IL is only partially bypassed then it is more difficult to make the determination that the reaction is present.

The frequency plot shows that when there is no IL, the peak of the imaginary impedance, also known as the summit frequency, occurs between 1 and 10 kHz. With the introduction of the IL, the peak shifts as the total resistance of the cell changes. Kulikovsky [156] presented a method to calculate the protonic conductivity of the IL based on the summit frequency of the Nyquist spectrum. The relationship can be

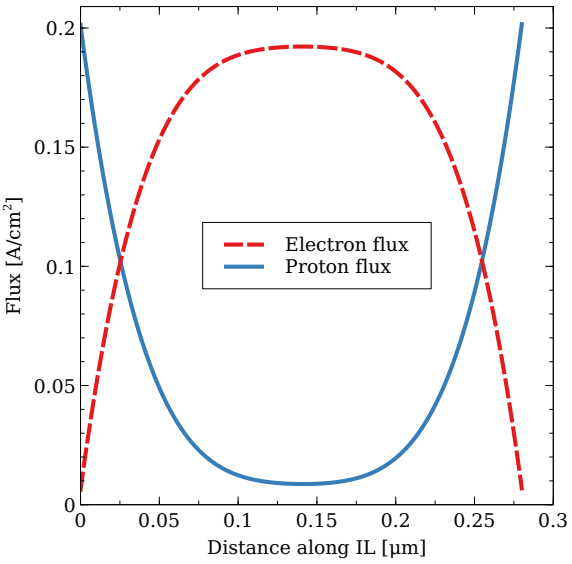

Figure 2.8: Proton and electron fluxes along the centre line indicated in Figure 2.9 for the Pt/C-IL at 50% RH.

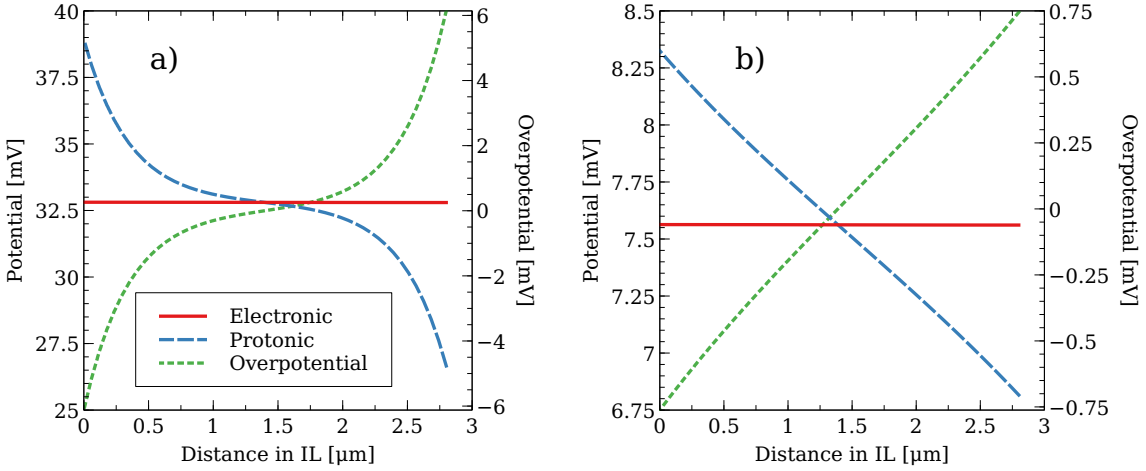

Figure 2.9: Profiles of the solid and ionomer potentials across the Pt/C-IL in the through-plane direction at 200 mA/cm^2, along with the overpotential (right axis). The RH is at (a) 50% RH, and (b) 100% RH.

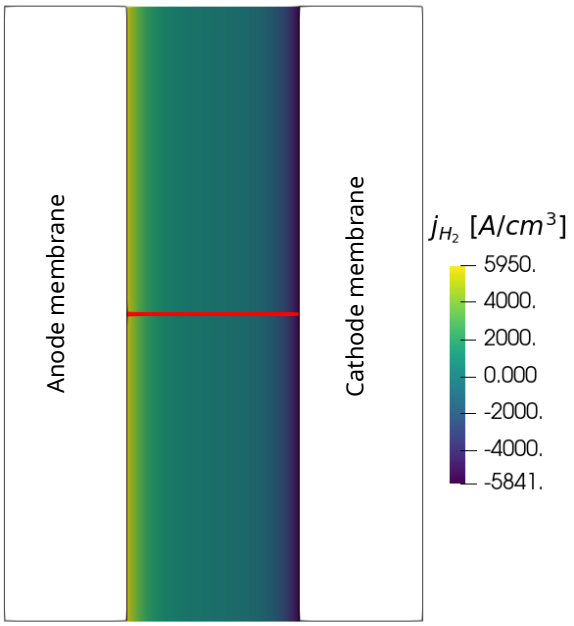

Figure 2.10: Location of the centreline used to obtain the potential profiles in Figure 2.9. Positive current is the HOR, while negative current is the HER.

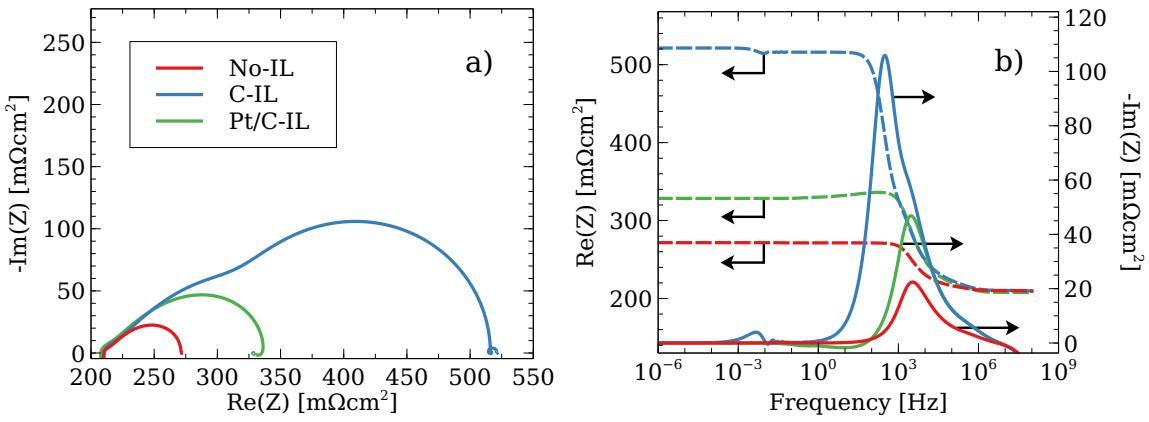

Figure 2.11: Numerically obtained impedance plots for the No-IL, C-IL and Pt/C-IL cells at 50% RH and a cell current density of 40 mA/m^2. The figure shows (a) a Nyquist plot, and (b) frequency against real (left axis, dashed lines) and imaginary impedance (right axis, solid lines).

arranged to give:

$$\sigma_m^{eff} = \frac{\omega_{max} C_{dl} l_t^2}{\tilde{\omega}_{max}^{\infty}} \left(1 - \frac{\omega_{max} C_{dl} l_t^2}{\sigma_s^{eff} \tilde{\omega}_{max}^{\infty}}\right), \quad \tilde{\omega}_{max}^{\infty} = 10.162 \tag{2.22}$$

where σ_s^{eff} is the electronic conductivity of the IL, C_{dl} is the double layer capacitance in F/cm^3, l_t is the IL thickness and ω_{max} is the summit frequency in rad s^{-1}. Using the summit frequency of the C-IL cell at 50% RH, which is 307 Hz, the equation above predicts a protonic conductivity of 1.22 mS/cm, which is very close to the value of 1.17 S/cm obtained experimentally in Figure 2.5, which was the input parameter to the model. When applying this method, it may be necessary to subtract the spectrum of the cell without an IL from that with an IL before finding the summit frequency. This is especially important if the impedance of the cell with an IL is not significantly higher than the cell without an IL. At 100% RH, the summit frequency is 8.8 kHz, corresponding to a conductivity of 34.2 mS/cm, which is close to the actual conductivity used in the model of 33.6 mS/cm.

2.4.2 Unsupported ILs

In PEM electrolysis, the high potentials in the anode catalyst layer make using catalyst supports difficult. As such, unsupported Ir and IrO_x catalyst layers are often used, which could potentially be active to the hydrogen reaction. Care must be taken when using the hydrogen pump method to measure their protonic conductivity, as the reactive pathway may be active, and unlike the carbon based ILs, the active component cannot be removed. Two unsupported catalysts are studied, an IrOx based IL, which has a low activity to the hydrogen reaction and low electronic conductivity, and an Ir based IL, which has a higher activity and conductivity.

Ir

The Ir black catalyst is known to be highly active to the hydrogen reaction [80], and the electronic conductivity was measured by Mandal [126] to be approximately 0.05 S/cm, i.e. significantly higher than that of the IrOx. As such, this catalyst is a good

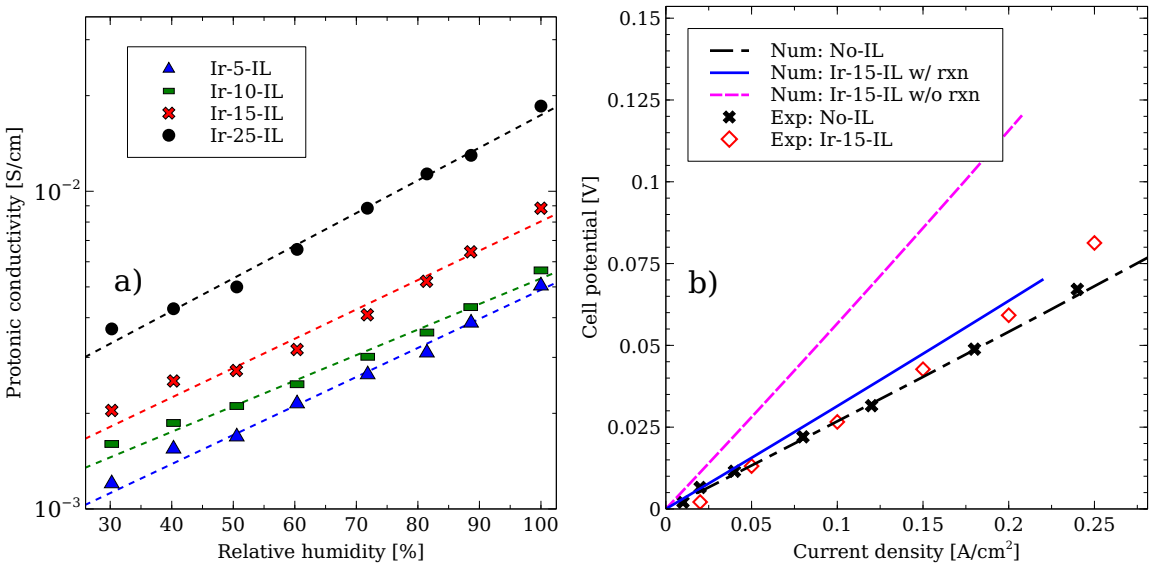

Figure 2.12: (a) Protonic conductivities of the Ir IL with different Nafion loadings, extracted from data provided in Mandal [126], where the ICR correction has not been applied. (b) Numerically and experimentally obtained polarisation curves for the No-IL and Ir-15-IL cells at 50% RH.

candidate to demonstrate the hypothesis that unsupported ACLs that are active to the hydrogen reaction might not be suitable for the hydrogen pump technique. It should be pointed out that an Ir black catalyst used in a PEMWE ACL will likely oxidise significantly during operation; it is assumed that any proton conductivity that is obtained from the proton pump method will still be representative of the in-situ proton conductivity even if significant oxidation occurs during PEMWE operation. The model was used to investigate whether the IL would induce the reactive pathway, using the protonic conductivity at 15% ionomer loading (Ir-15-IL) and at 50 % RH shown in Figure 2.12 a). To allow for an initial study, the conductivity shown was obtained without applying the ICR correction or considering the reactive pathway, i.e. obtained with what might be considered the naive application of the DC method. Figure 2.12 b) shows that neglecting the reactive pathway in Ir-based ILs leads to significantly higher voltage than measured experimentally. Good agreement is achieved when the reaction in the IL is enabled in the model, indicating that the reactive pathway is significant for this IL.

It is interesting that the protonic conductivities obtained without the ICR correction appear to be reasonable as shown in Figure 2.12 a), i.e. there is reasonable linearity, and the conductivity increases with increasing ionomer loading. However, there is not a significant drop in the protonic conductivity at low ionomer loadings, as was observed for the IrO_x based ILs tested in reference [125]. A drop in conductivity would indicate that a percolating network is not maintained at low ionomer loadings, therefore a lack of a significant drop could be used as an indication in future experiments that the IL is in fact reactive. Figure 2.13 a) shows how the experimentally obtained HFR changes with ionomer loading, which are significantly different to that of the No-IL cell. The difference decreases with increasing ionomer loading, indicating that a higher ionomer loading may reduce the contact resistance between the membrane and the IL. Figure 2.13 b) shows the polarisation curves after applying the ICR correction. Each polarisation curve collapses to the same performance as that of the No-IL cell, again suggesting that the reactive pathway is active and is bypassing the majority of the ionomer phase, as well as highlighting the importance of the ICR correction. While there was an order to how the HFR changed with changing ionomer loading in Figure 2.13 a), there is no such order in the ICR corrected polarisation curves, i.e. the polarisation curves mostly lie on top of each other. This shows that the differences in the polarisation curves for different ionomer loadings were only caused by the differences in the ICR, and therefore not by the IL. The Ir-25-IL curve appears to have a resistance that is lower than the no-IL cell. This is attributed to experimental error, as most of the data points lie on the no-IL curve, with only the final two points not following the trend.

The model predicts that for a cell current density of 200 mA/cm^2 and an RH of 50%, there will be a reaction current density of 195 mA/cm^2 in the IL when the reaction is active, causing most of the charge to be transferred through the electronic phase. While the carbon based IL induced a negligible resistance in the electronic phase, the resistance of the Ir IL is 5 $m\Omega.cm^2$. The resistance of the protonic phase

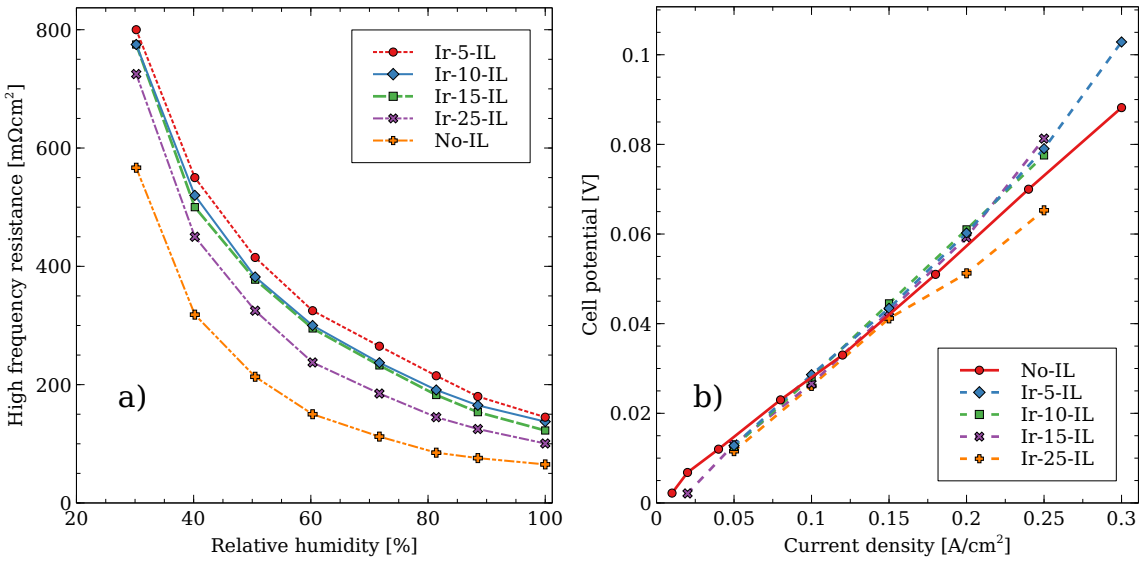

Figure 2.13: (a) HFR measured experimentally for different ionomer loadings with an Ir IL, compared to the No-IL cell. (b) Experimentally obtained polarisation curves with an Ir IL compared to the No-IL cell at 50% RH. The potential is corrected for the ICR.

if the reactive pathway is not active is 306 mΩ.cm^2, so the electronic resistance is not too significant, however any further reduction in the electronic conductivity will start to inhibit the reactive pathway, as is shown in the parametric studies below. The model also predicts that the ionic and reactive pathways are not balanced. The ionic pathway induces a resistance of 21.5 mΩ.cm^2, while the reactive pathway has a resistance of 25.7 mΩ.cm^2, again demonstrating the complex interaction between the two pathways in the IL. Given the model shows that the ionic pathway is being bypassed, the protonic conductivities shown in Figure 2.12 a) should be considered to be at best an upper limit of the actual conductivity.

It is difficult to determine the correct protonic conductivity for the Ir IL, however by using the model to vary the IL protonic conductivity, an approximate value can be obtained. Figure 2.14 shows the impact of changing the IL protonic conductivity for the Ir-15-IL cell. If the protonic conductivity is reduced by a factor of ten, the predicted polarisation curve deviates significantly from the experimental curve. The fit is slightly improved by increasing the conductivity by a factor of five, but the

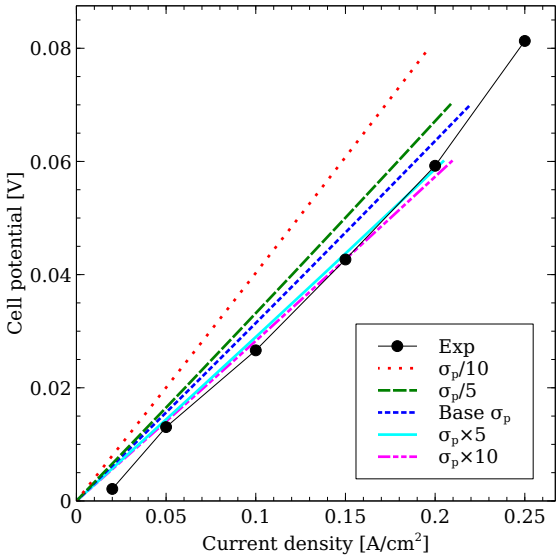

Figure 2.14: Impact of changing the protonic conductivity in the model for the Ir IL with an ionomer loading of 15%. The experimental data is corrected for the ICR.

curve does not change significantly with a ten times increase. Therefore the true conductivity is likely between five times higher and five times lower than that shown in Figure 2.12 a). This study demonstrates that it may be possible to obtain an estimate of the protonic conductivity of an active IL by using numerical modelling to choose a value that makes the model matches the experimental polarisation curve. There will be some uncertainty to this method that will depend on the accuracy of the electronic conductivity and activity of the IL. In addition, the fact that there is a significant reaction current in the IL studied here results in the polarisation curve of the cell with the IL being similar to that without an IL. A higher degree of confidence in the estimate of the IL protonic conductivity from the model would be obtained if the reactive pathway was less impactful, as the IL would induce a higher resistance and provide a stronger signal for the analysis.

IrOx

In contrast, the IrOx catalyst has a low activity to the hydrogen reaction and a very low electronic conductivity [125], so it expected that the reactive pathway does not

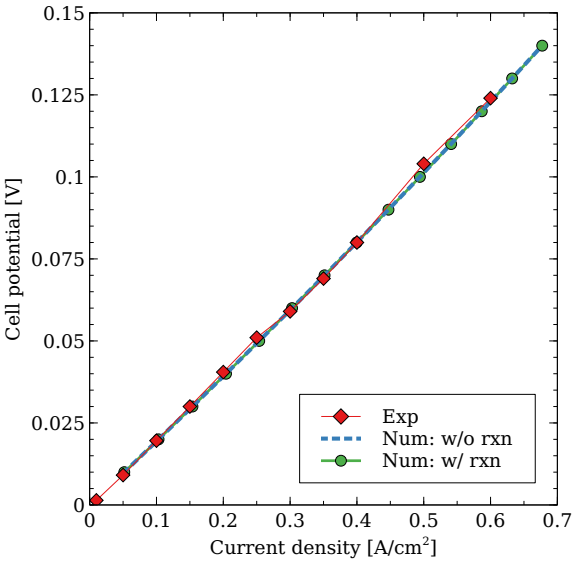

Figure 2.15: Comparison between an experimentally obtained polarisation curve and that predicted by the model with the reaction in the IL switched on and off, for the IrOx based IL. The experimental data is not corrected for the ICR.

interfere with the measurement of the protonic conductivity. A hydrogen pump cell with an IrOx IL from reference [125], denoted IrOx-35-IL, was simulated as shown in Figure 2.15 at an RH of 80%. The simulations show that there is good agreement between the experiment and model regardless of whether the reaction is simulated in the IL or not. The parametric studies presented later in this work will show that both the electronic conductivity and activity are individually too low for the reactive pathway to proceed. Specifically, even if the IrOx was as active as platinum, the low electronic conductivity prevents the occurrence of the reactive pathway. Similarly, if the IrOx was a conductive as carbon, the low activity to the hydrogen reaction would prevent reactive pathway. As such, it can be assumed with confidence that the ionic pathway is dominant during the measurement of the IrOx protonic conductivity.

There is still some uncertainty in the measurement of the protonic conductivity due to the ICR however. The idea that the HFR of the cell with and without an IL should be the same will not apply to the IrOx IL, as the electronic phase is lower than the protonic. As such, the resistance of the IL will not be bypassed at high

frequency and will contribute to the HFR, so the ICR correction method cannot be applied. As an example using equation (2.19): if the electronic conductivity is 5x10^{-5} S/cm, and the protonic is 5x10^{-3} S/cm, the contribution of a 4 μm IL to the HFR is approximately 80 mΩ.cm^2. Unfortunately, the protonic conductivity is what is being measured so the IL contribution cannot be accounted for before applying the ICR correction.

The ICR estimated for the Ir based IL could be used to get an estimate of the ICR for the IrOx. Mandal et al. [126] measured the protonic conductivity of both Ir and IrOx ILs with an ionomer loading of 10, 15 and 25% wt., so the ICR correction estimated from the Ir ILs can be applied to the IrOx. The 10 and 15% wt. IrOx ILs had extremely high cell resistances so the ICR correction would have very little effect. As such the measured conductivity for these ionomer loadings is likely accurate. Applying the ICR correction to the 25% wt. IrOx IL resulted in a doubling of conductivity at high RH, with a smaller gain at lower RH. The IrOx protonic conductivity was also measured at 35 and 55 % wt. ionomer loading but not for the Ir IL, preventing the application of the correction. However, Figure 2.13 a) shows that ICR correction reduces with increasing ionomer loading, so the correction will hopefully be less impactful at these higher ionomer loadings. It is difficult to apply the ICR correction in this manner, as it is not likely that ILs comprised of two different catalysts will have the same ICR at the same ionomer loading, particularly as the IrOx has a significantly higher surface area than the Ir. As discussed in Section 2.4.1, the impact of the ICR can be mitigated using thicker ILs so that the bulk resistance is higher than the interface.

2.4.3 HFR study

Figure 2.16 a) compares the HFR and cell resistance measured at different RH, for the C-IL and Pt/C-IL cells. The HFR obtained from the No-IL cell is also shown. The figure shows that the platinised IL exhibits a HFR and cell resistance that both

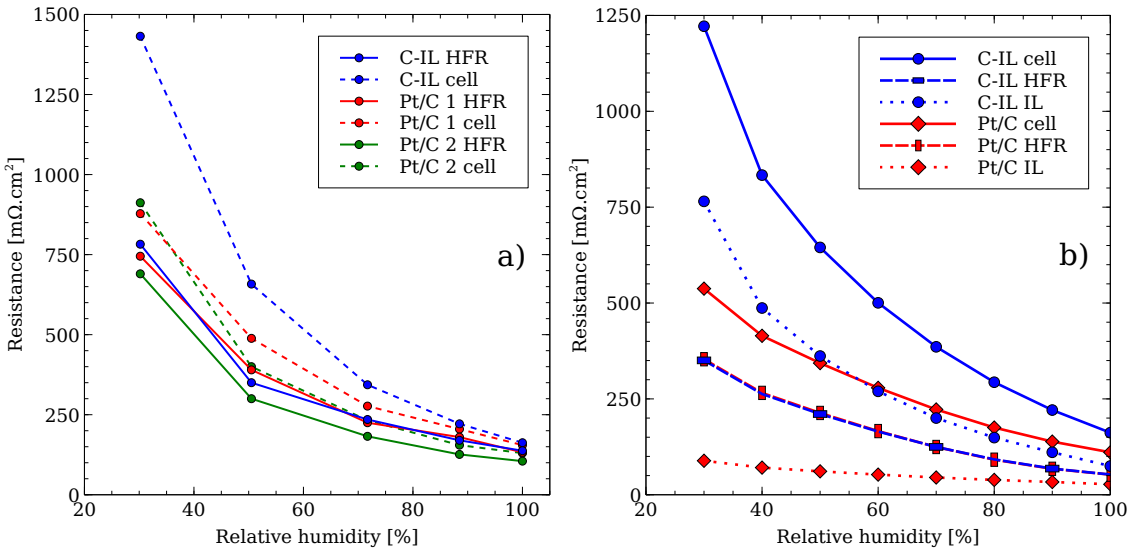

Figure 2.16: Comparison between (a) experimentally and (b) numerically obtained HFR and cell resistance with changing RH, with and without platinum in the IL. (a) also shows the HFR without an IL, while (b) also shows the resistance from the IL.

decrease with decreasing RH by a similar amount. In contrast, the unplatinised IL shows a large deviation between the cell resistance and HFR with decreasing RH. That the platinised IL does not exhibit a large increase in the cell resistance with decreasing RH is due to the reactive pathway bypassing the increasingly resistive IL, masking the impact of the lower RH on the protonic conductivity of the IL. If during an experiment, there is uncertainty about whether the reactive pathway is active, the trends observed in Figure 2.16 a) may serve as a clue. If a significant difference between the HFR and the cell resistance at low RH (or at low ionomer loading) is not observed, then it is possible that the reactive pathway is bypassing the IL.

The model can be used to explain the results in Figure 2.16 a), which showed how the experimentally obtained HFR and cell resistance changed with changing relative humidity at a constant ionomer loading. Figure 2.16 b) shows the same trend in the numerical model, i.e. that the HFR is independent of the IL, as the high frequency signal bypasses the protonic resistance regardless of the presence of the platinum. This results in the same HFR being predicted for the cells with and without Pt in the

IL, which is also equal to the predicted HFR of the cell without an IL. The significant divergence between the HFR and cell resistance is observed for the unplatinised IL and not for the platinised IL with decreasing RH. The cause of this is shown by the predicted resistance of the IL, which includes the ohmic resistance of both phases and the kinetics. The total IL resistance increases significantly with reducing RH without platinum, due to the protonic resistance of the layer. The platinised IL bypasses much of this, and exhibits a much smaller dependence on the RH, hence the difference in the divergence between the HFR and cell resistance with and without platinum.

AC method

In the AC method [134], the HFR of a cell is subtracted from the cell resistance, obtained from the slope of the polarisation curve, to obtain the resistance of the IL without needing to test a second cell that does not include an IL. To understand the validity of this method, it is necessary to understand how each of the ohmic and kinetic losses are manifested in the cell resistance and especially in the HFR. The resistance of the cell hardware, GDL, MPL and membranes will be the same for both and can be lumped into R_{other}. The contact resistances are also assumed to be the same for both, as per the ICR correction, and are lumped into R_{other}. The cell resistance will be comprised of:

$$R_{IL}^{DC} = R_{other} + \left(R_{CCL}^{e} + R_{CCL}^{p} + R_{CCL}^{kin}\right) + \left(R_{IL}^{e} + R_{IL}^{p} + R_{IL}^{kin}\right) + \left(R_{ACL}^{kin} + R_{ACL}^{e} + R_{ACL}^{p}\right) \tag{2.23}$$

where the superscript e refers to electronic ohmic losses, p refers to protonic, and kin refers to the apparent resistance from the kinetics of the hydrogen reaction. The HFR does not contain the contribution from the reactions, while the ohmic contribution of the catalyst layers to the HFR is computed using equation (2.19). The resistance at high frequency can therefore be given as:

$$R_{IL}^{HFR} = R_{other} + \frac{L_{CCL}}{\sigma_{CCL}^{e} + \sigma_{CCL}^{p}} + \frac{L_{ACL}}{\sigma_{ACL}^{e} + \sigma_{ACL}^{p}} + \frac{L_{IL}}{\sigma_{IL}^{e} + \sigma_{IL}^{p}} \tag{2.24}$$

Subtracting the HFR from the cell resistance gives the AC method:

$$R^{AC} = R^{e}_{CCL} + R^{p}_{CCL} + R^{kin}_{CCL} + R^{e}_{IL} + R^{p}_{IL} + R^{kin}_{IL} + R^{kin}_{ACL} + R^{e}_{ACL} + R^{p}_{ACL} - \left(\frac{L_{CCL}}{\sigma^{e}_{CCL}+\sigma^{p}_{CCL}} + \frac{L_{ACL}}{\sigma^{e}_{ACL}+\sigma^{p}_{ACL}} + \frac{L_{IL}}{\sigma^{e}_{IL}+\sigma^{p}_{IL}}\right) \quad (2.25)$$

This method results in contributions from several resistances which must cancel each other out or be minimised relative to the resistance of interest, namely the protonic resistance of the IL, R^{p}_{IL}.

Assuming the IL is not reactive, R^{kin}_{IL} and R^{e}_{IL} will be zero. It should be noted however, that the AC method will not mitigate the impact of the reactive pathway if the IL is active, as these resistances will be non-zero. The model can be used to estimate the remaining resistances. Given that Pt/C CLs are used in the anode and cathode, the parameters in Table 2.3 are applied, along with an RH of 50%. The high electronic conductivity of the CLs results in the DC electonic resistance of the ACL and CCL being predicted to be less than 0.1 mΩ.cm^2, so they do not contribute meaningfully to the resistance. The kinetic and protonic resistances are shown in Figure 2.17 with changing RH. There is a slight asymmetry between the anode and cathode due to the differences in transfer coefficient for the oxidation and reduction reaction. There is also a slight difference in the water content in each electrode from electro-osmotic drag. The kinetic and protonic resistances appear to be balanced in each electrode, in a similar manner to that discussed in Section 2.4.1 for the carbon based IL at 50% RH. The kinetic and protonic losses are approximately 16 mΩ.cm^2 each at 50% RH, in each electrode.

Finally the contribution from the CLs to the HFR is dominated by the highly conductive electronic phase, resulting in a resistance of less than 0.1 mΩ.cm^2 according to Equation (2.19), which is subtracted from the other resistances. This value assumes that the CLs are carbon based, other CL compositions could have a higher contribution to the HFR, depending on the thickness and phase conductivities. Summing the aforementioned resistances, the AC method will overpredict the IL protonic

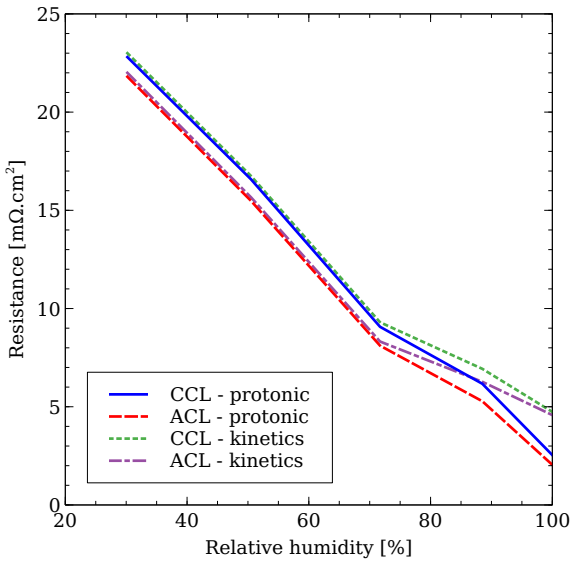

Figure 2.17: Kinetic and protonic resistance in the ACL and CCL with changing RH.

resistance by approximately 64.5 $m\Omega.cm^2$. At this RH, the model predicts a HFR of 210 $m\Omega.cm^2$ and a cell resistance of 527 $m\Omega.cm^2$. The AC method would therefore predict an IL resistance of 317 $m\Omega.cm^2$. The actual resistance of the IL protonic phase is 250 $m\Omega.cm^2$, as expected from the ACL and CCL kinetic and protonic resistances, an error of 25%. At 100% RH, the analysis is similar, with the kinetic resistances being 9.3 $m\Omega.cm^2$ in total, and the protonic resistances of the ACL and CCL at 4.6 $m\Omega.cm^2$. The AC method predicts an IL resistance of 22.1 $m\Omega.cm^2$, while the actual IL resistance is 12 $m\Omega.cm^2$ for an error of 84%.

These resistances can be estimated numerically, as demonstrated above, or obtained experimentally by testing a cell without an IL and computing the difference between the HFR and cell resistance. In the latter case, it may be preferable to simply apply the DC method however. A more accurate estimation of the IL conductivity can be found with the AC method if these resistances are also subtracted from the measured AC resistance (i.e. the result of equation (2.25)). The predicted conductivity from this modified AC method is compared to the standard AC method, along with that from the DC method, and the DC method with the ICR correction in Figure 2.18, for the

carbon based IL with no platinum. The modified AC method shows good agreement with the ICR corrected DC method, despite the analysis being very different, giving greater confidence to the applicability of both methods. It is also interesting to note that all methods are similar at lower RH, with the largest differences being seen at high RH. This dependence on RH is caused by the IL resistance being significantly higher at low RH, making the modifications to the DC and AC methods less impactful. This again highlights the importance of using ILs that maximise their resistance relative to the rest of the cell components, by reducing RH and increasing thickness when the layer is not active.

The errors induced by the AC method are not insignificant and difficult to estimate analytically without modelling the ACL and CCL to understand the kinetic and protonic losses there. However, the losses can be reduced experimentally, for example by increasing the platinum loading using a high platinum to carbon ratio in the ACL and CCL, which will minimise the kinetic losses without increasing the layer thickness, and by using a high ionomer loading in the ACL and CCL to minimise the protonic losses. The choice of carbon support has been shown to change the protonic conductivity of the CL, see the supporting information in reference [125], however changing the support may also reduce the activity of the layer. The use of a thicker IL will cause the errors induced by the AC method to decrease as the IL protonic resistance dominates the cell resistance. For example, Sabarirajan et al. [154] used a minimum thickness of 10 μm for their ILs and found good agreement between the DC and AC methods.

2.4.4 IL parametric studies

For the parametric studies, the parameters in Table 2.3 are used as the base case, with either the IL thickness, exchange current density or electronic conductivity being varied. The simulations are carried out at 50% RH, so an IL protonic conductivity of approximately 1.12 mS/cm is applied. The cell current density is constant at 200

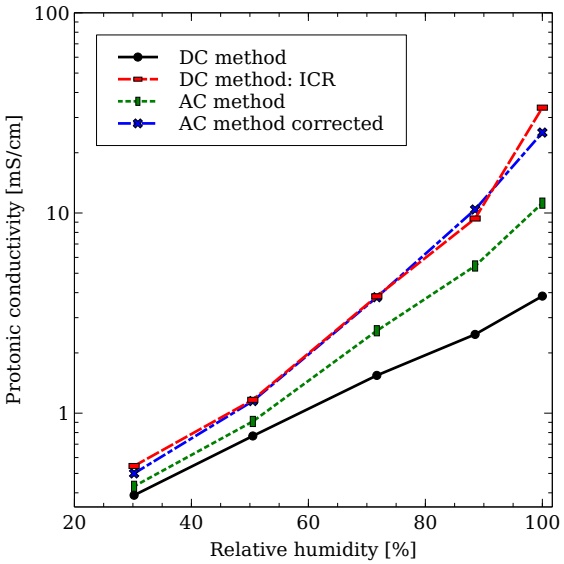

Figure 2.18: Experimentally obtained protonic conductivities on the unplatinised carbon IL computed using different methods.

mA/m^2 in each simulation, achieved by applying the appropriate cell potential in each case. As part of the parametric study the protonic conductivity is computed as described in Section 2.2.7 and compared to the model input to assess the impact of the reactive pathway.

Exchange current density

Figure 2.19 a) shows how the IL resistance changes with changing exchange current density for a Pt/C IL. An IL resistance of 249 mΩ.cm^2 is expected if all the current passes through the protonic phase, as discussed in Section 2.4.1. The total resistance gets close to that value once the IL reaction current density drops to less than 10 mA/cm^2, which is twenty times lower than the cell current density of 200 mA/cm^2. The estimated IL resistance is very sensitive to the exchange current density; as the latter is reduced, the IL reaction current falls off rapidly, causing the ionic pathway to dominate transport through the IL. If the exchange current density is changed from the base case of 0.24 to 0.01 A/cm$^2_{Pt}$, the total IL resistance is 204 mΩ.cm^2, corresponding to an IL conductivity of 1.37 mS/cm, which is very close to the conductivity

applied in the model.Table 2.3 shows that the Ir and Pt/C based ILs have exchange current densities above 0.01 A/cm^2, so the reactive pathway can be expected for these layers. The IrOx layer has an exchange current density of approx 2.51x10^{-6} A/cm^2, therefore the reactive pathway is suppressed, despite the high electronic conductivity of the IL simulated in this parametric study.

If there is uncertainty regarding whether the reactive pathway is active in an IL, changing the IL thickness is a possible method to determine if that is the case. The resistance should scale linearly with the thickness for inactive ILs, and will drop off at higher thicknesses for active ILs, which is shown in Figure 2.19 (c). At the lowest exchange current density of 10^{-6} A/cm$^2_{Pt}$, the resistance is linear with the thickness, indicating that the reactive pathway is not active at any thickness. This was confirmed by simulating a cell with an IL that had zero activity, which resulted in the same predicted resistances. Figure 2.19 b) shows that the conductivity is constant with changing thickness for this activity, indicating that the method is working correctly. With increasing activity, the thicker layers become more susceptible to the reactive pathway, as the apparent resistance is no longer linear. Then the computed conductivity increases with thickness, as the resistance is not increasing in step with the thickness. This suggests that if the IL is partially active to the hydrogen reaction, thinner layers may be preferable. The resistance of the ionic pathway will increase linearly with IL thickness, whereas kinetic resistance will be independent. For activities of 10^{-1} and 10^{-2} A/cm$^2_{Pt}$, the reactive pathway is active at every thickness, indicating that the hydrogen pump technique is not suitable for that particular IL. A reasonable conductivity is computed once the exchange current density is 10^{-4} A/cm$^2_{Pt}$ or lower. The curve at 10^{-4} A/cm$^2_{Pt}$ in Figure 2.19 (c) shows a significant change in the predicted IL resistance at 25μm, however the corresponding protonic conductivity in Figure 2.19 b) is close to the model input of 1.12 mS/cm. As such, the reactive pathway does not have to be completely shut down to obtain a reasonable estimate of the conductivity.

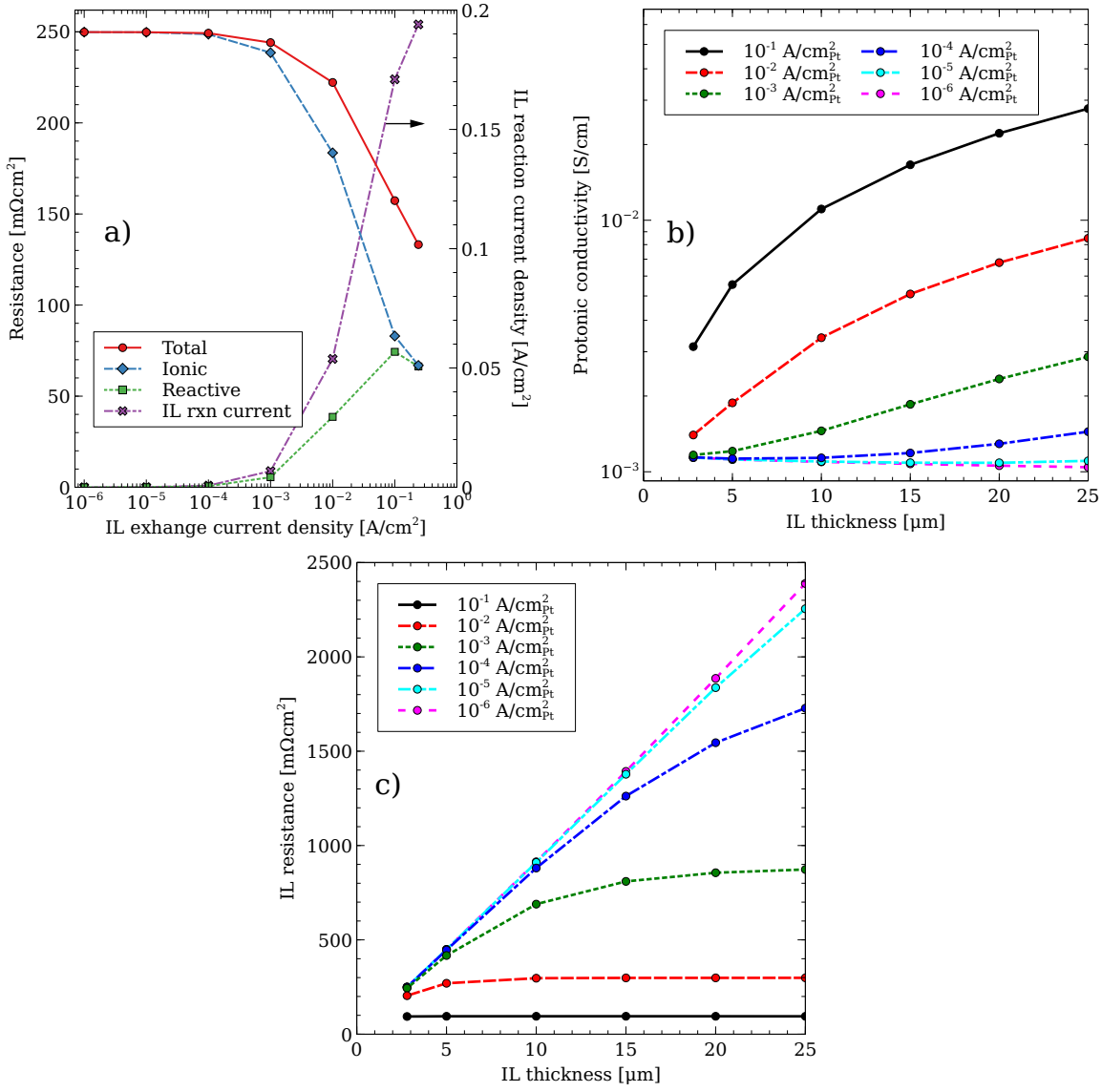

Figure 2.19: (a) Sensitivity of the sum of all resistances in the IL (Total) to the exchange current density. Also shown are the resistances from the ionic and reactive pathways, and the reaction current density in the IL. The impact of changing the IL thickness on (b) the protonic conductivity computed using the DC method and (c) the total IL resistance, for varying exchange current densities. The current density is 200 mA/cm^2 for each.

Electronic conductivity

Figure 2.20 a) shows the effect of changing the electronic conductivity when the reactive pathway is active. The electronic conductivity needs to be reduced to less than 10 mS/cm to start reducing the impact of the reactive pathway. At an electronic conductivity of approximately 3 mS/cm, which is close to the protonic conductivity of the IL, the ionic and reactive pathways induce a similar resistance. Both phases having the same conductivity does not induce the same resistance in each pathway, due to the additional resistance of the reaction. If the electronic conductivity is lower than the protonic, the losses through the reactive pathway are higher than the ionic, so the reactive pathway is shut down. Table 2.3 shows that the Ir and Pt/C ILs have higher conductivities than 3 mS/cm, so are susceptible to the reactive pathway On the other hand, the IrOx conductivity is $4.5\text{x}10^{-5}$ S/cm, which again completely suppresses reactive pathway despite the high activity of IL simulated in the parametric study.

Figure 2.20 b) shows the computed conductivity for changing IL thickness. There is a grouping of the curves to either being constant and close to the model input protonic conductivity in the case of low electronic conductivity ILs, or showing a dependence on the thickness in the case of high electronic conductivity ILs. Figure 2.20 (c) shows a similar trend for the IL resistance. This grouping can be explained by the ratio, k_σ, of the electronic to protonic conductivity in the IL, i.e. $k_\sigma = \sigma_s^{eff}/\sigma_m^{eff}$, which is shown in the legend in the figure. For an k_σ value of 1, the resistances are similar in the ionic and reactive pathways, leading to a protonic conductivity that is close to the model input. For lower k_σ values, the ionic pathway dominates as the electronic conductivity is too low for it to be efficient to use the reactive pathway. For higher k_σ values, the reactive pathway dominates and the computed protonic conductivity is not close to the model input. It is interesting to note that for an electronic conductivity of 1 mS/cm, the computed protonic conductivity does not vary with IL thickness,

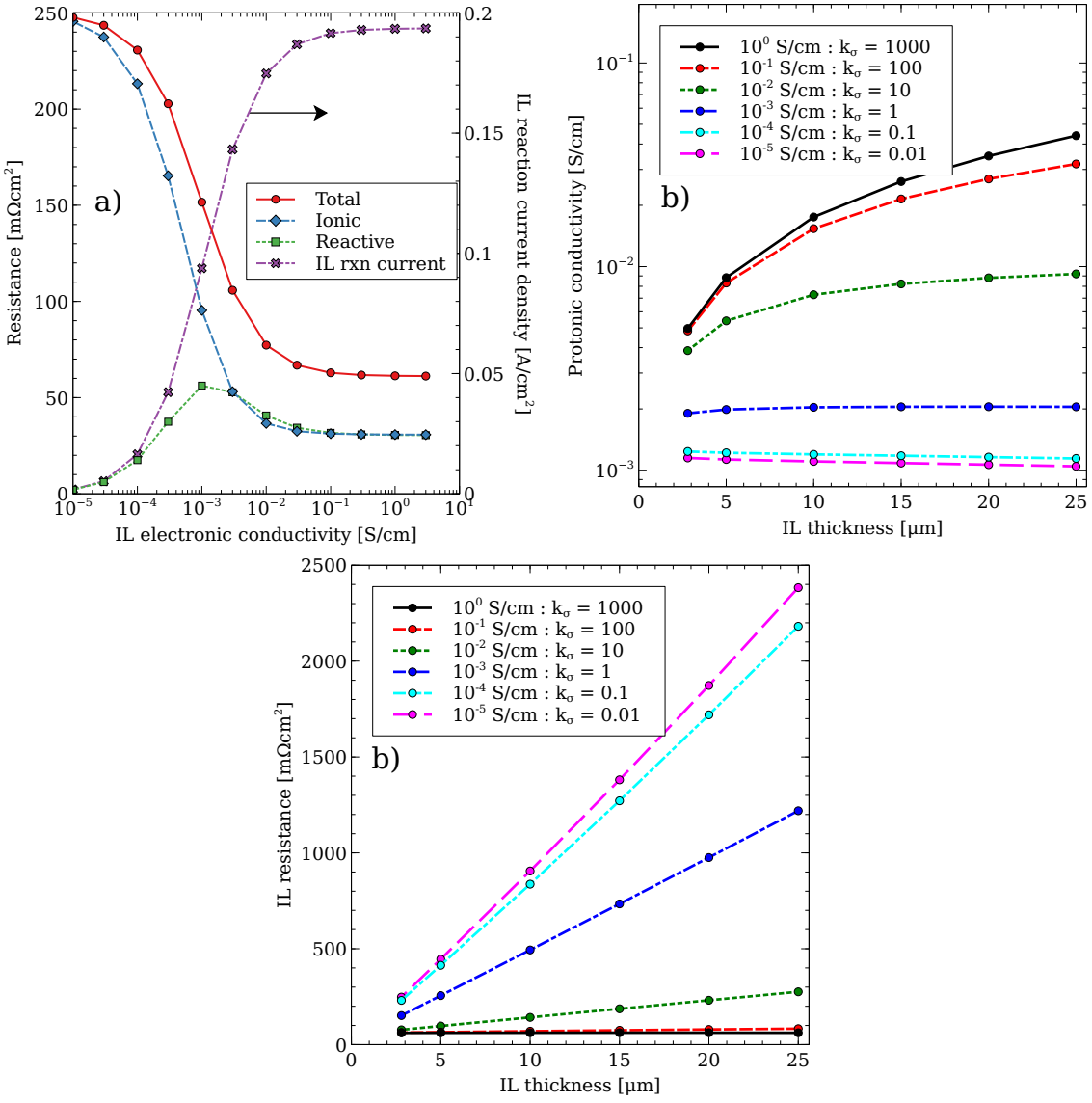

Figure 2.20: (a) Sensitivity of the total resistance in the IL to the electronic conductivity. Also shown are the resistances from the ionic and reactive pathways, and the reaction current density in the IL. The impact of changing the IL thickness on (b) the protonic conductivity computed using the DC method and (c) the total IL resistance, for varying electronic conductivities. k_σ in the legend is the ratio between the solid and protonic conductivities. The current density is 200 mA/cm^2 for each.

which would suggest that the reactive pathway is not active; however, the estimated conductivity is slightly overpredicted as there is a small contribution from the reactive pathway, as shown by the resistance in the reactive pathway being substantially lower than the ionic in Figure 2.20 a). This analysis indicates that the ratio of the IL conductivities is an important factor in determining the importance of the reactive pathway, and should be considered before applying the hydrogen pump method.

2.5 Conclusions

A hydrogen pump numerical model was developed, validated and used to study the effect of the IL thickness, catalyst activity and electronic conductivity when the H_2 pump method is used to measure the protonic conductivity of the catalyst layers used in PEM fuel cells and electrolysers. The protonic conductivity of ILs comprised of Ketjen black carbon without platinum was measured experimentally, and close agreement with literature data was obtained, once a correction for the interfacial contact resistance was applied. The hydrogen pump method was then applied to Ketjen black ILs that included platinum, and it was shown that the presence of platinum affects the measurement by significantly reducing the resistance of the cell. The difference is attributed to the reactive pathway, in which protons coming from the anode that arrive at the IL reduced to form hydrogen, which diffuses across the IL before oxidising to form the protons that travel on to the cathode. This pathway bypasses the protonic phase of the IL by transferring charge to the electronic phase, potentially reducing the resistance of the IL and resulting in an overprediction of the protonic conductivity. The same trend was observed for an Ir black catalyst; cells with different ionomer loadings each exhibited very little resistance once the ICR correction was applied, again indicating that the reactive pathway was active. These results show the importance of accounting for the ICR when studying thin ILs and the impact of the reactive pathway. In contrast, the IL comprised of the IrOx catalyst was not susceptible to the reactive pathway, as both electronic conductivity

and activity to the hydrogen reaction were too low to facilitate the hydrogen bypass. The impact of the ICR was difficult to assess, as the HFR could not be used to isolate it. Using thicker layers is therefore recommended when studying these layers.

Numerical modelling was used to examine the sensitivity of the reactive pathway to the IL thickness, exchange current density and electronic conductivity. When the reactive pathway is active, resistance and thickness do not scale linearly, resulting in a conductivity that increases with thickness. The IL resistance is significantly affected by the exchange current density, small reductions IL activity from that of platinum will significantly reduce the impact of the reactive pathway. If the electronic conductivity is more than ten times less than the protonic conductivity, the reactive pathway will also be diminished.

The model was also used to assess the AC method, whereby the HFR of a cell containing an IL is subtracted from the cell resistance. The method relies on a number of losses in the cell being negligible, such as the anode and cathode reaction kinetics, and electron transport in the IL. The model was used to estimate these losses and used to modify the conductivity predicted by the standard AC method. The modified AC method was found to predict protonic conductivities that were similar to those from the ICR corrected DC method, despite the two method having very different analysis methods, giving confidence to the validity of both approaches. The model was also validated by comparison to the analytical study done by Kulikovsky [156] who proposed an alternative method to compute the protonic conductivity of the IL based on the summit frequency of the EIS spectra. The model demonstrated the importance of accounting for the ACL and CCL when obtaining the summit frequency for use in Kulikovsky's method.

Potential methods that could be applied by an experimentalist to determine whether the reactive pathway is active in their IL were studied. The first is to examine the difference between the HFR and the cell resistance in the case of a platinised and unplatinised IL. As the RH is decreased, the cell resistance should grow significantly

compared to the HFR if the reactive pathway is not active, as the IL will induce significant resistance at lower RH. If the IL is active, the additional resistance from the IL is bypassed, so the cell resistance grows more slowly as the RH decreases. The second method is to change the thickness of the IL. If the IL is inactive, the conductivity should remain the same as the cell resistance will increase in line with the increase in the thickness. If it is active, the additional thickness does not induce significant additional resistance, causing the measured conductivity to increase.

Finally, a generalised approach is proposed for the application of the hydrogen pump method to measure the protonic conductivity of active and inactive ILs. The DC resistance and HFR of a cell with and without an IL should be obtained. If the resistance of the cells is very similar, then the IL resistance is not large enough to provide a measurable signal. In this case, a thicker IL should be attempted. In addition, the difference in the HFR between the cell with and without an IL should be obtained. The polarisation data from the cell with the IL should be corrected using that difference. This step should only be taken if the electronic conductivity is high enough to ensure that the AC current will bypass the protonic phase at high frequency. If the polarisation curves with and without the IL are still very similar, as was the case for the Ir and Pt/C ILs, then the layer is too active for the hydrogen pump technique to be used. If the curves are different, then the model should be used to estimate the importance of reactive pathway, and to adjust the protonic conductivity in the case that the IL protonic phase is being partially bypassed. The difference between the resistance from the ionic pathway to the reactive should be compared. The more significant the ionic pathway is relative to the reactive, the higher the confidence the experimenter should have in the accuracy of the adjusted conductivity.

Chapter 3

Numerical investigation into the impact of microstructure on two-phase flow in the anode[1]

3.1 Introduction

In this work, two-phase flow in the anode of a PEMWE cell is studied using a 2-D MEA model, with Darcy's law used to describe gas and liquid transport. The microstructure is parameterised using a pore size distribution (PSD) model that allows for the impact of PSD and contact angle to be studied. The PEMWE model is validated using polarisation data and the HFR. Mass transport is studied in both Ir and IrOx based ACLs, as previous works had shown that the electronic and protonic conductivities of these ACLs would cause oxygen to be formed either close to the membrane or close to the PTL, respectively. For the Ir ACL, the generated oxygen has to traverse the entire ACL to escape to the PTL, requiring very high pressures. Despite the high pressures, there is not significant displacement of water from the hydrophilic ACL, resulting in minimal reduction in performance. A parametric study on the PSD is performed to understand the impact of ACL microstructure on performance, and the coupling between the PTL and ACL saturation is explored. Experimental data

[1]This chapter has been published: M Moore, M Mandal, A Kosakian, and M Secanell, *Numerical study of the impact of two-phase flow in the anode catalyst layer on the performance of proton exchange membrane water electrolysers*, Journal of The Electrochemical Society, vol. 170, no. 4, 2023.

for this work was obtained in-house by Manas Mandal, with modelling support from Aslan Kosakian on the two-phase model.

3.2 Experimental

The experimental data for this work was obtained in-house, using the methodology detailed in the works of Mandal et al. [125, 203, 204]. The polarisation data for the IrOx (ELC-0110, TKK) catalyst is taken from reference [204] for the case where zero carbon was added as a pore former. This catalyst is described by the manufacturer as having a surface area of 100 m^2/g, while the volume mean diameter was estimated by Dhawan et al. [205] to be 7.2 nm. The polarisation data for the Ir black catalyst (3000020267 Umicore) was obtained for this work. The surface area was stated to be 25 m^2/g by the manufacturer, while Tan et al. [98] reported that the particles were flake-like, of size 100-200 nm and a thickness of 10-20 nm. The ACLs were fabricated with a Nafion loading of 35 wt.% for the IrOx catalyst, and 5 wt.% for the Ir, from a Nafion solution (Liquion LQ-1105 100EW 5 wt.%, Ion Power). The ink was deposited onto an N211 membrane using the inkjet printing method [206], to a loading of 1 mg/cm^2 for each catalyst, with an electrode area of 5 cm^2. The CCL had a Pt/C loading of 0.1 mg/cm^2 (46.7 wt.% Pt/C, TEC10EA50E, TKK), a Nafion loading of 30 wt.%, and was prepared using the methodology described in reference [125].

A single cell with single serpentine channel bipolar plates, consisting of a custom-made titanium plate in the anode and a graphite plate in the cathode, was used for testing. A sintered Ti PTL was used in the anode, while an SGL 28BC and an SGL 24BC were used in the cathode of the IrOx and Ir PEMWE cells, respectively. The cell was maintained at 80 ℃, while the water flow rate in the anode was 15 ml/min throughout testing. No gases are flown through the cathode; a water lock was used to collect any water exiting with the hydrogen. The cell was conditioned by applying current densities of 0.02, 0.1, 0.2 and 1 A/cm^2 for 15 minutes each,

followed by 5 minutes at 2 A/cm^2. Polarisation curves were obtained using linear sweep voltammetry with a potentiostat (SP300, Biologic). A scan rate of 1 mV/s was used to minimise transient effects. The potentiostat was also used to perform EIS in order to obtain the HFR for each cell.

3.3 Numerical model

A 2-D, across-the-channel, isothermal model is used. The model solves for the potential of the solid phase, ϕ_s, and ionomer phase, ϕ_m, using Ohm's Law. Two-phase flow is accounted for by solving for both gas, p_g, and liquid pressure, p_l using the Darcy equation, with a PSD model being used to obtain transport parameters, in a similar manner to that used by Zhou et al. [192] and Kosakian [196]. The ionomer phase is assumed to be liquid equilibrated, as electro-osmotic drag and diffusion will carry water to the cathode from the anode, with the anode being continually supplied with water. As such the water content of the ionomer is not solved for. Species transport is also not solved for, as the primary impact of species concentration is on the rate of the reactions in each electrode, in particular the OER. This impact is instead accounted for using the two-phase model to predict the water saturation in the ACL and reducing the active area to account for gas displacing water at the reaction site.

Figure 3.1 shows the domain in which the simulations are performed, which includes the membrane, ACL, CCL, GDL and MPL on the cathode and a PTL on the anode. The left and right boundary includes half of the channel and half of the land, with symmetry boundary conditions applied at the top and bottom of the domain.

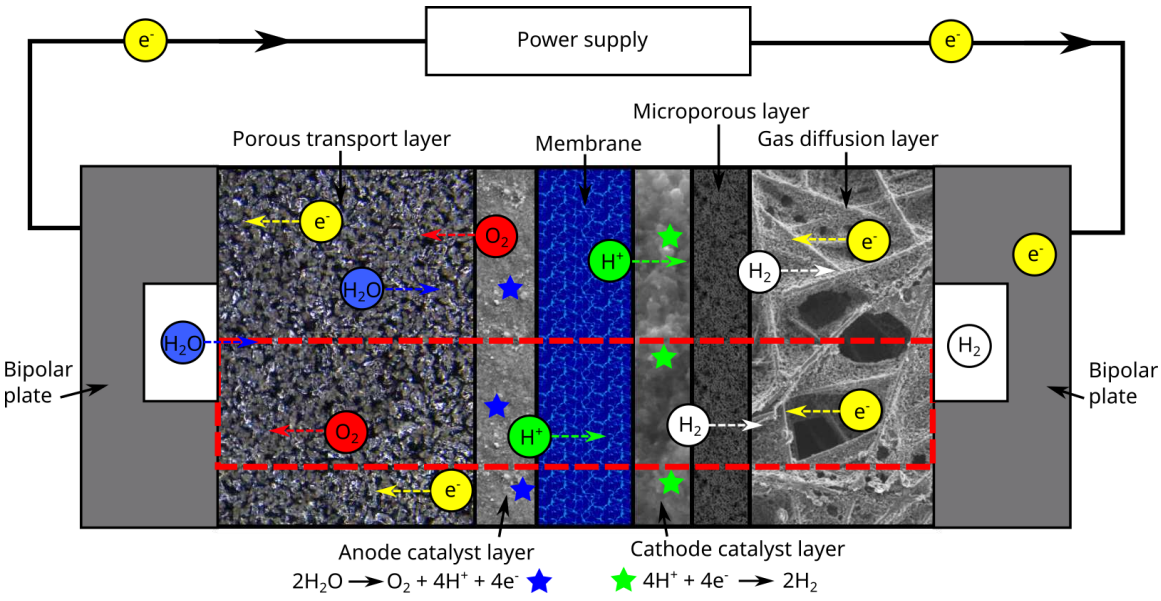

Figure 3.1: Transport processes within the cell. The computational domain for all simulations is shown in the red dashed line.

3.3.1 Governing equations

The governing equations are:

$$\nabla \cdot \left(\sigma_m^{eff} \nabla \phi_m\right) = S_{H^+} \tag{3.1}$$

$$\nabla \cdot \left(\sigma_s^{eff} \nabla \phi_s\right) = S_{e^-} \tag{3.2}$$

$$\nabla \cdot \left(\frac{\rho_g k_g}{\mu_g} \nabla p_g\right) = S_{gas} \tag{3.3}$$

$$\nabla \cdot \left(\frac{\rho_l k_l}{\mu_l} \nabla p_l\right) = S_{liquid} \tag{3.4}$$

where the source terms S_i for each equation are based on the current produced in each catalyst layer, as shown in Table 3.1 and is discussed below. The effective layer electronic conductivity is denoted σ_s^{eff}, while the protonic is σ_m^{eff}. k_i is the permeability, μ_i is viscosity and ρ_i is the density of phase i, which is either water or oxygen. Note that Zhou et al. [192] considered the evaporation and condensation of water as additional source terms for the liquid and gas pressure equations, however it is assumed in this work that the oxygen bubbles formed in the anode are fully humidified. Many of the assumptions made in reference [192] also apply in this work, namely: liquid trans-

Table 3.1: Source terms for the governing equations.

Source term	Anode	Cathode
S_{H^+}	j_{OER}	$-j_{HER}$
S_{e^-}	$-j_{OER}$	j_{HER}
S_{gas}	$j_{OER}M_{O_2}/4F$	$-j_{HER}M_{H_2}/2F$
S_{liquid}	$-j_{OER}M_{H_2O}/2F$	-

port is dominated by surface tension forces, there exists a representative elementary volume in each layer that contains homogeneous hydrophilic and hydrophobic pore networks, gas and liquid water are incompressible and the membrane is impermeable to water and gas. Note that because of the membranes impermeability, liquid water cannot exist on the cathode side. It is assumed that the cathode electrode does not contribute significantly to the cell performance and so two-phase flow is not studied there. The permeability of the liquid, k_l, and gas phase, k_g, is computed using the PSD model as is discussed below. The viscosity, μ_g, and density, ρ_g, of the gas phase are computed assuming a mixture of oxygen that is fully saturated with water vapour.

3.3.2 Kinetic models

The kinetics of the OER and HER are typically described by the Butler-Volmer or Tafel equation in the modelling literature [31], with the exception of Oliveira et al. [70, 107] who developed a multi-scale cell model with multi-step kinetics for the OER. The nature of the OER is not well understood, with numerous mechanisms proposed that have not been experimentally validated [88]. The primary concern for this work is a model that can capture any change in the Tafel slope for the OER, which is occasionally seen experimentally [106, 170]. Ma et al. [106] proposed a simplified reaction mechanism using the same methodology proposed by Wang et al. [109] for the ORR. The model assumes a single intermediate species with two intermediate reactions, and was used by the authors to capture the kinetics of the OER on Ir/Ru

oxide core-shell catalysts. This model is used in this work to capture the reaction kinetics as a Tafel model was not able to provide an accurate fit to the experimentally obtained polarisation curves as is discussed below. The model assumes the following intermediate steps:

$$1/2\ H_2O \rightleftarrows 1/2\ O_{ad} + H^+ + e^- \tag{3.5}$$

$$1/2\ H_2O + 1/2\ O_{ad} \rightleftarrows 1/2\ O_2 + H^+ + e^- \tag{3.6}$$

from which the current density can be computed using:

$$j_{OER} = s_L A_v j^* \left(g_{+1}(1-\theta_O) - g_{-1}\theta_O\right) \tag{3.7}$$

where the active area is given by A_v and the reference prefactor, j^*, is used to scale the reaction. In practice, it was found that this model was also not able to capture the kinetics of the OER for the TKK catalyst, as very low Tafel slopes were required, necessitating the use of transfer coefficients greater than one and therefore forward and backward transfer coefficients that are decoupled (i.e. the backward is not one minus the forward). Then, the coverage of the assumed intermediate species, θ_O, is given as:

$$\theta = \frac{g_{+1} + g_{-2}}{g_{+1} + g_{-1} + g_{+2} + g_{-2}} \tag{3.8}$$

and the g_i terms are given as:

$$g_{+1} = \exp\left(-(\Delta G_1^0 - \alpha_{1,f} e\eta)/kT\right) \tag{3.9}$$

$$g_{-1} = \exp\left(-(\Delta G_1^0 - \Delta G_{ad}^0 + \alpha_{1,b} e\eta)/kT\right) \tag{3.10}$$

$$g_{+2} = \exp\left(-(\Delta G_2^0 - \Delta G_{ad}^0 - \alpha_{2,f} e\eta)/kT\right) \tag{3.11}$$

$$g_{-2} = \exp\left(-(\Delta G_2^0 + (1-\alpha_{2,b}) e\eta)/kT\right) \tag{3.12}$$

where ΔG_i^0 are the activation energies of the assumed intermediate reactions, ΔG_{ad}^0 is the adsorption energy of the assumed intermediate species, $\alpha_{i,f}$ and $\alpha_{i,b}$ are the forward and backward transfer coefficients of reaction i respectively, and η is the

reaction overpotential. It is worth noting that the kinetic model is likely a major oversimplification of the true reaction mechanism, with a number of more complex mechanisms proposed [88], hence no insights regarding the nature of the OER are considered in this work. Furthermore, the original model assumed $\alpha_{i,f} + \alpha_{i,b} = 1$, however the use of fractional stoichometric coefficients in equations (3.5) and (3.6) implies that the assumed reactions are not single electron transfer reactions. Therefore both forward and backward transfer coefficients are fitted separately which helped to more accurately reproduce the reaction kinetics.

The inclusion of the liquid water saturation, s_L, in equation (3.7) accounts for blocking of the active area by gas bubbles and is the method used to induce mass transport losses. An alternative method is to use a concentration ratio and compute the concentration of water molecules at the reaction site, which allows for the possibility of water vapour within a gas bubble maintaining the OER at a reduced level. Reducing the active area was chosen to determine the worst case scenario with regard to the mass transport limitations predicted by the model. This method is commonly used in the literature however validation is required to determine the most appropriate method of accounting for mass transport limitations.

The hydrogen evolution reaction in the cathode proceeds on a platinum catalyst, which has been extensively researched in the literature. There are a number of models that can capture the kinetics of the reaction [84–86], however this work uses the model proposed by Wang et al. [82] for the HOR which was applied by Elbert et al. [83] to study both the HOR and HER on Pt/Ru core-shell catalysts. The model is given as:

$$j = A_v j^* \left(g_{+T}(1-\theta_H)^2 - g_{-T}\theta_H^2 + g_{+H}(1-\theta_H) - g_{-H}\theta_H \right) \tag{3.13}$$

where the intermediate adsorbed hydrogen coverage is denoted θ_H and the g_i terms

are exponentials given as:

$$g_{+T} = \exp(-\Delta G^{*0}_{+T}/kT) \tag{3.14}$$

$$g_{-T} = \exp(-(\Delta G^{*0}_{+T} + \Delta G^{0}_{ad})/kT) \tag{3.15}$$

$$g_{+H} = \exp(-(\Delta G^{*0}_{+H} - 0.5\eta)/kT) \tag{3.16}$$

$$g_{-H} = \exp(-(\Delta G^{*0}_{+H} + \Delta G^{0}_{ad} + 0.5\eta)/kT) \tag{3.17}$$

where ΔG^{*0}_{i} are the activation energies of the intermediate reactions. The values used in this work are not fitted as the losses incurred from the HER are significantly smaller than other losses, such as the OER and ohmic losses. The activation energies reported by Wang et al. [82] from RDE experiments are used in this work.

3.3.3 Micro-scale structural model of the porous media

The pore size distribution model is used to characterise the porous media present in the catalyst and transport layers. The PSD is used to relate the pressures computed by the Darcy equations to the water saturation at each point in the domain, and allows for the permeability of the gas and liquid phases to be computed. The model conceptualises the porous medium as being a bundle-of-capillaries and is described in greater detail in references [191, 192], with an updated formulation provided in reference [196] which is used in this work. The gas and liquid pressure is used to compute the capillary pressure within each pore, which is used to compute the critical radius according to the Young-Laplace equation:

$$r_c = -\frac{2\gamma cos\theta}{p_c} \tag{3.18}$$

where γ is the surface tension of the water, θ is the contact angle of the porous medium and the capillary pressure, p_c, is taken in this work as the difference between the liquid and gas pressures, i.e. $p_c = p_l - p_g$. The critical radius of a hydrophobic medium will be the smallest pore size that will be invaded by liquid water at a particular pressure, for a hydrophilic medium it will be the largest pore size invaded.

The PSD used in this work is given by

$$\frac{dX(r)}{dr} = \frac{dX_{HI}(r)}{dr} + \frac{dX_{HO}(r)}{dr} \tag{3.19}$$

where $X(r)$ is the volume of the liquid invaded pore space, normalised to the total pore volume, i.e. $X(r) = V_{lw}(r)/V_p$. $X(r)$ can be described using a log-normal distribution, which is given as:

$$\frac{dX(r)}{dr} = \sum_{i=HI,HO} F_i \sum_k \frac{f_{i,k}}{r s_{i,k}\sqrt{2\pi}} E_{i,k}^{(s)}(r) \tag{3.20}$$

where $E_{i,k}^{(s)}(r)$ is given by:

$$E_{i,k}^{(s)}(r) = \exp\left(-\left[\frac{\ln r - \ln r_{i,k}}{s_{i,k}\sqrt{2}}\right]^2\right) \tag{3.21}$$

The PSD can be comprised of a number of modes, k, each of which has a characteristic radius, $r_{i,k}$, and standard deviation, $s_{i,k}$, and take up a fraction, $f_{i,k}$, of the pore volume assigned to phase i. The hydrophobic/hydrophilic portions of the PSD are denoted by subscript i, with each having a fraction, F_i, of the total pore space, i.e., $F_{HO} + F_{HI} = 1$.

The water saturation is computed based on the local capillary pressure, as all the pores larger than the hydrophobic critical radius will be water filled, as will all pores smaller than the hydrophilic critical radius. As such the water saturation is computed by integrating over all the pores that have been invaded by water:

$$s_L = \int_0^{r_{c,HI}} \frac{dX_{HI}}{dr} dr + \int_{r_{c,HO}}^{\infty} \frac{dX_{HO}}{dr} dr \tag{3.22}$$

The analytical solution to this integral is given as:

$$s_L = \sum_{i=HI,HO} F_i \sum_k \frac{f_{i,k}}{2}\left[1 + \xi_i \text{erf}\left(\frac{\ln(r_{c,i}) - \ln(r_{i,k})}{s_{i,k}\sqrt{2}}\right)\right] \tag{3.23}$$

where $\xi_{HI} = 1$ and $\xi_{HO} = -1$. The computed water saturation defines the volume of the pore space that is filled with water, i.e.:

$$s_L = \frac{V(\text{water filled pores})}{V(\text{total pore volume})} \tag{3.24}$$

while the gas saturation is given by $s_G = 1 - s_L$.

The permeability can be computed by comparing the velocity of a fluid passing through a cylindrical pore according to Hagen-Poiseuille equation to that computed by the Darcy equation [196]:

$$k_l = \frac{P_{l-l}\epsilon_p}{16} \sum_{i=HI,HO} F_i \sum_k f_{i,k} r_{i,k}^2 \exp(2s_{i,k}^2 \left[1 + \xi_{i,k}^k(r)\right]) \tag{3.25}$$

where

$$E_{i,k}^{(k)} = \text{erf}\left(\frac{\ln(r_{c,i}) - \ln(r_{i,k})}{s_{i,k}\sqrt{2}} - s_{i,k}\sqrt{2}\right) \tag{3.26}$$

where P_{l-l} is the probability of a water-filled pore being in contact with another water-filled pore. The gas permeability can be found in a similar manner:

$$k_g = \frac{P_{g-g}\varepsilon_p}{18} \sum_{i=HI,HO} F_i \sum_k f_{i,k} r_{i,k}^2 \exp(2s_{i,k}^2 \left[1 - \xi_{i,k}^k(r)\right]) \tag{3.27}$$

where P_{g-g} is the probability of two gas filled pores being in contact. The probabilities are based on determining the water/gas cross-sectional area per unit volume and are given as:

$$P_{l-l} = \lambda_{PSD}\left(\frac{a_c}{a_{max}}\right)^2, P_{g-g} = \lambda_{PSD}\left(1 - \frac{a_c}{a_{max}}\right)^2 \tag{3.28}$$

where a_c is the water/gas cross-sectional area at a given capillary pressure, a_{max} is the total area for the entire pore volume and λ_{PSD} is the pore interconnectivity factor, which is used as a fitting factor.

3.3.4 Boundary conditions

Figure 3.2 shows the boundary conditions and where they are applied. The boundary conditions for the potential of the electronic phase are zero volts at the cathode GDL/land, and is the applied potential at the anode PTL/land, while no flux is applied elsewhere. A no flux boundary condition is applied for the protonic potential at all boundaries. Ohm's law for the protonic potential is not solved in the transport layers so the boundary condition is essentially applied at the CL/transport layer interface. The liquid pressure boundary condition is artificially set to a high negative

pressure at the cathode channel to ensure that the water saturation is zero. The anode boundary condition is set to atmospheric pressure plus half the pressure drop down the single serpentine channel. The gas pressure is set to atmospheric in the cathode channel, while on the anode the gas pressure is set to that required to generate a bubble half the size of the channel according to the Young-Laplace equation, i.e.:

$$p_g = p_l + 2\gamma/r \tag{3.29}$$

The boundary conditions used in the anode electrode are greatly simplified, and could be improved to better reflect the two-phase regimes that are present in the anode channel under different operating current densities. The transition between bubbly, slug and annular flow has been well studied in the literature, however the use of the two-phase model in this work is primary concerned with the impact of the liquid saturation in the ACL and how the differing catalyst conductivities impact the two-phase flow within the ACL and the subsequent impact on the cell performance. A study was performed on the boundary condition used for the gas pressure in the anode, and while the liquid saturation in the PTL reduced significantly with increasing gas pressure at the boundary, the liquid saturation in the ACL was hardly affected. This is because of the weak coupling of two-phase effects between the PTL and ACL as is shown below.

3.3.5 Post-processing

The ohmic resistance of each layer, including both phases in the CLs is computed using the ohmic heating method as described in Section 2.2.7. The HFR is predicted by the model using the same method as described in Section 2.2.7, with the contribution of the CLs computed using equation (2.19).

3.3.6 Implementation

The model described was implemented in OpenFCST, an in-house, open-source software developed to model electrochemical systems [200]. Second order Lagrange finite

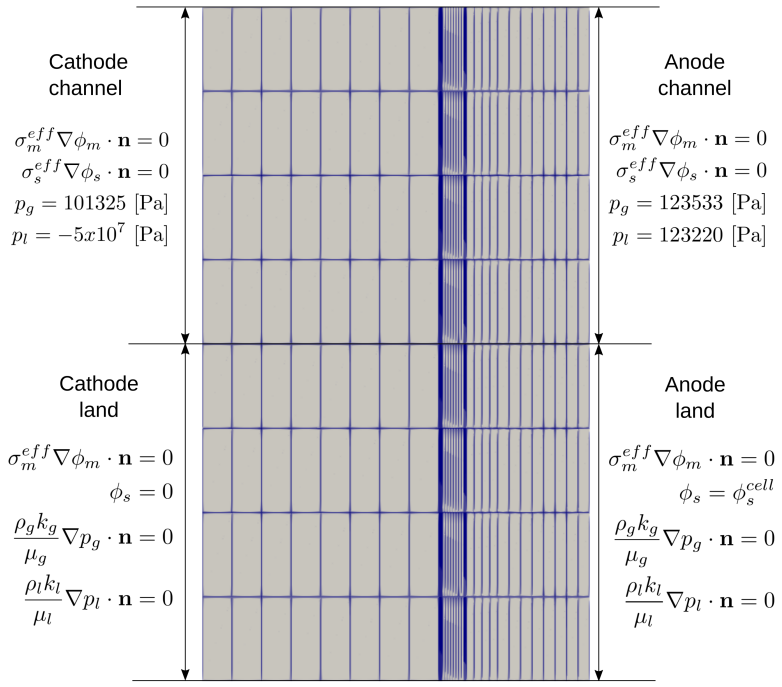

Figure 3.2: Boundary conditions applied for the electrolyser simulations, displayed using the coarsest mesh from Figure 3.3.

elements are used, with approximately 3000 cells, for a total of approximately 50,000 degrees of freedom. A refinement study was carried out with Figure 3.3 showing that the solution is grid independent with the chosen mesh. The governing equations are linearised using Newton's method, the resulting linear system is solved using UMFPACK. A tolerance of 10^{-8} was used for the residual of the Newton solver. A polarisation curve up to a cell potential of 2 V took approximately ten minutes to obtain, using an Intel® Core™ i7-8700K CPU at 3.7 GHz.

3.4 Model parameters

Tables 3.2 to 3.6 contain the parameters used in this work with further discussion provided for the parameters fitted to the experimental data used.

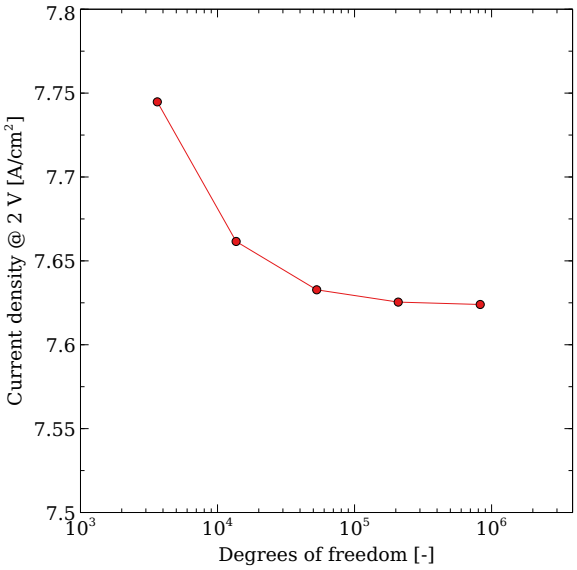

Figure 3.3: Refinement study showing that the predicted current density at 2 V is independent of the mesh.

Table 3.2: Layer thickness.

Layer	Thickness [μm]	Ref.
APTL	280	This work
ACL	4.48 (Ir), 4.4 (IrOx)	Ref. [204]
Membrane	25.4	Manufacturer
CCL	2.8	Ref. [29]
CMPL	37	Ref. [29]
CGDL	109	Ref. [29]
Channel height	800	This work
Land height	800	This work

Table 3.3: PSD parameters for Ti sinter PTL.

Parameter		Ref.
r_k [μm]	13.4, 10	This work
f_k [-]	0.562, 0.438	This work
s_k [-]	0.937, 0.318	This work
F_{HI} [-]	1	This work
θ_{HI} [-]	56	Ref. [207]
λ_{PSD} [-]	0.1	This work

Table 3.4: PSD parameters for the ACL.

	Small	Medium	Large
Parameter	Kosakian [29]	Hegge et al. [208]	Wrubel et al. [110]
HI VF [-]	0.9	0.9	0.8
θ_{HI} [-]	80	80	80
r_k HI [nm]	8.79, 22.2, 38.4	300, 900	800, 1650, 450, 6000
f_k HI [-]	0.09, 0.34, 0.57	0.75, 0.25	0.594, 0.281, 0.0625, 0.0625
s_k HI [-]	0.725, 0.446, 0.348	0.5, 0.4	0.225, 0.4, 0.2, 0.6
HO VF [-]	0.1	0.1	0.2
θ_{HO} [-]	107	107	107
r_k HO [nm]	8.79	300, 900	600
f_k HO [-]	1	0.75, 0.25	1
s_k HO [-]	0.725	0.5, 0.4	0.9
λ_{PSD}	4.1	0.75	0.75

Table 3.5: Kinetic and transport parameters for the ACLs.

Parameters	Ir CL	IrOx CL	Ref.
ΔG_1^{*0} [eV]	0.714	1.004	This work
ΔG_2^{*0} [eV]	1.123	1.479	This work
$\alpha_{1,f}$ [-]	0.589	1.174	This work
$\alpha_{1,b}$ [-]	0.669	0.462	This work
$\alpha_{2,f}$ [-]	0.813	1.362	This work
$\alpha_{2,b}$ [-]	0.033	1.468	This work
ΔG_O^{*0} [eV]	2.881	1.855	This work
j^* [A/cm$^2_{Ir}$]	2.42x10^5	9.42x10^7	This work
A_v [cm$^2_{Ir}$/cm$^3_{geo}$]	511011	618750	This work
σ_s^{eff} [S/cm]	2.9x10^{-2}	3.59x10^{-5}	Ref. [125]
σ_m^{eff} [S/cm]	5.03x10^{-3}	2.6x10^{-2}	Ref. [125]
ε [-]	0.545	0.215	Ref. [204]

Table 3.6: Kinetic and transport parameters for the CCL, PTL and membrane.

Operating conditions		
Cell temperature, [°C]	80	
Cell pressure, [Pa]	101325	
HOR Kinetic parameters		Ref.
ΔG_{+T}^{*0} [eV]	0.195	Ref. [83]
ΔG_{+H}^{*0} [eV]	0.294	Ref. [83]
ΔG_{ad}^{*0} [eV]	0.75	Ref. [83]
j^* [A/cm$^2_{Pt}$]	1000	[83]
Membrane		Ref.
σ_m^{eff} [S/cm]	0.2	This work
Ti sinter		Ref.
σ_s^{eff} [S/cm]	1802	This work

3.4.1 PSD parameters

The transport parameters for the cathode are the same as those presented by Kosakian et al. [29, 196], though this work used an SGL 28BC and an SGL 24BC, as opposed to the SGL 29BC used by Kosakian et al. The impact of the cathode is minimal on the performance of the cell and the difference between the two GDLs is unlikely to impact the results of this study. Similarly, the transport parameters for the CCL are the same as Kosakian et al., despite a slightly different catalyst being used (40 wt% Pt/C HySa-K40 vs. 46.7 wt% Pt/C TEC10EA50E TKK). The PSD for the titanium sinter was fitted to mercury intrusion porosimetry data obtained in house, and its pore connectivity factor was adjusted to fit the permeability value reported by Jung et al. [209]. The resulting relative gas and liquid permeabilities are shown in Figure 3.4, with a comparison to those computed using direct numerical simulation by Jung et al. [209]. The liquid permeability is underpredicted by the PSD model, however the PSD model is used as is, as the MEA model in general does not induce significant mass transport losses regardless.

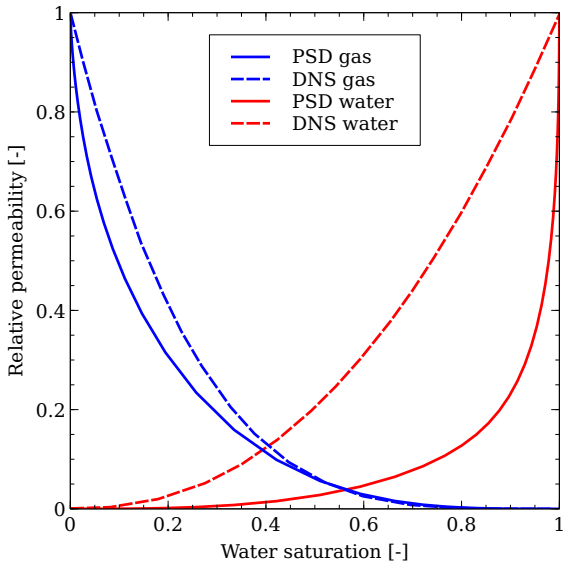

Figure 3.4: Relative gas and liquid permeabilities for the Ti sinter computed using the PSD model in this work and using direct numerical simulation [209].

Obtaining the PSD of the Ir and IrOx ACLs used in this work would require performing MIP or FIBSEM on the layers. The former is very challenging given the small thickness of the electrode, while the latter is expensive and time consuming. Instead several PSDs were used, representing extreme cases discussed in the literature. Three PSDs were available: a PSD with small pores used by Kosakian [196], a PSD from Hegge et al. [208] with medium pores sizes, and a PSD from Wrubel et al. [110] which had large pores. The base case uses the small PSD, while the other two PSDs are studied to provide a contrast. Each PSD will be applied in turn to both the Ir and IrOx based ACLs studied in this work, in order to understand the interplay between the reaction distribution and the ACL microstructure. The PSD from Hegge et al. [208] was obtained by performing FIBSEM on an IrRuOx layer from a commercial CCM, with pore sizes on the order of a few hundreds of nanometres, as shown in Figure 3.5 a). Wrubel et al. [110] used a similar numerical model to this work to study PTLs that had been chemically etched to obtained tunable features and used an intrusion curve based on a Pt/C layer. This intrusion curve was used in this work as the starting point to generate PSD under the assumption of an 80° contact angle, resulting in a PSD with a majority of pores close to a micron in size. The resulting PSD did not generate an intrusion curve that perfectly matched that from Wrubel et al., as their curve did not show zero water saturation. However, the resulting PSD was used as it was sufficiently different from the other two used in this work and allowed for the impact of having very large pore radii to be studied. It should be noted that a portion of this PSD has a characteristic pore radius of 6 μm, which is larger than the thickness of the layers used in this work. These pores are included as they are necessary to capture the intrusion curve used by Wrubel et al. despite perhaps being non-physical, though they could be considered to represent cracks through the ACL. The PSDs from Hegge et al. and Wrubel et al. have characteristic pore radii that do not appear to be present in surface SEM images of the catalyst layers used in this work; examples of these images can be seen in reference [204]. As such, a PSD

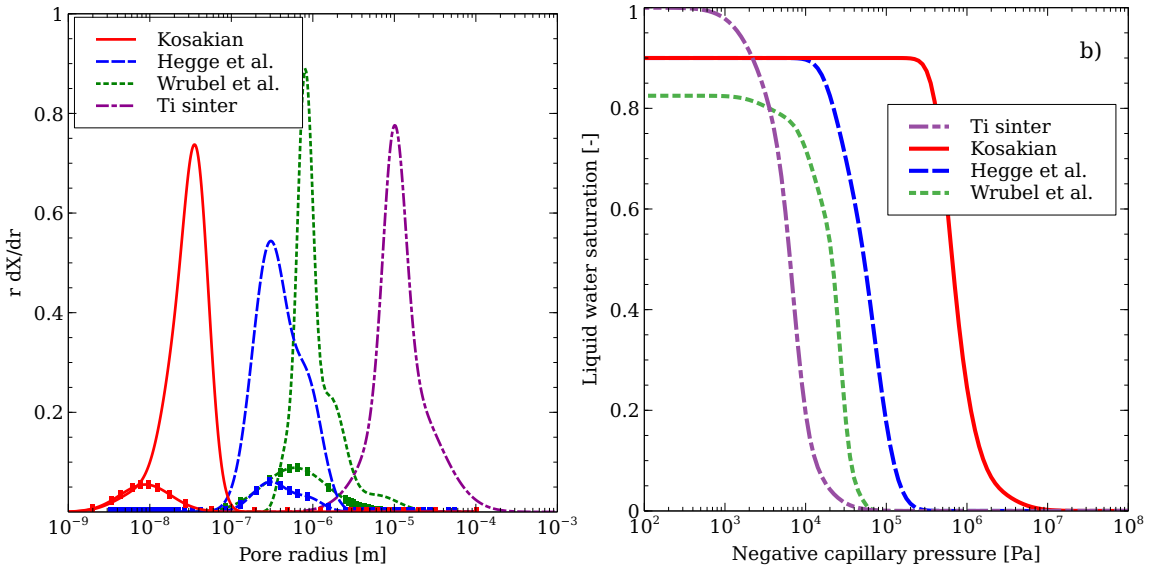

Figure 3.5: (Left) Comparison of the PSDs from Kosakian (small), Hegge et al. (medium) and Wrubel et al. (large), along with the Ti sinter PTL. The smaller curves with markers are the assumed hydrophobic portions of the PSDs, while those without markers are the hydrophilic. (Right) Intrusion curves for the same PSDs. Note the use of negative capillary pressure on the x-axis, positive pressures are not shown as they are not achieved in these simulations.

used by Kosakian [196] based on FIBSEM analysis of a Pt/C CCL used in PEM fuel cells [210] is also studied, as its characteristic pore radius is of the order of tens of nanometres.

There is considerable uncertainty regarding the remaining parameters used in the PSD model, namely the contact angle of the hydrophilic and hydrophobic portions of the ACL, the fraction of the PSD that is hydrophilic, and the pore connectivity, i.e. the parameter λ_{PSD} in equation (3.28), which determines the permeability of the layer. As such, these parameters will be part of a parametric study to determine their impact on performance. As a base case, it is assumed that the hydrophobicity of the ACL is caused by the ionomer, in particular its PTFE backbone. A value of 107° is used based on contact angle measurements on PTFE films [211]. The hydrophilic contact is assumed to be 80° as was used by Wu et al. [187] in their numerical simulations, though contact angle measurements on iridium oxide films

used in bioelectrodes suggest a contact angle closer to 10° [212, 213]. The values of the pore interconnectivity factor, λ_{PSD}, for the small and medium PSD is adjusted in order to obtain reasonable permeability values. Hegge et al. reported permeabilities of the order of $4x10^{-15}$ m^2, leading to a pore interconnectivity factor of 0.75 for the medium PSD. For the small PSD, the value of 4.1 reported by Kosakian [196] is used. The hydrophilic portion for these two PSDs is assumed to be 90% on the basis of the parametric study that follows. Kosakian assumed that only the smallest pores were hydrophobic, hence the use of only one mode for the hydrophobic portion. It is unknown which pores are hydrophobic in the PSD from Hegge et al., so each mode was included in the hydrophobic portion. For the large PSD, the intrusion curve used by Wrubel et al. implied both a hydrophilic and hydrophobic portion, as the curve showed part of the layer is invaded for both negative and positive capillary pressures, leading to a hydrophilic fraction of 80%. Wrubel et al. did not report permeability values so the interconnectivity factor for their PSD was assumed to be the same as that used for Hegge et al. The pore interconnectivity was found to have no impact on the two phase behaviour for this PSD. The assumption of a contact angle of 80° was made on the basis that smaller contact angles require larger pores in order to reproduce the intrusion curve used by Wrubel et al. For example, a contact angle of 40° results in an even larger PSD, with the majority of pores having a characteristic pore radius of 3.7 microns. The relative gas and liquid permeabilities for each PSD using the parameters described are shown in Figure 3.6.

3.4.2 Layer conductivities

The membrane ionic conductivity is adjusted to match the membrane resistance reported by Mandal et al. [125] for a liquid equilibrated N-211. Mandal et al. also reported the resistance of the cell hardware to be 19.7 $m\Omega.cm^2$, which included the cathode GDL, which is modelled in this work, as well as two current collectors and bipolar plates, which are not included in the model. The GDL electronic conductivity

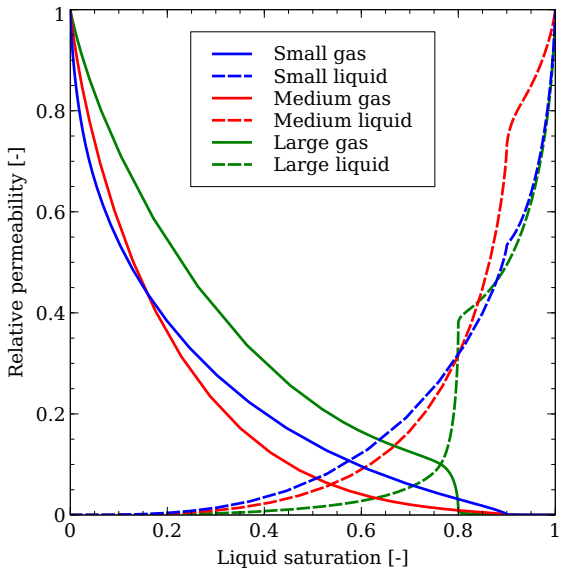

Figure 3.6: Relative gas and liquid permeabilities for each of the PSDs applied in the ACL in this work.

was taken from Kosakian et al. [29], which results in a resistance of approximately 7.5 $m\Omega.cm^2$ being computed using the ohmic heating method, see equation (2.17). The remaining 12.2 $m\Omega.cm^2$ from the cell hardware is attributed to components not included in these simulations, so the experimental data was corrected to account for this resistance. This resistance was also removed from the experimentally obtained HFR. The PTL conductivity was adjusted to match the resistance reported by Mandal et al. [125], who used a four point probe method to obtain the in-plane conductivity, which was assumed to match the through-plane conductivity due to isotropic nature of a sintered titanium PTL. The electronic and protonic conductivities of the cathode catalyst layer were again obtained from Kosakian et al. [29]. These layers were not found to contribute significantly to the resistance of the cell.

The conductivities of the solid, σ_s^{eff}, and ionomer, σ_m^{eff}, phases in the ACL are dependent on whether an Ir or IrOx catalyst is used. The IrOx ACL electronic and protonic conductivities were based on the values reported by Mandal et al. [125], using the data at 100% RH. It is assumed that the ICR is not significant due to

the high ionomer loading used, as discussed in Chapter 2. In addition, the protonic conductivity is adjusted slightly so that the HFR computed numerically would match that obtained experimentally (including the adjustment from the cell hardware resistance). The HFR from the numerical model is obtained by summing the electronic and protonic resistances of each layer computed from ohmic heating, besides the CCL and ACL. The contribution of an individual CL to the HFR can be estimated using Equation (2.19). The equation shows that the computed resistance will be dominated by the more conductive phase, which was assumed to be the protonic phase for the IrOx ACL, therefore only the conductivity of the more dominant phase was adjusted to match the HFR. The IrOx protonic conductivity was increased from a measured value of 0.011 S/cm to 0.026 S/cm, which is reasonable given that the ionomer will likely be more conductive when in contact with liquid water. In addition, the ICR correction, which was not applied to the IrOx protonic conductivity measurement, does not appear to be significant, as only a relatively small adjustment was needed.

The Ir ACL effective protonic conductivities were obtained at 100% RH, with an ionomer loading of 5%, which was measured as 5.03×10^{-3} S/cm [126]. The protonic conductivity at the same ionomer loading for the IrOx ACL was significantly lower, most likely due to the loss of a percolating network with such a low ionomer content. So it can be assumed that the reactive pathway bypassed the Ir IL during the hydrogen pump measurement, meaning that the true protonic conductivity should be lower, as discussed in Chapter 2. However, this value does not include the ICR correction, and the conductivity will also be improved by the presence of liquid water, making it difficult to know what value to use. For this study, the measured protonic conductivity of 5.03×10^{-3} S/cm was used due to the lack of alternative values. As the effective electronic conductivity was measured to be 0.048 S/cm, this value for the protonic conductivity does allow for the impact of having the reaction distribution close to the PEM to be studied. This uncertainty can be somewhat mitigated by considering the HFR, which required adjusting the electronic conductivity of the Ir ACL from the

measured value of 0.048 S/cm to 0.029 S/cm. It can be expected that the electronic conductivity of the ACL will be lower when liquid equilibrated compared to at 100% RH, as the swelling of the ionomer may cause loss of connectivity between catalyst particles [127]. The fact that the conductivity did not need major adjustment gives some confidence that the protonic conductivity used is not too unreasonable.

3.4.3 Kinetic parameters

The kinetic parameters were obtained by fitting to the experimental data at low current densities. Typically, the Tafel equation is used to describe the reaction kinetics of the OER and is obtained by fitting a straight line on a Tafel plot of the kinetic region of the experimentally obtained polarisation curve, that has been corrected to account for the HFR. Using this method failed to provide a reasonable fit for either catalyst, as did fitting the kinetic model from Ma et al. [106] instead of the Tafel equation, up to a current density of 0.5 A/cm^2. In order to obtain kinetic parameters that would result in a close fit to the experimental polarisation curve, it was necessary to account for the resistance of the ACL while fitting the kinetic model. To do this, 2-D simulations were run with the ACL only, in which the kinetic parameters were fit to experimental polarisation data that had the resistance of every other layer removed. The other layers were removed to minimise the computational requirements for the fitting procedure, which used a pattern search algorithm implemented in Dakota [214]. The fitting parameters were the free energies of activation, ΔG_i^0, free energy of adsorption ΔG_{ad}^0, and the forward and backward transfer cofficients for each intermediate step, $\alpha_{i,f}$ and $\alpha_{i,b}$. The current densities fitted ranged from 3-500 mA/cm^2, smaller current density ranges did not produce as good a fit, which may be because the change in Tafel slope occurs at a high potential, circa 1.4-1.5 V, as is shown in Figure 3.7. The resulting kinetic parameters are shown in Table 3.5, and were used to obtain the numerical polarisation curve shown in Figure 3.8 a). Figure 3.7 shows that the IrOx has a higher activity to the OER than the Ir black,

as indicated by the higher charge transfer coefficients for the IrOx in Table 3.5. A higher activity for the low conductivity IrOx compared to the higher conductivity Ir has been observed using RDE in the literature [98], and an inverse relationship between activity and conductivity has also been reported [112].

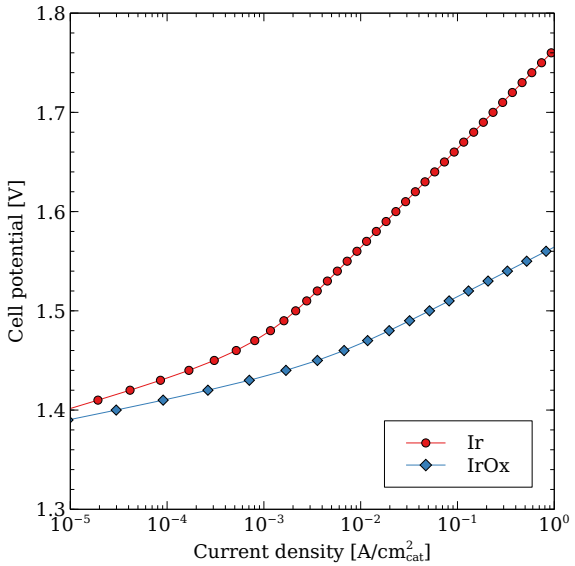

Figure 3.7: Predicted kinetic performance for each catalyst using the model from Ma et al. [106].

While the OER is a multi-step reaction which could exhibit a changing Tafel slope, and there is some experimental evidence for the change in Tafel slope in OER reaction kinetics [106, 170], it is possible that the use of the kinetic model from Ma et al. is actually capturing a different effect such as the interfacial resistance between the ACL and PTL. The extremely close fit between the numerical and experimental data suggests that the additional voltage loss at least mimics a change in Tafel slope. The fact that the ACL resistance needed to be accounted for when fitting the kinetic parameters raises a number of questions about how kinetic parameters should be determined in PEMWE, and what constitutes the kinetic region. These questions will be explored in more detail in Chapter 4. Finally, it should be noted that mass transport effects were not accounted for during the fitting of kinetic parameters, as

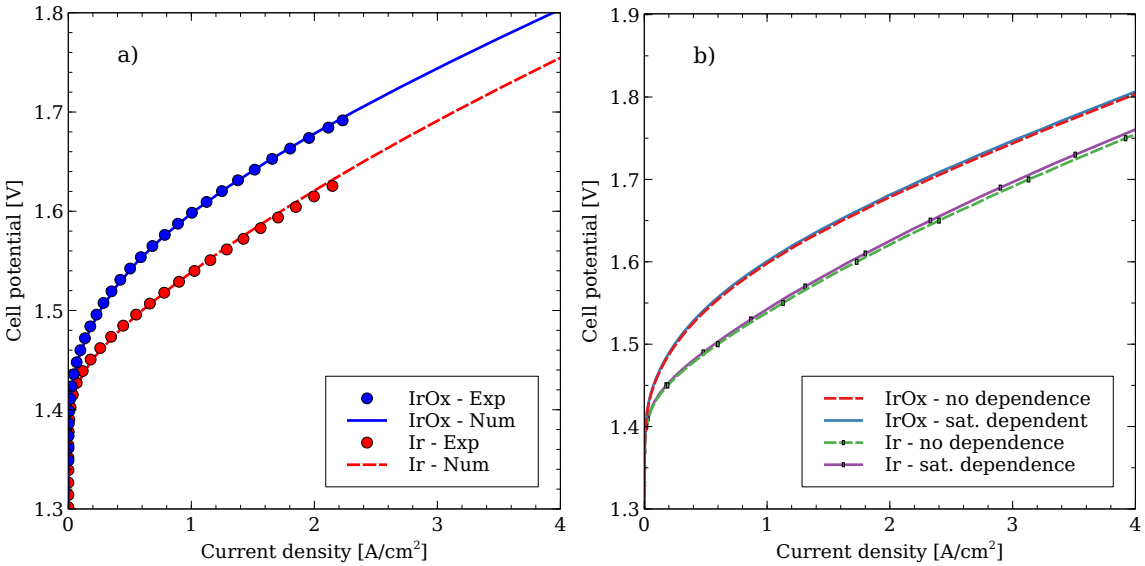

Figure 3.8: Comparison between experimentally and numerically obtained polarisation curves with an Ir and IrOx ACL (left), and the impact of including a water saturation dependent active area (right) with the small PSD.

relatively low current densities were used.

3.5 Results and discussion

3.5.1 Base case analysis

Figure 3.8 a) shows the fit of the numerical model to the experimental data for both the Ir and IrOx catalysts. A very close match is obtained, with the parameters indicated in Tables 3.2 to 3.6. The reason for studying the two catalysts noted in this work is the difference in the effective conductivities of the two phases in the ACL. The Ir based ACL has an electronic conductivity that is almost ten times that of the protonic phase, whereas the electronic conductivity of the IrOx based ACL is three orders of magnitude lower than the protonic. An interesting consequence of the fact that the electronic conductivity is higher for one catalyst and lower for the other is that the OER will tend to occur at opposite sides of the ACL, as shown in Figure 3.9. Overall, the numerical model is capable of reproducing the performance for both catalysts despite the very different behaviour exhibited between them.

The reaction distribution at 100 mA/cm^2 for the IrOx catalyst in Figure 3.9 is extremely localised to one side, requiring a log scale to allow the distribution to be seen. Note that the kinetic performance of the IrOx catalyst is higher than that of the Ir in Figure 3.7, however Figure 3.8 shows that the IrOx ACL has a lower performance in what appears to be the kinetic region, i.e. at low current densities. The reason for the lower performance is the extreme localisation of the current density in the IrOx ACL, due to the low electronic conductivity of the layer. As the reaction distribution tightens with increasing current density, the active area also decreases. This causes the polarisation curve to appear exponential at low current densities in Figure 3.8, even though there are significant ohmic effects occurring in the ACL. The reduced active area for the IrOx is compensated for by the very high activity of the catalyst, as shown in Table 3.5, so that a reasonable performance is achieved. Despite oxidised catalysts generally having a better activity than crystalline Ir [98], the latter has an improved performance in an MEA. This result shows that the effective conductivity of the ACL can have significant impact on performance, as has been noted by other researchers [112]. In this work, the cell containing the IrOx ACL used a Ti mesh as its PTL while the Ir used a Ti sinter. The latter likely provided a better contact between the ACL and PTL and may explain part of the improved performance of the Ir ACL. However, Mandal et al. [204] tested ACLs with the same catalysts and again showed that the Ir had better performance despite using a N212 membrane, compared to the thinner N211 used for the IrOx. As such, the improved performance of the Ir ACL in this work is not unexpected.

As a consequence of the reaction distribution, any oxygen bubbles created in the IrOx ACL will be produced close the PTL and will have an easy escape from the ACL. Figure 3.10 shows the gas, liquid and capillary pressures in the IrOx ACL at 4 A/cm^2, along with the water saturation. The gas pressure does not show a significant increase, particularly in comparison to the Ir ACL which is discussed later. The liquid pressure hardly changes at all. This suggests that the water consumed by the OER is rapidly

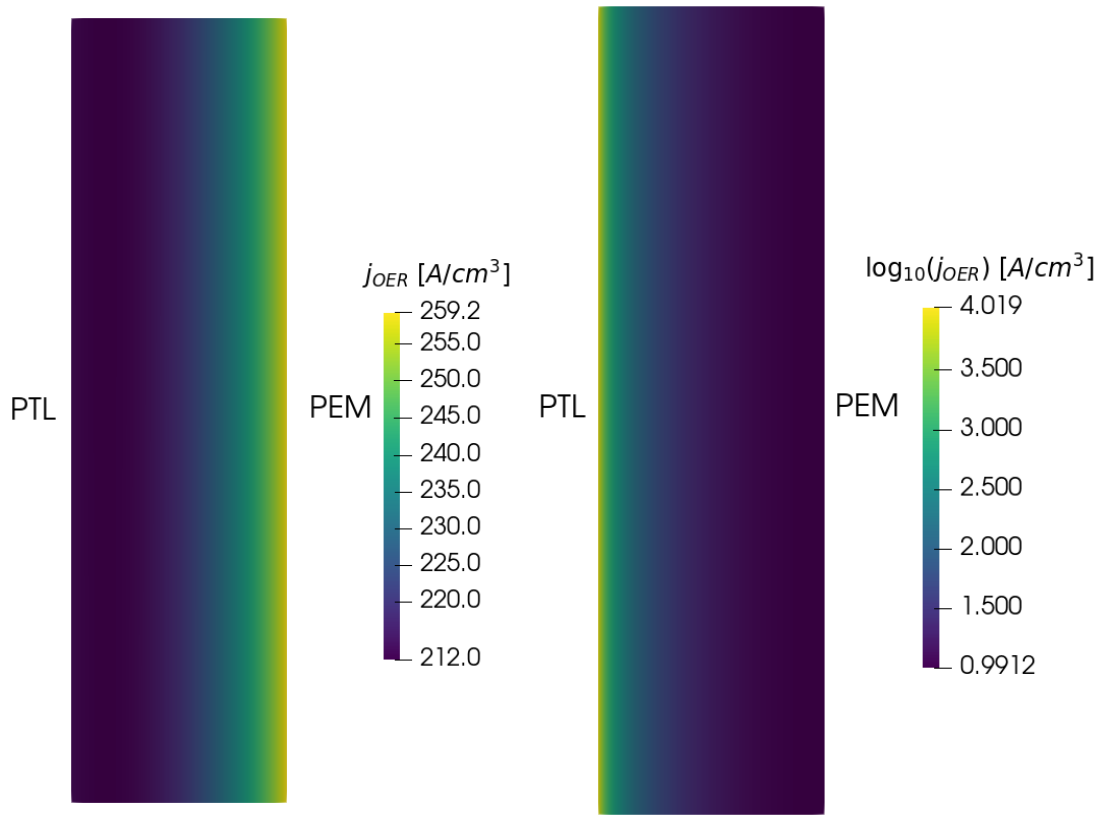

Figure 3.9: OER distribution for an Ir ACL (left) and an IrOx ACL (right) at 100 mA/cm^2. Note the use of a log scale for the IrOx ACL and that both images are stretched by 50 times in the x direction.

replenished by the PTL. This was found to be the case even if the average PTL water saturation dropped to 5%. Using Faraday's law, the flux of liquid water required to maintain a current density of 4 A/cm^2 is of the order of 1x10^{-4} ml/(cm^2.sec), which the model suggests can be easily transported by the PTL since the water saturation in the ACL is quite uniform even at high current densities. Zhao et al. [167] showed that water can be transported rapidly through micro-scale cracks and at the interfaces between Ti particles of very hydrophilic PTLs, which may explain the PTLs ability to transport water even at very high gas saturations. As such the water saturation in the ACL does not change with increasing current density and there is little impact on the predicted polarisation curves from mass transport losses, as shown in Figure 3.8 b).

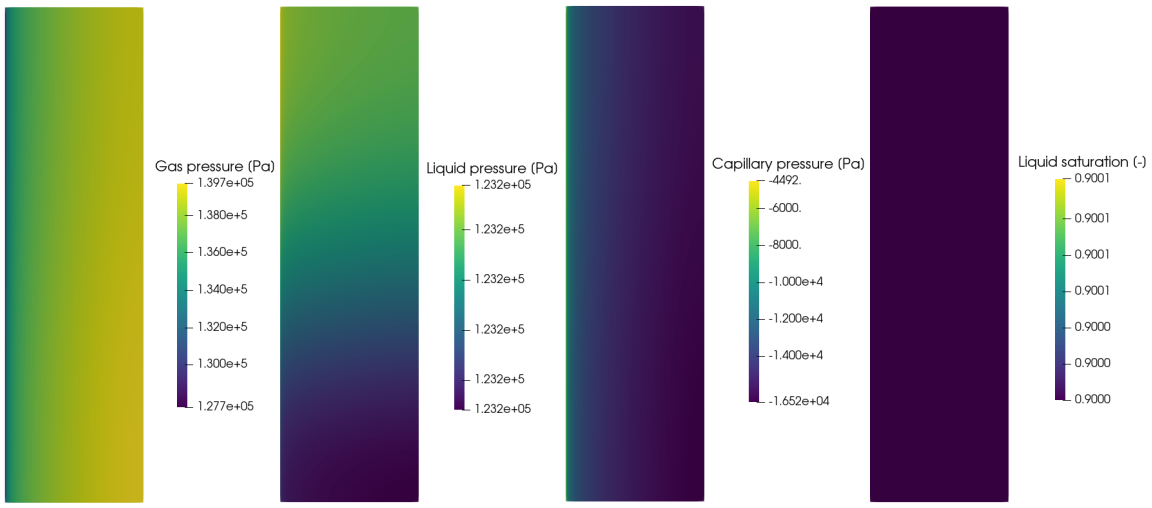

Figure 3.10: Gas, liquid and capillary pressure profiles, as well as the water saturation in the IrOx ACL at 4 A/cm^2. Note that the PEM is to the right of the ACL in these images.

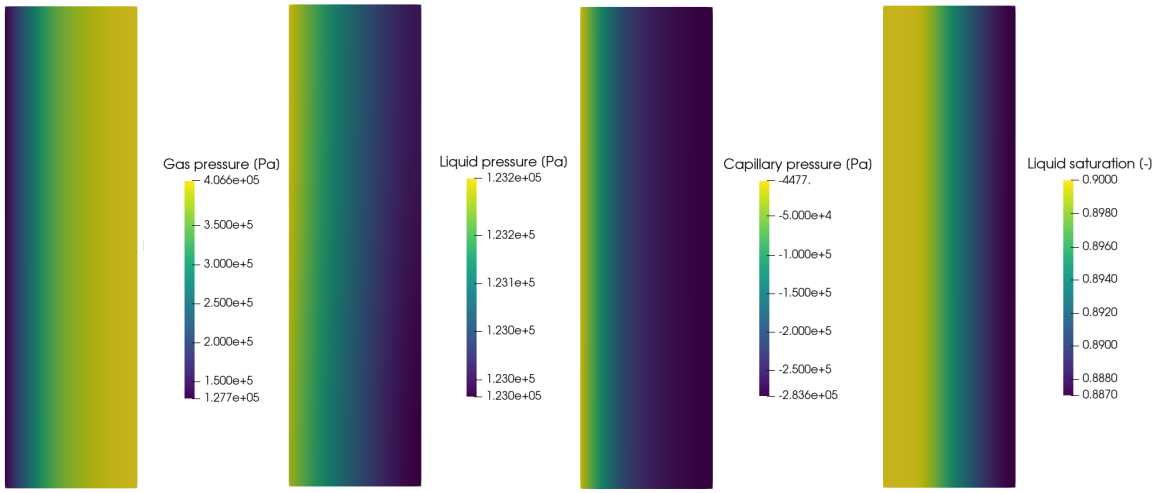

Figure 3.11: Gas, liquid and capillary pressure profiles, as well as the water saturation in the Ir ACL at 4 A/cm^2. Note that the PEM is to the right of the ACL in these images.

For the Ir catalyst, the bubbles will be produced close to the PEM, which will become more localised as the current density increases, requiring bubbles to traverse most of the ACL in order to escape to the PTL. That the gas bubbles must take a tortuous path to escape the Ir based ACL is highlighted in Figure 3.11, which shows the gas, liquid and capillary pressures in the ACL at 4 A/cm^2, along with the water saturation. Very high gas pressures are generated at the ACL/PEM interface because of the small, hydrophilic pores that comprise the small PSD. It is unlikely that the ACL can withstand such high pressures and the ACL would likely be damaged by gas trying to escape the layer. Despite the high gas pressures in the ACL, the resulting ACL water saturation is not changed significantly. The pores are of the order of tens of nanometres which theoretically would require extremely high pressures to displace the water, despite the relatively high contact angle of 80°. Figure 3.5 b) shows the intrusion curves for each of the PSDs examined in this work. The small PSD requires capillary pressures of the order of 7 bar to achieve a water saturation of 0.5, which is likely not feasible. The liquid pressure is not significantly changed, as the hydrophilic nature of the ACL allows for water to be quickly replenished at the OER sites. As such, there is very little change in the cell performance when the water saturation dependent active area is used, as shown in Figure 3.8 b). It would appear, therefore, to be very difficult to induce significant mass transport limitations with the small PSD and the catalysts used in this work, which is also true for the other PSDs, as will be discussed later.

At this point it is worth noting that the homogeneous nature of the model used in this work fails to capture the impact of discrete blockages. For example, it would not capture a large gas bubble being trapped at a particular location, e.g. in the PTL at the ACL/PTL interface, and blanking a large section of the ACL. That the pressures, and therefore water saturation, and ACL properties are averaged throughout the domain means that there is always a hydrophobic fraction of pores that can move gas bubbles out of the ACL. This study would therefore suggest that research into

mass transport limitations should be concerned with determining the conditions under which these discrete blockages can occur. For example, if performing neutron or x-ray imaging of the gas buildup in a PTL during operation, the focus should be on reporting the size and frequency of gas bubbles close to the PTL/ACL interface, rather than the average gas saturation across the entire PTL.

There is some evidence for the very high gas pressures in the Ir based ACL in the literature. Mandal et al. [204] obtained polarisation curves up to 4 A/cm^2 for both the Ir and IrOx catalysts used in this work, with a very similar cell construction. Post operation SEM imaging revealed the presence of a large number of small cracks throughout the surface of the Ir ACL that were not present prior to operation. The cracks had a volcanic appearance and may have been caused by the gas bubbles building significant pressure deep within in the ACL before rupturing the layer to release this pressure. These volcano-like cracks did not appear on the IrOx based ACL, indicating that a pressure buildup did not occur during operation, as predicted by the numerical model in this work. It should be noted that the Ir based ACL used a Ti felt PTL on the anode, while the IrOx ACL used a sinter. Furthermore, Mandal et al. [204] studied the impact of adding carbon particles, as a pore former, to the ACL ink before fabrication, with the intent of corroding these particles during operation, thereby altering the porosity and PSD of the layer. With the addition of the pore former to the Ir ACL, the volcano-like cracks did not appear after operation, indicating that the change in porosity and PSD induced by the pore former prevented the gas pressure from building up. The fact that the ACL could be ruptured by the gas pressure buildup suggests that an ACL with a small PSD will have its microstructure altered during operation, resulting in an increase in the mean pore size and permeability of the layer. As such, it may not longer be possible to build high enough gas pressures to displace the water from the pores, as shown will be shown in the case of the larger PSDs discussed below.

Other possible evidence for the build up of gas pressure in the ACL is from Trinke

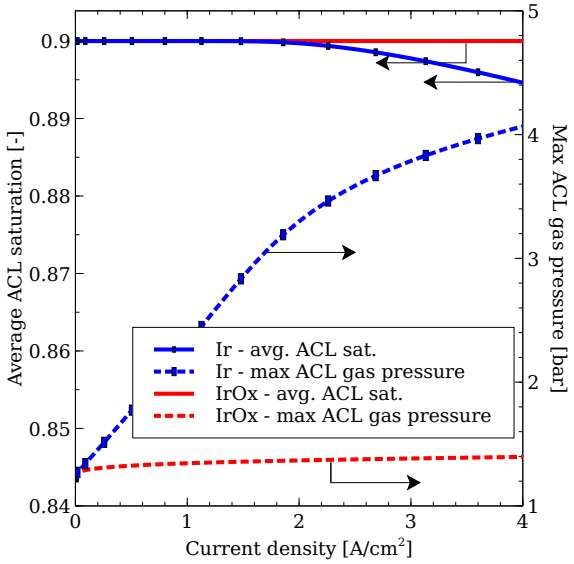

Figure 3.12: Comparison between between the averaged water saturation in the ACL and the maximum gas pressure reached in the ACL with an Ir and IrOx catalyst with the small PSD.

et al. [215] who studied gas permeation through the membrane during PEMWE operation, using an Ir black catalyst in the ACL that likely has similar effective conductivities to the Umicore Ir black catalyst studied in this work. The authors noted that the rate of oxygen permeation through the PEM to the cathode increases with increasing current density. The authors attributed this increased flux to an oxygen supersaturation in the ACL; this supersaturation may have been caused by an increased oxygen pressure generated at the PEM/ACL interface, due to the nature of the OER distribution with an Ir black catalyst. Figure 3.12 shows that the maximum gas pressure generated in the ACL is dependent on the current density for the Ir catalyst, whereas the pressure changes very little for the IrOx catalyst. As such, it is possible that Trinke et al. would not have made their observation had they used a different catalyst.

3.5.2 Impact of PTL

The PTL used in this work is a Ti sinter, with its PSD and intrusion curve shown in Figure 3.5. Figure 3.13 a) shows the average gas saturation in the in-plane direction in front of the channel, and is plotted at a number of points in the through plane direction. Figure 3.14 shows the locations of this averaging. There is a build up of gas within the PTL with increasing current density, in agreement with observations by De Angelis et al. [159] using x-ray tomography. The rapid increase in the gas saturation moving from the channel into the PTL was not observed by De Angelis et al., and may be an artifact of the Dirichlet boundary conditions used at the channel for the gas pressure. Of particular interest, however, is that at the ACL/PTL interface, there is a significant jump in gas saturation, which was also noted by Garica-Salaberri [186]. This is not unexpected, as the gas and liquid pressures must be continuous. Therefore, there must be a jump in saturation between the two layers due to the significant differences between their PSDs and their intrusion curves. This result means that experimental observations of the gas saturation in the PTL may not be representative of the gas saturation in the ACL, and in fact the PTL gas saturation could be significantly higher than the ACL. As such, the importance of mass transport limitations may be overpredicted based on these experimental observations. It is also interesting to note that ACL gas saturation appears to be independent of the PTL gas saturation, as the ACL gas saturation is very similar at each current density, while the PTL gas saturation varies significantly. This is a result of the much smaller PSD in the ACL and would indicate that determining ACL PSD properties is vital for understanding the impact of mass transport limitations in PEMWE.

Again it should be pointed out that the homogeneous nature of the model means that if the model predicts a gas saturation of 30% at the PTL/ACL interface at 4 A/cm^2, that also means that there is 70% water saturation at the same location which will provide enough water for the ACL to wick into the layer. It is more likely that

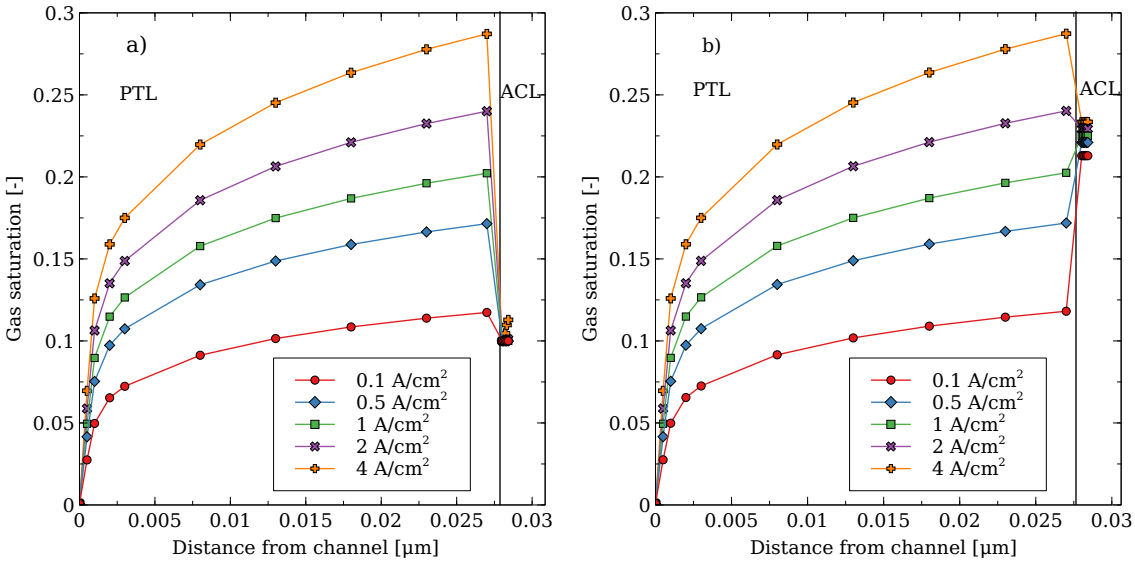

Figure 3.13: Profile of gas saturation in the PTL and ACL at different current densities, for the small (left) and large (right) PSDs.

the gas bubbles that comprise that 30% gas saturation are concentrated into a single capillary finger, in which a significant portion of the ACL is blanked from receiving water, an effect not captured by volume-averaged models such as the one presented. This process would likely induce more significant mass transport losses and would depend on the morphology of the PTL to determine the size of the area blanked by the gas, and on whether the liquid permeability of the ACL is high enough to allow water to be drawn to the blanketed area from other portions of the ACL in the in-plane direction. However, the ability of the ACL to transport water in the in-plane direction is likely determined by the PSD, hence further study on the structure of these layers is required. This idea implies that greater insights into these losses may be obtained from experimental imaging works that report localised gas saturations close to the PTL rather than averaged across the layer, e.g. using tomography [159].

3.5.3 Impact of the ACL pore size distribution

The impact of changing the ACL PSD was assessed by studying the medium and large PSDs shown in Figure 3.5 a). These PSDs have significantly larger pore sizes

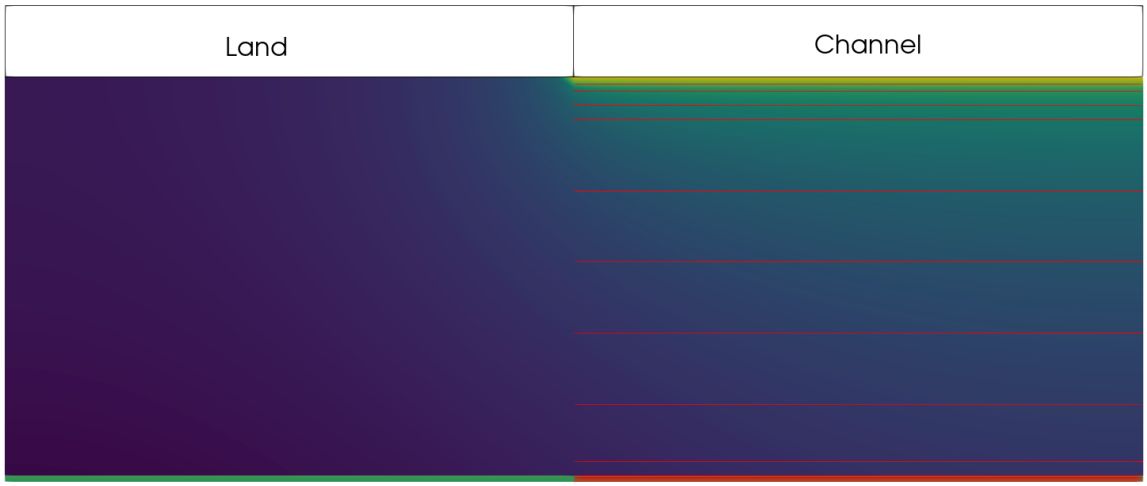

Figure 3.14: Lines over which gas saturations were averaged to obtain current densities dependent saturations in the anode electrode.

than the small PSD, though it should be noted that there are also differences in the hydrophilic volume fraction and the pore interconnectivity factor. The impact of the water saturation dependent active area using the medium and large PSD is given in Figure 3.15. The IrOx catalyst shows a very minor change in performance, though it is larger for the largest PSD. This is due to the hydrophilic volume fraction, which is 0.9 for the small and medium PSD, and 0.8 for the largest PSD. The Ir catalyst also shows very minor changes for the medium PSD, however a noticeable difference is seen for the large PSD, indicating that the model used in this work is capable of inducing mass transport losses for certain PSDs. Interestingly, mass transport effects can be observed throughout the polarisation curve, rather than at high current densities only. The importance of the hydrophilic fraction can be shown by considering the intrusion curves. The maximum capillary pressures at 4 A/cm^2 induced by the Ir based ACLs are 2.8 bar, 12 kPa and 1.3 kPa for the small, medium and large PSDs respectively, each of which are close to the 'knee' for their respective intrusion curves, as shown in Figure 3.5 b). As such, the impact of the saturation based kinetics is controlled by the hydrophilic portion of the PSD and does not vary with current density.

Figure 3.16 shows the average ACL water saturation and maximum gas pressures

observed for both PSDs and catalysts. The medium PSD shows significantly lower pressures are induced in the ACL for the Ir, as compared to the small PSD in Figure 3.12, because the larger PSDs are more permeable to gas. The water saturation for the IrOx catalyst remains at 0.9, while the Ir only has a small deviation at higher current densities. In general, the medium PSD results in water saturation and pressures profiles that are more similar to each other as compared to the small PSD when changing catalysts. This effect is clearly demonstrated for the large PSD, where pressure and water saturation profiles are identical for both catalysts, indicating that the mass transport behaviour of the layer is no longer dictated by the reaction distribution. The very large pores present in the large PSD, as well as the reduced hydrophilic content, greatly improve the transport of gas out of the layer, alleviating the large gas pressures predicted with the small PSD. It is interesting to note that the volcano-like cracks observed by Mandal et al. [204] in Ir based ACLs post operation are of the order of a few microns across, in a layer that appears to have very small pores. The volcano-like cracks, once formed, are of a similar size to the 6 μm pores present in the large PSD, and so likely significantly improve the permeability of the ACL, as implied by the results obtained for the large PSD. In addition, the large PSD shows a slightly stronger coupling between the PTL and the ACL. This is shown in Figure 3.13 b), where the gas saturation in the ACL for the large PSD shows some variation with current density and therefore PTL gas saturation. That the PTL exerts a greater influence can be expected, as the intrusion curves for the the large PSD is the closest to that of the Ti sinter compared to the other two PSDs, as shown in Figure 3.5 b).

It is interesting to note that despite the ACL water saturation in the largest PSD being identical for both catalysts, the Ir ACL sees a larger drop in performance in Figure 3.15 b) compared to the IrOx when mass transport effects are accounted for. At 4 A/cm^2, the Ir ACL has a mass transport induced voltage loss of 13.4 mV, compared to 6.9 mV for the IrOx. This discrepancy can be explained by examining the kinetics of the OER, and is demonstrated using the Tafel equation for simplicity.

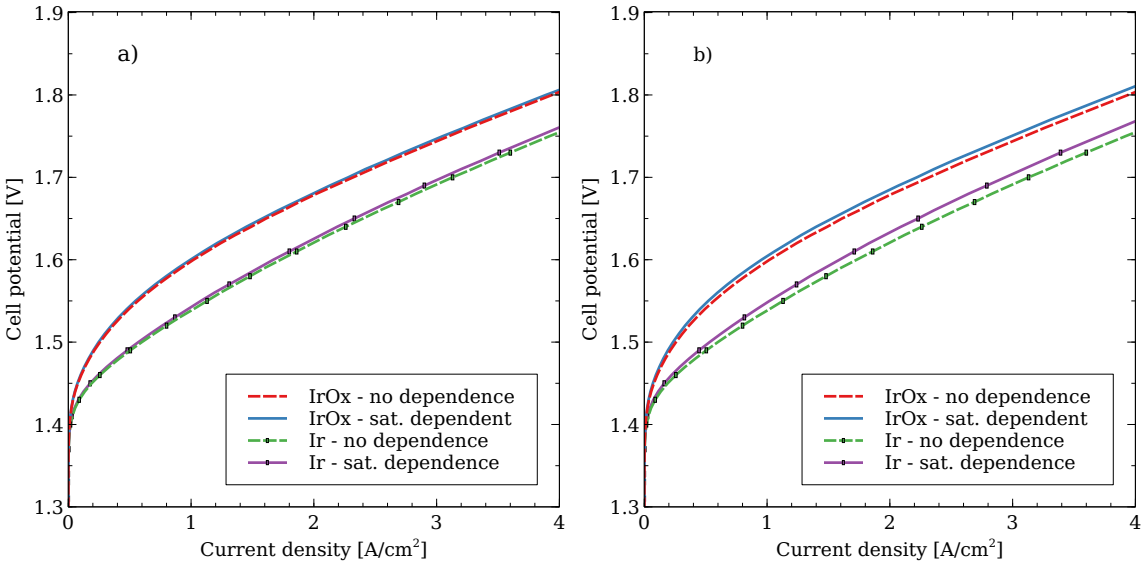

Figure 3.15: Impact of accounting for a water saturation dependent active area for the medium (left) and large (right) PSDs.

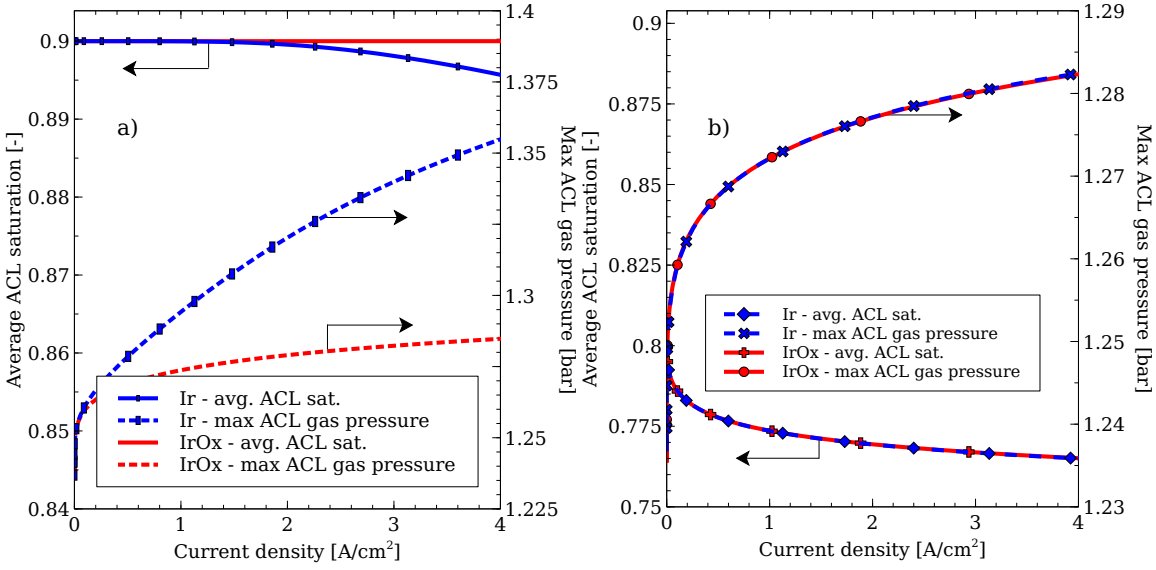

Figure 3.16: Dependence of the average ACL water saturation, and the maximum gas pressure in the ACL, for the medium (left) and large (right) PSDs, and for both catalysts.

A multi-step model was used in this work, however the model will behave as a Tafel model at potentials that are sufficiently higher than the potential at which the change in Tafel slope occurs (approximately 1.4-1.5 V for parameters used in this work). The Tafel equation, including the water saturation dependent active area, is given as:

$$j = s_L A_v j_0 \exp\left(\frac{2.303\eta}{b}\right) \tag{3.30}$$

where b is the Tafel slope in Volts per decade, which can be extracted from Figure 3.7, and i_0 is the exchange current density. The equation can be rearranged to obtain the overpotential, η:

$$\eta = \frac{b}{2.303}\left(\ln(j) - \ln(s_L A_v j_0)\right) \tag{3.31}$$

The voltage loss induced by a reduction in the water saturation can be obtained by subtracting the overpotential obtained at a water saturation of one (i.e., no mass transport losses), from the overpotential obtained with a lower water saturation. The result is given as:

$$\eta_{s_L=1} - \eta_{s_L} = \frac{b}{2.303}\ln\left(s_L\right) \tag{3.32}$$

Using the equation above, the voltage loss from mass transport can be computed for each catalyst. At 4 A/cm^2, both catalysts had an average water saturation of approximately 0.765. At high cell potentials, the Ir catalyst has a Tafel slope of 118.2 mV/dec, giving a voltage loss of 13.74 mV, while the IrOx layer has a Tafel slope of 59.25 mV/dec, giving a voltage loss of 6.89 mV. These values match very closely with those obtained from the difference in the polarisation curve. This result highlights the importance of understanding the activity of the catalyst when studying mass transport losses. It should be noted however, that the analytical method described will not be as accurate if the water saturation distribution depends strongly on the reaction distribution, or there is a significant variation throughout the ACL.

3.5.4 Effect of PSD model parameters

Due to the uncertainty in obtaining certain PSD parameters, such as the hydrophilic portion, pore connectivity factor and the contact angle for the hydrophilic and hydrophobic portions, a parametric study was carried out on these parameters, using the three PSDs. Both catalysts were studied, however the IrOx did not show significant changes in behaviour, so the results are not shown here. The study varied one parameter at a time, at a current density of 4 A/cm^2, where mass transport limitations should be most significant. The hydrophobic contact angle was not found to induce any change in behaviour for either PSD or catalyst so is not shown. As the gas pressure will always be higher than the liquid pressure, the capillary pressure in the ACL will always be negative. As such, it is not possible for the water to invade the hydrophobic pores, so changing the contact angle of these pores cannot affect the mass transport behaviour.

Figure 3.17 a), d) and g) show that changing the hydrophilic contact angle can have a significant effect on the average water saturation and maximum gas pressure in the ACL, as well as the cell potential. For low contact angles, the water saturation is close to 0.9 or 0.8, which is the hydrophilic volume fraction of the ACL. At contact angles close to 90°, the water saturation drops dramatically for each PSD, as the pores are unable to hold onto the liquid water, and voltage losses increase. The largest PSD sees a very large decrease in ACL water saturation causing a large increase in the voltage required to reach 4 A/cm^2, as large pores with a high contact angle require very little pressure to invade. As such it may be possible to induce very significant mass transport losses with this homogeneous PSD model. However, it is not likely that the contact angle of the iridium based catalysts are close to 90°, particularly in light of the values reported by Cruz et al. [212] and Chung et al. [213] which were closer to 10°. Note that varying the IrOx hydrophilic contact angle also showed the same behaviour for the water saturation as the Ir did, i.e. at very high contact

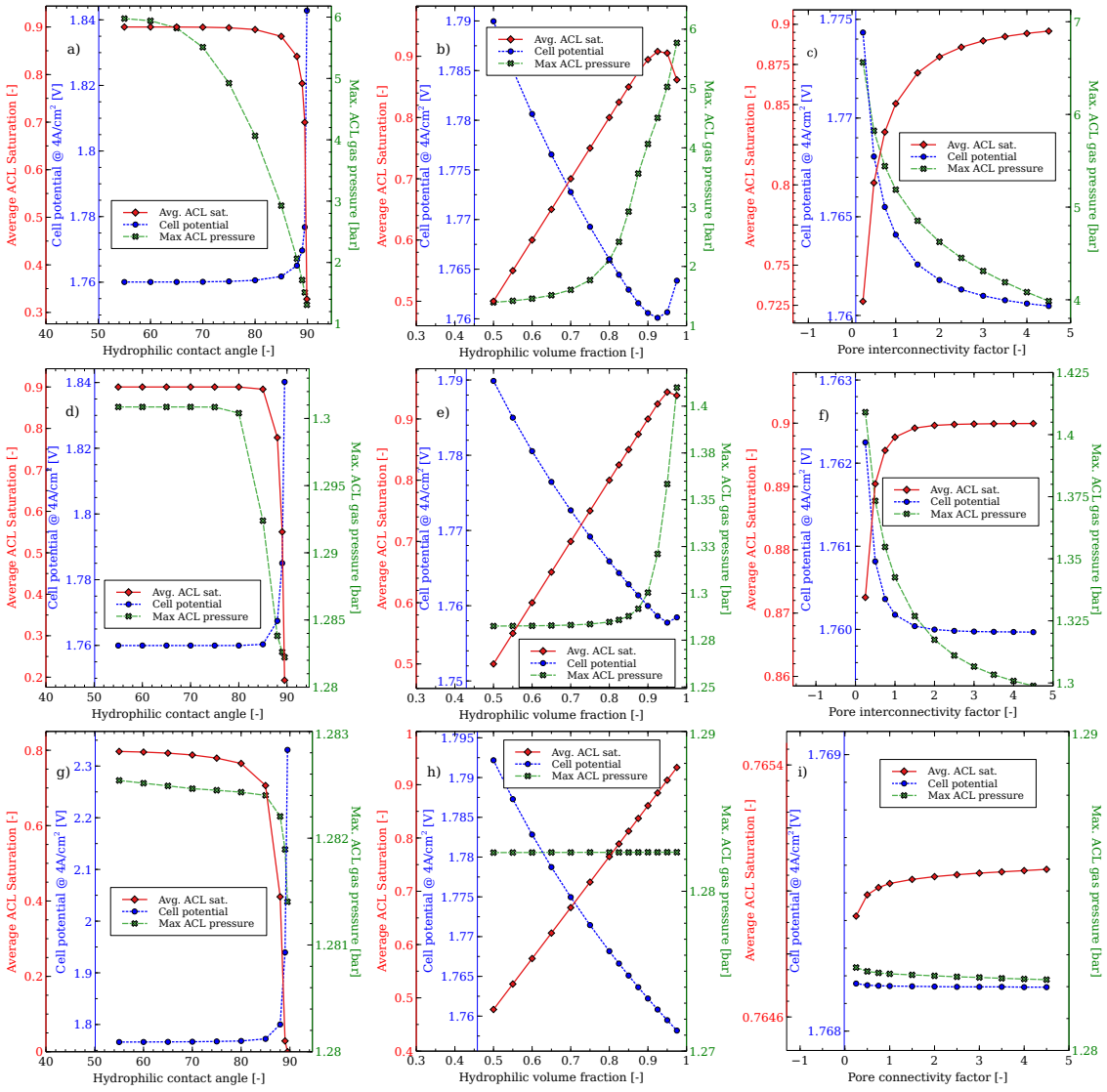

Figure 3.17: Parametric study on PSD parameters and their impact on the average ACL water saturation and maximum gas pressure in the ACL for the small (top row), medium (middle row) and large PSDs (bottom row) at 4 A/cm^2.

angles, the water saturation dropped significantly. The gas pressure for the smallest PSD is strongly impacted by the contact angle, as lower angles prevent the gas from invading liquid filled pores, requiring high pressures to escape through hydrophobic section, which only makes up the remaining 10% of the volume. The gas pressure for the other two PSDs is less affected, due to their larger pore sizes which prevent gas pressure buildup.

The change in the hydrophilic volume fraction induces an almost linear change in the water saturation, up to a volume fraction of approximately 0.9 for the small and medium PSDs, as the ACL water saturation essentially matches the hydrophilic volume fraction. As was discussed previously, the hydrophobic portion of the ACL is never invaded by the water, and provides an increasingly permeable pathway for the gas with decreasing hydrophilic volume fraction. This result suggests that an ACL with a hydrophobic portion of 50% means that 50% of the active area is unavailable for the OER, causing a significant reduction in the catalyst utilisation. At very high HI volume fractions, the trend deviates from linearity for the smaller PSDs, as the reduced hydrophobic volume fraction reduces the permeability of the layer, requiring higher gas pressures to move the gas out. The increased gas pressure allows for more of the hydrophilic portion to be invaded by the gas, thereby reducing the water saturation. However, significantly reducing the water saturation again requires very high gas pressures.

Finally, the pore interconnectivity factor reduces the water saturation in the ACL, as it makes the ACL less permeable. However, there is a corresponding rise in the gas pressure, to values that would likely damage the ACL. The larger the PSD, the less impactful the interconnectivity factor becomes.

3.6 Conclusions

In this work, a 2-D macro-homogeneous model describing the MEA of a PEM water electrolyser was presented. Charge transport is accounted for using Ohm's Law,

while the mass transport effects were accounted for by considering the local water saturation in the ACL. Darcy's law was used to predict liquid and gas pressures throughout the domain, while a PSD model is used to relate capillary pressure to the water saturation and to obtain gas and liquid permeabilities. The governing equations were solved using the finite element method. A detailed fitting procedure was described, in which the layer conductivities are chosen to match the cell resistance and the high-frequency resistance. It was found that the standard Tafel equation was not capable of matching the experimentally obtained polarisation data in the kinetic region, instead a model that could account for a change in the Tafel slope was used and fitted with a model that accounted for the low effective conductivities of Ir and IrOx based ACLs reported by Mandal et al. [125]. The fitted model was found to have very good agreement with the experimentally obtained polarisation data.

The impact of mass transport losses was investigated by obtaining polarisation curves up to 4 A/cm^2 with and without the active area being reduced by the local water saturation in the ACL. It was found that in general it is very difficult to significantly reduce the water saturation, as the pores in the ACL were considered to be the order of tens of nanometres and hydrophilic, based on experimental data, requiring very high gas pressures to force the water out. Larger pores in the ACL are easier to invade, and minor mass transport losses were observed for pore radii of the order of 700 nm, however it is also difficult to build the gas pressures required to remove larger amounts of water from the ACL and cause a large drop in performance. The quantity of liquid water consumed is extremely low and is readily supplied by the PTL, even at low PTL water saturations. The model presented here is, however, a volume-averaged model that cannot account for discrete events, such as a single large bubble blocking a large portion of the ACL and preventing water from reaching the active sites. The model suggests that if there are mass transport losses in PEMWE, they are unlikely to be caused by the generation of a distributed network of gas that significantly reduces the water saturation across the entire ACL, and so may be caused

by the discrete events instead.

The reaction distribution was found to have a significant impact on mass transport in the MEA. The IrOx ACL has a significantly lower electronic conductivity as compared to the protonic, resulting in the reaction occurring close to the PTL. As such, any evolved oxygen can quickly escape the ACL to the PTL and be removed in the channel. In contrast, the Ir based ACL has a lower protonic conductivity compared to the electronic, so the gas is evolved close to the membrane. The gas is then forced to pass through much of the ACL, which can induce very high gas pressures if the pores are in the tens of nanometres range. Such high pressure can potentially damage the ACL, as evident from volcano-shaped cracks observed in post-operation layers [204]. In addition, the high oxygen pressures at the membrane interface may induce a flux of oxygen to the cathode that will increase with increasing current density, as was observed by Trinke et al. [215]. These observations suggest that researchers studying mass transport limitations in PEMWE should note the nature of the catalyst used in the ACL, as catalysts that produce oxygen close to the membrane may have very different mass transport characteristics compared to those that produce the oxygen close to the PTL.

The study also examined the impact of changing the ACL PSD to reflect catalyst micro-structures reported in the literature that had large characteristic pore radii. The larger pores were easier to invade, and therefore more susceptible to mass transport limitations. The presence of such large pore sizes (several hundreds of nanometres) in the ACL may be difficult to realise due to the need to reduce ACL loadings and therefore ACL thicknesses, which are already of the order of only a few microns. Cracks could be introduced to improve ACL permeability if the average pore size is very small [216–218], though consideration would have to be given to its impact on the in-plane conductivity [219]. Other microstructural parameters were also examined, such as the hydrophilic contact angle and the hydrophilic fraction of the PSD. It was found that water will not occupy the pores of the ACL that are hydrophobic, as the

capillary pressure will always be negative. Therefore, any portion of the ACL that is hydrophobic will not have access to water, and would be unavailable to the OER. However, it is likely that the only component of the ACL that is hydrophobic would be the Teflon backbone of the Nafion ionomer; the catalyst surface should always be hydrophilic and therefore have access to water. Varying the hydrophilic contact angle showed that significant mass transport losses can be induced when the angle is very close to 90°, however this is not likely in PEMWE ACLs. It was demonstrated using the developed model that the wettability of the ACL and its pore size have a significant impact on the PEMWE performance. Therefore, accurate characterization of those layers is a crucial step in the further development of the technology.

Finally, the impact of the PTL on the ACL water saturation was assessed. It was found that the water saturation in the PTL was current density dependent, however the ACL saturation exhibited little change. The water saturation in the ACL appears to be only very weakly coupled to that in the PTL, as each layer has a very different intrusion curve. Measurements of the water saturation in the PTL using neutron or x-ray imaging are likely not representative of the saturation in the ACL.

Chapter 4

Characterisation and mitigation of ACL electron transport limitations[1]

4.1 Introduction

In this chapter, the impact of the low electronic conductivity of IrOx based ACLs discussed in the introduction is studied in more detail. First, the measurement of low electronic conductivity by Mandal et al. [125] is validated using a different ex-situ technique. The technique allows for the impact of compression on the conductivity to be explored and reveals order of magnitude changes can be induced. The extremely low conductivity of the ACL is further validated by using numerical modelling to simulate the experiments of Mo et al. [113] who directly imaged the OER occurring in a PEMWE that had a transparent flow field and a PTL comprised of large pores etched in a Ti film. The model shows that the ACL conductivity likely needs to be less than 1 mS/cm in order to prevent bubbles forming in the centre of the pore, as observed by Mo et al.

The numerical model from the previous chapter is then used to study the impact of having an extremely low electronic conductivity in an MEA. The impact on reaction distribution, determining kinetic parameters and a voltage breakdown is presented.

[1]The studies performed in this chapter are being prepared for an upcoming publication: M. Moore, E. Beaulieu, M. Mandal, M. Secanell "A Numerical Study on the Impact of Anode Catalyst Layer Electronic Conductivity on Performance in Proton Exchange Membrane Water Electrolysis".

The potential for loading reductions is explored numerically and experimentally, using both experimental data obtained in-house and from the literature. The in-house experimental data was obtained in collaboration with Eric Beaulieu and Manas Mandal. Finally, the use of higher compression and electronically conducting polymers to improve electronic conductivity is investigated experimentally, using polarisation data, EIS and CV measurements.

4.2 Numerical model

The model used for the MEA simulations in this chapter is the same as that presented in the previous chapter. As this work is primarily focused on the impact of the ACL conductivity on the cell performance, the Tafel equation is used to describe the OER kinetics for simplicity. In the previous chapter, a more detailed kinetic model from Ma et al. [106] is used in order to obtain a close fit with experimentally obtained polarisation curves. The use of the Tafel equation in this work allows for the impact of changing the kinetic parameters to be studied, by modifying familiar parameters such as the exchange current density and the transfer coefficient. The Tafel equation used is given as:

$$j_{OER} = s_l A_v j_0 \exp\left(\frac{\alpha_a F \eta}{RT}\right) \tag{4.1}$$

where j_0 is the exchange current density and α_a is the anodic transfer coefficient. There is significant variation in the literature for the values of these parameters with Aubras et al. [57] noting that the exchange current density used in PEMWE modelling literature spanned several orders of magnitude. The choice of kinetic parameters for the model depends on the simulation, and is discussed in more detail in the following subsections.

4.2.1 Perforated porous transport layer cell model

The experimental results from Mo et al. [113] are simulated in order to determine the order of magnitude required for the ACL electronic conductivity to reproduce their

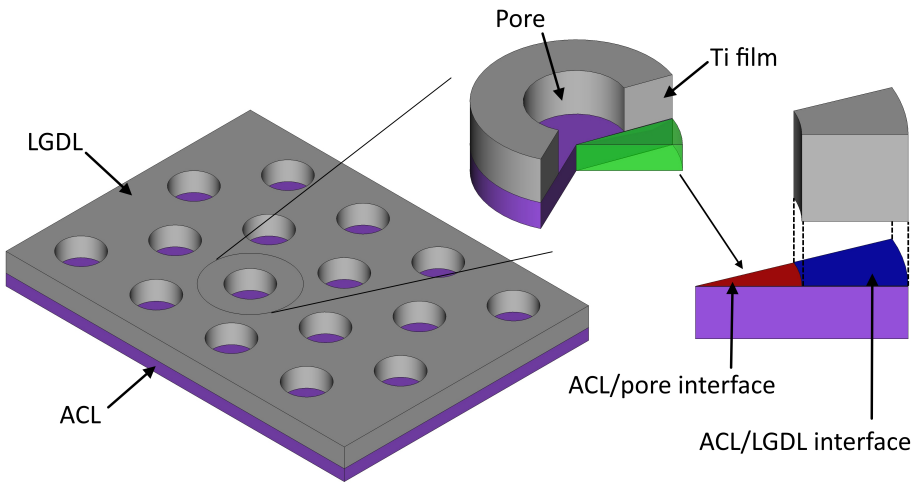

Figure 4.1: Representation of the LGDL used by Mo et al. [113], and the subdomain used in the 3D simulations.

observations. As discussed in the introduction, the authors used a perforated thin Ti film as the PTL (termed a liquid gas diffusion layer (LGDL)), and a transparent flow field that allowed for the direct visualisation of the oxygen bubbles emerging from the ACL. Zero bubble formation was observed in the 50 μm diameter pore of their LGDL at 2 A/cm^2, indicating that the electronic conductivity is severally limiting. This work recreates the experiment using a 3-D model of the ACL and uses boundary conditions to account for the contact between the LGDL/pore and the ACL. The ratio of the current density produced in the ACL below the pore compared to the total current density produced is used to estimate how low the conductivity needs to be to prevent bubble formation in the pore. The results from the LGDL with 50 μm pores were chosen, as the small diameter reduces the computational requirement for the 3-D simulations and provides the smallest in-plane transport distance for the electrons. Only the ACL is simulated to reduce the computational load and is shown in Figure 4.1.

Figure 4.2 shows the initial mesh used in the 3D simulations. The yellow/green region is the pore region for the purposes of determining the fraction of the current density produced in the pore compared to the total current density. The pore/ACL

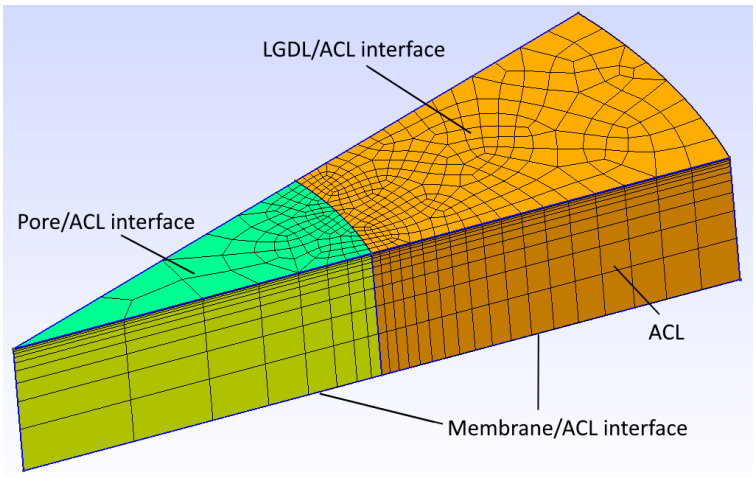

Figure 4.2: Initial mesh for the 3D simulations indicating the boundaries.

surface is where Dirichlet BCs are applied for the liquid and gas pressure (i.e. the red surface in Figure 4.1), while the LGDL/ACL interface is where the electronic potential is applied, equal to that of the cell potential (i.e. the blue surface in Figure 4.1). The membrane/ACL BC of zero protonic potential is applied to both regions. No flux conditions are applied at other boundaries. At the pore, a small negative capillary pressure is applied, representing a water filled pore.

To obtain the transfer coefficient and exchange current density for the 3-D model, the HFR corrected polarisation curve in reference [208] is approximately fitted to for each ACL conductivity studied in order to obtain reasonable agreement between the experiment and model at high current densities. These parameters are shown in Table 4.1 and reveal that the kinetic parameters can change significantly depending on the conductivity of the layer. The PSD model is used to describe the microstructure of the catalyst and transport layers. The PSD used for the 3-D simulations is taken from Hegge et al. [208], who obtained the PSD of a $Ir_{0.5}Ru_{0.5}Ox$ EZ CCM from FuelCellsEtc using FIB-SEM. Fortunately, this CCM is the same as that used by Mo et al. [113] in their imaging of oxygen bubbles leaving the ACL. The PSD parameters are shown in Table 3.4, with discussion on the choice of parameters in the previous chapter.

Table 4.1: Tafel parameters used in the 3-D model for different assumed ACL electronic conductivities.

σ_s^{eff} [S/cm]	i_0 [A/cm$^2_{cat}$]	α_a
10^0	4x10^{-2}	1.15
10^{-1}	2x10^{-2}	1.2
10^{-2}	5x10^{-4}	1.7
10^{-3}	5x10^{-3}	1.7
10^{-4}	4x10^{-2}	1.85
10^{-5}	4x10^{-1}	1.85

The mesh is adaptively refined 5 times; the 5% of cells that show the highest error according to the error estimator from Kelly et al. [202] are further divided into four cells. The initial mesh has 4,100 cells and 142,884 degrees of freedom, after five refinements there are 13,634 cells and 543,484 degrees of freedom. Greater refinement is applied in the through-plane direction at the LGDL side, as low electronic conductivities will produce a very concentrated reaction distribution. The large number of adaptive refinements also ensure that the solution is mesh independent.

4.2.2 MEA simulation

The MEA simulations are the same as those in the previous chapter, with the exception of the use of the Tafel equation. The domain is shown in Figure 3.1, with the governing equations from Section 3.3.1. The simulation parameters are also the same as those presented in Tables 3.2 - 3.4 and 3.6 unless otherwise noted. The membrane used in this chapter is the N212 which has a thickness of 50.8 μm, while the ACL thickness is assumed to be that of the IrOx ACL, i.e. 4.4 μm for an ionomer loading of 25%. The OER kinetic parameters for the Tafel equation were chosen to give a reasonable fit to in-house polarisation data obtained at 1 mg/cm^2, assuming an ACL electronic conductivity of 1×10^{-3} S/cm. This conductivity was chosen, as it represents an average of the ACL electronic conductivity values studied. The transfer

coefficient is set to 1.75, with an exchange current density of 5x10^{-10} A/cm^2. The PSD of a Pt/C fuel cell CL used by Kosakian [196] was also applied in this study, as it better represented the pore sizes of the IrOx ACLs studied in this work as discussed in the previous chapter. The model implementation, mesh and computation time is similar to the previous chapter.

4.2.3 Post-processing

In Chapter 2, the ohmic heating method was used to obtain the resistance of individual layers. The method can be extended to obtain the corresponding voltage losses from this resistance:

$$V_{ohmic,protonic} = \frac{1}{iA}\int(\sigma_m \nabla\phi_m \cdot \nabla\phi_m)dV, \tag{4.2}$$

$$V_{ohmic,electronic} = \frac{1}{iA}\int(\sigma_s \nabla\phi_s \cdot \nabla\phi_s)dV \tag{4.3}$$

where i is the current density of the cell and A is the geometric area of the cell

In addition, the voltage losses from the kinetic reactions are computed using Equation (2.20).

4.3 Experimental

4.3.1 Compression dependent conductivity

The through-plane conductivity of an ACL comprised of the TKK IrOx (ELC-0110, Tanaka Kikinzoku Kogyo (TKK)) was measured. This ACL is the same as that investigated by Mandal et al. [125], this measurement was performed to ensure that the extremely low conductivity measured is reasonable. The Nafion loading was set to 25 wt.% while the IrOx loading was approximately 1 mg/cm^2. Three samples each with an area of 5 cm^2 were printed onto a copper plate that had a gold coating to reduce the contact resistance. A gold coated copper anvil with a base of 4 cm^2 was placed on top of the electrode, with the assembly placed into a compression jig controlled by a pressurised nitrogen line. A picture of the assembly is shown in

Figure 4.3. A VersaStat 4 potentiostat was used in a four-probe configuration to apply a linear sweep of the voltage to 100 mV, scanned at 10 mV/s. The resistance of the assembly was found using the slope of the measured current against the applied voltage. Good linearity was observed, as shown in Figure 4.4. Compressions of 0.34, 0.72, 1.1, 1.4, 2.8, 4.2, 5.6, and 6.5 bar were applied by increasing the nitrogen pressure, which was measured using a pressure sensor (Alicat flowmeter M-5SLPM-D/5M). A constant potential of 50 mV was maintained across the layer while the compression was increased and the resulting current was monitored. The linear sweep was performed once the current has stabilised and the slope of the curve was taken as the layer resistance. In addition, the resistance of the setup was found with only the anvil to get the resistance at as close to zero compression as possible. This measurement provides an estimate of the conductivity of the layer when not contacted by the PTL or when in an RDE.

The conductivity is found by dividing the layer thickness by the measured resistance. The layer is assumed to be 4 microns based on SEM measurements performed by Mandal et al. with the same ionomer and IrOx loading. It is possible that the thickness of the layer will decrease with increasing pressure, which is not accounted for in this work. The measured conductivities will be shown to change by orders of magnitude, therefore accounting for small changes in thickness will not likely be significant.

4.3.2 MEA characterisation

The performance of MEAs were assessed using the same methodology as described in the previous chapter. CCMs were prepared using the same cathode as before printed on an N212 membrane. To perform the catalyst loading study, ACLs were fabricated with the TKK IrOx or the Umicore Ir (3000020267) catalyst, with loadings of approximately 0.25, 0.5, 0.75 and 1 mg/cm^2. The thicknesses of each layer were measured using scanning electron microscopy (SEM) (Zeiss Sigma 300 VP-FESEM) after freeze

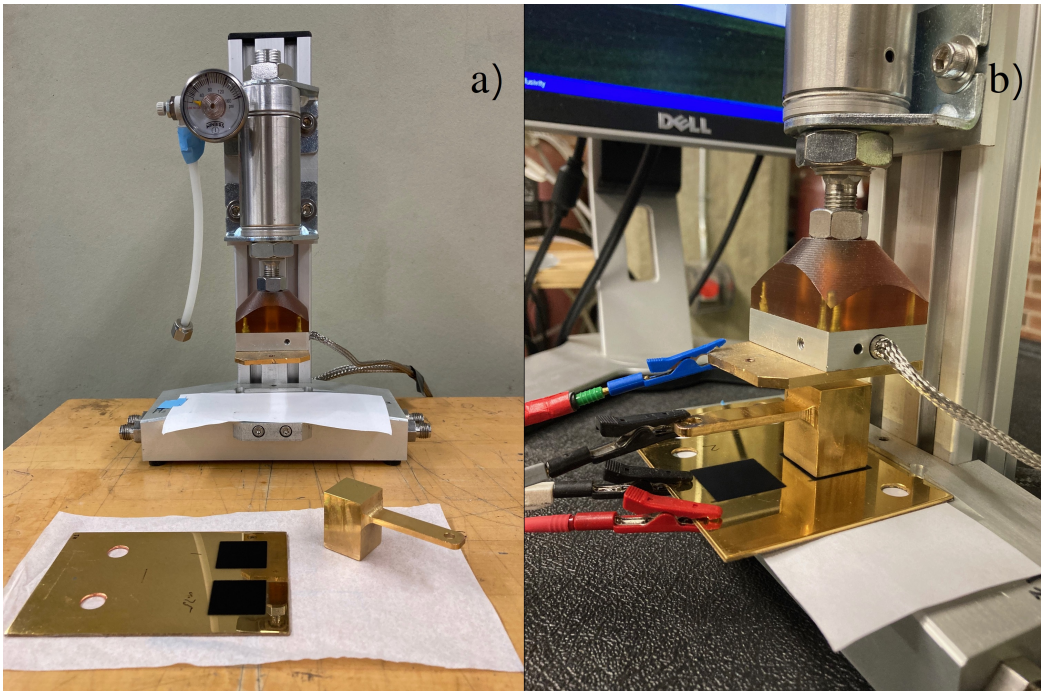

Figure 4.3: a) Compression jig with an ACL printed on the gold coated plate, b) assembled setup showing the connections to the potentiostat.

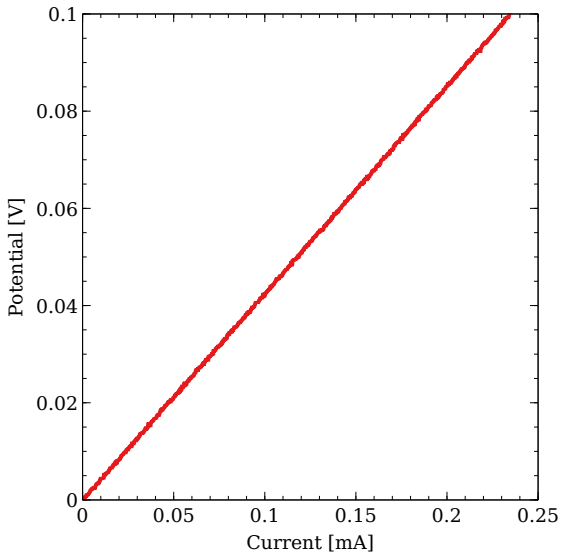

Figure 4.4: Example of the LSV experiment used to obtain the resistance of the ACL at a compression of 0.34 bar.g, which exhibits good linearity.

fracturing using liquid nitrogen. The IrOx ACL used a Nafion loading of 25 wt.%, while the Ir ACL had a loading of 15 wt.%. The PTL used was a Ti felt (2GDL10-0.25, Bekaert) with a Pt coating. To mitigate the impact of the low ACL electronic conductivity, an electronically conductive polymer, poly 3,4-ethylenedioxythiophene-polystyrenesulfonate (PEDOT-PSS) from Sigma-Aldrich (739332, 1.1% in water surfactant free, high conductivity) was added. The Nafion loading was reduced to 13.9 wt.%, with PEDOT added at a loading of 3.4 wt.%. The IrOx catalyst was used with a loading of 1 mg/cm^2.

The cell hardware and testing protocol was the same as the previous chapter. The compression on the cell is controlled by the choice of sealing gasket on the anode. A low compression is achieved by using a 245 μm gasket that has a similar thickness to the PTL, thereby no additional compression is generated on the anode side. A 145 μm gasket caused a pinch of approximately 100 μm on the anode side, resulting in a higher compression on the ACL. This gasket was applied for the loading study. The cathode gasket was chosen to provide a compression of 20 % on the SGL 28BCA and was the same for all cells. In addition, cyclic voltammetry was performed to study oxide formation for the different CCMs, and determine if the ECSA improved from the application of higher compression or the use of PEDOT. CVs were performed once the cell was conditioned and after the polarisation curve, by flowing hydrogen at 100% RH and 0.2 slpm in the cathode, with stagnant water in the anode. The cell temperature was 30 ℃. The potential was scanned at 40 mV/s from 0.005 - 1.35 V.

4.4 Results and discussion

4.4.1 Electronic conductivity measurement

As the electronic conductivity of the IrOx ACL measured by Mandal et al. [125] was substantially lower than that measured by Schuler et al. [127], the conductivity was measured again in this work as described in the previous section. It was hypothesised

that the ACL conductivity would vary under compression, due to studies in the literature that measured the powder conductivity of IrOx catalysts. The powder conductivity is typically measured by compressing the catalyst in a small pellet and measuring its resistance [119]. At a certain compression, the resistance is independent of the compression, which is used to calculate the bulk conductivity of the sample [129]. Bernt et al. [112] used a compression of 1 GPa to obtain the conductivity of one catalyst, a pressure that is not likely to be achieved in a cell. That such a high pressure was used may indicate that the catalyst conductivity varied significantly with compression, which may be caused by the interfacial contact resistance between the catalyst particles [128]. This contact resistance could be significant if the ACL is not compressed enough, such that the bulk conductivity of the catalyst is achieved. If the catalyst powder varies with compression, the ACL effective conductivity will likely show a higher variance, as the addition of the ionomer will further reduce catalyst connectivity.

Figure 4.5 shows how the conductivity of the IrOx catalyst layer used in this work varies with compression. The conductivity at high compressions is approximately 1×10^{-5} S/cm, which is 5-10 times lower than that measured by Mandal et al. [125]. The inset shows that the conductivity is increasing linearly with increasing compression, however the compression used by Mandal et al. is not known. It is possible that the compression felt by their ACL was higher as it was measured in a cell, particularly for the parts of the ACL that are under the land. It is clear that the conductivity of the IrOx ACL is extremely low however. The conductivity reduces by orders of magnitude at lower compression, reaching an order of 1×10^{-7} S/cm close to zero compression. This result is in line with the observations by Mo et al. [113] when they found that bubbles only emerged from the ACL in contact with the PTL.

Further research is needed to confirm the low conductivity of the ACL, which may be due to high contact resistance for this specific catalyst, or the inkjet printing method used to fabricate the layers. The experiment should be repeated for layers of

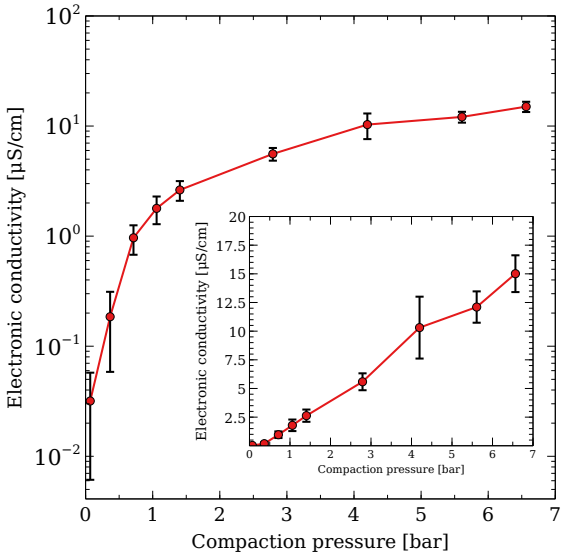

Figure 4.5: Through plane electronic conductivity of the IrOx ACL with changing compression with a catalyst loading of 1 mg/cm^2. The inset shows the conductivity on a linear scale.

different loadings. Such a study which would allow for the conductivity to be obtained by the two thickness method, and remove any contact resistance effects.

4.4.2 Perforated porous transport layer cell model

The conductivities measured by Mandal et al. [125] and by this work for the TKK IrOx catalyst are extremely low at approximately 1x10^{-5} S/cm, five orders of magnitude lower than that measured by Schuler et al. [127] at 100% RH. The former measurement was in the though-plane direction, while the latter was in the in-plane direction, using very different methods, however the difference is stark. To further ensure that such low conductivities are realistic, the experimental results from Mo et al. [113] were simulated using the model described in Section 4.2.1. Figure 4.6 shows the percentage of the OER current produced in the region under the pore compared to the total current density. As the region under the pore comprises one quarter of the total volume, 25% is the maximum the pore region can contribute in the case where the reaction is perfectly distributed. For the highest electronic conductivity,

the fraction is greater than 25%, as the electron transport is not limiting and instead two-phase effects under the LGDL reduce the current density produced there. The figure shows that for the conductivity measured by Schuler et al. [127], which was of the order of 1x10^{-2} S/cm, 10% of the total current is still produced in the pore region. It is difficult to know for which current densities no bubbles will be formed in the pore region, however conductivities lower than 1x10^{-3} S/cm are needed to achieve close to zero current. As such, conductivities of 1x10^{-4} or 1x10^{-5} S/cm may be required to produce zero oxygen bubbles in the pore as observed by Mo et al. It should be noted that the catalyst used by Schuler et al. is quite different from that used by Mo et al.; these simulations suggest that the conductivity of the ACL varies substantially depending on the catalyst used. Kang et al. [114], from the same group as Mo et al., also modelled the interaction between the ACL and LGDL and found that electronic conductivities of the order of 5 S/cm caused significant limitations under the pore. The model was 0-D and included a contact resistance between the LGDL and ACL to account for the lack of contact under the pore. A contact resistance is not included in this work, as pore and land are distinguished in the model. However, the model does assume that there is no interfacial contact resistance between the ACL and land, which may account for the discrepancy between the two models. As discussed in the previous section, performing the conductivity measurements using multiple thicknesses will allow for the impact of the contact resistance to be assessed.

Figure 4.7 shows the volumetric current density in the 3D domain at 2 A/cm^2 for high and low electronic conductivities. Very high current densities of 1x10^7 and 1x10^4 A/cm^3 are predicted for the low and high conductivity cases respectively. Such high values obscure the variation in the predicted current densities, as such the same data is shown with a maximum current density range of 1000 A/cm^3 to make the difference between the high and low conductivity more apparent. The high conductivity case exhibits a more uniform distribution, while the low conductivity case has the reaction extremely focused under the LGDL. It is likely that gas bubbles will form in the pore

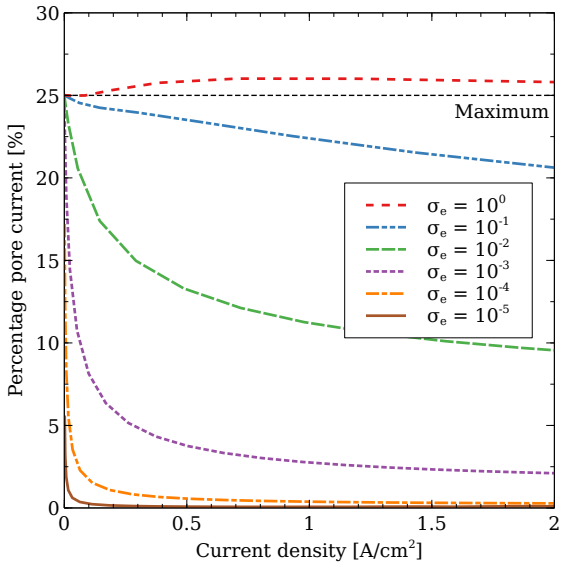

Figure 4.6: Percentage of total current produced under the pore for different ACL electronic conductivities, with changing total current density.

region for the high conductivity case but not for the low conductivity case.

It is interesting to note that for low conductivity catalysts the percentage of current in the pore space plateaus at very low current densities. For a conductivity of 1x10^{-4} S/cm, the reaction distribution will be concentrated at the LGDL with little reaction in the pore above current densities of 200 mA/cm^2. Therefore, the reaction is dominated by through-plane effects as in-plane transport is severely limited. The impact of in-plane transport is effectively a reduction in the active area available: if 50% of a poorly conducting ACL surface is contacted by the PTL, then that ACL at high current densities will behave similarly to an ACL with half the active area that is perfectly contacted by a PTL. For the macro-homogeneous MEA simulations that follow, modelling the ACL under these conditions without capturing the roughness of the PTL, and therefore in-plane effects, may be justified if the active area/exchange current density is a fitted parameter that will account for this reduction in the effective active area. At higher conductivities, e.g. 1x10^{-1} S/cm, Figure 4.6 suggests that in-plane electron transport does not significantly impact cell performance for

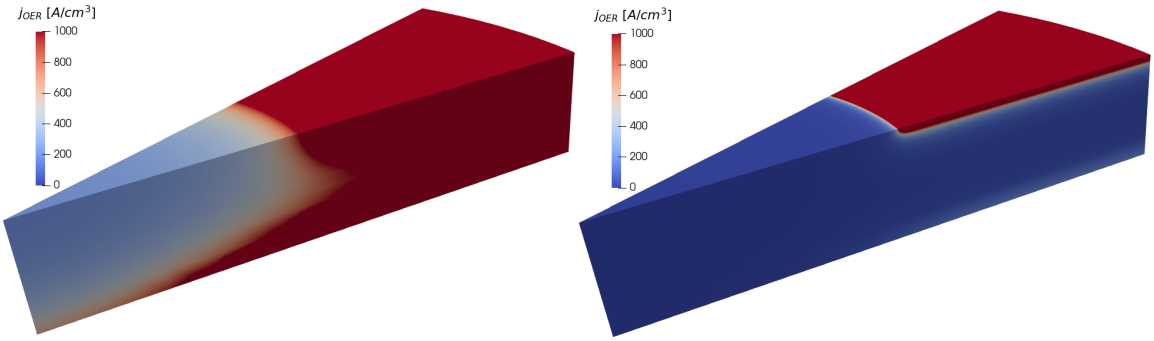

Figure 4.7: Volumetric current density at 2 A/cm^2 for an ACL electronic conductivity of (left) 1x10^{-2} S/cm, and (right) 1x10^{-4} S/cm. The current density range is set to a maximum of 1000 A/cm^3 to allow for better visualisation of the current. The maximum current density predicted is 1x10^4 and 1x10^7 A/cm^3 for the high and low conductivity case respectively.

pore sizes of 50 μm. The pore sizes of PTLs used in this work are closer to 20 μm, as discussed in the previous chapter. As such, the macro-homogeneous assumption is also justified for higher conductivities.

4.4.3 Reaction distribution in an MEA

In order to elucidate the impact of having a low ACL electronic conductivity on cell performance, polarisation data was generated using the MEA model for two cells, one with an ACL conductivity of 1x10^{-1} S/cm and a second with 1x10^{-5} S/cm. These cells represent the order of magnitude of the electronic conductivities obtained by Mandal et al. [126] for the Ir and IrOx ACLs at 100% RH. The protonic conductivity is maintained at 1x10^{-2} S/cm because it is the approximate average of the protonic conductivities measured for the Ir and IrOx ACLs. This value was used for simplicity due to the uncertainties in measuring the protonic conductivities of these ACLs, as noted in Chapter 2.

Figure 4.8 shows a large difference in performance induced by the low ACL electronic conductivity. The lower conductivity ACL exhibits a higher slope in the ohmic region, with the kinetic region also significantly affected. The latter is clearly revealed

in the Tafel plot in the inset of Figure 4.8 b), with a large deviation in the predicted performance at current densities as low as 1 mA/cm^2. The two simulations had identical kinetic models, indicating that the current density region typically considered to be purely kinetic (i.e. between 1-100 mA/cm^2), is in fact impacted by the low conductivity of the ACL. Figure 4.9 shows the OER distribution for each ACL at a current density of 0.1 mA/cm^2, both of which exhibit uniformity. As such each layer has the same potential at this current, indicating that the losses are purely kinetic. At 10 mA/cm^2, the high conductivity ACL is still uniform, so this current is still in the kinetic region. The low conductivity ACL exhibits an almost two order of magnitude difference between each side of the layer, with the reaction concentrating at the ACL/PTL interface due to the low electronic conductivity. At higher current densities, the distribution becomes more concentrated, such that the majority of the ACL is inactive. Therefore there is the potential for a reduction in the catalyst loading.

The Tafel plot in Figure 4.8 shows that the performance of the low conductivity ACL at low current densities is not purely kinetically limited. It is common for researchers to characterise the kinetic performance of their ACLs by fitting the Tafel equation between current densities of 1-100 mA/cm^2, obtaining the Tafel slope and exchange current density. This is generally justified by the presence of a linear region in the Tafel plot at these current densities. However, the inset of Figure 4.8 b) shows that an apparent linear region can still be obtained even if significant ohmic losses are present. While ohmic resistances should not appear linear on a Tafel plot, the ohmic resistance is also causing a reduction in the active area for the reaction. This summation of the ohmic resistance and the diminishing active area appear to produce a linear trend on the Tafel plot. Both high and low conductivity cases have the same kinetic model, however a naive analysis of the data in the inset would suggest that the low conductivity ACL has a higher Tafel slope and a higher exchange current density than the high conductivity ACL. This effect has been demonstrated experimentally by Chung et al. [220] in the case of the HER on the MoS_2. The

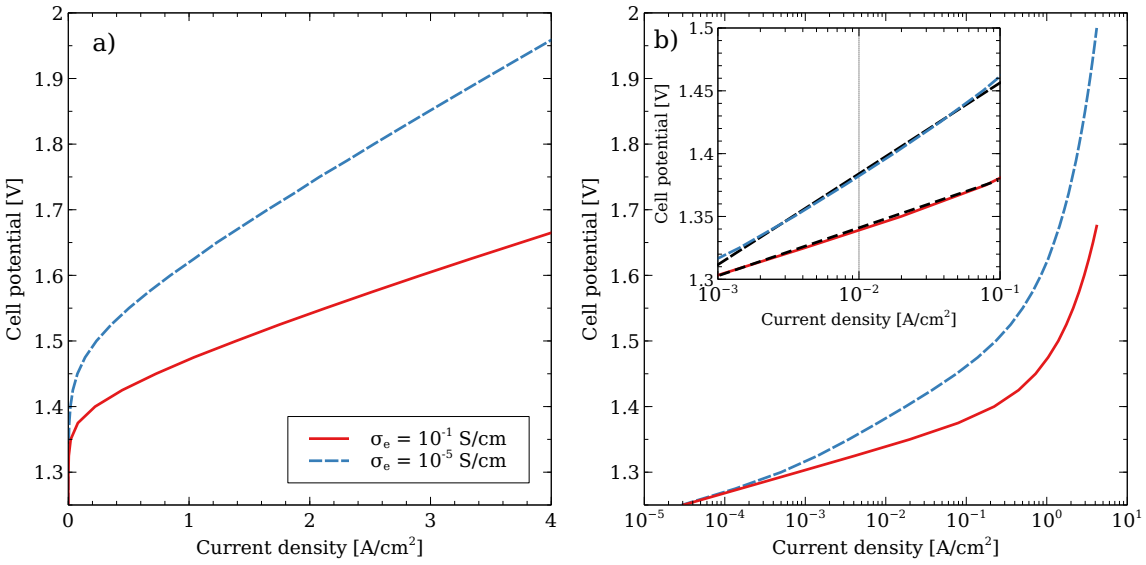

Figure 4.8: Comparison of (a) a polarisation curve, and (b) Tafel plot, obtained numerically for ACLs with high and low conductivities. Inset shows the apparent kinetic region only, i.e. 1-100 mA/cm^2, and reasonable linearity for both curves as indicated by the straight dashed lines.

addition of non-reactive carbon was shown to improve the conductivity of the MoS_2 electrode, thereby altering the measured kinetic parameters. Similarly, Yang et al. [221] used gold nanolayers of varying thicknesses to improve electronic conductivity and showed that Tafel slope was significantly altered by the improved conductivity. Kroschel et al. [120] and Yu et al. [222] have shown how the choice of PTL can affect the Tafel slope or activity measured in the kinetic region, which both attributed the poor ACL electronic conductivity. This discussion shows that very low conductivity ACLs may require analysis at lower current densities in order to mitigate ohmic effects and obtain the true kinetic performance.

4.4.4 Voltage breakdown

Using equations (4.2) and (2.20), the kinetic overpotentials from each reaction and the ohmic losses from each layer can be computed at each current density. The HFR can be estimated by summing the resistance from each layer, besides the two catalyst layers. The contribution to the HFR from the CLs is computed using Equation

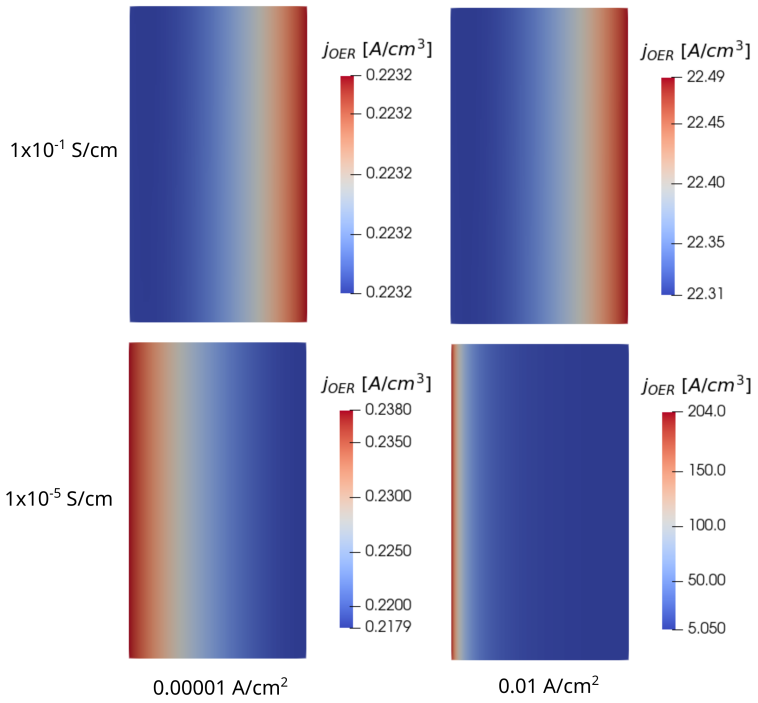

Figure 4.9: OER distributions for (top) high conductivity and (bottom) low conductivity ACLs, at 0.1 mA/cm^2 and 10 mA/cm^2.

(2.19). Figure 4.10 shows the breakdown for the low and high conductivity cases. The voltage loss from the OER is shown, however the losses from the HER are not as they were significantly smaller than the other losses. Also shown are the losses from ohmic resistances, including: both phases in the ACL, the predicted HFR, and the sum of all ohmic losses in every layer, including the PEM and cathode. The OER losses dominate the overall losses in the cell, with higher losses induced for the low conductivity layer. This difference is caused by the very poorly distributed reaction in the case of the low conductivity ACL, essentially reducing the active area available to the OER at current densities above 10 mA/cm^2 as discussed in the previous section.

It is interesting to note the impact of changing only the ACL electronic conductivity on both of the ohmic losses in the ACL. For the high conductivity case, both phases induce minor voltage losses, while significant losses are induced in both phases when the electronic conductivity is reduced. The cause of the increase in both phases

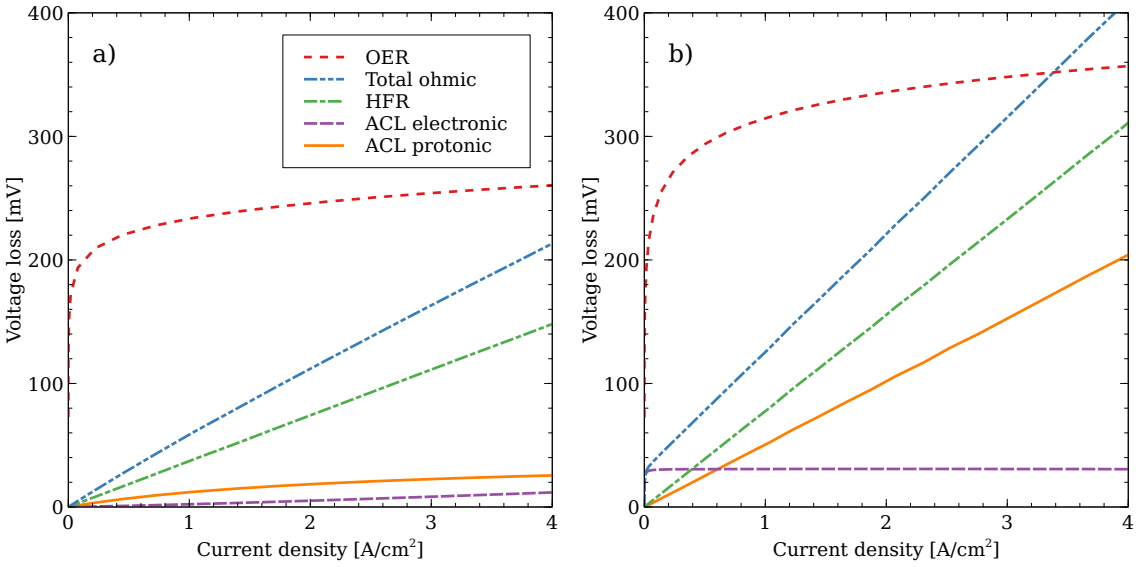

Figure 4.10: Voltage breakdown including OER losses, ohmic losses from the electronic and protonic phase in the ACL, as well as the HFR losses and total ohmic losses from all layers. The electronic conductivity of the ACL is a) $1\text{x}10^{-1}$ S/cm, and b) $1\text{x}10^{-5}$ S/cm.

can be explained by considering the reaction distribution. For the high conductivity case, the electronic conductivity ($1\text{x}10^{-1}$ S/cm) is higher than the protonic ($1\text{x}10^{-2}$ S/cm), causing the reaction to occur closer to the membrane at high current densities. As such the ohmic losses in the protonic phase are minimised, as electrons traverse most of the layer through the relatively conductive electronic phase, inducing minimal losses. With the reduction in the electronic conductivity to $1\text{x}10^{-5}$ S/cm, the reaction distribution will instead be concentrated at the ACL/PTL interface to minimise ohmic losses in the electronic phase. As such, protons are now forced to cross much of the ACL, inducing higher losses through the more resistive ionomer phase.

The ACL electronic phase losses in Figure 4.10 b) exhibit an unusual profile, being seemingly constant for all current densities. Figure 4.11 shows the ACL voltage losses predicted by the MEA simulations and the corresponding resistance (computed using Equation (2.17)) against the current density for the low conductivity case. The electronic losses actually show an exponential increase below 10 mA/cm^2, which corresponds to having a constant ACL resistance of approximately 14 Ωcm^2.

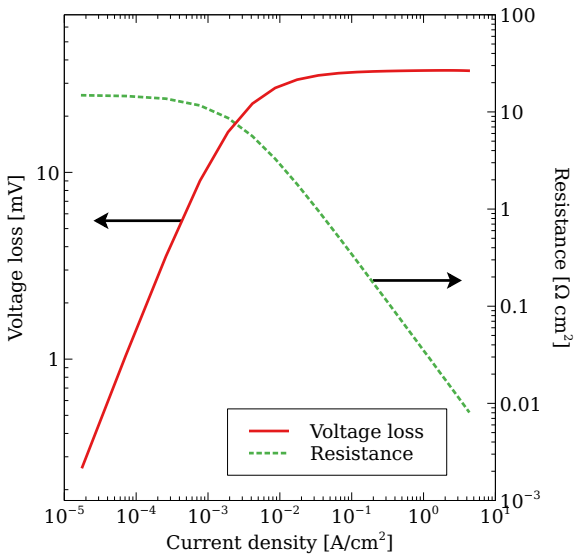

Figure 4.11: Voltage losses from the ACL electronic phase for the low conductivity case, along with its resistance.

This extremely high resistance is only achieved at low current densities when the reaction is uniformly distributed throughout the ACL. At higher current densities, having such a high resistance would induce enormous voltage losses, so the reaction distribution concentrates close to the PTL/ACL interface. This concentration causes the resistance of the ACL to drop exponentially, causing the voltage losses to plateau to a constant value.

It is interesting that the current density and resistance show an exponential relationship, considering that Ohm's Law is a linear function. This trend arises from the exponential nature of the Tafel equation, which controls how quickly the reaction distribution can be concentrated. Any narrowing of the distribution caused by a high ACL resistivity will reduce the active area available to OER, thereby increasing the OER kinetic losses. Therefore the reaction distribution that is induced in a CL is a balance between the kinetic and resistive losses. As the relationship between the active area and the kinetic overpotential is exponential, the trends in Figure 4.11 are also exponential.

Finally, Figure 4.10 shows the voltage losses induced by the ohmic resistance of every layer, including both phases in the ACL and CCL. Comparing these losses to the voltage losses predicted by the HFR shows that there is a significant difference between the two. The HFR is commonly used to characterise the total resistance of the PEMWE cell, particularly in 0-D models used to estimate mass transport losses. The contribution to the HFR from the CLs is given by equation (2.19), and will be constant with changing current density, i.e. it is not affected by the concentration of the reaction distribution by higher current densities, while the resistance of the CL will be. That the HFR is current density independent was confirmed by obtaining EIS spectra at different current densities for the low conductivity case, as shown in Figure 4.12. Note that the HFR may be observed to vary in experiments, e.g. in reference [145], which could be due to changes not captured by this model, e.g. the changing hydration state of the membrane.

The idea that the HFR is representative of the total cell resistance may be reasonable under certain circumstances, e.g. in PEM fuel cells. The high electronic conductivity provided by the carbon support reduces the electronic ohmic losses, and results in the reaction being concentrated at the membrane, thereby minimising protonic ohmic losses. The CCL modelled in this work is similar to those used in PEM fuel cells; the model predicts that the CCL ohmic resistance is approximately 3 $m\Omega.cm^2$, mainly from the protonic phase, while the HFR contribution is dominated by the electronic conductivity and is 0.1 $m\Omega.cm^2$. So while the contribution of the CCL to the total cell resistance is not particularly accurate, the error in omitting the actual resistance of the layer when assuming that the HFR is equal to the total cell resistance is likely to be small. For PEMWE, the assumption that the HFR is representative of total cell resistance is aided by the fact the protonic conductivity is likely higher than that in PEMFC, due to the presence of liquid water. However, that the electronic conductivity of the ACL is significantly lower than that of the carbon support in PEMFC, makes the assumption questionable, as shown by the difference

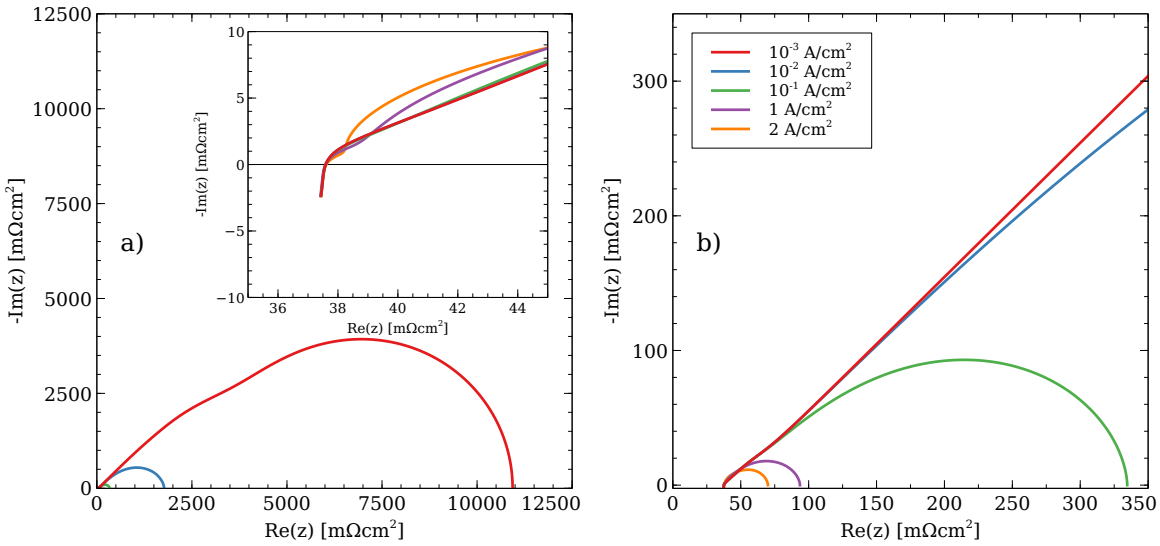

Figure 4.12: Numerically obtained EIS spectra obtained for the low conductivity case at a) low current densities and b) high current densities. The inset shows where the spectra cross the real axis at high frequency.

in the HFR and total cell losses in Figure 4.10, and as discussed by Kosakian et al. [30].

4.4.5 Impact of catalyst loading

The reaction distribution shown in Figure 4.9 for the low conductivity layer suggests that the layer is very poorly utilised for much of the operating current density range, and may allow for a reduction in the catalyst loading. Figure 4.13 shows the predicted impact of a change in the ACL loading with a high and low electronic conductivity. The high conductivity ACL shows the expected trend; there is a stepwise decrease in performance in the low current density region as the loading is reduced. This performance is more obvious in the Tafel plot insets and is due to the lower kinetic performance of the ACL with the reduction in the total electrochemical surface area available for the OER. The performance of each layer converges at higher current densities, as ohmic resistances dominate. As the electronic conductivity is higher than the protonic, the reaction will occur at the membrane interface. Making the ACL thinner will result in the electrons having a shorter path to traverse, reducing

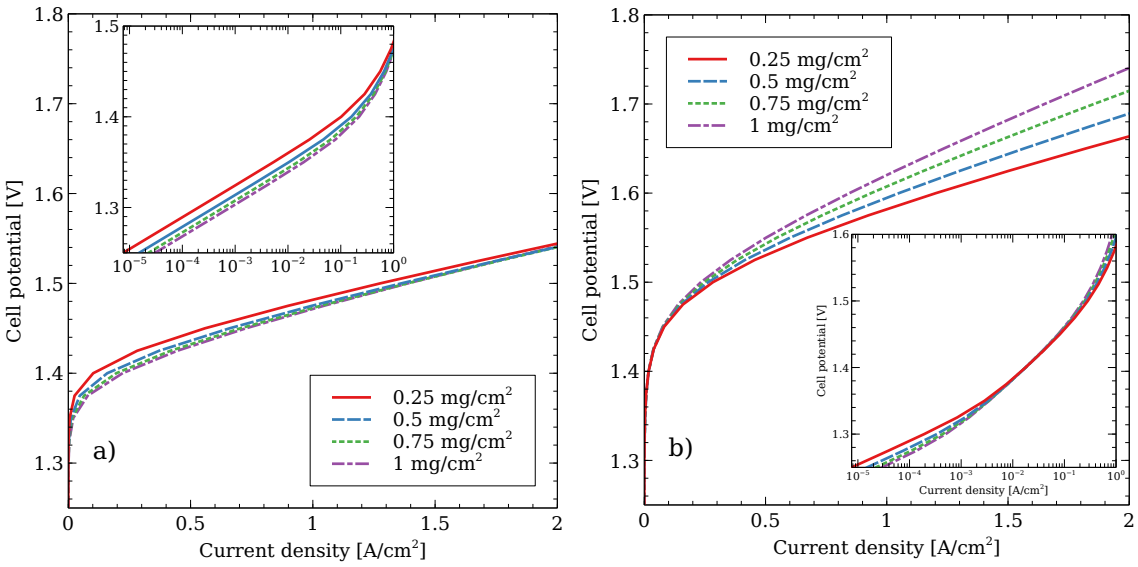

Figure 4.13: Simulated polarisation curves for different loadings using an ACL electronic conductivity a) 0.1 S/cm and b) 10^{-5} S/cm. Insets show the low current density regions.

the ohmic losses.

The low electronic conductivity layer exhibits very different behaviour at low current densities. The performance is very similar on the polarisation curve, and only at current densities less than 1 mA/cm^2 is the expected reduction in performance with reduced loading seen. This effect is again indicative of the limited range of current densities that can be considered kinetically dominated, as discussed in the previous section. At higher current densities, the lowest loaded ACL has the best performance, with a substantially lower slope than the highest loaded ACL. As the electronic conductivity of the ACL is now lower than the protonic, the reaction occurs close to the PTL. Thinning the layer reduces the path length for protons travelling to the membrane. The change in the slope of the polarisation curve at higher current densities with reduced loading is greater for the low conductivity ACL than for the high. In both cases, the thinning of the ACL reduces the path length of the more conductive phase, however the conductivity of that phase is different for each case (low conductivity ACL: protonic phase is more conductive at 1x10^{-2} S/cm, high conductivity

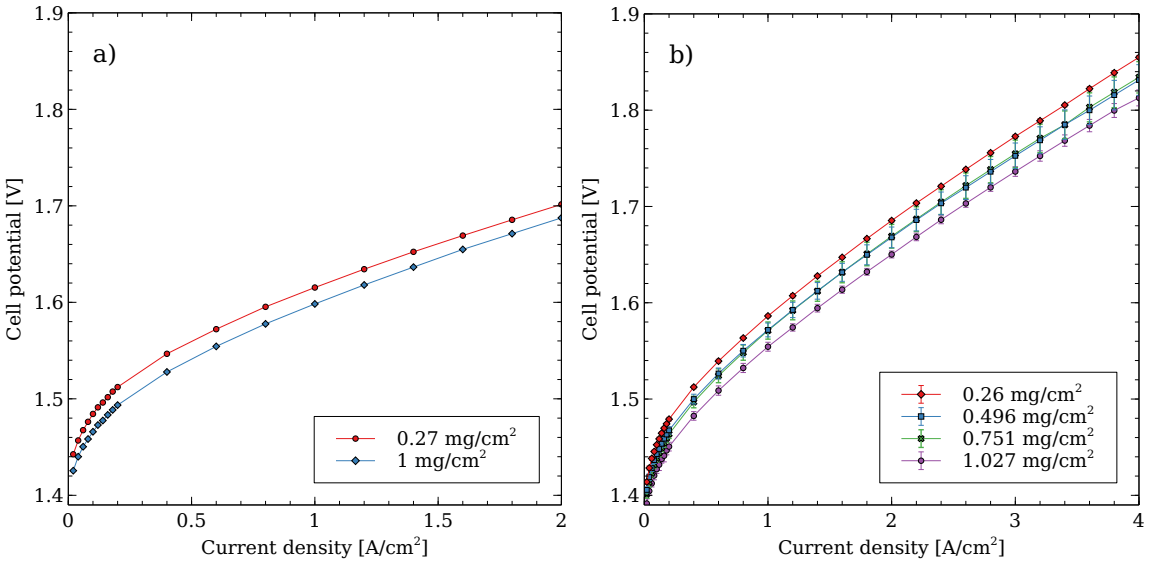

Figure 4.14: Experimental loading study with a) a Umicore Ir and b) a TKK IrOx based ACL.

ACL: electronic phase is more conductive at 1x10^{-1} S/cm). As such the impact of reducing the thickness of the layer is greater for the low conductivity case, as losses through the less conductive protonic phase are minimised. This result indicates that a loading study could be used to assert if the ACL electronic conductivity is limiting.

Figure 4.14 shows experimentally obtained polarisation data for ACLs made with either a Umicore Ir catalyst, or a TKK IrOx catalyst. Note that the simulations were not calibrated to the experimental data. As such the experiments and simulations are not compared directly, with the focus on the trends in performance in the kinetic and ohmic regions. The IrOx catalyst was measured by Mandal et al. [125] to have conductivities of approximately 1x10^{-2} S/cm for the protonic phase, and 1x10^{-5} S/cm for the electronic while the Ir layer had conductivities of 1x10^{-3} S/cm for the protonic phase and 1x10^{-2} S/cm for the electronic. As such, the IrOx layer is similar to the simulated polarisation curves for the low conductivity case, while the Ir catalyst is closer to the high conductivity case. The Ir based ACL displays the expected trends; there is a clear improvement in the polarisation curve in the kinetic region with the increased loading which is maintained through the current density region.

The IrOx catalyst does not show the expected trend and instead is similar to the high conductivity case. However, as discussed in the literature review, there are a number of works that demonstrate the trends for the low conductivity catalyst in Figure 4.13. In particular, the work of Jang et al. [142] showed both a reduction in performance in the ohmic region, and no change in performance in the kinetic region, with increasing catalyst loading, as shown in Figure 4.15 a), which are in line with the model predictions. In addition, Fujita et al. [144] and Rozain et al. [123] found that the performance is constant at low current densities with increasing catalyst loading, as shown in Figure 4.15 b). However in both works, the performance was constant at higher current densities, so the experimental data is only partially in line with the model. The data presented by Fujita et al. and Rozain et al., i.e. cell potential required to reach a certain current density (0.1, 1 or 2 Acm^2) for different ACL loadings, presents a convenient method for assessing the impact of the ACL conductivities on the cell performance. Figure 4.16 shows the predicted performance of the cell with varying ACL loading and electronic conductivity, with the same ACL protonic conductivity of $1x10^{-2}$ S/cm. The results show that an electronic conductivity of at most $1x10^{-4}$ S/cm is required to keep the cell potential constant for loadings above 0.3 mg/cm^2, inline with the results from Fujita et al., again indicating that the electronic conductivity measured by Mandal et al. [125] and this work is not unreasonable.

Figure 4.16 shows that at 2 A/cm^2 the performance is not constant, in contrast to Fujita et al. A voltage breakdown analysis shows that for an ACL electronic conductivity of $1x10^{-5}$ S/cm, the difference in performance of the cell with a loading of 0.25 and 1 mg/cm^2 at the same current density is due to protonic transport through the ACL. As the reaction distribution is focused at the PTL/ACL interface, the thicker layers have a longer transport path for protons. If the distribution is extremely concentrated, then the protons from the OER will have to traverse the entire ACL. As such, the profiles in Figure 4.16 b) could be used to obtain the protonic conductivity

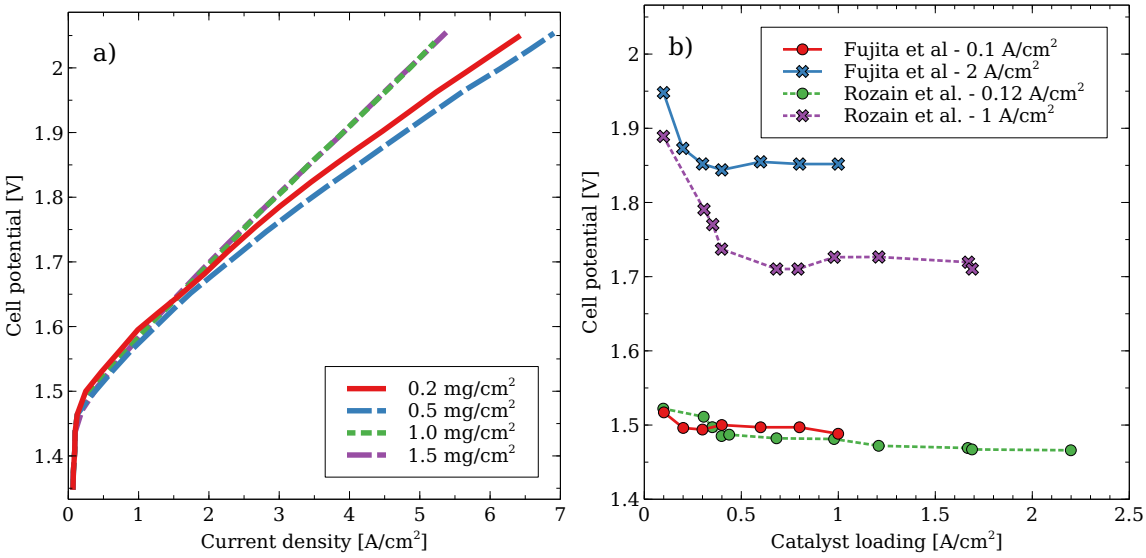

Figure 4.15: a) Loading study using experimental data taken from Jang et al. [142] and b) change in cell potential to reach the current density indicated in the legend with changing ACL loading, using data from references [123, 144].

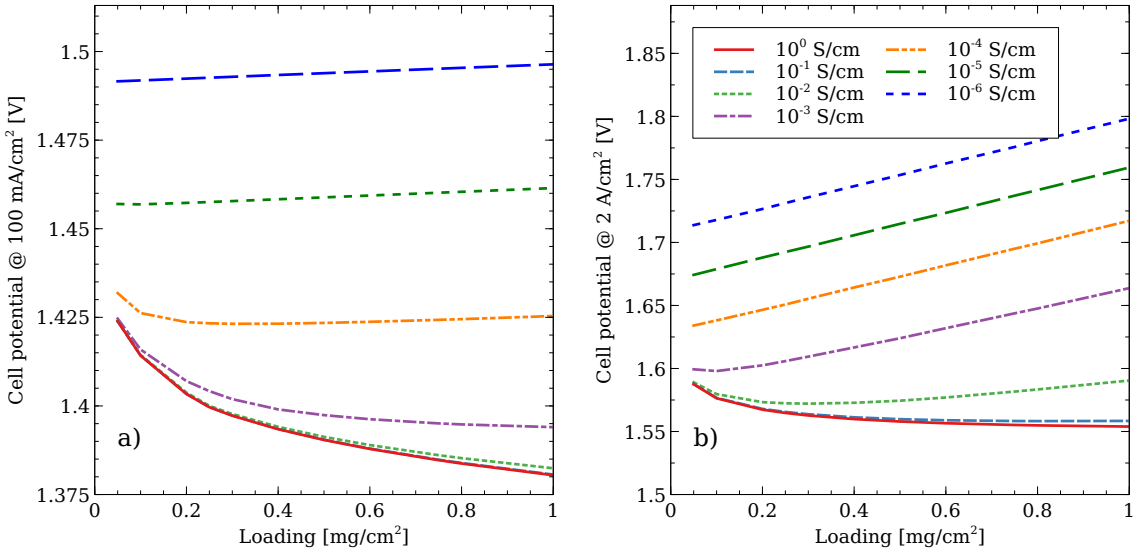

Figure 4.16: Simulated cell potential at a current density of a) 100 mA/cm^2 and b) 2 A/cm^2 for varying ACL catalyst loadings and ACL electronic conductivities. The ACL protonic conductivity is 1x10^{-2} S/cm.

of the ACL. The slope of a curve divided by the current density of 2 A/cm^2 will return the resistivity of the layer, which can be inverted to get the conductivity. This method predicts a protonic conductivity of approximately 0.0105 S/cm for electronic conductivities of 1x10^{-4} S/cm and lower, which is very close to that used in the model. As the reaction distribution becomes less concentrated at 1x10^{-3} S/cm, the predicted value increases to 0.012 S/cm, and the prediction worsens significantly for higher conductivities as the reaction redistributes throughout the ACL. The profiles in Figure 4.16 have not been observed in the literature to date, however most experiments use a fibre or sintered PTL that will cause an uneven contact with the ACL. The thin film PTL used by the group of Zhang [113] may be more suitable to this experiment as a more controlled contact is obtained between the PTL and the ACL.

Figure 4.17 shows the same simulations but with a protonic conductivity of 1x10^{-1} S/cm. The cell potential at 2 A/cm^2 shows significantly less variation with loading for electronic conductivities lower than 1x10^{-3} S/cm, and is more in line with the experimental trends that have been observed in the literature. Such a effective protonic conductivity is close to the conductivity a Nafion membrane, for example Bernt et al. [24] referenced a value of 142 mΩcm^2 as that of a liquid equilibrated N212 for their estimation of the protonic resistance. It is not clear that the effective protonic conductivity of an ACL could be comparable to the bulk value, though it should be noted that the protonic conductivities measured by Mandal et al. were for a hydrogen pump equilibrated with humidified nitrogen and not liquid water.

An alternative method to reduce the proton transport losses is to reduce the thickness of the ACL. The thickness used in this work is based on SEM imaging of the ACL pre- and post-operation, which did not capture localised indentation of the ACL from the fibrous PTL. Post-operation surface SEM imaging can show significant indentation, as shown by Schuler et al. [223] and Mandal et al. [204]. If in-plane electronic conductivity is severely limiting, then the reaction will be mostly concentrated under the contact between the PTL and the ACL, as discussed in Section 4.4.2 and also

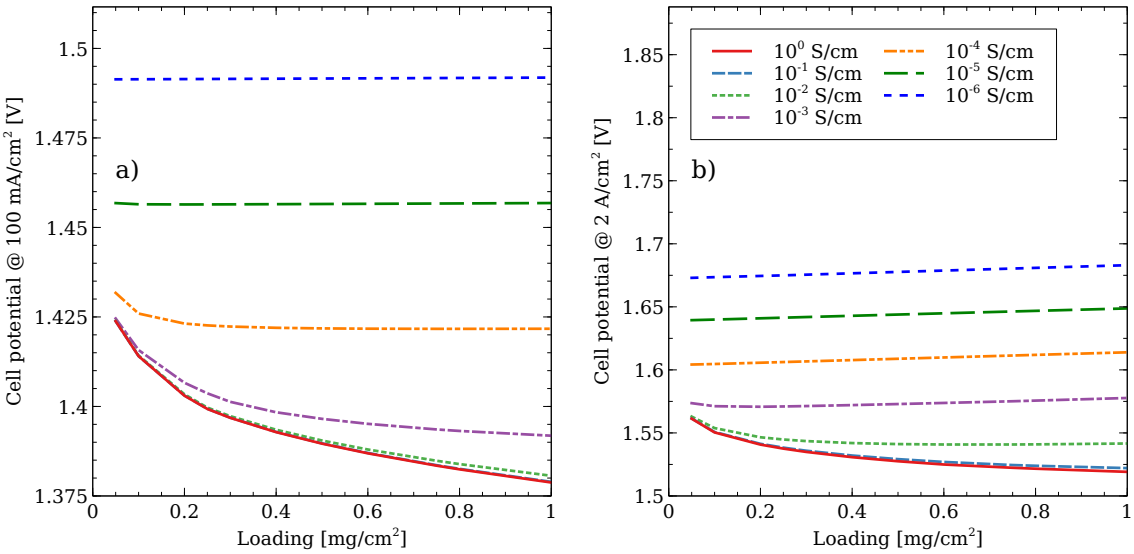

Figure 4.17: Loading dependence on the potential to reach a) 100 mA/cm^2 and b) 2 A/cm^2 for different ACL electronic conductivities, with an ACL protonic conductivity of 1x10^{-1} S/cm.

by Kwen et al. [224]. As such the effective transport length for the protons will be governed by the amount of indentation experienced by the ACL. More research is needed to determine the effective conductivity of the protonic phase in liquid water for these catalyst layers, and the importance of the indentation and the reduced transport path.

4.4.6 Mitigation

It is clear from Figure 4.16 that improving the electronic conductivity of a poorly conducting ACL can induce a significant increase in performance. Methods to assess the potential improvement in performance that can be obtained from improving the electronic conductivity include: a) increasing the compression on the cell, and b) to use an electronically conductive polymer such as PEDOT:PSS. Note that these methods may decrease the durability of the PEMWE cell, so are applied here to assess the beginning of life performance and gain insight into the impact of the low ACL electronic conductivity.

Starting with the impact of the compression, Figure 4.18 shows the cell perfor-

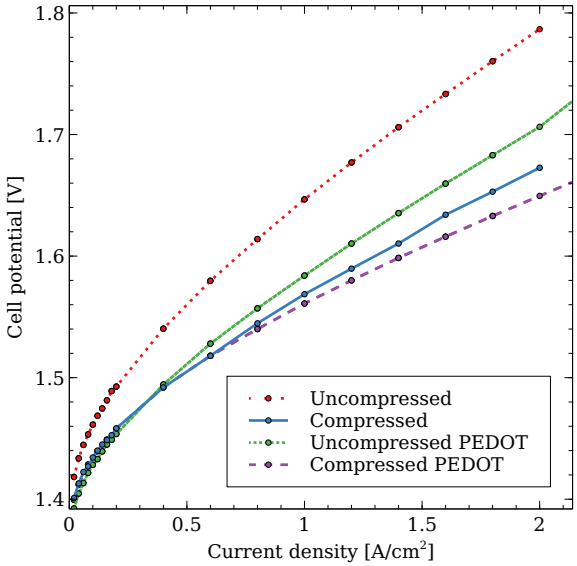

Figure 4.18: Impact of compression and the addition of PEDOT on polarisation curves.

mance when a thin gasket is used (denoted 'Compressed', which corresponds to the experimental results in Figure 4.14 b)), and a thick gasket is used (denoted 'Uncompressed', where there is no pinch on the anode PTL). The actual compression force applied to the ACL is not known in either case. Bernt et al. [24] choose gaskets that resulted in a compression of 25% on the cathode GDL (with no compression applied to the PTL) and estimated the compression force to be 1.7 MPa. The Uncompressed case in this work likely has a compressive force comparable to Bernt et al., with a significantly higher compressive force being applied for the Compressed case. Note that the Compressed case has a slightly lower performance compared to the 1 mg/cm^2 curve in Figure 4.14 b), this is attributed to a change in the ink cartridge used as part of the printing process, which may have resulted in a change in the microstructure of the ACL.

There is a clear decrease in performance when the compression on the cell is reduced. A higher compression is applied with the intent of reducing ohmic losses, and there is a clear reduction in the slope of the polarisation curves in the ohmic

Table 4.2: HFR measured for each case.

Case	HFR [mΩ.cm^2]
Uncompressed, no PEDOT	106
Compressed, no PEDOT	63.5
Uncompressed, with PEDOT	91.8
Compressed, with PEDOT	52.2

region relative to the Uncompressed case. This is confirmed by the measured HFR in Table 4.2. Compressing the cell causes a significant reduction of 43 mΩ.cm^2 in the HFR, which is generally attributed to a reduction in the contact resistance. This term is somewhat vague, and could refer to the contact between a variety of layers. The increased compression could also be reducing the bulk resistance in layers such as the GDL, and the ACL due to the change in conductivity shown in Figure 4.5. If the improvement in the HFR is caused by improved ACL conductivity, then the improvement must be high enough to affect the denominator of equation (2.19). The compression might also reduce the effective thickness of the ACL, as the PTL does imprint onto the ACL, as shown in the SI of reference [204]. It is therefore difficult to determine the primary cause of the improvement in performance from the higher compression, as a number of factors are affected.

The compression also induces a significant increase in performance in the kinetic region. Figure 4.19 a) shows the impact of a higher compression on the Tafel plot: the cell potential of the Compressed cell at 20 mA/cm^2 is 1.4 V, while the cell potential for the Uncompressed cell at 20 mA/cm^2 is approximately 20 mV higher. Figure 4.19 b) shows that compressing the cell causes a significantly higher integrated charge, indicating a higher ECSA. This result demonstrates that at lower compressions, much of the available ECSA in the IrOx ACL is not accessible due to the low ACL electronic conductivity, as has been discussed in the literature. Compressing the cell may allow for a higher ECSA by a combination of: a) increasing the electronic conductivity of

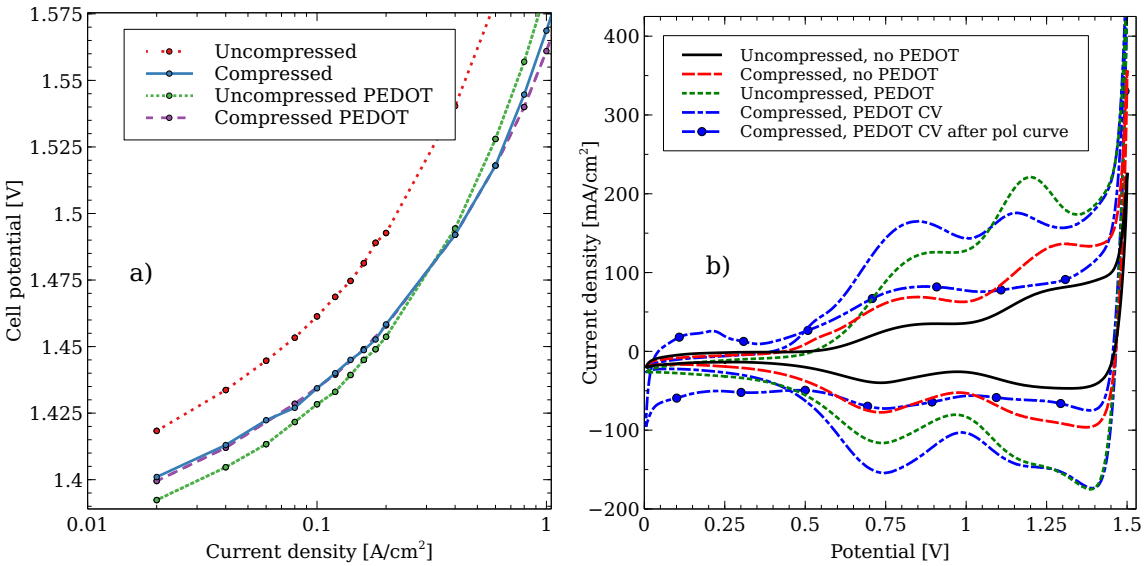

Figure 4.19: (Left) Tafel plots and (right) CVs obtained after conditioning with either a higher compression or the addition of PEDOT. The additional CV for the compressed case with PEDOT was obtained after the polarisation curve.

the ACL under the contact points, thereby improving the reaction distribution in the through plane direction, and b) allowing for a larger contact area between the ACL and PTL as the ACL is pushed into the PTL pore space, bringing secondary PTL fibres into contact. Note that the increase in the voltammagram is achieved at current densities that are lower than 100 mA/cm^2, again demonstrating the very low conductivity of the IrOx ACL.

It is clear that compressing the cell can result in a significant improvement in cell performance, which has also been demonstrated in the literature, as discussed in Chapter 1. However it is not clear whether the Uncompressed or Compressed case is more representative of the compression used in the literature, as most works do not report the compression. The Uncompressed case is likely comparable to Bernt et al. as discussed, and to Suermann et al. [165] who used a cell compression of 2.5 MPa. Kim et al. [166] used a pinch of 15% on both PTL and GDL, while Lee et al. [66] used a 240 μm gasket on 250 μm Ti sintered PTLs on the anode and cathode. These cells are also likely closer to the Uncompressed case, as the compressed case in this

work used a 140 μm gasket on a 250 μm PTL on the anode.

Relative to the Uncompressed case, the addition of the PEDOT has a similar impact to compressing the cell, there is a significant improvement in the kinetic and ohmic regions, giving a much higher performance for the Uncompressed PEDOT cell. The ohmic resistance in the polarisation curve is reduced compared to the Uncompressed case, though not to the same extent as the Compressed case. The HFR is decreased by only approximately 14 mΩ.cm^2, compared to the 43 mΩ.cm^2 improvement from the higher compression. The PEDOT might not be increasing the ACL conductivity to the same extent that the compression is, and will not reduce the ACL thickness. The PEDOT loading in this work was much lower than the Nafion loading, so it may be possible to further improve the layer conductivity and further reduce the HFR with higher PEDOT loadings. However the fact that the addition of the PEDOT affected the HFR shows that the ACL does in fact contribute to the HFR. This further implies that the highest conductivity in the denominator of Equation (2.19) is quite low. To obtain a HFR from a 4 μm thick CL of 14 mΩ.cm^2, the sum of the conductivities needs to be of the order of 10^{-2} S/cm. This value would therefore be an upper bound of the electronic conductivity of the ACL in the cell.

The PEDOT will also improve electronic transport in the in-plane direction of the ACL, increasing the ECSA. This is reflected in the Tafel plot, where the PEDOT cell has the highest performance at the lowest current densities. The CV for the cell with PEDOT shows a much larger voltammagram compared to the Compressed cell, suggesting that there are significant sections of the ACL that are inaccessible without PEDOT, even under high compressions. The utilisation of the ACL is therefore very low, so there is the possibility of the Compressed case to have a higher performance still. This assumes that the PEDOT is not contributing to the measured current density and only serves to better connect the catalyst. In contrast to the applying higher compression, adding PEDOT to the ACL should only affect the electronic conductivity of the ACL. As such there is less ambiguity when determining the cause

of performance. Therefore, adding electronically conducting polymers to the ACL might be a useful method to study the impact of poor ACL electronic conductivity on PEMWE performance. The gains in performance are impressive, however the durability of such polymers in the harsh environment in the ACL has not been proven.

The final case tested was an ACL with PEDOT with the same compression as the Compressed case. The best performance is obtained with this arrangement, though the performance is similar to the high compression case without PEDOT. The HFR is the lowest, at 52.2 $m\Omega.cm^2$, meaning that the HFR has halved from the Uncompressed case without PEDOT. It is interesting to note that a similar reduction in HFR is achieved with the addition of PEDOT or with a higher compression, i.e. compressing the cell induces an approximately 40 $m\Omega.cm^2$ reduction either with or without PEDOT, while adding PEDOT reduces the HFR by about 14 $m\Omega.cm^2$ with a high or low compression. This again suggests that the PEDOT does not cause the electronic conductivity to be significantly higher than the protonic conductivity. Figure 4.5 shows that higher compression is not enough for the electronic conductivity to be higher than the protonic conductivity, however it is likely to reduce the effective thickness of the ACL and reduce the resistance of other layers. The CV of the compressed cell with PEDOT exhibits a similar integrated charge to the uncompressed case with PEDOT suggesting that the addition of the PEDOT raises the conductivity enough to access all of the ACL. An additional CV is shown for this case, obtained after the polarisation curve had been obtained. The integrated area has been reduced, which may indicate that the PEDOT is not stable under the conditions in the anode. The CV for the Uncompressed case with PEDOT also exhibited a reduction in the area with later CVs, but not as much as the compressed case. In addition, the CV appears to exhibit underpotentially deposited hydrogen which is not shown in any other cases. Oxidised Ir typically does not exhibit a H_{upd} region, which must therefore be attributed to the PEDOT. The activity of electronically conducting polymers has been demonstrated in the literature, as discussed in the review from Kumaravel et al.

[225], however an in-depth discussion is beyond the scope of this work.

4.5 Conclusions

In this work, the impact of having a low ACL electronic conductivity on performance was studied, both numerically and experimentally. First, the extremely low conductivities that were measured by Mandal et al. [125] were verified experimentally using a new ex-situ measurement technique that allowed for the impact of compression on the measured conductivity to be studied. The conductivities measured in this work, at the highest allowable compression, were slightly lower than Mandal et al., however the setup used was limited in how much compression could be applied to the ACL. In addition, the conductivity decreased by over two orders of magnitude at close to zero compression. This result implies that any part of the ACL that is not in direct contact with the PTL in a PEMWE cell will be electronically isolated, as was observed experimentally by Mo et al. [113].

Numerical modelling was performed to verify that the ACL needs to have a very low conductivity to explain experimental observations. In particular, the model was used to reproduce the results from Mo et al. who observed no reaction occurring in the centre of a 50 μm pore at 2 A/cm^2, using a transparent flow field and a thin Ti, perforated film. The model suggests that conductivities below 0.1 mS/cm are required to reduce the current produced under the pore to less than 1% of the total current density, again confirming that the extremely low conductivities measured in this work and by Mandal et al. are not unreasonable. Visualisation of predicted reaction distribution shows that current is extremely localised for low ACL conductivities, in both the in-plane and through plane directions.

PEMWE MEAs with ACLs of varying electronic conductivity were simulated in order to get further insights into how the electronic conductivity impacts cell performance. The study revealed a significant drop in performance with decreasing electronic conductivity, in both the ohmic and the apparent kinetic region. Tafel

plots showed that the actual kinetic region (i.e., where there were no ohmic effects) of the low conductivity ACL occurred for current densities lower than 1 mA/cm^2. Experimental studies rarely use such low current densities to determine the kinetic performance of their catalyst, which may result in the ACL being mischaracterised. Furthermore, the model shows that the Tafel plot for the low conductivity ACL is still approximately linear between 1-100 mA/cm^2 despite significant ohmic transport effects being present, which may falsely lead experimenters to conclude that the performance is purely kinetic in this region.

The MEA model was used to generate voltage breakdowns, thereby deconvoluting the losses from the reaction kinetics and the ohmic resistance of each individual layer. The low ACL electronic conductivity would induce enormous losses if not for the reaction distribution becoming very localised at the PTL/ACL interface. As such, protons have to traverse much of the ACL, inducing high ohmic losses. If the electronic conductivity is improved to the point that it is higher than the protonic, there is a significant improvement in performance as the reaction instead occurs close to the membrane, thereby minimising losses from proton transport through the ACL. The voltage breakdown also shows that the losses from the HFR can be very different to the total ohmic losses. The HFR does not contain exactly the ohmic losses from the CLs, causing the discrepancy. As such, care should be taken when using the HFR to characterise the total resistance of a PEMWE cell. 0-D models based on the HFR and kinetic parameters obtained between 1-100 mA/cm^2 are commonly used in the literature, particularly when assessing mass transport losses in PEMWE. If the ACL is as poorly conducting as the IrOx studied in this work, then this method will be quite inaccurate. As such it is recommended that the ACL electronic conductivity be measured before applying the method.

The localised reaction distribution in the through plane direction allows for the possibility of reducing the loading of low conductivity ACLs. The model predicts that if the loading of such an ACL is reduced there will be little change in the

apparent kinetic region on the polarisation curve. There will also be a reduction in the ohmic resistance of the ACL, as the proton transport path is reduced, leading to an improved performance at high current densities for lower loadings. The model demonstrates that this trend can be used to obtain the protonic conductivity of the ACL. An experimental loading study performed in-house did not show either trend, i.e. a constant performance at low current densities and the improved performance at higher current density with lower loadings, which may be due to the ACL conductivity being higher than that simulated due to the compression exerted on the ACL. However there are loading studies in the literature than exhibit one or both of these trends. The reason why the data obtained in-house did not match the model, while literature data did, is not known. Possible reasons include a higher than expected protonic conductivity in the ACL or the thinning of the ACL from the indentation of the PTL into the ACL. Future research that can bridge this gap would be very useful in understanding how to reduce the iridium loadings in PEMWE, which is a crucial step to further commercialising the technology.

To experimentally test our hypothesis that the electronic conductivity can have a large effect on cell performance, two experimental approaches were identified: a) reduce the cell compression, and b) the addition of an electronically conducting polymer to the ACL. Higher compressions and the addition of PEDOT were found to significantly improve the cell performance: the potential at 2 A/cm^2 is 140 mV lower for a compressed cell with PEDOT in the ACL, compared to one with a low compression and no PEDOT. Both methods were found to reduce the HFR of the cell and increase the ECSA, resulting in improved performance in both the kinetic and ohmic regions. Increasing the compression can affect a number of factors in the cell, however adding PEDOT to the ACL should only impact the ACL itself. As such, its addition to the ACL may be a useful method for assessing the impact of low electronic conductivity in the ACL.

Chapter 5

Conclusions and future work

5.1 Conclusions

This thesis focused on understanding phenomena occurring within the anode catalyst layer of PEM water electrolysers, which was identified as a key limiting component to the performance of electrolyser cells. As these layers are of the order of a few microns and difficult to study experimentally, numerical modelling was used to gain insights into the ACL processes, allowing for the future design and optimisation of the layers. Simulations were performed using an in-house developed finite element solver, in both 2-D and 3-D, at steady-state to study cell performance, and in transient to study EIS spectra. The electrolyser model was used to study the effect of the low electronic conductivity of the ACL on the reaction distribution. The model was also used to study the impact of the two-phase flow on performance, and provide insights into the impact of ACL microstructure and conductivity on gas accumulation. In addition to studying PEM electrolysis, a hydrogen pump was also simulated, as it is used to measure the protonic conductivity of CLs used in electrolysis. The study focused on validating the method and understanding which CLs could be accurately characterised using the technique.

As this work was focused on charge transport in the ACL, accurately measuring the conductivity of both phases was of particular importance. The hydrogen pump technique was used to measure the protonic conductivity of CLs. This work stud-

ied the reactive pathway, in which protons transport across the CL is bypassed via the hydrogen reaction, both numerically and experimentally for the first time in the literature. Numerical simulations of the hydrogen pump were carried with CLs that are active and inactive to the hydrogen reaction, which revealed the conditions under which the reactive pathway would occur. In addition to being active, the CLs must also have a reasonably high electronic conductivity. The simulations showed that Pt/C and Ir black based CLs are both active and conductive enough for the reactive pathway to almost entirely bypass the protonic phase. On the other hand, unplatinised carbon based CLs had no activity, and IrOx CLs were both too inactive and non-conducting to allow for the reactive pathway, so their protonic conductivity could be measured. These numerical results were validated experimentally, proving for the first time the presence of the reactive pathway. Furthermore, it was found that the experimentally obtained polarisation data could be misinterpreted due to the interfacial contact resistance between the CL and the membranes. Numerical simulations showed that the HFR of the cell with and without a conductive IL should not change, thereby providing a method to estimate the ICR, correct the polarisation data and accurately measure the CL protonic resistance. The numerical model was used to study impedance spectra and was compared to analytical modelling in the literature. The AC method was studied to quantify its accuracy; the model showed that the additional resistance of the anode and cathode of the hydrogen pump could affect the measured conductivity. These resistances were quantified using the model and subtracted from the experimental data to obtain a conductivity that showed close agreement with that measured using the ICR method.

In addition to charge transport limitations, the impact of mass transport in PEMWE is not well understood and was studied in this work. Two-phase flow was captured using the Darcy equation, while the microstructure was described using a PSD model. The study focused on mass transport in PEMWE cells that included Ir and IrOx ACLs, whose measured electronic and protonic conductivities suggest reaction distri-

butions that would be more active on opposite sides of the ACL. A thorough validation process was used, in which the kinetics of the OER were captured by using a multistep kinetic model that accounted for the ACL conductivities, and the HFR was matched in addition to the polarisation curve. The model predicted that it is extremely difficult to displace water from the ACL, as the hydrophilic pores are of the order of tens of nanometres, requiring gas pressures of several bar. These pressures were predicted to be generated in the Ir ACL, as the OER occurs close to the membrane, forcing the bubbles to traverse the entire ACL to escape. In contrast, the OER will occur close to the PTL in the IrOx ACL and therefore can easily escape to the PTL. Due to the difference in PSD between the PTL and ACL, it was noted that the saturation in one was only weakly coupled to the other, meaning that PTL saturations might not be a reliable indicator of the saturation in the ACL. A qualifier was presented, namely that this numerical model uses a volume averaged approach that does not allow for discrete phenomena to be captured, e.g. a large gas bubble at the interface between the ACL and PTL. It is suggested that experimental studies that attempt to visualise bubble formation focus on the ACL-PTL interface to understand mass transport limitations in PEMWE.

Finally, the impact of the low electronic conductivity of the ACL on cell performance was studied. The extremely low conductivity of the IrOx ACL was measured experimentally, and validated a prior measurement by our group. The setup also allowed for the impact of compression on the ACL to be assessed for the first time in the literature. The measurement showed that the conductivity dropped by two orders of magnitude at close to zero compression, demonstrating the importance of direct contact between the ACL and PTL. In addition, the compression dependence suggests that cell compression could be used to mitigate the poor electronic conductivity of these layers. To further ensure that the electronic conductivity was extremely low, 3-D numerical simulations of the etched thin film Ti PTLs used by Zhang group were performed. They observed no bubble formation in 50 μm pores at current densities

of 2 A/cm^2, which the model predicted required electronic conductivities lower than 1x10^{-4} S/cm, again confirming that PEMWE ACLs can have an extremely low electronic conductivity. Next, MEA simulations were carried out to study the impact of low ACL electronic conductivity on performance. The simulations showed that significant ohmic resistances were induced at the low current densities (less than 100 mA/cm^2) typically used to obtain Tafel parameters. Also shown was that these Tafel plots can still appear linear despite the ohmic resistance, resulting in a false confidence in the method and significant inaccuracies in the estimated Tafel parameters. Voltage breakdowns also revealed that the HFR did not include the electronic resistance of the ACL, which could be significant. As such, the use of 0-D models that are based on the HFR and Tafel parameters could be problematic. The model also predicted that the loading of low conductivity ACLs could be reduced and lead to an increase in performance, as the utilisation of thick layers is very low and have a long proton transport path. This trend was not seen in in-house experimental data, but was observed in the literature. Finally, the conductivity of the ACL was shown to be improved by increasing cell compression and adding electronically conductive polymers. Both methods reduced the HFR and increased the ECSA, showing that the ohmic resistance was affecting the catalyst utilisation.

5.1.1 Contributions

The numerical models used in this work were developed in an open source simulation software, OpenFCST, and will be made available for future use by other researchers, along with working examples and tutorials on their use. The contributions of this work to the field of electrochemical modelling include:

1. the development of a generic framework within OpenFCST to allow for the simulation of systems other than fuel cells, including water electrolysis and hydrogen pumps, in acidic or alkaline media. In addition, more than one reaction in an electrode can be studied, allowing for simulations to study crossover or

dissolution in PEMFCs for example.

2. the development of a hydrogen pump MEA model that can be used to study the protonic conductivity measurement, or electrochemical hydrogen pumps

3. the application of the PSD model to water electrolysis simulations to allow for the impact of microstructure on mass transport to be assessed

The contributions of this work to the field of the PEM water electrolysis and hydrogen pumps include:

1. demonstrating the existence of the reactive pathway the IL of a hydrogen pump that is being used to measure its protonic conductivity, and how the IL activity and electronic conductivity influence the accuracy of the measurement

2. analysis of the impact of mass transport limitations on PEMWE performance while accounting for varying reaction distributions and PSDs

3. assessing the impact of the low ACL electronic conductivity on PEMWE performance, including ex-situ conductivity measurements, voltage loss breakdowns and mitigation strategies

Two journal articles have been published based on the work presented in this thesis [226, 227], with another in preparation [228]. In addition, a numerical study on hydrogen crossover in PEM fuel cells has been published [194] that is not part of this work.

5.2 Future work

The hydrogen pump model developed in Chapter 2 could be further refined by explicitly including the contact resistance between the catalyst layers and the membrane, so that the experimental data does not need to be adjusted. Qi et al. [155] compared the CL protonic conductivity measured using the hydrogen pump technique

and using hydrogen/nitrogen EIS and noted the discrepancy between the two. The numerical model used in this work could be used to predict conductivity using the hydrogen pump, in conjunction with the transient framework developed by Kosakian et al. [30] to predict the conductivity obtained from hydrogen/nitrogen EIS. The variations in percolating ionomer network discussed by Qi et al. could be simulated using both approaches to provide insights into the discrepancy. Finally, the hydrogen pump model captures hydrogen and sorbed water transport, despite not being crucial to the prediction of the protonic conductivity. This additionality allows for the model to be applied to electrochemical hydrogen compression, an ongoing area of research [229, 230].

The main outcome from the mass transport limitation study in Chapter 3 was that the macro-homogeneous model cannot induce significant transport limitations. Therefore any limitations are likely caused by discrete events like the formation of a large bubble at the ACL/PTL interface. Future experimental studies using neutron or x-ray imaging [159, 178, 231], or novel PTLs with in-situ visualisation [232], should focus on characterising the bubbles that form at the interface, with numerical modelling being performed at the pore scale to assess how these bubbles reduce cell performance. The numerical model was limited by the lack of experimental characterisation of the ACL microstructure. Measurements of the PSD and hydrophilicity of the layer are needed to improve the model predictions of two-phase flow, along with conductivity measurements to ensure the reaction distribution is properly captured. Simulation of ACLs similar to the Ir ACL studied in this work would help understand the gas pressure buildup and the volcano-like cracks that were seen in surface SEMs. Furthermore, the gas pressure buildup in the ACL may help to explain the increased oxygen crossover with increasing current density measured by Trinke et al. [215]; there may be a link between reaction distribution and the increased crossover that could be studied numerically. This work also neglected the pressure buildup in the cathode; again Trinke et al. [233] noted that the hydrogen crossover increased with

increasing current density, which could be explored in a similar manner to the oxygen crossover.

Finally, Chapter 4 focused on the impact of having a low electronic conductivity in the ACL and there are a number of areas for future research. The impact of compression on the electronic conductivity should be further explored: higher compressions should be applied during the ex-situ measurement to understand how high the conductivity will increase under realistic cell construction. The compression felt by different parts of the ACL in a PEMWE cell should be measured to understand the resulting variations in conductivity and the resulting impact on performance. This work noted the potential for significant inaccuracies when applying the 0-D model to PEMWE polarisation data; further research is needed to understand the errors that the 0-D model induces when applied to cells with different ACLs. Such a study would require the protonic and electronic conductivities of various ACLs to be measured along with the kinetic parameters, so that the performance can be simulated with the model from this work and compared to the 0-D model.

This work also predicted that the IrOx loading could be reduced without impacting performance; this trend was not seen in in-house experimental data, but was observed in the literature. Understanding why the loading could be reduced in one case but not the other will be crucial to achieving low loadings. Finally, the impact of compression and the application of electronically conducting polymers in improving performance was demonstrated. Understanding the former was discussed already, however applying the XTM techniques demonstrated in references [127, 223, 234, 235] to determine the interfacial surface areas could be augmented by compression studies to better understand how the contact between the PTL and ACL changes with compression. The use of electronically conductivity polymers has been shown to significantly improve performance, however the durability of the polymers is yet to be demonstrated in the harsh conditions of the ACL. However, even if these polymers are not durable, they may be useful for beginning of life studies to assess how impactful ACL electron

transport is for different PEMWE constructions.

Bibliography

[1] Z. Zhongming, L. Linong, Y. Xiaona, Z. Wangqiang, L. Wei, *et al.*, "AR6 synthesis report: Climate change 2022," 2022.

[2] S. Bouckaert, A. F. Pales, C. McGlade, U. Remme, B. Wanner, L. Varro, D. D'Ambrosio, and T. Spencer, "Net zero by 2050: A roadmap for the global energy sector," 2021.

[3] I. P. on Climate Change, "Global warming of 1.5°C: An IPCC special report on the impacts of global warming of 1.5° c above pre-industrial levels and related global greenhouse gas emission pathways, in the context of strengthening the global response to the threat of climate change, sustainable development, and efforts to eradicate poverty," Tech. Rep., 2018.

[4] N. Brandon and Z Kurban, "Clean energy and the hydrogen economy," *Philosophical Transactions of the Royal Society A: Mathematical, Physical and Engineering Sciences*, vol. 375, no. 2098, p. 20 160 400, 2017.

[5] K. E. Ayers, E. B. Anderson, C. Capuano, B. Carter, L. Dalton, G. Hanlon, J. Manco, and M. Niedzwiecki, "Research advances towards low cost, high efficiency PEM electrolysis," *ECS transactions*, vol. 33, no. 1, p. 3, 2010.

[6] U. Babic, M. Suermann, F. N. Büchi, L. Gubler, and T. J. Schmidt, "Critical review-identifying critical gaps for polymer electrolyte water electrolysis development," *Journal of The Electrochemical Society*, vol. 164, no. 4, F387–F399, 2017.

[7] M. Carmo, D. L. Fritz, J. Mergel, and D. Stolten, "A comprehensive review on PEM water electrolysis," *International journal of hydrogen energy*, vol. 38, no. 12, pp. 4901–4934, 2013.

[8] Q. Feng, X. Yuan, G. Liu, B. Wei, Z. Zhang, H. Li, and H. Wang, "A review of proton exchange membrane water electrolysis on degradation mechanisms and mitigation strategies," *Journal of Power Sources*, vol. 366, pp. 33 –55, 2017. DOI: https://doi.org/10.1016/j.jpowsour.2017.09.006.

[9] A. Buttler and H. Spliethoff, "Current status of water electrolysis for energy storage, grid balancing and sector coupling via power-to-gas and power-to-liquids: A review," *Renewable and Sustainable Energy Reviews*, vol. 82, pp. 2440–2454, 2018.

[10] A. Godula-Jopek, *Hydrogen production: by electrolysis*. John Wiley & Sons, 2015.

[11] H. A. Miller, K. Bouzek, J. Hnat, S. Loos, C. I. Bernäcker, T. Weißgärber, L. Röntzsch, and J. Meier-Haack, "Green hydrogen from anion exchange membrane water electrolysis: A review of recent developments in critical materials and operating conditions," *Sustainable Energy & Fuels*, vol. 4, no. 5, pp. 2114–2133, 2020.

[12] T. Gül, U. Remme, and J. M. B. Menendez, "Global hydrogen review 2022," *International Energy Agency*, 2022.

[13] E. Taibi, H. Blanco, R. Miranda, and M. Carmo, "Green hydrogen cost reduction: Scaling up electrolysers to meet the 1.5c climate goal," *International Renewable Energy Agency*, 2020.

[14] P. Millet, "9 - hydrogen production by polymer electrolyte membrane water electrolysis," in *Compendium of Hydrogen Energy*, ser. Woodhead Publishing Series in Energy, V. Subramani, A. Basile, and T. N. Veziroğlu, Eds., Oxford: Woodhead Publishing, 2015, pp. 255 –286. DOI: https://doi.org/10.1016/B978-1-78242-361-4.00009-1.

[15] D. Bessarabov, A. Kruger, S. M. Luopa, J. Park, A. A. Molnar, and K. A. Lewinski, "Gas crossover mitigation in PEM water electrolysis: Hydrogen cross-over benchmark study of 3M's Ir-NSTF based electrolysis catalyst-coated membranes," *ECS Transactions*, vol. 75, no. 14, pp. 1165–1173, 2016. DOI: 10.1149/07514.1165ecst.

[16] P. Shirvanian and F. van Berkel, "Novel components in proton exchange membrane water electrolyzers (PEMWE): Status, challenges and future needs," *Electrochemistry Communications*, p. 106 704, 2020. DOI: https://doi.org/10.1016/j.elecom.2020.106704.

[17] K. Ayers, "The potential of proton exchange membrane–based electrolysis technology," *Current Opinion in Electrochemistry*, vol. 18, pp. 9 –15, 2019. DOI: https://doi.org/10.1016/j.coelec.2019.08.008.

[18] M. Clapp, C. M. Zalitis, and M. Ryan, "Perspectives on current and future iridium demand and iridium oxide catalysts for PEM water electrolysis," *Catalysis Today*, vol. 420, p. 114 140, 2023.

[19] U.S. Department of Energy, *Hydrogen shot*. [Online]. Available: https://www.energy.gov/eere/fuelcells/hydrogen-shot.

[20] B. S. Pivovar, M. F. Ruth, D. J. Myers, and H. N. Dinh, "Hydrogen: Targeting $1/kg in 1 decade," *The Electrochemical Society Interface*, vol. 30, no. 4, p. 61, 2021.

[21] A. J. Bard and L. R. Faulkner, *Electrochemical methods: fundamentals and applications*. wiley New York, vol. 2.

[22] M. Suermann, T. J. Schmidt, and F. N. Büchi, "Investigation of mass transport losses in polymer electrolyte electrolysis cells," *ECS Transactions*, vol. 69, no. 17, pp. 1141–1148, 2015. DOI: 10.1149/06917.1141ecst.

[23] B.-S. Lee, H.-Y. Park, I. Choi, M. K. Cho, H.-J. Kim, S. J. Yoo, D. Henkensmeier, J. Y. Kim, S. W. Nam, S. Park, K.-Y. Lee, and J. H. Jang, "Polarization characteristics of a low catalyst loading PEM water electrolyzer operating at elevated temperature," *Journal of Power Sources*, vol. 309, pp. 127 –134, 2016. DOI: https://doi.org/10.1016/j.jpowsour.2015.12.139.

[24] M. Bernt and H. A. Gasteiger, "Influence of ionomer content in IrO2/TiO2electrodes on PEM water electrolyzer performance," *Journal of The Electrochemical Society*, vol. 163, no. 11, F3179–F3189, 2016. DOI: 10.1149/2.0231611jes.

[25] *Porous Transport Layer Related Mass Transport Losses in Polymer Electrolyte Membrane Electrolysis: A Review*, vol. ASME 2016 14th International Conference on Nanochannels, Microchannels, and Minichannels, International Conference on Nanochannels, Microchannels, and Minichannels, Jul. 2016. DOI: 10.1115/ICNMM2016-7974.

[26] X.-Z. R. Yuan, C. Song, H. Wang, and J. Zhang, *Electrochemical impedance spectroscopy in PEM fuel cells: fundamentals and applications*, 420. Springer Science & Business Media, 2010, vol. 13.

[27] H. Wang, X.-Z. Yuan, and H. Li, *PEM fuel cell diagnostic tools*. CRC press, 2011.

[28] R. O'Hayre, S.-W. Cha, W. Colella, and F. B. Prinz, *Fuel cell fundamentals*. John Wiley & Sons, 2016.

[29] A Kosakian, L. P. Urbina, A Heaman, and M Secanell, "Understanding single-phase water-management signatures in fuel-cell impedance spectra: A numerical study," *Electrochimica Acta*, p. 136 204, 2020.

[30] A. Kosakian and M. Secanell, "Estimating charge-transport properties of fuel-cell and electrolyzer catalyst layers via electrochemical impedance spectroscopy," *Electrochimica Acta*, vol. 367, p. 137 521, 2021.

[31] B. Bensmann and R. Hanke-Rauschenbach, "(Invited) engineering modeling of PEM water electrolysis: A survey," *ECS Transactions*, vol. 75, no. 14, pp. 1065–1072, 2016. DOI: 10.1149/07514.1065ecst.

[32] D. Falcão and A. Pinto, "A review on PEM electrolyzer modelling: Guidelines for beginners," *Journal of cleaner production*, vol. 261, p. 121 184, 2020.

[33] F. Aouali, M. Becherif, H. Ramadan, M. Emziane, A. Khellaf, and K. Mohammedi, "Analytical modelling and experimental validation of proton exchange membrane electrolyser for hydrogen production," *International Journal of Hydrogen Energy*, vol. 42, no. 2, pp. 1366 –1374, 2017. DOI: https://doi.org/10.1016/j.ijhydene.2016.03.101.

[34] A. Awasthi, K. Scott, and S. Basu, "Dynamic modeling and simulation of a proton exchange membrane electrolyzer for hydrogen production," *International Journal of Hydrogen Energy*, vol. 36, no. 22, pp. 14779 –14 786, 2011. DOI: https://doi.org/10.1016/j.ijhydene.2011.03.045.

[35] C. Biaku, N. Dale, M. Mann, H. Salehfar, A. Peters, and T. Han, "A semiempirical study of the temperature dependence of the anode charge transfer coefficient of a 6kW PEM electrolyzer," *International Journal of Hydrogen Energy*, vol. 33, no. 16, pp. 4247 –4254, 2008. DOI: https://doi.org/10.1016/j.ijhydene.2008.06.006.

[36] P. Choi, D. G. Bessarabov, and R. Datta, "A simple model for solid polymer electrolyte (SPE) water electrolysis," *Solid State Ionics*, vol. 175, no. 1, pp. 535 –539, 2004. DOI: https://doi.org/10.1016/j.ssi.2004.01.076.

[37] N. Dale, M. Mann, and H Salehfar, "Semiempirical model based on thermodynamic principles for determining 6kw proton exchange membrane electrolyzer stack characteristics," *Journal of Power Sources*, vol. 185, no. 2, pp. 1348–1353, 2008.

[38] D. Fritz, J. Mergel, and D. Stolten, "PEM electrolysis simulation and validation," 19, vol. 58, 2014, pp. 1–9. DOI: 10.1149/05819.0001ecst.

[39] R. García-Valverde, N. Espinosa, and A. Urbina, "Simple PEM water electrolyser model and experimental validation," *International Journal of Hydrogen Energy*, vol. 37, no. 2, pp. 1927 –1938, 2012. DOI: https://doi.org/10.1016/j.ijhydene.2011.09.027.

[40] B. Han, S. M. Steen, J. Mo, and F.-Y. Zhang, "Electrochemical performance modeling of a proton exchange membrane electrolyzer cell for hydrogen energy," *International Journal of Hydrogen Energy*, vol. 40, no. 22, pp. 7006 – 7016, 2015. DOI: https://doi.org/10.1016/j.ijhydene.2015.03.164.

[41] V. Liso, G. Savoia, S. S. Araya, G. Cinti, and S. K. Kær, "Modelling and experimental analysis of a polymer electrolyte membrane water electrolysis cell at different operating temperatures," *Energies*, vol. 11, no. 12, p. 3273, 2018.

[42] F. Marangio, M. Santarelli, and M. Calì, "Theoretical model and experimental analysis of a high pressure PEM water electrolyser for hydrogen production," *International Journal of Hydrogen Energy*, vol. 34, no. 3, pp. 1143 –1158, 2009. DOI: https://doi.org/10.1016/j.ijhydene.2008.11.083.

[43] M. Suermann, T. J. Schmidt, and F. N. Büchi, "Cell performance determining parameters in high pressure water electrolysis," *Electrochimica Acta*, vol. 211, pp. 989 –997, 2016. DOI: https://doi.org/10.1016/j.electacta.2016.06.120.

[44] A. Tugirumubano, H.-J. Shin, S.-H. Go, M.-S. Lee, L. K. Kwac, and H.-G. Kim, "Electrochemical performance analysis of a PEM water electrolysis with cathode feed mode based on flow passage shape of titanium plates," *International Journal of Precision Engineering and Manufacturing*, vol. 17, no. 8, pp. 1073–1078, 2016. DOI: 10.1007/s12541-016-0130-9.

[45] J. Garcia-Navarro, M. Schulze, and K. Friedrich, "Measuring and modeling mass transport losses in proton exchange membrane water electrolyzers using electrochemical impedance spectroscopy," *Journal of Power Sources*, vol. 431, pp. 189–204, 2019. DOI: 10.1016/j.jpowsour.2019.05.027.

[46] R Garcia-Valverde, C Miguel, R Martínez-Béjar, and A Urbina, "Optimized photovoltaic generator–water electrolyser coupling through a controlled dc–dc converter," *International Journal of Hydrogen Energy*, vol. 33, no. 20, pp. 5352–5362, 2008.

[47] M. Espinosa-López, C. Darras, P. Poggi, R. Glises, P. Baucour, A. Rakotondrainibe, S. Besse, and P. Serre-Combe, "Modelling and experimental validation of a 46 kW PEM high pressure water electrolyzer," *Renewable Energy*, vol. 119, pp. 160 –173, 2018. DOI: https://doi.org/10.1016/j.renene.2017.11.081.

[48] H. Görgün, "Dynamic modelling of a proton exchange membrane (PEM) electrolyzer," *International journal of hydrogen energy*, vol. 31, no. 1, pp. 29–38, 2006.

[49] M. Lebbal and S. Lecœuche, "Identification and monitoring of a PEM electrolyser based on dynamical modelling," *International journal of hydrogen energy*, vol. 34, no. 14, pp. 5992–5999, 2009.

[50] M. Santarelli, P Medina, and M Cali, "Fitting regression model and experimental validation for a high-pressure PEM electrolyzer," *International Journal of Hydrogen Energy*, vol. 34, no. 6, pp. 2519–2530, 2009.

[51] J. Li, Y. Zhu, W. Chen, Z. Lu, J. Xu, A. Pei, Y. Peng, X. Zheng, Z. Zhang, S. Chu, *et al.*, "Breathing-mimicking electrocatalysis for oxygen evolution and reduction," *Joule*, vol. 3, no. 2, pp. 557–569, 2019.

[52] J. Kai, R. Saito, K. Terabaru, H. Li, H. Nakajima, and K. Ito, "Effect of temperature on the performance of polymer electrolyte membrane water electrolysis: Numerical analysis of electrolysis voltage considering gas/liquid two-phase flow," *Journal of The Electrochemical Society*, vol. 166, no. 4, F246–F254, 2019. DOI: 10.1149/2.0521904jes.

[53] A. Nouri-Khorasani, E. T. Ojong, T. Smolinka, and D. P. Wilkinson, "Model of oxygen bubbles and performance impact in the porous transport layer of PEM water electrolysis cells," *International journal of hydrogen energy*, vol. 42, no. 48, pp. 28 665–28 680, 2017.

[54] M. Schalenbach, G. Tjarks, M. Carmo, W. Lueke, M. Mueller, and D. Stolten, "Acidic or alkaline? Towards a new perspective on the efficiency of water electrolysis," *Journal of the Electrochemical Society*, vol. 163, no. 11, F3197–F3208, 2016. DOI: 10.1149/2.0271611jes.

[55] S. Grigoriev, P. Millet, S. Volobuev, and V. Fateev, "Optimization of porous current collectors for PEM water electrolysers," *International Journal of Hydrogen Energy*, vol. 34, no. 11, pp. 4968 –4973, 2009. DOI: https://doi.org/10.1016/j.ijhydene.2008.11.056.

[56] M. Sartory, E. Wallnöfer-Ogris, P. Salman, T. Fellinger, M. Justl, A. Trattner, and M. Klell, "Theoretical and experimental analysis of an asymmetric high pressure PEM water electrolyser up to 155 bar," *International Journal of Hydrogen Energy*, vol. 42, no. 52, pp. 30493 –30 508, 2017. DOI: https://doi.org/10.1016/j.ijhydene.2017.10.112.

[57] F Aubras, J Deseure, J.-J. Kadjo, I Dedigama, J Majasan, B Grondin-Perez, J.-P. Chabriat, and D. Brett, "Two-dimensional model of low-pressure PEM electrolyser: Two-phase flow regime, electrochemical modelling and experimental validation," *International Journal of Hydrogen Energy*, vol. 42, no. 42, pp. 26 203–26 216, 2017.

[58] M. Chandesris, V. Médeau, N. Guillet, S. Chelghoum, D. Thoby, and F. Fouda-Onana, "Membrane degradation in PEM water electrolyzer: Numerical modeling and experimental evidence of the influence of temperature and current density," *International Journal of Hydrogen Energy*, vol. 40, no. 3, pp. 1353 –1366, 2015. DOI: https://doi.org/10.1016/j.ijhydene.2014.11.111.

[59] D. Ferrero and M. Santarelli, "Investigation of a novel concept for hydrogen production by PEM water electrolysis integrated with multi-junction solar cells," *Energy Conversion and Management*, vol. 148, pp. 16 –29, 2017. DOI: https://doi.org/10.1016/j.enconman.2017.05.059.

[60] S. Grigoriev and A. Kalinnikov, "Mathematical modeling and experimental study of the performance of PEM water electrolysis cell with different loadings of platinum metals in electrocatalytic layers," *International Journal of Hydrogen Energy*, vol. 42, no. 3, pp. 1590 –1597, 2017. DOI: https://doi.org/10.1016/j.ijhydene.2016.09.058.

[61] B. Han, J. Mo, Z. Kang, and F.-Y. Zhang, "Effects of membrane electrode assembly properties on two-phase transport and performance in proton exchange membrane electrolyzer cells," *Electrochimica Acta*, vol. 188, pp. 317–326, 2016.

[62] B. Han, J. Mo, Z. Kang, G. Yang, W. Barnhill, and F.-Y. Zhang, "Modeling of two-phase transport in proton exchange membrane electrolyzer cells for hydrogen energy," *International Journal of Hydrogen Energy*, vol. 42, no. 7, pp. 4478–4489, 2017.

[63] S. Katukota, J. Nie, Y. Chen, R. Boehm, and H.-T. Hsieh, "Numerical modeling of electrochemical process for hydrogen production from PEM electrolyzer cell," 2007, pp. 31–38. DOI: 10.1115/ES2007-36108.

[64] M. Kaya and N. Demir, "Numerical investigation of PEM water electrolysis performance for different oxygen evolution electrocatalysts," *Fuel Cells*, vol. 17, no. 1, pp. 37–47, 2017. DOI: 10.1002/fuce.201600216.

[65] H. Kim, M. Park, and K. S. Lee, "One-dimensional dynamic modeling of a high-pressure water electrolysis system for hydrogen production," *International Journal of Hydrogen Energy*, vol. 38, no. 6, pp. 2596–2609, 2013.

[66] C. Lee, J. Lee, B. Zhao, K. Fahy, J. LaManna, E. Baltic, D. Hussey, D. Jacobson, V. Schulz, and A. Bazylak, "Temperature-dependent gas accumulation in polymer electrolyte membrane electrolyzer porous transport layers," *Journal of Power Sources*, vol. 446, p. 227 312, 2020. DOI: https://doi.org/10.1016/j.jpowsour.2019.227312.

[67] M. Ni, M. Leung, and D. Leung, "Electrochemistry modeling of proton exchange membrane (PEM) water electrolysis for hydrogen production," vol. 1, 2006, pp. 33–39.

[68] E. T. Ojong, J. T. H. Kwan, A. Nouri-Khorasani, A. Bonakdarpour, D. P. Wilkinson, and T. Smolinka, "Development of an experimentally validated semi-empirical fully-coupled performance model of a PEM electrolysis cell with a 3-d structured porous transport layer," *International Journal of Hydrogen Energy*, vol. 42, no. 41, pp. 25831 –25 847, 2017. DOI: https://doi.org/10.1016/j.ijhydene.2017.08.183.

[69] A. C. Olesen, S. H. Frensch, and S. K. Kær, "Towards uniformly distributed heat, mass and charge: A flow field design study for high pressure and high current density operation of pem electrolysis cells," *Electrochimica acta*, vol. 293, pp. 476–495, 2019.

[70] L. F. L. Oliveira, C. Jallut, and A. A. Franco, "A multiscale physical model of a polymer electrolyte membrane water electrolyzer," *Electrochimica Acta*, vol. 110, no. Supplement C, pp. 363 –374, 2013. DOI: https://doi.org/10.1016/j.electacta.2013.07.214.

[71] S. Qu, G. Chen, J. Duan, W. Wang, and J. Li, "Computational fluid dynamics study on the anode feed solid polymer electrolyte water electrolysis," *Korean Journal of Chemical Engineering*, vol. 34, no. 6, pp. 1630–1637, 2017. DOI: 10.1007/s11814-017-0094-1.

[72] S. Toghyani, E. Afshari, E. Baniasadi, S. Atyabi, and G. Naterer, "Thermal and electrochemical performance assessment of a high temperature PEM electrolyzer," *Energy*, vol. 152, pp. 237 –246, 2018. DOI: https://doi.org/10.1016/j.energy.2018.03.140.

[73] Y. Wang, Y. Pang, H. Xu, A. Martinez, and K. S. Chen, "PEM fuel cell and electrolysis cell technologies and hydrogen infrastructure development: A review," *Energy & Environmental Science*, 2022.

[74] S. Grigoriev, V. Fateev, D. Bessarabov, and P Millet, "Current status, research trends, and challenges in water electrolysis science and technology," *International Journal of Hydrogen Energy*, vol. 45, no. 49, pp. 26 036–26 058, 2020.

[75] A. Eftekhari, "Electrocatalysts for hydrogen evolution reaction," *International Journal of Hydrogen Energy*, vol. 42, no. 16, pp. 11053 –11 077, 2017. DOI: https://doi.org/10.1016/j.ijhydene.2017.02.125.

[76] H. Wang and L. Gao, "Recent developments in electrochemical hydrogen evolution reaction," *Current Opinion in Electrochemistry*, vol. 7, pp. 7–14, 2018.

[77] J. Hughes, J Clipsham, H Chavushoglu, S. Rowley-Neale, and C. Banks, "Polymer electrolyte electrolysis: A review of the activity and stability of non-precious metal hydrogen evolution reaction and oxygen evolution reaction catalysts," *Renewable and Sustainable Energy Reviews*, vol. 139, p. 110 709, 2021.

[78] M. Tavares, S. Machado, and L. Mazo, "Study of hydrogen evolution reaction in acid medium on pt microelectrodes," *Electrochimica Acta*, vol. 46, no. 28, pp. 4359 –4369, 2001. DOI: https://doi.org/10.1016/S0013-4686(01)00726-5.

[79] C. Zalitis, J Sharman, E Wright, and A. Kucernak, "Properties of the hydrogen oxidation reaction on Pt/C catalysts at optimised high mass transport conditions and its relevance to the anode reaction in pefcs and cathode reactions in electrolysers," *Electrochimica Acta*, vol. 176, pp. 763–776, 2015.

[80] J. Durst, C. Simon, F. Hasche, and H. Gasteiger, "Hydrogen oxidation and evolution reaction kinetics on carbon supported Pt, Ir, Rh, and Pd electrocatalysts in acidic media," *Journal of the Electrochemical Society*, vol. 162, no. 1, F190–F203, 2015. DOI: 10.1149/2.0981501jes.

[81] J. X. Wang, T. E. Springer, and R. R. Adzic, "Dual-pathway kinetic equation for the hydrogen oxidation reaction on pt electrodes," *Journal of the Electrochemical Society*, vol. 153, no. 9, A1732–A1740, 2006.

[82] J. X. Wang, T. E. Springer, P. Liu, M. Shao, and R. R. Adzic, "Hydrogen oxidation reaction on Pt in acidic media: Adsorption isotherm and activation free energies," *The Journal of Physical Chemistry C*, vol. 111, no. 33, pp. 12 425–12 433, 2007.

[83] K. Elbert, J. Hu, Z. Ma, Y. Zhang, G. Chen, W. An, P. Liu, H. S. Isaacs, R. R. Adzic, and J. X. Wang, "Elucidating hydrogen oxidation/evolution kinetics in base and acid by enhanced activities at the optimized Pt shell thickness on the Ru core," *ACS Catalysis*, vol. 5, no. 11, pp. 6764–6772, 2015.

[84] P. Quaino, M. G. De Chialvo, and A. Chialvo, "Hydrogen electrode reaction: A complete kinetic description," *Electrochimica acta*, vol. 52, no. 25, pp. 7396–7403, 2007.

[85] S. A. Vilekar, I. Fishtik, and R. Datta, "Kinetics of the hydrogen electrode reaction," *Journal of The Electrochemical Society*, vol. 157, no. 7, B1040–B1050, 2010. DOI: 10.1149/1.3385391.

[86] A. R. Kucernak and C. Zalitis, "General models for the electrochemical hydrogen oxidation and hydrogen evolution reactions: Theoretical derivation and experimental results under near mass-transport free conditions," *The Journal of Physical Chemistry C*, vol. 120, no. 20, pp. 10 721–10 745, 2016. DOI: 10.1021/acs.jpcc.6b00011.

[87] E. Fabbri, A. Habereder, K. Waltar, R. Kötz, and T. J. Schmidt, "Developments and perspectives of oxide-based catalysts for the oxygen evolution reaction," *Catalysis Science & Technology*, vol. 4, no. 11, pp. 3800–3821, 2014.

[88] T. Reier, H. Nong, D. Teschner, R. Schlögl, and P. Strasser, "Electrocatalytic oxygen evolution reaction in acidic environments – reaction mechanisms and catalysts," *Advanced Energy Materials*, vol. 7, no. 1, 2017. DOI: 10.1002/aenm.201601275.

[89] F. M. Sapountzi, J. M. Gracia, C. K.-J. Weststrate, H. O. Fredriksson, and J. H. Niemantsverdriet, "Electrocatalysts for the generation of hydrogen, oxygen and synthesis gas," *Progress in Energy and Combustion Science*, vol. 58, no. Supplement C, pp. 1 –35, 2017. DOI: https://doi.org/10.1016/j.pecs.2016.09.001.

[90] H. Wu, Y. Wang, Z. Shi, X. Wang, J. Yang, M. Xiao, J. Ge, W. Xing, and C. Liu, "Recent developments of iridium-based catalysts for oxygen evolution reaction in acidic water electrolysis," *Journal of Materials Chemistry A*, 2022.

[91] C. Fu, T. O'Carroll, S. Shen, L. Luo, J. Zhang, H. Xu, and G. Wu, "Metallic-Ir-based anode catalysts in PEM water electrolyzers: Achievements, challenges, and perspectives," *Current Opinion in Electrochemistry*, p. 101 227, 2023.

[92] S. Song, H. Zhang, X. Ma, Z. Shao, R. T. Baker, and B. Yi, "Electrochemical investigation of electrocatalysts for the oxygen evolution reaction in PEM water electrolyzers," *International Journal of Hydrogen Energy*, vol. 33, no. 19, pp. 4955 –4961, 2008. DOI: https://doi.org/10.1016/j.ijhydene.2008.06.039.

[93] S. Cherevko, S. Geiger, O. Kasian, N. Kulyk, J.-P. Grote, A. Savan, B. R. Shrestha, S. Merzlikin, B. Breitbach, A. Ludwig, *et al.*, "Oxygen and hydrogen evolution reactions on Ru, RuO2, Ir, and IrO2 thin film electrodes in acidic and alkaline electrolytes: A comparative study on activity and stability," *Catalysis Today*, vol. 262, pp. 170–180, 2016.

[94] Y. Lee, J. Suntivich, K. J. May, E. E. Perry, and Y. Shao-Horn, "Synthesis and activities of rutile IrO2 and RuO2 nanoparticles for oxygen evolution in acid and alkaline solutions," *The Journal of Physical Chemistry Letters*, vol. 3, no. 3, pp. 399–404, 2012. DOI: 10.1021/jz2016507.

[95] S. Siracusano, N. V. Dijk, E. Payne-Johnson, V. Baglio, and A. Aricò, "Nano-sized IrOx and IrRuOx electrocatalysts for the O2 evolution reaction in PEM water electrolysers," *Applied Catalysis B: Environmental*, vol. 164, pp. 488 – 495, 2015. DOI: https://doi.org/10.1016/j.apcatb.2014.09.005.

[96] F Andolfatto, R Durand, A Michas, P Millet, and P Stevens, "Solid polymer electrolyte water electrolysis: Electrocatalysis and long-term stability," *International Journal of Hydrogen Energy*, vol. 19, no. 5, pp. 421–427, 1994.

[97] J. Ahmed and Y. Mao, "Ultrafine iridium oxide nanorods synthesized by molten salt method toward electrocatalytic oxygen and hydrogen evolution reactions," *Electrochimica Acta*, vol. 212, pp. 686–693, 2016.

[98] X. Tan, J. Shen, N. Semagina, and M. Secanell, "Decoupling structure-sensitive deactivation mechanisms of Ir/IrOx electrocatalysts toward oxygen evolution reaction," *Journal of Catalysis*, vol. 371, pp. 57 –70, 2019. DOI: https://doi.org/10.1016/j.jcat.2019.01.018.

[99] C. Rozain, E. Mayousse, N. Guillet, and P. Millet, "Influence of iridium oxide loadings on the performance of PEM water electrolysis cells: Part II – advanced oxygen electrodes," *Applied Catalysis B: Environmental*, vol. 182, pp. 123 – 131, 2016. DOI: https://doi.org/10.1016/j.apcatb.2015.09.011.

[100] V. K. Puthiyapura, M. Mamlouk, S. Pasupathi, B. G. Pollet, and K. Scott, "Physical and electrochemical evaluation of ATO supported IrO2 catalyst for proton exchange membrane water electrolyser," *Journal of Power Sources*, vol. 269, pp. 451 –460, 2014. DOI: https://doi.org/10.1016/j.jpowsour.2014.06.078.

[101] E. Rasten, G. Hagen, and R. Tunold, "Electrocatalysis in water electrolysis with solid polymer electrolyte," *Electrochimica Acta*, vol. 48, no. 25, pp. 3945 –3952, 2003. DOI: https://doi.org/10.1016/j.electacta.2003.04.001.

[102] Z. Taie, X. Peng, D. Kulkarni, I. V. Zenyuk, A. Z. Weber, C. Hagen, and N. Danilovic, "Pathway to complete energy sector decarbonization with available iridium resources using ultralow loaded water electrolyzers," *ACS Applied Materials & Interfaces*, vol. 12, no. 47, pp. 52 701–52 712, 2020.

[103] T. Binninger, R. Mohamed, K. Waltar, E. Fabbri, P. Levecque, R. Kötz, and T. J. Schmidt, "Thermodynamic explanation of the universal correlation between oxygen evolution activity and corrosion of oxide catalysts," *Scientific reports*, vol. 5, p. 12 167, 2015.

[104] O. Kasian, J.-P. Grote, S. Geiger, S. Cherevko, and K. Mayrhofer, "The common intermediates of oxygen evolution and dissolution reactions during water electrolysis on iridium," *Angewandte Chemie - International Edition*, vol. 57, no. 9, pp. 2488–2491, 2018. DOI: 10.1002/anie.201709652.

[105] G. Hu, J. Fan, S. Chen, Y. Liu, and K. Cen, "Three-dimensional numerical analysis of proton exchange membrane fuel cells (PEMFCs) with conventional and interdigitated flow fields," *Journal of Power Sources*, vol. 136, no. 1, pp. 1–9, 2004.

[106] Z. Ma, Y. Zhang, S. Liu, W. Xu, L. Wu, Y.-C. Hsieh, P. Liu, Y. Zhu, K. Sasaki, J. N. Renner, K. E. Ayers, R. R. Adzic, and J. X. Wang, "Reaction mechanism for oxygen evolution on RuO2, IrO2, and RuO2@IrO2 core-shell nanocatalysts," *Journal of Electroanalytical Chemistry*, 2017. DOI: https://doi.org/10.1016/j.jelechem.2017.10.062.

[107] L. F. L. Oliveira, S. Laref, E. Mayousse, C. Jallut, and A. A. Franco, "A multiscale physical model for the transient analysis of PEM water electrolyzer anodes," *Phys. Chem. Chem. Phys.*, vol. 14, pp. 10 215–10 224, 29 2012. DOI: 10.1039/C2CP23300B.

[108] D. A. García-Osorio, R. Jaimes, J. Vazquez-Arenas, R. H. Lara, and J. Alvarez-Ramirez, "The kinetic parameters of the oxygen evolution reaction (OER) calculated on inactive anodes via EIS transfer functions: •OH formation," *Journal of The Electrochemical Society*, vol. 164, no. 11, E3321–E3328, 2017. DOI: 10.1149/2.0321711jes.

[109] J. X. Wang, J. Zhang, and R. R. Adzic, "Double-trap kinetic equation for the oxygen reduction reaction on Pt (111) in acidic media," *The Journal of Physical Chemistry A*, vol. 111, no. 49, pp. 12 702–12 710, 2007.

[110] J. A. Wrubel, Z. Kang, L. Witteman, F.-Y. Zhang, Z. Ma, and G. Bender, "Mathematical modeling of novel porous transport layer architectures for proton exchange membrane electrolysis cells," *International Journal of Hydrogen Energy*, 2021.

[111] A. Kusoglu and A. Z. Weber, "New insights into perfluorinated sulfonic-acid ionomers," *Chemical reviews*, vol. 117, no. 3, pp. 987–1104, 2017. DOI: https://doi.org/10.1021/acs.chemrev.6b00159.

[112] M Bernt, C Schramm, J Schröter, C Gebauer, J Byrknes, C Eickes, and H. Gasteiger, "Effect of the IrOx conductivity on the anode electrode/porous transport layer interfacial resistance in pem water electrolyzers," *Journal of The Electrochemical Society*, vol. 168, no. 8, p. 084 513, 2021.

[113] J. Mo, Z. Kang, S. T. Retterer, D. A. Cullen, T. J. Toops, J. B. Green, M. M. Mench, and F.-Y. Zhang, "Discovery of true electrochemical reactions for ultrahigh catalyst mass activity in water splitting," *Science advances*, vol. 2, no. 11, e1600690, 2016.

[114] Z. Kang, J. Mo, G. Yang, Y. Li, D. A. Talley, B. Han, and F.-Y. Zhang, "Performance modeling and current mapping of proton exchange membrane electrolyzer cells with novel thin/tunable liquid/gas diffusion layers," *Electrochimica Acta*, vol. 255, pp. 405 –416, 2017. DOI: https://doi.org/10.1016/j.electacta.2017.09.170.

[115] Z. Kang, J. Mo, G. Yang, S. T. Retterer, D. A. Cullen, T. J. Toops, J. B. Green Jr, M. M. Mench, and F.-Y. Zhang, "Investigation of thin/well-tunable liquid/gas diffusion layers exhibiting superior multifunctional performance in low-temperature electrolytic water splitting," *Energy & Environmental Science*, vol. 10, no. 1, pp. 166–175, 2017.

[116] J. Mo, Z. Kang, G. Yang, Y. Li, S. T. Retterer, D. A. Cullen, T. J. Toops, G. Bender, B. S. Pivovar, J. B. Green Jr, *et al.*, "In situ investigation on ultrafast oxygen evolution reactions of water splitting in proton exchange membrane electrolyzer cells," *Journal of Materials Chemistry A*, vol. 5, no. 35, pp. 18 469–18 475, 2017.

[117] J. Mo, G. Yang, Y. Li, Z. Kang, G. Bender, B. S. Pivovar, J. B. Green Jr, and F.-Y. Zhang, "Experimental studies on the effects of sheet resistance and wettability of catalyst layer on electro-catalytic activities for oxygen evolution reaction in proton exchange membrane electrolysis cells," *International Journal of Hydrogen Energy*, vol. 45, no. 51, pp. 26 595–26 603, 2020.

[118] W. Wang, S. Yu, K. Li, L. Ding, Z. Xie, Y. Li, G. Yang, D. A. Cullen, H. Yu, Z. Kang, *et al.*, "Insights into the rapid two-phase transport dynamics in different structured porous transport layers of water electrolyzers through high-speed visualization," *Journal of Power Sources*, vol. 516, p. 230 641, 2021.

[119] F. Karimi and B. A. Peppley, "Metal carbide and oxide supports for iridium-based oxygen evolution reaction electrocatalysts for polymer-electrolyte-membrane water electrolysis," *Electrochimica Acta*, vol. 246, pp. 654–670, 2017. DOI: https://doi.org/10.1016/j.electacta.2017.06.048.

[120] M. Kroschel, A. Bonakdarpour, J. T. H. Kwan, P. Strasser, and D. P. Wilkinson, "Analysis of oxygen evolving catalyst coated membranes with different current collectors using a new modified rotating disk electrode technique," *Electrochimica Acta*, vol. 317, pp. 722–736, 2019.

[121] S. M. Alia, B. Rasimick, C. Ngo, K. Neyerlin, S. S. Kocha, S. Pylypenko, H. Xu, and B. S. Pivovar, "Activity and durability of iridium nanoparticles in the oxygen evolution reaction," *Journal of The Electrochemical Society*, vol. 163, no. 11, F3105, 2016.

[122] L. Ma, S. Sui, and Y. Zhai, "Investigations on high performance proton exchange membrane water electrolyzer," *International Journal of Hydrogen Energy*, vol. 34, no. 2, pp. 678–684, 2009.

[123] C. Rozain, E. Mayousse, N. Guillet, and P. Millet, "Influence of iridium oxide loadings on the performance of PEM water electrolysis cells: Part I–Pure IrO2-based anodes," *Applied Catalysis B: Environmental*, vol. 182, pp. 153 –160, 2016. DOI: https://doi.org/10.1016/j.apcatb.2015.09.013.

[124] U. Babic, E. Nilsson, A. Pătru, T. J. Schmidt, and L. Gubler, "Proton transport in catalyst layers of a polymer electrolyte water electrolyzer: Effect of the anode catalyst loading," *Journal of The Electrochemical Society*, vol. 166, no. 4, F214, 2019.

[125] M. Mandal, M. Moore, and M. Secanell, "Measurement of the protonic and electronic conductivities of PEM water electrolyzer electrodes," *ACS Applied Materials & Interfaces*, vol. 12, no. 44, pp. 49 549–49 562, 2020.

[126] M. K. Mandal, "Understanding the physical phenomena limiting the inkjet printed PEM water electrolyzer performance," PhD thesis, University of Alberta, Apr. 2022.

[127] T. Schuler, J. M. Ciccone, B. Krentscher, F. Marone, C. Peter, T. J. Schmidt, and F. N. Büchi, "Hierarchically structured porous transport layers for polymer electrolyte water electrolysis," *Advanced Energy Materials*, vol. 10, no. 2, p. 1 903 216, 2020.

[128] M. Ahadi, M. Tam, J. Stumper, and M. Bahrami, "Electronic conductivity of catalyst layers of polymer electrolyte membrane fuel cells: Through-plane vs. in-plane," *international Journal of Hydrogen Energy*, vol. 44, no. 7, pp. 3603–3614, 2019.

[129] B. Han, M. Risch, S. Belden, S. Lee, D. Bayer, E. Mutoro, and Y. Shao-Horn, "Screening oxide support materials for oer catalysts in acid," *Journal of The Electrochemical Society*, vol. 165, no. 10, F813, 2018.

[130] D. Böhm, M. Beetz, C. Gebauer, M. Bernt, J. Schröter, M. Kornherr, F. Zoller, T. Bein, and D. Fattakhova-Rohlfing, "Highly conductive titania supported iridium oxide nanoparticles with low overall iridium density as OER catalyst for large-scale PEM electrolysis," *Applied Materials Today*, vol. 24, p. 101 134, 2021.

[131] C. Hao, H. Lv, C. Mi, Y. Song, and J. Ma, "Investigation of mesoporous niobium-doped TiO2 as an oxygen evolution catalyst support in an SPE water electrolyzer," *ACS Sustainable Chemistry & Engineering*, vol. 4, no. 3, pp. 746–756, 2016.

[132] W. Xu and K. Scott, "The effects of ionomer content on PEM water electrolyser membrane electrode assembly performance," *International Journal of Hydrogen Energy*, vol. 35, no. 21, pp. 12 029–12 037, 2010.

[133] U. Babic, T. J. Schmidt, and L. Gubler, "Communication—contribution of catalyst layer proton transport resistance to voltage loss in polymer electrolyte water electrolyzers," *Journal of The Electrochemical Society*, vol. 165, no. 15, J3016, 2018.

[134] H. Iden, A. Ohma, and K. Shinohara, "Analysis of proton transport in pseudo catalyst layers," *Journal of The Electrochemical Society*, vol. 156, no. 9, B1078–B1084, 2009.

[135] H. Iden, K. Sato, A. Ohma, and K. Shinohara, "Relationship among microstructure, ionomer property and proton transport in pseudo catalyst layers," *Journal of The Electrochemical Society*, vol. 158, no. 8, B987–B994, 2011.

[136] C. Marr and X. Li, "Composition and performance modelling of catalyst layer in a proton exchange membrane fuel cell," *Journal of Power Sources*, vol. 77, no. 1, pp. 17–27, 1999.

[137] K. C. Neyerlin, W. Gu, J. Jorne, and H. A. Gasteiger, "Study of the exchange current density for the hydrogen oxidation and evolution reactions," *Journal of the Electrochemical Society*, vol. 154, no. 7, B631–B635, 2007.

[138] M. F. Tovini, A. Hartig-Weiß, H. A. Gasteiger, and H. A. El-Sayed, "The discrepancy in oxygen evolution reaction catalyst lifetime explained: RDE vs MEA-dynamicity within the catalyst layer matters," *Journal of The Electrochemical Society*, vol. 168, no. 1, p. 014 512, 2021.

[139] T. Schuler, T. Kimura, T. J. Schmidt, and F. N. Büchi, "Towards a generic understanding of oxygen evolution reaction kinetics in polymer electrolyte water electrolysis," *Energy & Environmental Science*, vol. 13, no. 7, pp. 2153–2166, 2020.

[140] H. Ohno, S. Nohara, K. Kakinuma, M. Uchida, and H. Uchida, "Effect of electronic conductivities of iridium oxide/doped SnO2 oxygen-evolving catalysts on the polarization properties in proton exchange membrane water electrolysis," *Catalysts*, vol. 9, no. 1, p. 74, 2019.

[141] G. Yang, S. Yu, Y. Li, K. Li, L. Ding, Z. Xie, W. Wang, and F.-Y. Zhang, "Role of electron pathway in dimensionally increasing water splitting reaction sites in liquid electrolytes," *Electrochimica Acta*, vol. 362, p. 137 113, 2020.

[142] Y. Jang, C. Seol, S. M. Kim, and S. Jang, "Investigation of the correlation effects of catalyst loading and ionomer content in an anode electrode on the performance of polymer electrode membrane water electrolysis," *International Journal of Hydrogen Energy*, vol. 47, no. 42, pp. 18 229–18 239, 2022.

[143] E. C. Ortiz, F. Hegge, M. Breitwieser, and S. Vierrath, "Improving the performance of proton exchange membrane water electrolyzers with low Ir-loaded anodes by adding PEDOT: PSS as electrically conductive binder," *RSC Advances*, vol. 10, no. 62, pp. 37 923–37 927, 2020.

[144] M. Fujita, I. Arima, H. Goto, S. Konaka, and T. Tada, "The relationship between activity and durability of surface area and catalyst loading of IrOx anode catalyst in proton exchange membrane water electrolysis (PEMWE)," in *ECS Meeting Abstracts*, IOP Publishing, 2020, p. 2466.

[145] M. Bernt, A. Siebel, and H. A. Gasteiger, "Analysis of voltage losses in PEM water electrolyzers with low platinum group metal loadings," *Journal of The Electrochemical Society*, vol. 165, no. 5, F305–F314, 2018. DOI: 10.1149/2.0641805jes.

[146] M. Bühler, F. Hegge, P. Holzapfel, M. Bierling, M. Suermann, S. Vierrath, and S. Thiele, "Optimization of anodic porous transport electrodes for proton exchange membrane water electrolyzers," *Journal of Materials Chemistry A*, vol. 7, no. 47, pp. 26 984–26 995, 2019.

[147] S. Al Shakhshir, X. Cui, S. Frensch, and S. K. Kær, "In-situ experimental characterization of the clamping pressure effects on low temperature polymer electrolyte membrane electrolysis," *International Journal of Hydrogen Energy*, vol. 42, no. 34, pp. 21 597–21 606, 2017.

[148] E. Borgardt, L. Giesenberg, M. Reska, M. Müller, K. Wippermann, M. Langemann, W. Lehnert, and D. Stolten, "Impact of clamping pressure and stress relaxation on the performance of different polymer electrolyte membrane water electrolysis cell designs," *International journal of hydrogen energy*, vol. 44, no. 42, pp. 23 556–23 567, 2019.

[149] S. H. Frensch, A. C. Olesen, S. S. Araya, and S. K. Kær, "Model-supported characterization of a PEM water electrolysis cell for the effect of compression," *Electrochimica Acta*, vol. 263, pp. 228 –236, 2018. DOI: https://doi.org/10.1016/j.electacta.2018.01.040.

[150] A. Martin, P. Trinke, M. Stähler, A. Stähler, F. Scheepers, B. Bensmann, M. Carmo, W. Lehnert, and R. Hanke-Rauschenbach, "The effect of cell compression and cathode pressure on hydrogen crossover in PEM water electrolysis," *Journal of The Electrochemical Society*, vol. 169, no. 1, p. 014 502, 2022.

[151] M. Stähler, A. Stähler, F. Scheepers, M. Carmo, W. Lehnert, and D. Stolten, "Impact of porous transport layer compression on hydrogen permeation in pem water electrolysis," *International Journal of Hydrogen Energy*, vol. 45, no. 7, pp. 4008–4014, 2020.

[152] M. Secanell, A. Putz, S. Shukla, P. Wardlaw, M. Bhaiya, L. M. Pant, and M. Sabharwal, "Mathematical modelling and experimental analysis of thin, low-loading fuel cell electrodes," *ECS Transactions*, vol. 69, no. 17, p. 157, 2015.

[153] M. R. Gerhardt, L. M. Pant, J. C. M. Bui, A. R. Crothers, V. M. Ehlinger, J. C. Fornaciari, J. Liu, and A. Z. Weber, "Methods—practices and pitfalls in voltage breakdown analysis of electrochemical energy-conversion systems," *Journal of The Electrochemical Society*, 2021.

[154] D. C. Sabarirajan, J. Liu, Y. Qi, A. Perego, A. T. Haug, and I. V. Zenyuk, "Determining proton transport in pseudo catalyst layers using hydrogen pump DC and AC techniques," *Journal of The Electrochemical Society*, vol. 167, no. 8, p. 084 521, 2020.

[155] Y. Qi, J. Liu, D. C. Sabarirajan, Y. Huang, A. Perego, A. T. Haug, and I. V. Zenyuk, "Interpreting ionic conductivity for polymer electrolyte fuel cell catalyst layers with electrochemical impedance spectroscopy and transmission line modeling," *Journal of the Electrochemical Society*, vol. 168, no. 5, p. 054 502, 2021.

[156] A. Kulikovsky, "Proton and electron transport impedance of inactive catalyst layer embedded in PEM fuel cell," *Journal of The Electrochemical Society*, vol. 168, no. 3, p. 034 501, 2021.

[157] M Maier, K Smith, J Dodwell, G Hinds, P. Shearing, and D. Brett, "Mass transport in PEM water electrolysers: A review," *International Journal of Hydrogen Energy*, 2021.

[158] B. J. Etzold, U. Krewer, S. Thiele, A. Dreizler, E. Klemm, and T. Turek, "Understanding the activity transport nexus in water and CO2 electrolysis: State of the art, challenges and perspectives," *Chemical Engineering Journal*, p. 130 501, 2021.

[159] S. De Angelis, T. Schuler, M. A. Charalambous, F. Marone, T. J. Schmidt, and F. N. Büchi, "Unraveling two-phase transport in porous transport layer materials for polymer electrolyte water electrolysis," *Journal of Materials Chemistry A*, vol. 9, no. 38, pp. 22 102–22 113, 2021.

[160] S. Shukla, D. Stanier, M. S. Saha, J. Stumper, and M. Secanell, "Analysis of inkjet printed pefc electrodes with varying platinum loading," *Journal of The Electrochemical Society*, vol. 163, no. 7, F677–F687, 2016. DOI: 10.1149/2.1111607jes.

[161] C. Rozain and P. Millet, "Electrochemical characterization of polymer electrolyte membrane water electrolysis cells," *Electrochimica Acta*, vol. 131, pp. 160–167, 2014. DOI: https://doi.org/10.1016/j.electacta.2014.01.099.

[162] P. Lettenmeier, R. Wang, R. Abouatallah, S. Helmly, T. Morawietz, R. Hiesgen, S. Kolb, F. Burggraf, J. Kallo, A. S. Gago, *et al.*, "Durable membrane electrode assemblies for proton exchange membrane electrolyzer systems operating at high current densities," *Electrochimica Acta*, vol. 210, pp. 502–511, 2016.

[163] K. A. Lewinski, D. van der Vliet, and S. M. Luopa, "NSTF advances for PEM electrolysis - the effect of alloying on activity of NSTF electrolyzer catalysts and performance of NSTF based PEM electrolyzers," *ECS Transactions*, vol. 69, no. 17, pp. 893–917, 2015. DOI: 10.1149/06917.0893ecst.

[164] H. Ito, T. Maeda, A. Nakano, A. Kato, and T. Yoshida, "Influence of pore structural properties of current collectors on the performance of proton exchange membrane electrolyzer," *Electrochimica Acta*, vol. 100, pp. 242 –248, 2013. DOI: https://doi.org/10.1016/j.electacta.2012.05.068.

[165] M. Suermann, A. Pătru, T. J. Schmidt, and F. N. Büchi, "High pressure polymer electrolyte water electrolysis: Test bench development and electrochemical analysis," *International Journal of Hydrogen Energy*, vol. 42, no. 17, pp. 12076 –12 086, 2017. DOI: https://doi.org/10.1016/j.ijhydene.2017.01.224.

[166] P. Kim, J. Lee, C. Lee, K. Fahy, P Shrestha, K Krause, H. Shafaque, and A Bazylak, "Tailoring catalyst layer interface with titanium mesh porous transport layers," *Electrochimica Acta*, vol. 373, p. 137 879, 2021.

[167] B. Zhao, C. Lee, J. K. Lee, K. F. Fahy, J. M. LaManna, E. Baltic, D. L. Jacobson, D. S. Hussey, and A. Bazylak, "Superhydrophilic porous transport layer enhances efficiency of polymer electrolyte membrane electrolyzers," *Cell Reports Physical Science*, vol. 2, no. 10, p. 100 580, 2021.

[168] J. M. Spurgeon and N. S. Lewis, "Proton exchange membrane electrolysis sustained by water vapor," *Energy Environ. Sci.*, vol. 4, pp. 2993–2998, 8 2011. DOI: 10.1039/C1EE01203G.

[169] M. Müller, M. Carmo, A. Glüsen, M. Hehemann, S. Saba, W. Zwaygardt, and D. Stolten, "Water management in membrane electrolysis and options for advanced plants," *International Journal of Hydrogen Energy*, vol. 44, no. 21, pp. 10147 –10 155, 2019. DOI: https://doi.org/10.1016/j.ijhydene.2019.02.139.

[170] J.-M. Hu, J.-Q. Zhang, and C.-N. Cao, "Oxygen evolution reaction on IrO2-based DSA® type electrodes: Kinetics analysis of tafel lines and EIS," *International Journal of Hydrogen Energy*, vol. 29, no. 8, pp. 791 –797, 2004. DOI: https://doi.org/10.1016/j.ijhydene.2003.09.007.

[171] A. Parthasarathy, S. Srinivasan, A. J. Appleby, and C. Martin, "Temperature dependence of the electrode kinetics of oxygen reduction at the platinum/-nafion(r) interface - a microelectrode investigation," *Journal of the Electrochemical Society*, vol. 139, no. 9, pp. 2530–2537, 1992.

[172] V. I. Basura, P. D. Beattie, and S. Holdcroft, "Solid-state electrochemical oxygen reduction at Pt Nafion 117 and Pt BAM3G 407 interfaces," *Journal of Electroanalytical Chemistry*, vol. 458, no. 1-2, pp. 1–5, 1998.

[173] A. Kulikovsky, "A model for impedance of a PEM fuel cell cathode with poor electron conductivity," *Journal of electroanalytical chemistry*, vol. 801, pp. 122–128, 2017.

[174] O. Selamet, U. Pasaogullari, D. Spernjak, D. Hussey, D. Jacobson, and M. Mat, "Two-phase flow in a proton exchange membrane electrolyzer visualized in situ by simultaneous neutron radiography and optical imaging," *International Journal of Hydrogen Energy*, vol. 38, no. 14, pp. 5823 –5835, 2013. DOI: https://doi.org/10.1016/j.ijhydene.2013.02.087.

[175] J. Seweryn, J. Biesdorf, T. J. Schmidt, and P. Boillat, "Communication—neutron radiography of the water/gas distribution in the porous layers of an operating electrolyser," *Journal of The Electrochemical Society*, vol. 163, no. 11, F3009–F3011, 2016.

[176] M. Zlobinski, T. Schuler, F. N. Büchi, T. J. Schmidt, and P. Boillat, "Transient and steady state two-phase flow in anodic porous transport layer of proton exchange membrane water electrolyzer," *Journal of the electrochemical society*, vol. 167, no. 8, p. 084 509, 2020.

[177] F. Arbabi, A. Kalantarian, R. Abouatallah, R. Wang, J. Wallace, and A. Bazylak, "Feasibility study of using microfluidic platforms for visualizing bubble flows in electrolyzer gas diffusion layers," *Journal of Power Sources*, vol. 258, pp. 142 –149, 2014. DOI: https://doi.org/10.1016/j.jpowsour.2014.02.042.

[178] E. Leonard, A. D. Shum, S. Normile, D. C. Sabarirajan, D. G. Yared, X. Xiao, and I. V. Zenyuk, "Operando x-ray tomography and sub-second radiography for characterizing transport in polymer electrolyte membrane electrolyzer," *Electrochimica Acta*, vol. 276, pp. 424–433, 2018.

[179] I. Dedigama, P. Angeli, K. Ayers, J. Robinson, P. Shearing, D. Tsaoulidis, and D. Brett, "In situ diagnostic techniques for characterisation of polymer electrolyte membrane water electrolysers – flow visualisation and electrochemical impedance spectroscopy," *International Journal of Hydrogen Energy*, vol. 39, no. 9, pp. 4468 –4482, 2014. DOI: https://doi.org/10.1016/j.ijhydene.2014.01.026.

[180] Y. Li, Z. Kang, J. Mo, G. Yang, S. Yu, D. A. Talley, B. Han, and F.-Y. Zhang, "In-situ investigation of bubble dynamics and two-phase flow in proton exchange membrane electrolyzer cells," *International Journal of Hydrogen Energy*, vol. 43, no. 24, pp. 11223 –11 233, 2018. DOI: https://doi.org/10.1016/j.ijhydene.2018.05.006.

[181] Z. Wang, C. Xu, X. Wang, Z. Liao, and X. Du, "Numerical investigation of water and temperature distributions in a proton exchange membrane electrolysis cell," *Science China Technological Sciences*, vol. 64, no. 7, pp. 1555–1566, 2021.

[182] W. Wang, Z. Xie, K. Li, S. Yu, L. Ding, and F.-Y. Zhang, "Recent progress in in-situ visualization of electrochemical reactions in electrochemical energy devices," *Current Opinion in Electrochemistry*, p. 101 088, 2022.

[183] W. Wang, K. Li, L. Ding, S. Yu, Z. Xie, D. A. Cullen, H. Yu, G. Bender, Z. Kang, J. A. Wrubel, *et al.*, "Exploring the impacts of conditioning on proton exchange membrane electrolyzers by in situ visualization and electrochemistry characterization," *ACS Applied Materials & Interfaces*, vol. 14, no. 7, pp. 9002–9012, 2022.

[184] P. Lettenmeier, S. Kolb, F. Burggraf, A. Gago, and K. Friedrich, "Towards developing a backing layer for proton exchange membrane electrolyzers," *Journal of Power Sources*, vol. 311, pp. 153 –158, 2016. DOI: https://doi.org/10.1016/j.jpowsour.2016.01.100.

[185] Q. Chen, Y. Wang, F. Yang, and H. Xu, "Two-dimensional multi-physics modeling of porous transport layer in polymer electrolyte membrane electrolyzer for water splitting," *International Journal of Hydrogen Energy*, vol. 45, no. 58, pp. 32 984–32 994, 2020.

[186] P. A. García-Salaberri, "1D two-phase, non-isothermal modeling of a proton exchange membrane water electrolyzer: An optimization perspective," *Journal of Power Sources*, vol. 521, p. 230 915, 2022.

[187] L. Wu, G. Zhang, B. Xie, C. Tongsh, and K. Jiao, "Integration of the detailed channel two-phase flow into three-dimensional multi-phase simulation of proton exchange membrane electrolyzer cell," *International Journal of Green Energy*, vol. 18, no. 6, pp. 541–555, 2021.

[188] A. Z. Weber and J. Newman, "Modeling transport in polymer-electrolyte fuel cells," *Chemical Reviews*, vol. 104, no. 10, pp. 4679–4726, 2004.

[189] A. Z. Weber and J. Newman, "Effects of microporous layers in polymer electrolyte fuel cells," *Journal of the Electrochemical Society*, vol. 152, no. 4, A677–A688, 2005.

[190] R. J. Balliet and J. Newman, "Cold start of a polymer-electrolyte fuel cell i. development of a two-dimensional model," *Journal of the Electrochemical Society*, vol. 158, no. 8, B927, 2011. DOI: https://doi.org/10.1149/1.3592430.

[191] J Zhou, A Putz, and M Secanell, "A mixed wettability pore size distribution based mathematical model for analyzing two-phase flow in porous electrodes i. mathematical model," *Journal of The Electrochemical Society*, vol. 164, no. 6, F530–F539, 2017.

[192] J. Zhou, S. Shukla, A. Putz, and M. Secanell, "Analysis of the role of the microporous layer in improving polymer electrolyte fuel cell performance," *Electrochimica Acta*, vol. 268, pp. 366 –382, 2018. DOI: https://doi.org/10.1016/j.electacta.2018.02.100.

[193] A. Goshtasbi, P. García-Salaberri, J. Chen, K. Talukdar, D. G. Sanchez, and T. Ersal, "Through-the-membrane transient phenomena in PEM fuel cells: A modeling study," *Journal of The Electrochemical Society*, vol. 166, no. 7, F3154, 2019. DOI: https://doi.org/10.1149/2.0181907jes.

[194] M. Moore, S. Shukla, S. Voss, K. Karan, A. Weber, I. Zenyuk, and M. Secanell, "A numerical study on the impact of cathode catalyst layer loading on the open circuit voltage in a proton exchange membrane fuel cell," *Journal of The Electrochemical Society*, vol. 168, no. 4, p. 044 519, 2021.

[195] T. Springer, T. Zawodzinski, and S. Gottesfeld, "Polymer electrolyte fuel cell model," *Journal of the Electrochemical Society*, vol. 138, no. 8, pp. 2334–2342, Aug. 1991.

[196] A. Kosakian, "Transient numerical modeling of proton-exchange-membrane fuel cells," PhD thesis, University of Alberta, Sep. 2021.

[197] R. B. Bird, W. E. Stewart, and E. Lightfoot, *Transport Phenomena*, 2nd. J. Wiley and Sons, 2002.

[198] M. Secanell, "Computational modeling and optimization of proton exchange membrane fuel cells," PhD thesis, University of Victoria, 2007.

[199] A. Kulikovsky, "Hydrogen crossover impedance of a PEM fuel cell at open circuit," *Electrochimica Acta*, vol. 247, pp. 730 –735, 2017. DOI: https://doi.org/10.1016/j.electacta.2017.07.004.

[200] M. Secanell, A. Putz, P. Wardlaw, V. Zingan, M. Bhaiya, M. Moore, J. Zhou, C. Balen, and K. Domican, "OpenFCST: An open-source mathematical modelling software for polymer electrolyte fuel cells," *ECS Transactions*, vol. 64, no. 3, pp. 655–680, 2014.

[201] A. Kosakian and M. Secanell, "Membrane-electrode-assembly modeling using OpenFCST," in *PEM fuel cells. Characterization and modeling*, J. Jankovic and J. Stumper, Eds. de Gruyter, 2023 (In print).

[202] D. W. Kelly, J. P. de S. R. Gago, O. C. Zienkiewicz, and I. Babuska, "A posteriori error analysis and adaptive processes in the finite element method: Part i - error analysis," *International Journal for Numerical Methods in Engineering*, vol. 19, no. 11, pp. 1593–1619, Nov. 1983.

[203] M. Mandal, A. Valls, N. Gangnus, and M. Secanell, "Analysis of inkjet printed catalyst coated membranes for polymer electrolyte electrolyzers," *Journal of The Electrochemical Society*, vol. 165, no. 7, F543, 2018.

[204] M. Mandal and M. Secanell, "Improved polymer electrolyte membrane water electrolyzer performance by using carbon black as a pore former in the anode catalyst layer," *Journal of Power Sources*, vol. 541, p. 231 629, 2022.

[205] H. Dhawan, X. Tan, J. Shen, J. Woodford, M. Secanell, and N. Semagina, "Strong metal-support interactions in zro2-supported irox catalyst for efficient oxygen evolution reaction," *ChemCatChem*, e202300668,

[206] S Shukla, K Domican, K Karan, S Bhattacharjee, and M Secanell, "Analysis of low platinum loading thin polymer electrolyte fuel cell electrodes prepared by inkjet printing," *Electrochimica Acta*, vol. 156, pp. 289–300, 2015.

[207] K. Bromberger, J. Ghinaiya, T. Lickert, A. Fallisch, and T. Smolinka, "Hydraulic ex situ through-plane characterization of porous transport layers in pem water electrolysis cells," *International Journal of Hydrogen Energy*, vol. 43, no. 5, pp. 2556 –2569, 2018. DOI: https://doi.org/10.1016/j.ijhydene.2017.12.042.

[208] F. Hegge, R. Moroni, P. Trinke, B. Bensmann, R. Hanke-Rauschenbach, S. Thiele, and S. Vierrath, "Three-dimensional microstructure analysis of a polymer electrolyte membrane water electrolyzer anode," *Journal of Power Sources*, vol. 393, pp. 62 –66, 2018. DOI: https://doi.org/10.1016/j.jpowsour.2018.04.089.

[209] S. Jung, M. Sabharwal, A. Jarauta, F. Wei, M. Gingras, J. Gostick, and M. Secanell, "Estimation of relative transport properties in porous transport layers using pore-scale and pore-network simulations," *Journal of The Electrochemical Society*, vol. 168, no. 6, p. 064 501, 2021.

[210] M. Sabharwal, L. M. Pant, N. Patel, and M. Secanell, "Computational analysis of gas transport in fuel cell catalyst layer under dry and partially saturated conditions," *Journal of The Electrochemical Society*, vol. 166, no. 7, F3065, 2019. DOI: https://doi.org/10.1149/2.0081907jes.

[211] J. Włoch, A. P. Terzyk, M. Wisniewski, and P. Kowalczyk, "Nanoscale water contact angle on polytetrafluoroethylene surfaces characterized by molecular dynamics–atomic force microscopy imaging," *Langmuir*, vol. 34, no. 15, pp. 4526–4534, 2018.

[212] A. Cruz, L. Abad, N. Carretero, J Moral-Vico, J Fraxedas, P Lozano, G Subías, V Padial, M Carballo, J. Collazos-Castro, *et al.*, "Iridium oxohydroxide, a significant member in the family of iridium oxides. stoichiometry, characterization, and implications in bioelectrodes," *The Journal of Physical Chemistry C*, vol. 116, no. 8, pp. 5155–5168, 2012.

[213] T.-W. Chung, C.-N. Huang, P.-C. Chen, T. Noda, T. Tokuda, and J. Ohta, "Fabrication of iridium oxide/platinum composite film on titanium substrate for high-performance neurostimulation electrodes," *Coatings*, vol. 8, no. 12, p. 420, 2018.

[214] B. M. A. et al., "Dakota, a multilevel parallel object-oriented framework for design optimization, parameter estimation, uncertainty quantification, and sensitivity analysis: Version 6.7 user's manual," Sandia National Laboratory, Tech. Rep. 2014-4633, 2014.

[215] P. Trinke, B. Bensmann, and R. Hanke-Rauschenbach, "Experimental evidence of increasing oxygen crossover with increasing current density during PEM water electrolysis," *Electrochemistry Communications*, vol. 82, pp. 98 –102, 2017. DOI: https://doi.org/10.1016/j.elecom.2017.07.018.

[216] S. M. Kim, C.-Y. Ahn, Y.-H. Cho, S. Kim, W. Hwang, S. Jang, S. Shin, G. Lee, Y.-E. Sung, and M. Choi, "High-performance fuel cell with stretched catalyst-coated membrane: One-step formation of cracked electrode," *Scientific reports*, vol. 6, no. 1, pp. 1–7, 2016. DOI: 10.1038/srep26503.

[217] C.-Y. Ahn, S. Jang, Y.-H. Cho, J. Choi, S. Kim, S. M. Kim, Y.-E. Sung, and M. Choi, "Guided cracking of electrodes by stretching prism-patterned membrane electrode assemblies for high-performance fuel cells," *Scientific reports*, vol. 8, no. 1, pp. 1–9, 2018. DOI: https://doi.org/10.1038/s41598-018-19861-6.

[218] N. Kumano, K. Kudo, A. Suda, Y. Akimoto, M. Ishii, and H. Nakamura, "Controlling cracking formation in fuel cell catalyst layers," *Journal of Power Sources*, vol. 419, pp. 219–228, 2019. DOI: https://doi.org/10.1016/j.jpowsour.2019.02.058.

[219] T. Tranter, M Tam, and J. Gostick, "The effect of cracks on the in-plane electrical conductivity of PEFC catalyst layers," *Electroanalysis*, vol. 31, no. 4, pp. 619–623, 2019. DOI: https://doi.org/10.1002/elan.201800553.

[220] D. Y. Chung, S. Park, P. P. Lopes, V. R. Stamenkovic, Y.-E. Sung, N. M. Markovic, and D. Strmcnik, "Electrokinetic analysis of poorly conductive electrocatalytic materials," *ACS Catalysis*, vol. 10, no. 9, pp. 4990–4996, 2020.

[221] G. Yang, S. Yu, Z. Kang, Y. Li, G. Bender, B. S. Pivovar, J. B. Green Jr, D. A. Cullen, and F.-Y. Zhang, "Building electron/proton nanohighways for full utilization of water splitting catalysts," *Advanced Energy Materials*, vol. 10, no. 16, p. 1 903 871, 2020.

[222] S. Yu, K. Li, W. Wang, Z. Xie, L. Ding, Z. Kang, J. Wrubel, Z. Ma, G. Bender, H. Yu, *et al.*, "Tuning catalyst activation and utilization via controlled electrode patterning for low-loading and high-efficiency water electrolyzers," *Small*, vol. 18, no. 14, p. 2 107 745, 2022.

[223] T. Schuler, T. J. Schmidt, and F. N. Büchi, "Polymer electrolyte water electrolysis: Correlating performance and porous transport layer structure: Part ii. electrochemical performance analysis," *Journal of The Electrochemical Society*, vol. 166, no. 10, F555, 2019.

[224] J. Kwen, G. Doo, S. Choi, H. Guim, S. Yuk, D.-H. Lee, D. W. Lee, J. Hyun, and H.-T. Kim, "Identification of the electrical connection in the catalyst layer of the polymer electrolyte membrane water electrolyzer," *International Journal of Hydrogen Energy*, vol. 47, no. 30, pp. 14 017–14 026, 2022.

[225] S. Kumaravel, E. Kim, B. B. Kale, A. Adhikari, R. Patel, and S. Kundu, "Recent developments in conductive polymer-based electro-/photoelectrocatalytic materials for effective hydrogen/oxygen evolution reactions: A review," *ChemElectroChem*, vol. 9, no. 19, e202200724, 2022.

[226] M Moore, M Mandal, A Kosakian, and M Secanell, "Numerical study of the impact of two-phase flow in the anode catalyst layer on the performance of proton exchange membrane water electrolysers," *Journal of The Electrochemical Society*, vol. 170, no. 4, p. 044 503, 2023.

[227] M. Moore, M. Mandal, A. Kosakian, and M. Secanell, "Good practices and limitations of the hydrogen pump technique for catalyst layer protonic conductivity estimation," *ACS Applied Materials & Interfaces*, vol. 15, no. 31, pp. 37 312–37 326, 2023.

[228] M Moore, E Beauliu, M Mandal, and M Secanell, "A numerical study on the impact of anode catalyst layer electronic conductivity on performance in proton exchange membrane water electrolysis (in preparation),"

[229] M. Rhandi, M. Trégaro, F. Druart, J. Deseure, and M. Chatenet, "Electrochemical hydrogen compression and purification versus competing technologies: Part i. pros and cons," *Chinese Journal of Catalysis*, vol. 41, no. 5, pp. 756–769, 2020.

[230] D. Marciuš, A. Kovač, and M. Firak, "Electrochemical hydrogen compressor: Recent progress and challenges," *International journal of hydrogen energy*, vol. 47, no. 57, pp. 24 179–24 193, 2022.

[231] M Maier, J Dodwell, R Ziesche, C Tan, T Heenan, J Majasan, N Kardjilov, H Markötter, I Manke, L Castanheira, *et al.*, "Mass transport in polymer electrolyte membrane water electrolyser liquid-gas diffusion layers: A combined neutron imaging and x-ray computed tomography study," *Journal of Power Sources*, vol. 455, p. 227 968, 2020.

[232] W. Wang, L. Ding, Z. Xie, S. Yu, B. Canfield, G. Bender, J. A. Wrubel, B. S. Pivovar, and F.-Y. Zhang, "Discovering reactant supply pathways at electrode/pem reaction interfaces via a tailored interface-visible characterization cell," *Small*, p. 2 207 809, 2023.

[233] P. Trinke, B. Bensmann, and R. Hanke-Rauschenbach, "Current density effect on hydrogen permeation in PEM water electrolyzers," *International Journal of Hydrogen Energy*, vol. 42, no. 21, pp. 14355 –14 366, 2017. DOI: https://doi.org/10.1016/j.ijhydene.2017.03.231.

[234] T. Schuler, R. De Bruycker, T. J. Schmidt, and F. N. Büchi, "Polymer electrolyte water electrolysis: Correlating porous transport layer structural properties and performance: Part i. tomographic analysis of morphology and topology," *Journal of The Electrochemical Society*, vol. 166, no. 4, F270, 2019.

[235] D. Kulkarni, A. Huynh, P. Satjarutanun, M. O'Brien, S. Shimpalee, D. Parkinson, P. Shevchenko, F. DeCarlo, N. Danilovic, K. E. Ayers, *et al.*, "Elucidating effects of catalyst loadings and porous transport layer morphologies on operation of proton exchange membrane water electrolyzers," *Applied Catalysis B: Environmental*, p. 121 213, 2022.